

An Investigation of the Archean Climate Using the NCAR CCM

Gregory S. Jenkins

A dissertation submitted to The University of Michigan in partial fulfillment of the requirements for the degree of Doctor of Philosophy, Department of Atmospheric and Space Sciences, based on research conducted in cooperation with the scientific staff of the Climate and Global Dynamics Division, National Center for Atmospheric Research, Boulder, Colorado.

Mr. Jenkins received a B.S. degree in 1987 from Lincoln University and an M.S. degree in 1989 from The University of Michigan.

NCAR



Cooperative Thesis No. 132

The University of Michigan and
National Center for Atmospheric Research

1991

This thesis is dedicated to my late mother and father, Senia and Kirby for their love, patience and insistence of education, and to many deceased friends who have influenced my life, Wayne, Miss Kang, Miss Redmon, Mr. Seals, Mr. Merrit, Mr. Lewis, Miss Delores, Uncle Jerry, Uncle Dave, Aunt Ruth, and to God who delivered me through the trials and tribulations of graduate school.

ACKNOWLEDGEMENTS

I wish to thank Professor William Kuhn, James Walker, Levi Thompson and Dr. Warren Washington for serving as members of my doctoral committee, and for carefully reviewing my thesis.

In particular I would like to thank Professor Kuhn for allowing me to undertake the research of this thesis by providing funds and computer resources. A special thanks to Warren Washington for accommodating me as a visiting scientist at NCAR and providing computing resources for the research. Without Bill and Warren's support, the research would not have been possible.

I owe special thanks to Ann Modahl of NCAR for her extra efforts in assisting in with editing aspects of this thesis and to Linda VerPlank for her instruction on running the cray supercomputer and to Gerry Meehl for his discussion of the NCAR processor.

I would to thank my wife, Helen for her patience, support and love during many turbulent and good times in graduate school. I would also like to acknowledge the many friends that I have been associated with at the University, and to the friends and family of Philadelphia who constantly supported my efforts.

This research has been supported by the department of Atmospheric, Oceanic, and Space Sciences and NASA grant NGT-70120.

TABLE OF CONTENTS

DEDICATION	ii
ACKNOWLEDGEMENTS	iii
LIST OF FIGURES	vi
LIST OF TABLES	xi
CHAPTER	
I. INTRODUCTION	1
1.1 Faint-Young Sun Paradox	
1.2 Background Review of Climatic Conditions of the Early Archean	
1.3 Overview of Thesis	
II. MODEL DESCRIPTION and PLANNED EXPERIMENTS	13
2.1 Climate Models	
2.2 Model Description of NCAR CCM	
2.3 Comparison of CCM to Observed Climate	
2.4 CO ₂ -Induced Climate Change	
2.5 Planned Experiments	
III. ARCHEAN CLIMATE SIMULATIONS	33
3.1 The Effects of Faster Rotation Rate on the Climate System	
3.2 Zero Land Fraction and Lower Solar Luminosity Experiments	
3.3 CO ₂ and Rotation Rate under Lower Solar Luminosity Conditions	
3.4 Sensitivity Experiments with Combined Climatic Factors	
IV. DISCUSSION	134
4.1 Rotation Rate	
4.2 Land Fraction	
4.3 Solar Luminosity	
4.4 Carbon Dioxide	

4.5 Experiments with Combined Factors

V. CONCLUSIONS AND RECOMMENDATIONS 147

5.1 Conclusion

5.2 Recommendations

BIBLIOGRAPHY 151

LIST OF FIGURES

Figure

1.1	Evolution of land fraction (Kuhn et al., 1989).	4
1.2	Ages of crustal formation (Broecker, 1985).	4
1.3	Evolution of solar luminosity (Kuhn et al., 1989).	5
1.4	Evolution of rotation rate (Kuhn et al., 1989).	6
1.5	Physics of daily tides (Goldreich, 1972).	8
2.1	Cloud scheme for the NCAR CCM (Ramanathan et al., 1983). . . .	18
2.2	Zonally averaged surface of temperature in degrees Kelvin. (a) ob- served; (b) simulated.	21
2.3	Latitude-height plot of temperature in degrees Kelvin. (a) observed; (b) simulated.	23
2.4	Latitude-height distribution of (a) observed zonal wind; (c) stream- function (Oort and Peixóto, 1983).	24
2.5	Latitude-height distribution of zonal wind and streamfunction. (a) zonal wind; (b) streamfunction.	25
2.6	Tropospheric distribution of mixing ratio. (a) observed; (b) simulated.	26
2.7	Zonally averaged total cloud fraction. (a) observed; (b) simulated. .	28
2.8	Zonally averaged annual precipitation. (a) observed; (b) simulated. .	29
3.1	Zonally averaged surface temperature in degrees Kelvin.	35
3.2	300-mb Northern Hemisphere geopotential heights. (a) control; (b) FastL. Units: meters	36
3.3	Atmospheric temperature difference in degrees Kelvin. FastL minus control.	37
3.4	(a) Zonal wind distribution; (b) mean meridional streamfunction for FastL.	39
3.5	Transient eddy heat transport for the control and FastL. (a) control; (b) FastL. Contour interval: 3 K m s^{-1}	42

3.6	Stationary eddy heat transport for the control and FastL. (a) control; (b) FastL. Contour interval: 2 K m s^{-1}	43
3.7	Difference in eddy heat transport. (a) transient; (b) stationary: FastL minus control.	44
3.8	Observed distribution of transient eddy heat transport at 200 mb. Units: K m s^{-1}	45
3.9	Geographical transient heat at .189S (near 200mb) over North America. (a) control; (b) FastL.	46
3.10	Spectral kinetic energy. (a): control; (b): FastL. Units: J kg^{-1}	47
3.11	Total cloud fraction.	48
3.12	Difference in (a) cloud field; (b) relative humidity. FastL minus control.	49
3.13	Difference in mixing ratio: FastL minus control. Units: g kg^{-1}	50
3.14	Difference in clouds. FastL minus control. (a) convective; (b) non-convective. Units: percent	51
3.15	Zonally averaged precipitation cm yr^{-1}	52
3.16	(a) Absorbed solar radiation; (b) OLR. Units: W m^{-2}	54
3.17	Zonally averaged surface temperature (degrees Kelvin).	56
3.18	Temperature difference (degrees Kelvin). (a) Glocean minus control; (b) ColdO minus control.	57
3.19	Geographical sea-ice distribution. Top: control; middle: Glocean; bottom: ColdO. Units: meters	60
3.20	Zonal wind distribution. (a) Glocean; (b) ColdO.	61
3.21	Mean meridional streamfunction. (a) Glocean; (b) ColdO.	63
3.22	Transient eddy heat transport. (a) Glocean; (b) ColdO.	66
3.23	Difference in transient eddy heat transport. (a) Glocean minus control; (b) ColdO minus control.	67
3.24	Zonally averaged total cloud fraction.	68
3.25	Latitude-height difference in cloud field. Glocean minus control. (a) all clouds; (b) convective clouds.	69
3.26	Latitude-height differences. ColdO minus control. (a) clouds; (b) relative humidity.	71
3.27	Zonally averaged precipitation rates (cm yr^{-1}).	72
3.28	Latitude-height difference for water-vapor mixing ratio (a) Glocean minus control; (b) ColdO minus control.	73

3.29	Surface evaporation (cm yr^{-1}).	74
3.30	Outgoing longwave radiation. Units: W m^{-2}	75
3.31	(a) Absorbed solar radiation by the earth-atmosphere system; (b) planetary albedo.	77
3.32	Zonally averaged surface temperature. Units: degrees Kelvin.	80
3.33	Difference in atmospheric temperatures. (a) 4ColdO minus ColdO; (b) 8ColdO minus ColdO.	82
3.34	Difference in atmospheric temperatures (degrees Kelvin). 14hrColdO minus ColdO.	83
3.35	Zonal wind. (a) 8ColdO; (b) 14hrColdO.	84
3.36	Mean meridional streamfunction. (a) 8ColdO; (b) 14hrColdO.	85
3.37	Transient eddy heat transport. (a) 8ColdO; (b) 14hrColdO.	88
3.38	Difference in transient eddy heat transport. (a) 8ColdO minus ColdO; (b) 14hrColdO minus ColdO.	89
3.39	Spectral kinetic energy. (a) ColdO; (b) 14hrColdO. Units: J kg^{-1}	90
3.40	Zonally averaged cloud field.	91
3.41	Latitude-height difference in clouds. (a) 4ColdO minus ColdO; (b) 8ColdO minus ColdO.	92
3.42	Latitude-height difference of relative humidity. (a) 4ColdO minus ColdO; (b) 8ColdO minus ColdO.	93
3.43	Latitude-height difference of mixing ratio. (a) 4ColdO minus ColdO; (b) 8ColdO minus ColdO	94
3.44	(a) Latitude-height difference of condensed moisture; (b) convective cloud difference. 8ColdO minus ColdO.	95
3.45	Vertical velocity. (a) ColdO; (b) 8ColdO.	96
3.46	Vertical velocity for 14hrColdO. Contour interval: $4 \times 10^{-3} \text{ mb s}^{-1}$	97
3.47	(a) Difference in cloud field; (b) difference in relative humidity. 14hrColdO minus ColdO. Units: percent.	98
3.48	Difference in cloud field. (a) convective; (b) nonconvective. 14hrColdO minus ColdO.	100
3.49	Zonal averaged precipitation. Units: cm yr^{-1}	101
3.50	(a) Difference in mixing ratio. 14hrColdO minus ColdO; (b) Zonally averaged evaporation rates.	102

3.51	Zonally averaged absorbed solar radiation and outgoing longwave radiation.	104
3.52	Geographical sea ice distribution: Top: 4ColdO; middle: 8ColdO; bottom: 14hrColdO. Units: meters.	105
3.53	Zonally averaged surface temperature. Units: degrees Kelvin	107
3.54	Geographical surface temperature: Top: Ice1; middle: Ice2; bottom: Ice3. Units: degrees Kelvin.	109
3.55	Atmospheric temperatures. (a) Ice1; (b) difference in temperature: Ice1 minus Glocean.	110
3.56	Atmospheric temperatures. (a) Ice2; (b) difference in temperature: Ice2 minus Glocean.	111
3.57	Atmospheric temperatures. (a) Ice3; (b) difference in temperature: Ice3 minus Glocean.	112
3.58	Geographical sea ice distribution: Top: Ice1; middle: Ice2; bottom: Ice3. Units: meters	114
3.59	Zonal wind distribution: (a) Ice1; (b) Ice2.	115
3.60	Zonal wind distribution. Ice3. Contour interval: 5 m s ⁻¹	116
3.61	Mean meridional streamfunction: (a) Ice1; (b) Ice2.	117
3.62	Mean meridional streamfunction for Ice3. Contour interval: 1 × 10 ¹⁰ kg s ⁻¹	118
3.63	Transient eddy heat transport. (a) Ice1; (b) difference in heat transport: Ice1 minus Glocean.	119
3.64	Transient eddy heat transport. (a) Ice2; (b) difference in heat transport: Ice2 minus Glocean.	121
3.65	Transient eddy heat transport. (a) Ice3; (b) difference in heat transport: Ice3 minus Glocean.	122
3.66	Spectral kinetic energy. (a) Ice1; (b) Ice2. Units: J kg ⁻¹	123
3.67	Spectral kinetic energy. Ice3. Units: J kg ⁻¹	124
3.68	Zonally averaged cloud field.	125
3.69	Latitude-height difference in clouds. (a) Ice1 minus Glocean; (b) Ice2 minus Glocean.	126
3.70	Latitude-height difference in clouds. Ice3 minus Glocean. Units: percent.	127
3.71	Latitude-height difference of relative humidity. (a) Ice1 minus Glocean; (b) Ice2 minus Glocean.	128

3.72	Latitude-height difference in relative humidity. Ice3 minus Glocean. Units: percent	129
3.73	Latitude-height difference of mixing ratio. (a) Ice1 minus Glocean; (b) Ice2 minus Glocean.	130
3.74	Latitude-height difference in mixing ratio. Ice3 minus Glocean. Units: g kg^{-1}	131
3.75	Precipitation. Units: cm yr^{-1}	131
3.76	Surface evaporation. Units: cm yr^{-1}	132
3.77	Absorbed solar radiation. Units: W m^{-2}	132
3.78	Outgoing longwave radiation. Units: W m^{-2}	133
4.1	Poleward flux of sensible and latent heat for FastL and the control. (a) sensible; (b) latent.	137
4.2	Poleward flux of sensible and latent heat for 14hrColdO and ColdO. (a) sensible; (b) latent.	138
4.3	Poleward flux of latent heat. Units: Watts.	140
4.4	Poleward flux of latent heat. Units: Watts.	142
4.5	Poleward flux of sensible heat. Units: Watts.	143
4.6	Difference in eddy kinetic energy. ColdO minus control. Units: m^{-2} s^{-2}	144
4.7	Poleward flux of latent heat. Units: Watts.	145
4.8	Poleward flux of latent heat. Units: Watts.	145

LIST OF TABLES

Table

2.1	Global values for observed and simulated data	20
3.1	Global mean values for the control and FastL.	35
3.2	Global mean values for control, Glocean, and ColdO.	58
3.3	Global values for ColdO, 4ColdO, 8ColdO and 14hrColdO.	79
3.4	Global mean values for Ice1, Ice2, and Ice3.	107

CHAPTER I

INTRODUCTION

1.1 Faint-Young Sun Paradox

Stellar models (Newman and Rood, 1977; Gough, 1977) indicate that, early in our Sun's history its energy output was significantly lower than at present—some 15–25% lower than present by 3.8 Ga ($\text{Ga} = 1 \times 10^9$ years). Energy balance models (EBMs) predict temperatures below the freezing point of water, even at the equator, for the Sun's reduced energy output (Budyko, 1969; Sellers, 1969; North, 1975). These models predict that, if solar luminosity is reduced by a few percent, a frozen earth evolves (known as the ice-albedo catastrophe). Contrary to model results, the geologic record shows that water was flowing at the earth's surface 3.8 Ga (Walker, 1987).

Atmospheric carbon dioxide (CO_2) in large concentrations (Kasting, 1987) is considered to be the greenhouse gas that likely offset the lower energy output of the Sun, and allowed water to flow at the surface. The large concentrations of CO_2 of the Archean (2.5 to 3.8 Ga) are extrapolated from one-dimensional-radiative-convective (1DRC) models. CO_2 is increased in these models until a balance has been achieved between the lower solar luminosity and the warming effects of higher CO_2

concentrations. The results should be viewed with caution because only radiative and convective properties of the atmosphere are included in 1DRC models. Moreover, there is no firm evidence for very large amounts of atmospheric CO_2 in the early atmosphere. Other possible feedbacks, such as cloud amount and atmospheric and oceanic transports, are only beginning to receive attention.

A general circulation model (GCM) is used in this study to consider CO_2 concentrations as well as other important climatic factors for the Archean. This study is the first of its kind to apply a GCM to the investigation of the Archean climate. Because simple climate models do not incorporate many of the processes incorporated in a GCM, they cannot give the most accurate account of the Archean climate. In essence, primary and secondary feedbacks are allowed because of the inclusion of atmospheric dynamics, interactive clouds, and the hydrologic cycle that are not included in simpler models. While earlier studies have promoted considerable understanding of the Archean climate, the simpler climate models have been criticized for their limited capacity to simulate present climatic conditions. The GCM in this study makes use of a swamp ocean surface to calculate sea surface temperatures for very uncertain atmospheric conditions. The GCM has been used with some success to study other past climates, such as the Cretaceous (Barron, 1984). This study should minimize the uncertainties of simpler climate models and guide future Archean GCM studies.

1.2 Background Review of Climatic Conditions of the Early Archean

This thesis investigates the climatic factors in the Archean with a GCM. These factors—land fraction, solar luminosity, rotation rate, and CO_2 —are reviewed briefly in the following sections, along with ozone concentrations and the origins of life.

Land fraction

The rock record begins at 3.8 Ga from the first data found at Isua in West Greenland. The evidence from these earliest sedimentary rocks indicates that they were deposited under water (Walker, 1987). Just how much water? Speculation is that the primitive ocean may have been 1–2 km in depth (Cogley and Henderson-Sellers, 1984). It has also been proposed that a steam atmosphere existed with pockets of water near geothermal vents, and that the rock samples of West Greenland were formed near these pockets of water (Towe, 1983).

The widely accepted views of land fraction are that there was little or no land prior to 3 Ga and that the land fraction relative to today grew rapidly between 2 and 3 Ga. The evidence for the hypothesis is as follows: (1) Continental rock (granitic) is sparse in the early Archean and becomes more abundant with geologic time. (2) Very few continental platforms are found in the Archean. (3) Greenstones are found only in the Archean. Greenstones are metamorphosed volcanic rock associated with sedimentation, and they imply that volcanos spewed lava into the nearby ocean. The evolution of land fraction is shown in Figure 1.1 (Kuhn et al., 1989). The oldest crustal formations are shown in Figure 1.2 (Broecker, 1985).

Land fraction is important to climate from radiative and dynamical points of view. Land has a higher surface albedo than ocean, especially in the low latitudes and, therefore, its removal would allow the absorption of larger amounts of solar radiation at the ocean surfaces. This additional energy changes atmospheric and oceanic transports, precipitation, and surface-energy fluxes. Because land has a lower heat capacity than water, the atmosphere transports much of the heat over continents. If the early Archean is represented by small land fraction, warmer conditions could evolve from both the lower albedo and larger oceanic heat transport.

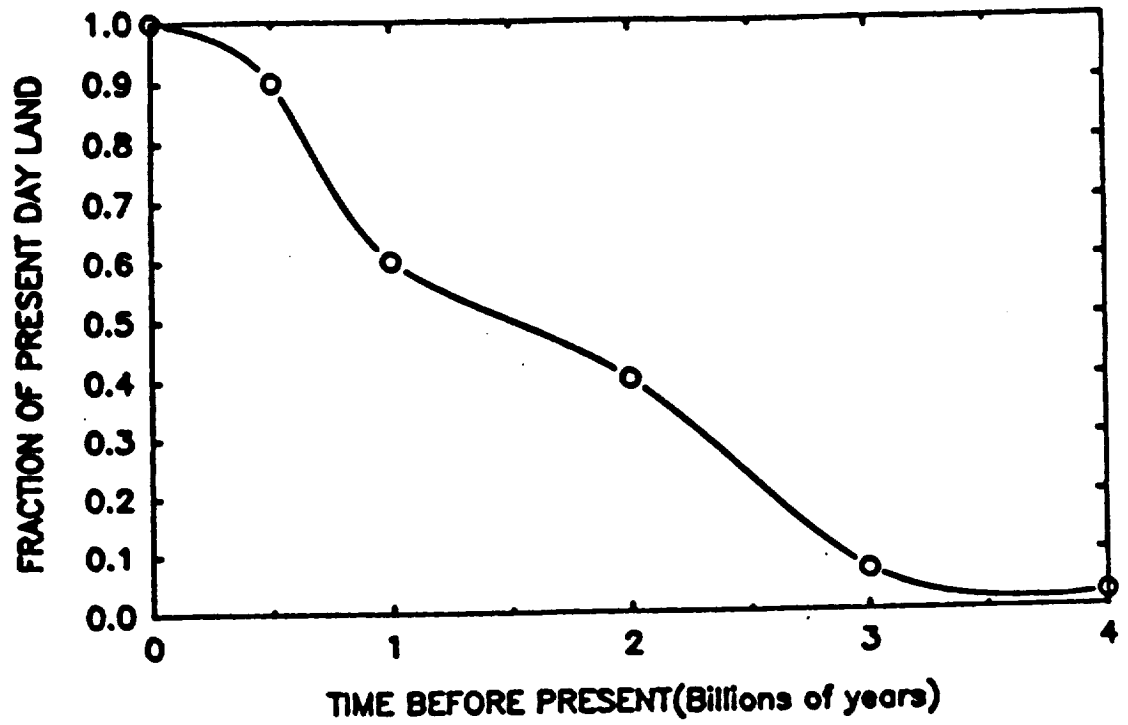


Figure 1.1: Evolution of land fraction (Kuhn et al., 1989).

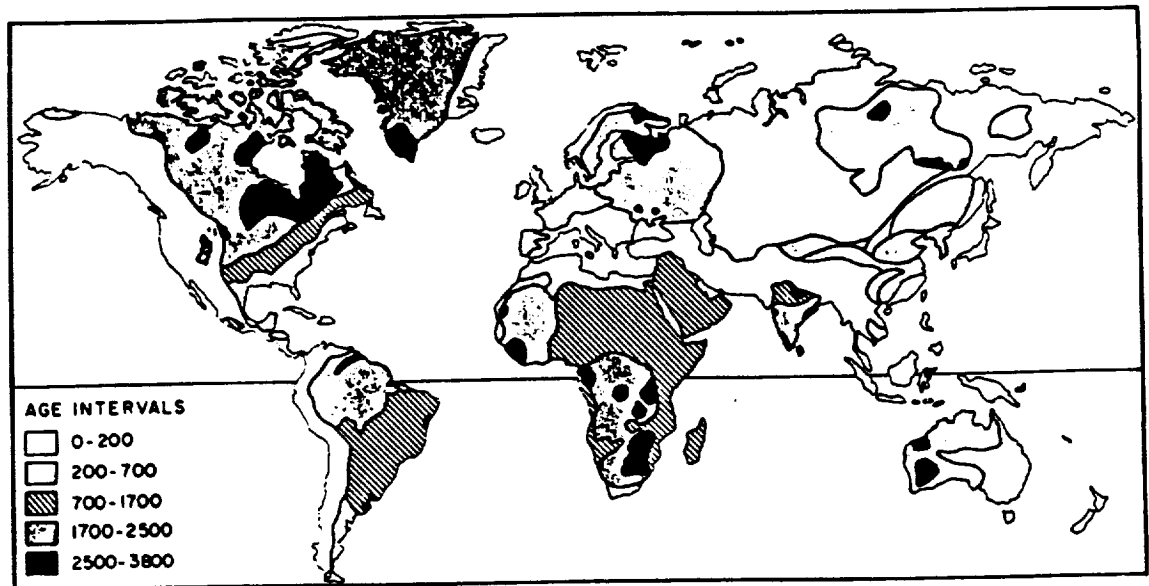


Figure 1.2: Ages of crustal formation (Broecker, 1985).

Solar luminosity

As mentioned in the prior section, solar luminosity was much lower than it is today. Estimates from Newman and Rood (1977) indicate that solar luminosity may have been some 15–25% lower for a time period of 4 to 3.5 Ga. This lower solar luminosity should have caused a frozen earth by allowing sea ice and snow to form at all latitudes because of subfreezing temperatures. The rock record, however, shows no evidence of a frozen earth in the form of glaciogenic deposits from the Archean except, possibly, for 2.65 Ga in Witwatersrand (Walker, 1981). Thus, some mechanism must have kept temperatures of the earth above freezing. The evolution of solar luminosity is shown in Figure 1.3 (Kuhn et al., 1989).

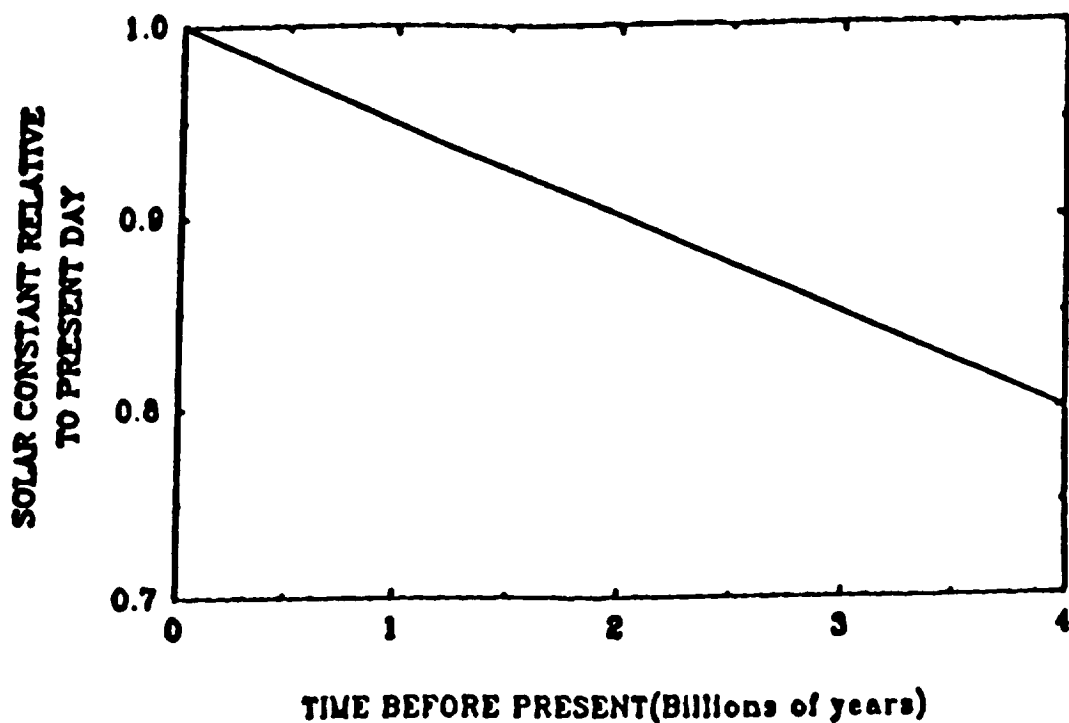


Figure 1.3: Evolution of solar luminosity (Kuhn et al., 1989).

Rotation rate

The rotation rate is a variable that has changed over geologic time and that has been closely linked to our near neighbor, the moon. For the period of interest here (4 to 3.5 Ga), the earth-moon distance was considerably closer. The rotation rate may have been up to 1.7 times the present rotation rate, thus corresponding to approximately a 14-hr day. The evolution of the rotation rate is shown in Figure 1.4 (Kuhn et al., 1989).

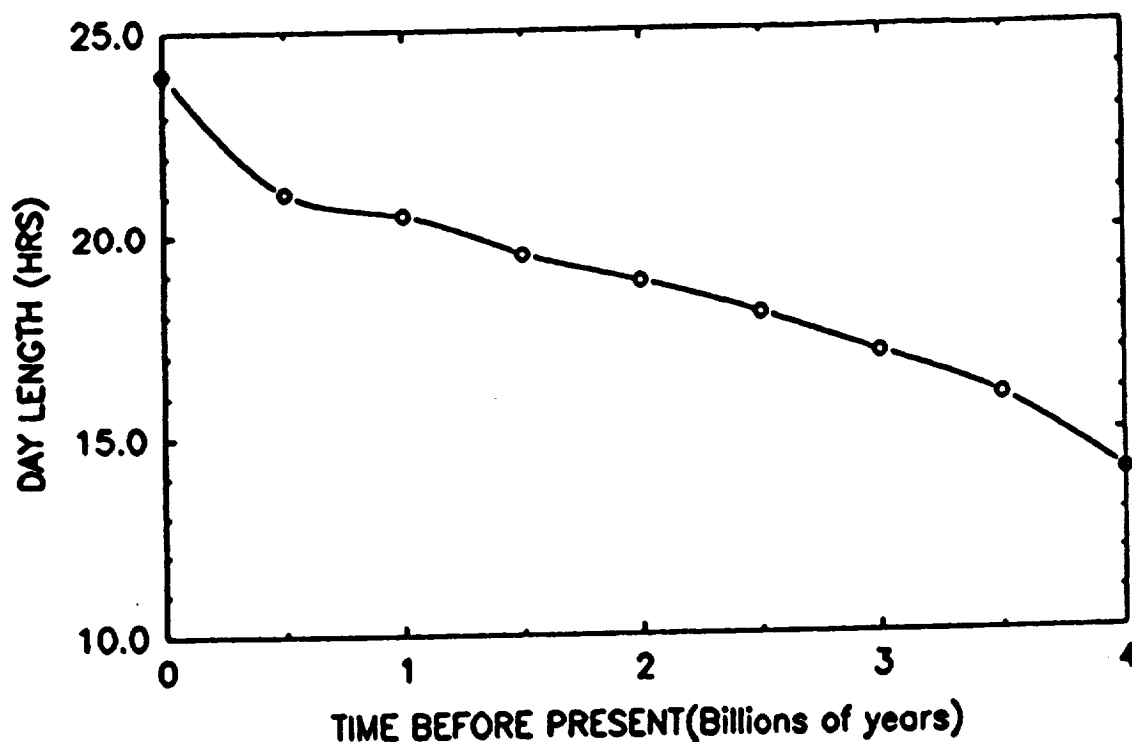


Figure 1.4: Evolution of rotation rate (Kuhn et al., 1989).

What evidence is there for a 14-hr day? Information on the daylength or yearlength can be derived from the growth grooves of fossil corals and molluscs. The daily, monthly, and yearly grooves indicate a larger number of days per year in the past, but data of this type extend back only 500 Ma ($\text{Ma} = 1 \times 10^9$ years). These data show that the daylength was approximately 21 hr, some 500 Ma. Beyond this

time, the only source of data is a Banded Iron Formation (BIF), known as the Weeli Wolli formation of the Hamersley Group in Western Australia and dating from 2.45 Ga. A 23.3-year cycle observed in the BIF indicates that the earth-moon distance was some 52 radii, which corresponds to nearly an 18-hr earth day (Walker and Zahnle, 1986). The lunar nodal tide is currently 18.6 years and has been detected in tree rings, temperature, and rainfall data.

One can relate the lunar nodal tide to the earth-moon distance from the following relationship (Walker and Zahnle, 1986):

$$P = P_o \left(\frac{\cos I_o}{\cos I} \right) \left(\frac{a_o}{a} \right)^{1.5} \quad (1.1)$$

Modern values are

$P_o = 18.6$ years, lunar nodal tide;

$I_o = 5.15$ degrees, Inclination of the lunar orbits to the ecliptic; and

$a_o = 3.84 \times 10^{10}$ cm, present earth-moon distance.

What is the relationship between the earth and moon? Presently, the moon is receding from the earth at approximately 3–4 cm per year, while the earth's daylength is increasing approximately 2 milliseconds per year. Tidal forces caused by the gravitational attraction between the earth and moon are responsible for the longer daylength and receding moon. The daily cycle of high and low tides is a result of the gravitational attraction of mass between the earth and moon and the centrifugal acceleration of the two bodies about their centers of mass. These forces cause two tidal bulges in the oceans, as shown in Figure 1.5 (Goldreich, 1972). The moon raises tides in the earth's oceans, atmosphere, and solid body, but the tides in the earth's oceans deserve the most attention. The interaction of the oceans with the sea floor creates a drag that dissipates energy. This dissipation of energy slows down the earth's rotation and allows the lost energy to be fed to the moon's orbit.

In the earth's past, the distance between the moon and the earth was much

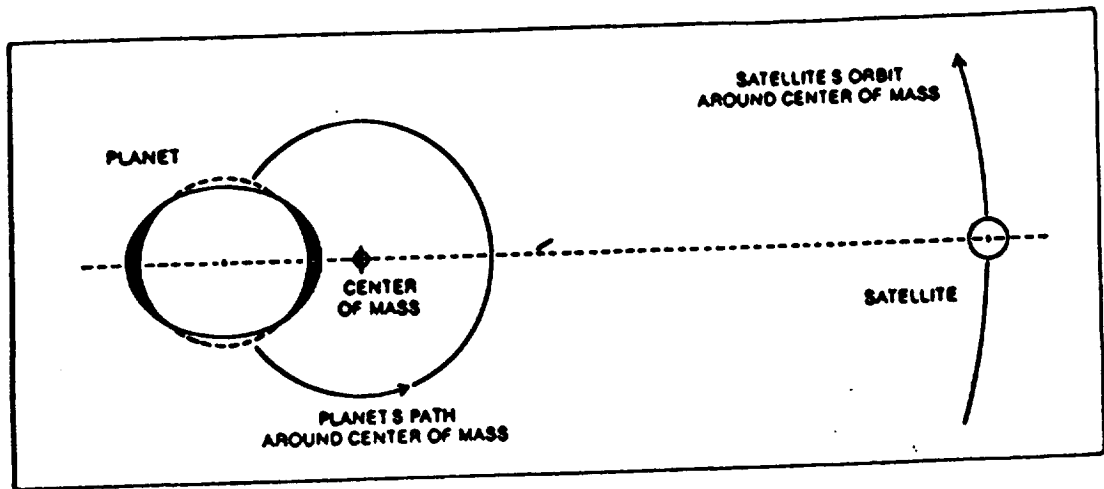


Figure 1.5: Physics of daily tides (Goldreich, 1972).

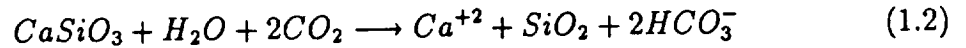
less and the gravitational force was stronger, thus creating larger tides and causing more dissipation of energy at the sea floor. It is currently believed that the energy dissipation was less than at present; otherwise, the earth and moon would have had a near collision some 2 billion years ago. There are no large scars on the earth or moon to suggest such a collision.

Both dishpan experiments (Fultz, 1959; Hide, 1981) and GCM simulations (Hunt, 1979; Williams, 1988) have been undertaken to understand the role of rotation rate in the earth's climate. The net effects of a faster rotation rate on the climate system are lower polar temperatures and higher equatorial temperatures. The temperature change is due to less efficient heat transport by atmospheric eddies which become smaller with faster rotation rates. The GCM results were somewhat limited because of fixed clouds and relative humidity which exclude the possibility of secondary feedbacks that affect the climate system. Nevertheless, these studies do replicate the primary results of the dishpan experiments. Rotation-rate experiments will be repeated in this study with an interactive cloud scheme and unfixed relative humidity. Results similar to those above are expected.

CO₂ concentrations

While CO₂ is currently at 350 ppm and increasing, it is likely that it was substantially larger for the Archean. CO₂, methane (CH₄), and ammonia (NH₃) were first proposed as the primary greenhouse gases to compensate for the lower solar luminosity of the early Archean (Sagan and Mullen, 1972). Further research with IDRC models has demonstrated that the amount of CO₂ needed to balance the lower solar constant ranged from hundreds to thousands of times the present atmospheric concentrations (Kasting, 1987; Kiehl and Dickinson, 1987; Kuhn et al., 1989). Calculations show that these high partial pressures of CO₂ caused neither a runaway greenhouse nor highly corrosive oceans (Walker, 1990).

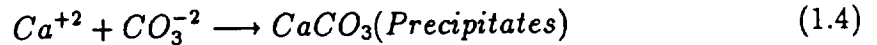
If very large CO₂ concentrations did exist in the Archean, a likely process to remove them would have been carbon-silicate weathering. This process breaks down silicate rocks by precipitation which releases calcium ions to solution. The calcium ions then precipitate as calcium carbonate on the sea floor and extract carbon from the ocean and atmosphere. The exact relationship of carbon-silicate is



Followed by



Then,



CO₂ is important to the climate system because it alters the effective emitting temperature of the earth-atmosphere system. CO₂ acts as a greenhouse gas, decreasing the amount of outgoing longwave radiation (OLR) emitted into space, and thereby warming the troposphere and cooling the stratosphere.

Ozone

Ozone was limited in the early Archean because of the lack of molecular oxygen. The production of ozone is given by



Where M is a third body and k_{12} is a rate constant.

Given the above reaction, molecular and atomic oxygen was necessary in the early atmosphere. Molecular oxygen was not present in significant amounts before large quantities of microbes developed pigment for oxygenic photosynthesis (Walker, 1978). Oxygenic photosynthesis is largely responsible for much of the oxygen in the present atmosphere and, hence, oxygen concentrations increased after 2 Ga when the pigmented microbes became available (Kasting, 1987).

The fact that anaerobic microbes were present 3.5 Ga indicates that these organism were able to (1) live in the presence of currently dangerous UV radiation, (2) shield or shelter themselves from harmful radiation, or (3) survive because ozone was present in sufficient amounts. In view of the oxygen amounts of the early Archean, (1) and (3) can be ruled out. Walker (1987) noted that the earliest microbes could have lived in mat-like colonies, such that the microbes at the top were killed by the harmful UV radiation but the organisms below survived. If the microbes lived in mud or beneath rocks then, they could have also been shielded from dangerous UV radiation.

Ozone is important to the climate system because it absorbs shortwave radiation. Large solar heating rates occur in the stratosphere because of ozone. Ozone also absorbs longwave radiation at $9.6 \mu m$. The troposphere is separated from the stratosphere because of changes in the temperature profile. In contrast to the troposphere, the stratosphere has temperatures increasing with height due to the absorption of

shortwave radiation by ozone. Thus, a different stratospheric climate could be expected without ozone. In their study of the effects of reduced ozone concentrations with a GCM, Kiehl and Boville (1988) predicted large temperature decreases in both the upper troposphere and the entire stratosphere for a 100% reduction in ozone and significant changes in the zonal wind.

Earliest forms of life

The oldest well-preserved sediments are found in the Pibbara block of western Australia and the Barberton mountain land of South Africa and date back to 3.5 Ga. They contain the first evidence of life in the form of simple-celled microbiota, thereby setting a constraint on the limits of the earth's climate. The earth's surface had a temperature constraint between 0°C and 100°C at some location in order for the microbes to exist. After 3.5 Ga, greater quantities of more complex forms of microbes flourished.

1.3 Overview of Thesis

The goal of this thesis is to investigate the Archean climate using the community climate model (CCM) developed at the National Center for Atmospheric Research (NCAR). A possible solution to the "Faint-Young Sun Paradox" is examined and negative climatic feedbacks from sensitivity experiments are stressed. It is hypothesized that when additional atmospheric effects of the GCM are taken into account, very large concentrations of atmospheric CO₂ will not be needed to balance the lower energy output from the young Sun.

Chapter 2 describes the model, a comparison of the model results to observation, the experimental outline, along with model-integration time and time-averaging procedures for each experiment, and the relationship of CO₂ to the climate system.

Chapter 3 introduces results from various sensitivity experiments and the roles of rotation rate, zero land fraction, various degrees of a lower solar constant, and higher CO₂ concentrations to be explored.

Section 3.1 involves a simulation in which the rotation rate has been adjusted to correspond to a 14-hr earth day. Present-day land distribution is used in this experiment and the results compared to the simulated present-day climate control. Section 3.2 investigates the effects of reduced land fraction and lower solar luminosity on the climate system. Two sensitivity experiments are performed: (1) the land fraction is given a value of zero; and (2) the solar constant is lower by 10% for the zero land-fraction case. The equatorward shift in the sea-ice line is noted. These two simulations are compared to the present-day climate control case.

In section 3.3, the roles of CO₂ and the rotation rate are explored in reference to the above experiment, i.e., zero land fraction and a 10% reduction in the solar constant. Three experiments are carried out with CO₂ concentrations increased by 4 times and 8 times the control values (330 ppm) and the rotation rate increased to equal that of a 14-hr earth day. The results of the three cases are compared to the case of a 10% decrease in solar constant and zero land fraction. In section 3.4, CO₂, faster rotation rate, and zero land fraction are combined in a series of sensitivity experiments. CO₂ concentrations are increased to 8 times the present-day value, the rotation rate is increased to correspond to a 14-hr day, and the land fraction is set to zero. Three cases are examined with the solar constant lowered by 10, 15, and 20%. The results for all three case are compared to the global ocean simulation of section 3.2.

Chapter 4 is a discussion of the results from chapter 3, and chapter 5 summarizes the major results of this study and recommends future studies.

CHAPTER II

MODEL DESCRIPTION and PLANNED EXPERIMENTS

2.1 Climate Models

Energy balance models

An EBM usually solves for surface temperature in a latitudinal direction and incorporates simple physical processes that include solar radiation absorbed at the surface, OLR and heat transport between latitudes. The amount of solar radiation absorbed at the surface is prescribed and depends on the planetary albedo which, in turn, depends on the surface and cloud albedo. The surface albedo can be varied as a function of temperature in the EBM, allowing one to take into account an ice-albedo feedback process. The amount of OLR is also prescribed by some empirical formulation which includes surface temperature. Finally, heat is transported between latitudes by some simple relationship. For instance, heat transport may be proportional to the difference in temperature between adjacent latitudes. Any changes in the surface temperature will be related to these three processes. When

the sum of these three terms goes to zero after some finite amount of time, the equilibrium surface temperature is obtained. Zonally averaged cloud fraction and land fraction can be included. For additional discussion of EBMs, see North (1975).

One-dimensional radiative-convective models

The 1DRC model solves for temperature as a function of height rather than latitude and can include processes such as clouds, scattering by molecules and particles, absorption of longwave radiation by molecules of CO_2 , water vapor and other trace gases.

A convective-adjustment process is used in these models, since the actual temperature structure depends on radiative processes like latent heat release. The convective-adjustment process involves an adjustment of the lapse rate in a model layer, if it exceeds some critical lapse rate. For many 1DRC models, this critical lapse rate is -6.5 K km^{-1} . If the layer lapse rate is greater than the critical lapse rate, then the layer lapse rate is set back to the critical lapse rate while conserving moist static energy. The radiative properties of the layer are then recalculated and the convective-adjustment process is again invoked until the lapse rate does not exceed the critical value throughout the troposphere. At this point, there is radiative-convective equilibrium. This model suffers from lack of atmospheric dynamics, fixed relative humidity which inhibits interactive cloud schemes, and a simple surface. For further discussion, see Ramanathan and Coakley (1978).

General circulation models

A GCM is a computer program that solves the equations of motions for the atmosphere and gives an equilibrium climate state. The momentum equations, continuity equation, moisture equation, equation of state, and the first law of thermodynamics

are all solved for distinct points in the atmosphere. The radiative-transfer equations of the atmosphere are solved in the vertical direction. These equations are integrated out to an equilibrium state. The integration time varies and is based on the ocean circulation invoked in the GCM. The more realistic the ocean type, the longer the integration time. Fully coupled atmosphere-ocean GCMs with ocean circulation and heat-storage properties have the longest integration time.

In a sense, a GCM is an extension of a numerical weather prediction model, but the time step and integration of a GCM are much longer and the spatial scale generally much larger. The numerical weather prediction model forecast has new boundary conditions every 12 hr and is integrated for several days—up to a week. The climate model has only one starting boundary condition and is integrated until an equilibrium climate state is reached.

A GCM differs spatially from an EBM and a 1DRC model. A GCM is three-dimensional and it solves atmospheric variables in all three directions on the sphere— ϕ , λ , Z , where ϕ represents latitudinal direction, λ longitudinal direction, and Z vertical direction.

2.2 Model Description of NCAR CCM

History of community climate model

CCM0A, an early version of the CCM first developed in 1977 at NCAR, is based on the Australian spectral model developed by Bourke et al. (1977) and documented by McAvaney et al. (1978). Improvements in the radiation code (Ramanathan et al., 1983) and simulation of present-day climate with these modifications are documented by Pitcher et al. (1983). A description of the spectral technique and the model

equations is given in Washington and Parkinson (1986). CCM0A, the model version used in this study, is described by Washington and VerPlank (1986).

Model description

CCM0A is used with swamp ocean formulation, temperature-dependent sea ice, interactive clouds, predictive hydrology, realistic geography, and smoothed topography. This model has low resolution and thus excludes small scale processes. Some of these small-scale processes (subgrid-scale) are thunderstorms, individual clouds, hurricanes, and mesoscale events. Therefore, parameterized horizontal and vertical diffusion of heat, moisture, and momentum is adapted to take into account subgrid-scale processes. The resolution of this model is 4.5° latitude and 7.5° longitude between each grid point. (If one wanted to investigate changes in climate for a small region such as a state, then the model resolution would be inadequate.) There are 9 levels in the vertical, ranging from the surface to approximately 10 mb. The vertical coordinates are given in sigma coordinates that vary between 0 and 1.

The swamp ocean in this model can be considered idealistic in that the energy balance equation is solved over it to determine surface temperature. Realistically, a swamp does not have vertical or horizontal motions to a first-order approximation. The swamp ocean in the CCM has no ocean circulation in the vertical or horizontal, and because this model ocean cannot store heat, the seasonal cycle is not used. Primarily, the swamp ocean acts as a source of moisture, and for these reasons the swamp model will give only first-order approximations to real oceanic systems. The swamp formulation does have an advantage over fixed sea-surface temperature experiments because of its ability to affect the climate of land points near the ocean. This is especially true of simulations such as CO_2 experiments, where the ocean could show temperature changes due to atmospheric warming.

The swamp ocean takes advantage of the energy balance to derive its sea-surface temperature. The energy balance equation has the following form:

$$S + F \downarrow + F \uparrow - \eta - L\beta + Q_i = 0 \quad (2.1)$$

where S is the absorbed solar flux, $F \downarrow$ downward infrared flux, $F \uparrow$ upward infrared flux, η sensible heat flux, $L\beta$ latent heat flux, and Q_i heat flux conducted into or away from the sea ice. The Newton-Raphson iterative method solves for the surface temperature.

Two meters of ice form when the ocean temperature falls below 271.2 K. A small amount of heat is conducted into or away from the ice, depending on the exact surface temperature. Sea-ice amounts can be considered a frequency distribution ranging from 0 to 2 m. The swamp ocean tends to produce ice too far equatorward compared to the observed value, with lack of oceanic heat transport and storage the primary causes. The location of the sea-ice edge at .1 m corresponds approximately to 280 K instead of 271.2 K, the approximate freezing point of sea water. Instead, a value of 1 m for sea ice corresponds most closely to 271.2 K on average and will be used in future chapters to indicate the average sea-ice edge.

The CCM uses an interactive cloud scheme wherein clouds grow or decay as a function of relative humidity and equivalent potential temperature. The relative humidity is written as

$$Rh = \frac{e}{e_s} \quad (2.2)$$

and the equivalent potential temperature is

$$\Theta_e = \Theta e^{\frac{Lq_s}{C_p}} \quad (2.3)$$

where e is the water vapor pressure, e_s saturation water vapor pressure, which is a function of temperature, L latent heat of vaporization, q_s saturation mixing ratio, Θ potential temperature, and C_p specific heat at constant pressure.

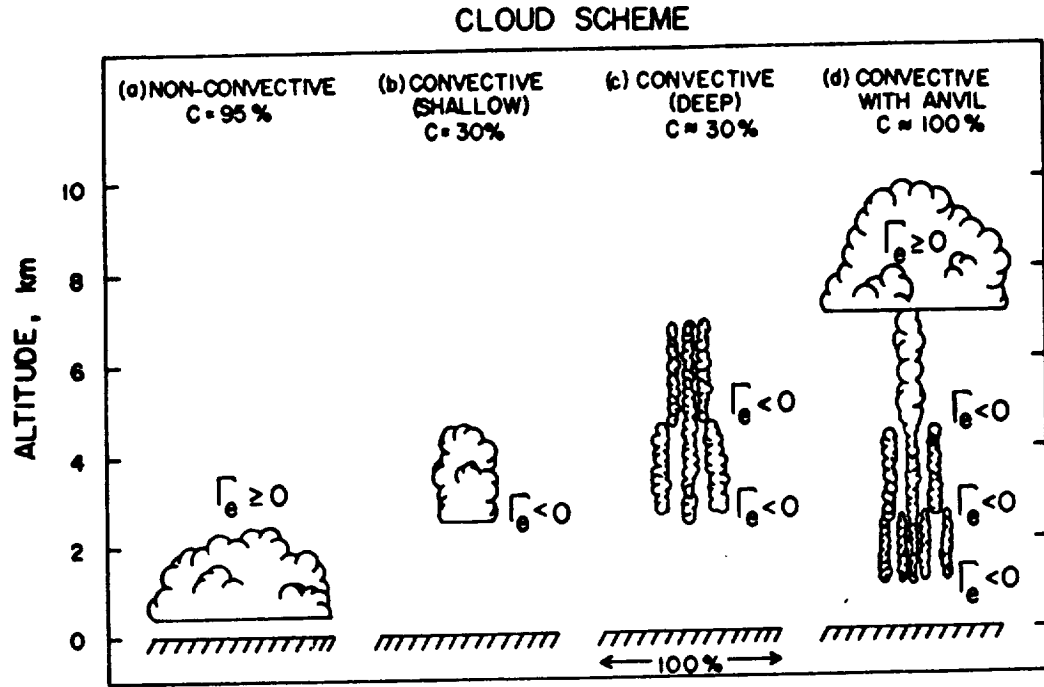


Figure 2.1: Cloud scheme for the NCAR CCM (Ramanathan et al., 1983).

There are two types of clouds—convective and nonconvective. Convective clouds have a maximum cloud fraction of .3 and are representative of cumulus clouds. Non-convective clouds have a cloud fraction of .95 and are representative of stratus clouds. Cloud types are shown in Figure 2.1 (Ramanathan et al., 1983). For all clouds to form, the relative humidity must be greater than 80%. For convective clouds, the equivalent potential temperature with respect to height must be less than zero. This represents an air parcel that is warmer than the surrounding environment which rises—an unstable atmosphere. For nonconvective clouds, the equivalent potential temperature with respect to height must be greater than or equal to zero. These conditions are summarized as follows:

$$\text{Convective clouds } \frac{\partial \theta_e}{\partial z} \leq 0$$

$$\text{Nonconvective clouds } \frac{\partial \theta_e}{\partial z} \geq 0$$

The cloud fraction of convective clouds is usually less than .3, with the maximum convective cloud fraction for any column at .3. The actual cloud fraction for convective clouds is .3 divided by the number of unstable layers for a given column.

The albedo of the surface is prescribed as follows:

Desert \equiv .25

Other land surfaces \equiv .13

Snow \equiv .8

Sea ice \equiv .35 if $T \geq 263$

Sea ice \equiv .70 if $T < 263$

Ocean \equiv Varies as a function of zenith angle

The albedo scheme of the sea ice in this study has been tested (Washington and Meehl, 1986) and has a somewhat greater sensitivity than the traditional GCM albedo scheme for sea ice and snow. Snow or sea-ice albedo values are not allowed to change until all of the snow or sea ice disappears at a particular grid point making an ice-albedo catastrophe less likely. The interactive hydrology in this model includes precipitation, evaporation, soil moisture, and runoff. When precipitation is greater than evaporation at the surface and more than 15 cm of water have been absorbed in the soil, a runoff occurs. The simulation also takes place under annual mean conditions. Solar forcing is obtained from an averaged zenith-angle value that is obtained from integrating at each latitude over an entire year; declination angle, hour angle, and latitude are taken into account.

2.3 Comparison of CCM to Observed Climate

In this section, we focus on how well the CCM performs when compared to the observed climate (Oort and Peixóto, 1983). The vertical scales are different since the CCM is computed on sigma surfaces (scaled by 1000) and the observed climate is given in millibars. Observed data are usually averaged over all seasons of the year and

Variable	Observed	Simulated
T_{air} K	285.6	284.96
Cloud fraction	0.55	0.423
Precipitation (cm yr^{-1})	100.4	114.2

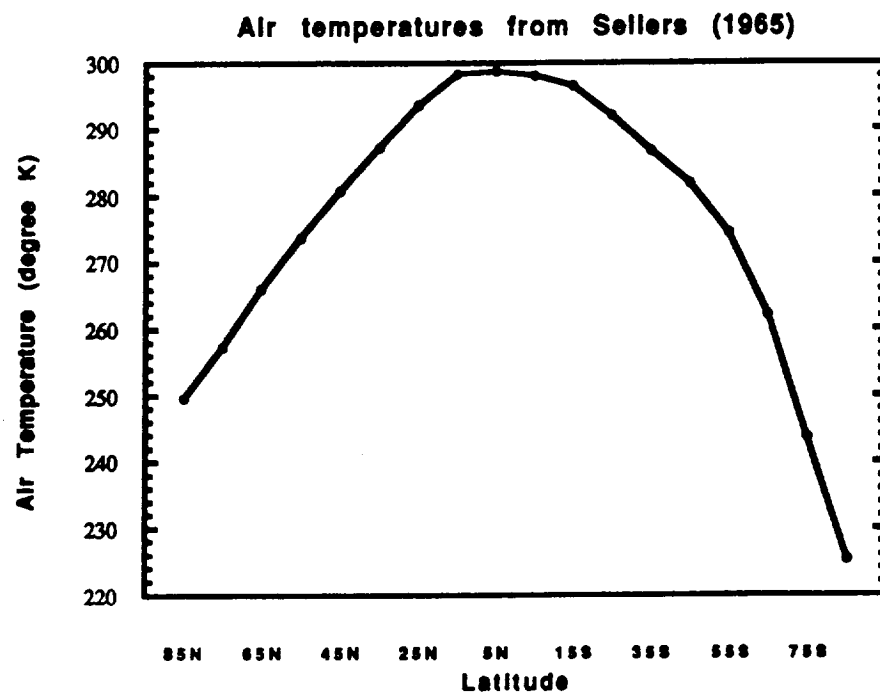
Table 2.1: Global values for observed and simulated data

then over a number of years. In any given year, observed data may vary significantly from the long-term observed values. In the climate simulation shown here, annual forcing is the external boundary condition and, therefore, one should not expect a one-to-one correspondence between the observed and simulated climate. Many observed features of the atmosphere have larger variations from summer to winter. A better comparison would be to incorporate the seasonal cycle into the model and compare the simulated winter and summer to the observed. The present-day climate simulation was integrated for 300 days and time averaged over the last 100 days.

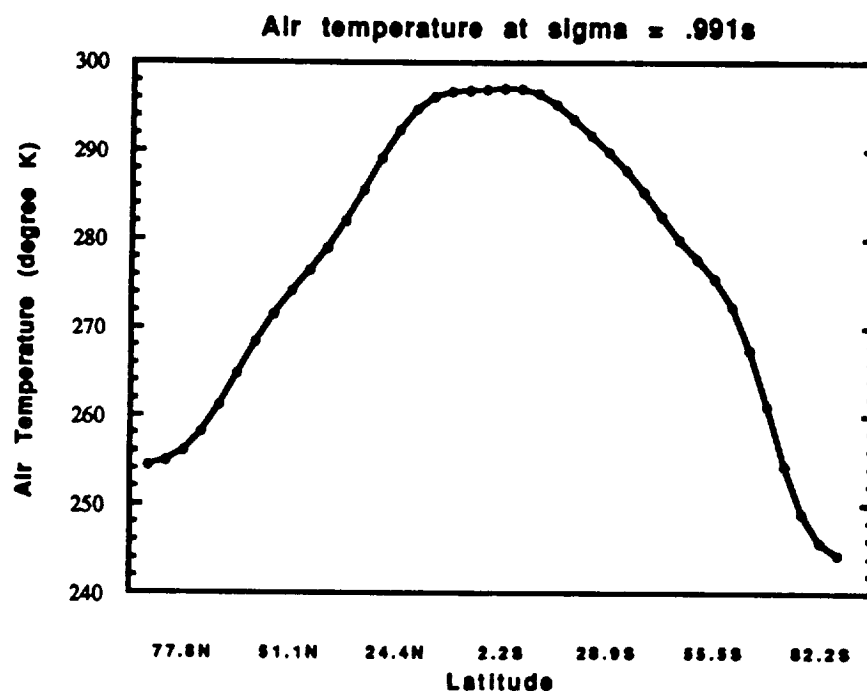
Simulated temperature versus observation

The surface temperature in Figure 2.2 is compared to that of Sellers (1965). Simulated temperatures in the polar regions are too warm for both hemispheres compared to observations (especially true in the Southern Hemisphere). On the other hand, equatorial temperatures are somewhat cooler than the observed temperatures. Globally, the simulated temperatures are slightly colder than the observed (Table 2.1).

The latitude-height temperature field for observations (Washington and Meehl, 1983; Figure 2) and the climate simulation are shown in Figure 2.3. While the over-



(a) Observed air temperature (data from Sellers, 1965).



(b) Simulated air temperature at $\sigma = .991s$.

Figure 2.2: Zonally averaged surface of temperature in degrees Kelvin. (a) observed; (b) simulated.

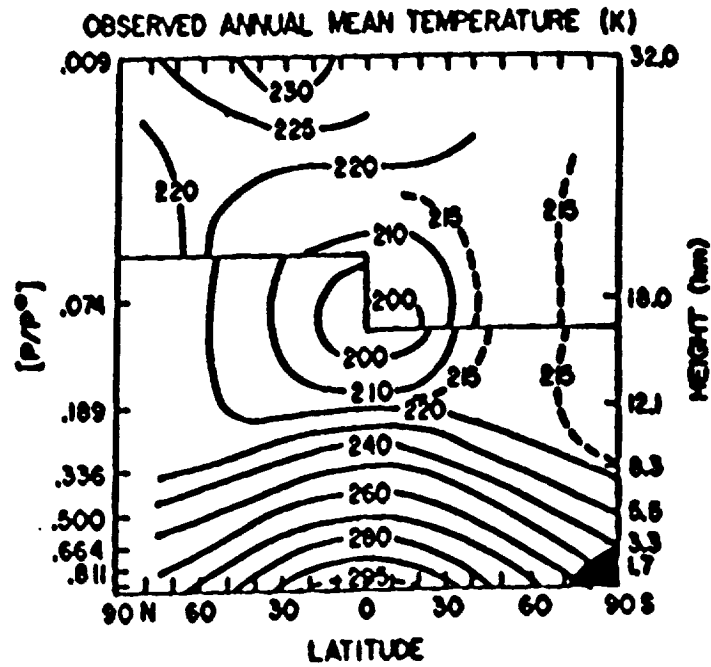
all structure of the temperature field is captured, a slight cold bias in the model simulation is most noteworthy in the upper troposphere and in the tropopause regions. A different stratospheric temperature structure from the observed is shown in the model results because the observed stratospheric temperature structure varies significantly over seasons.

Simulated zonal wind versus observation

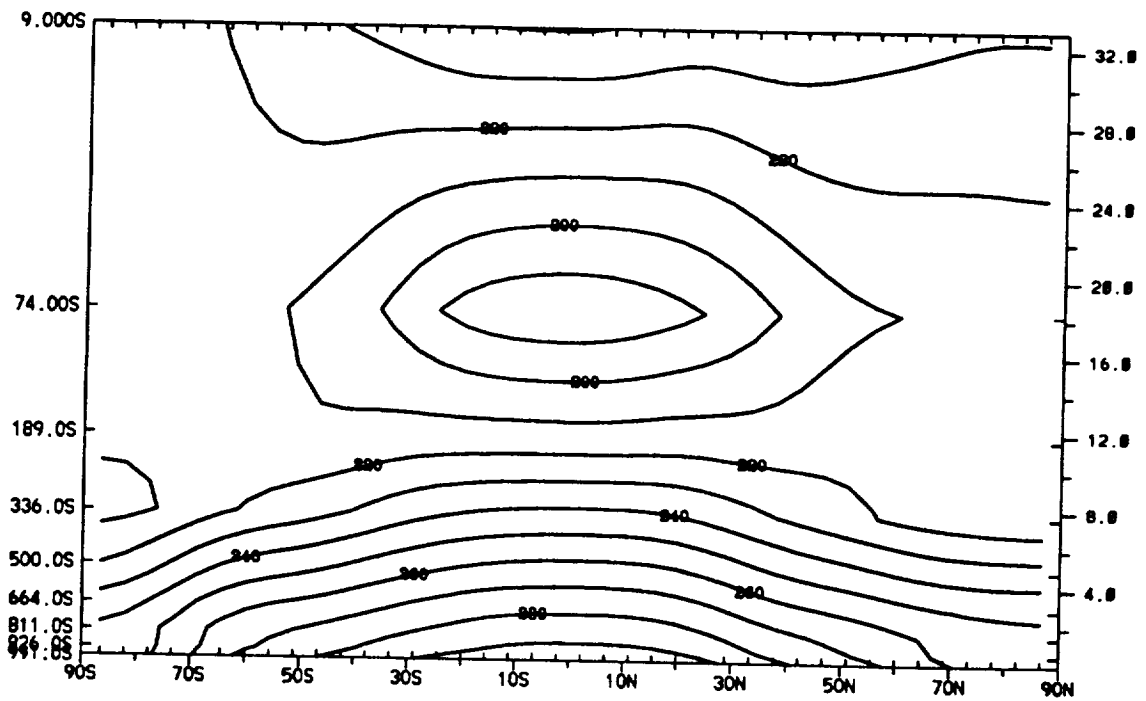
The latitude-height distribution of observed zonal wind (Oort and Peixóto, 1983) in Figure 2.4 displays both similarities with and differences from the simulated wind field (Figure 2.5). The simulated jet-wind velocity is very close to the observed values, and its position is also very close to the observed. Deficiencies in the model simulation are (1) larger simulated easterly wind in the lower troposphere and stratosphere than observed in the tropics; and (2) a region of simulated westerly winds in the mid-to-upper-equatorial troposphere; easterly winds are observed in this region.

Simulated mean meridional streamfunction versus observation

The observed mean meridional streamfunction is shown in Figure 2.4 (Oort and Peixóto, 1983) with the simulated values in Figure 2.5. The CCM does capture the structure of the Hadley and Ferrel cells. The intensity of the Hadley cell is larger than the observed by a factor of approximately 1.5 in both hemispheres. The Southern Hemisphere Hadley cell shows two areas of maximum mass flow. The area centered at 10°S and approximately 800 mb is observed. The second maximum is not found in the observed. The Northern Hemisphere Hadley cell shows a maximum mass flow occurring at a higher altitude than observed. The latitudinal positions of the Hadley and Ferrel cells are close to the observed. Seasonality has probably caused some differences between the simulated and observed values. Both the strength and position



(a) Observed temperature distribution (Washington and Meehl, 1983).



(b) Simulated temperature distribution.

Figure 2.3: Latitude-height plot of temperature in degrees Kelvin.
(a) observed; (b) simulated.

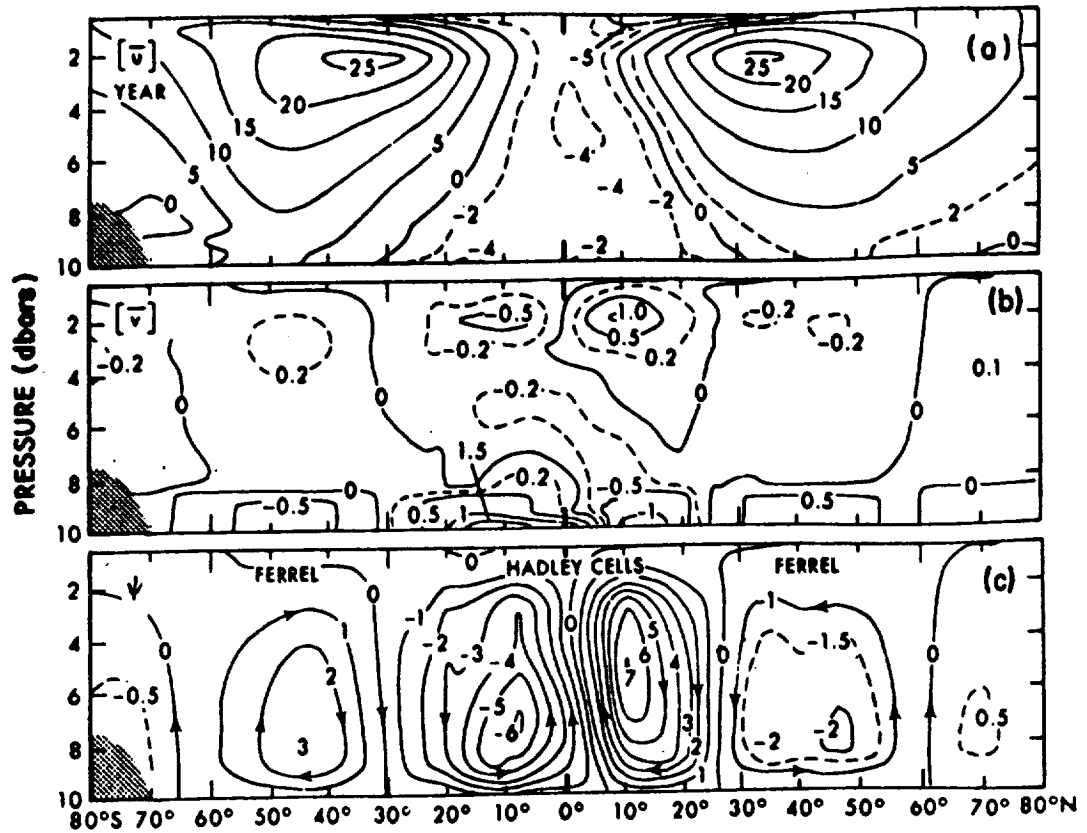
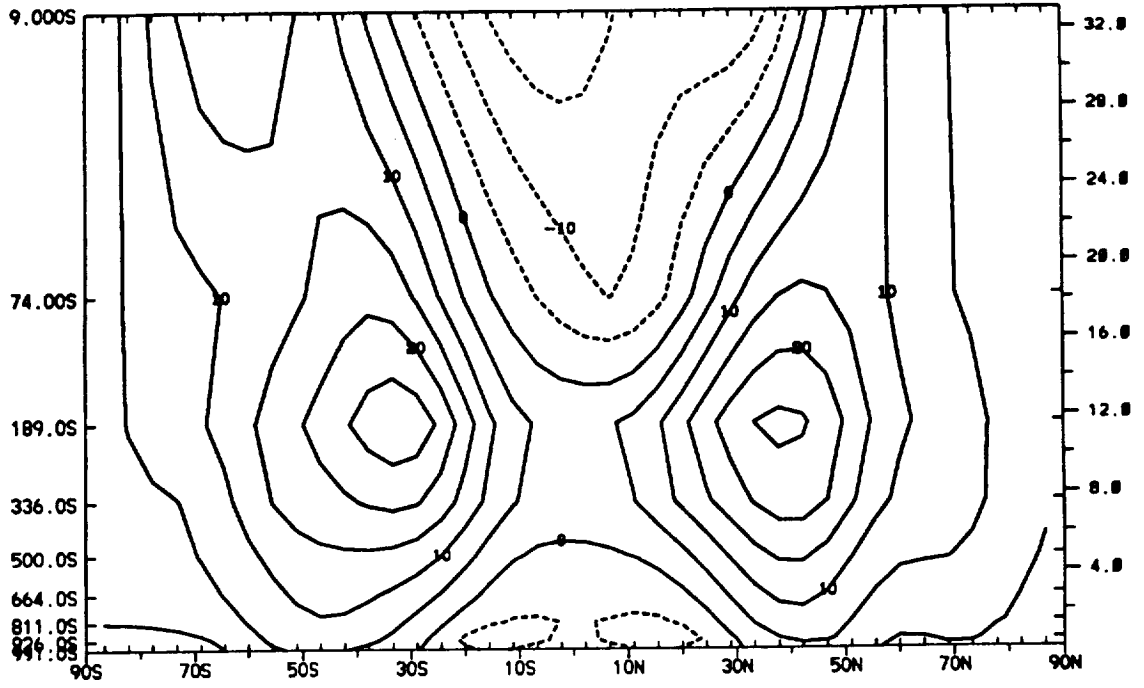


Figure 2.4: Latitude-height distribution of (a) observed zonal wind; (c) streamfunction (Oort and Peixóto, 1983).

of the Hadley cell change with season with the Hadley cell being stronger in the winter than in summer. Seasonality should be taken into account in order to properly evaluate the model-derived streamfunction against the observed streamfunction.

Simulated latitude-height water vapor mixing ratio versus observation

The observed and simulated mixing ratio is shown in Figure 2.6. The agreement is very good between the observed (Oort and Peixóto, 1983) and simulated data. The model underestimates the water-vapor amount near the equator by a factor of 1.2, and the simulated data are more zonally symmetric than the observed data.



(a) Simulated zonal wind

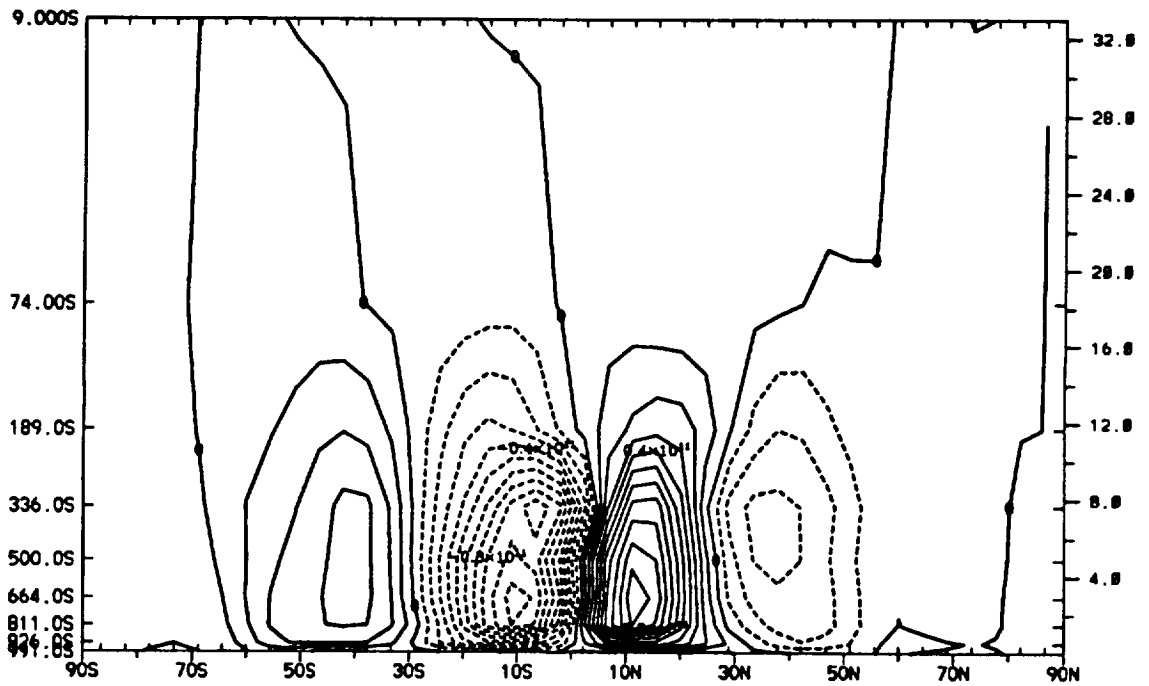
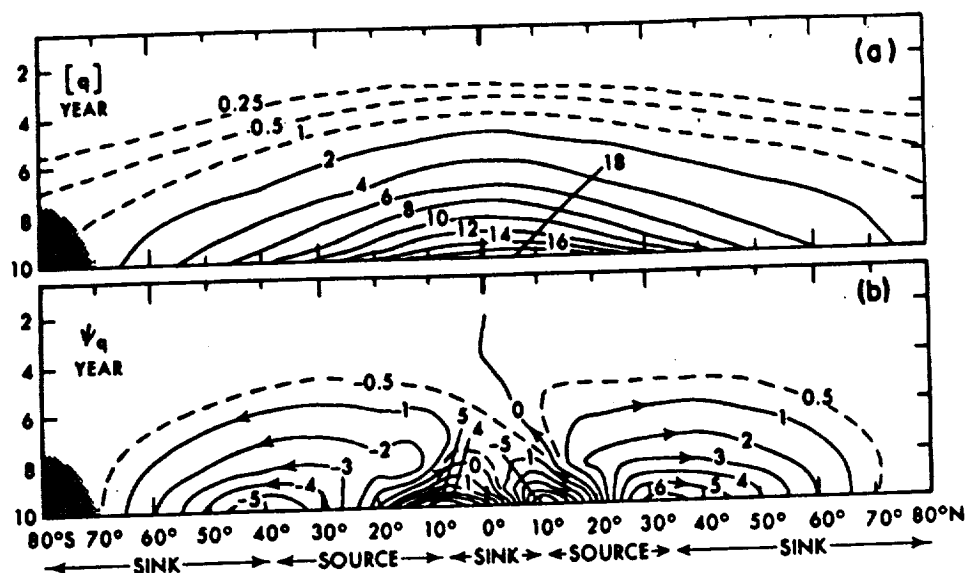
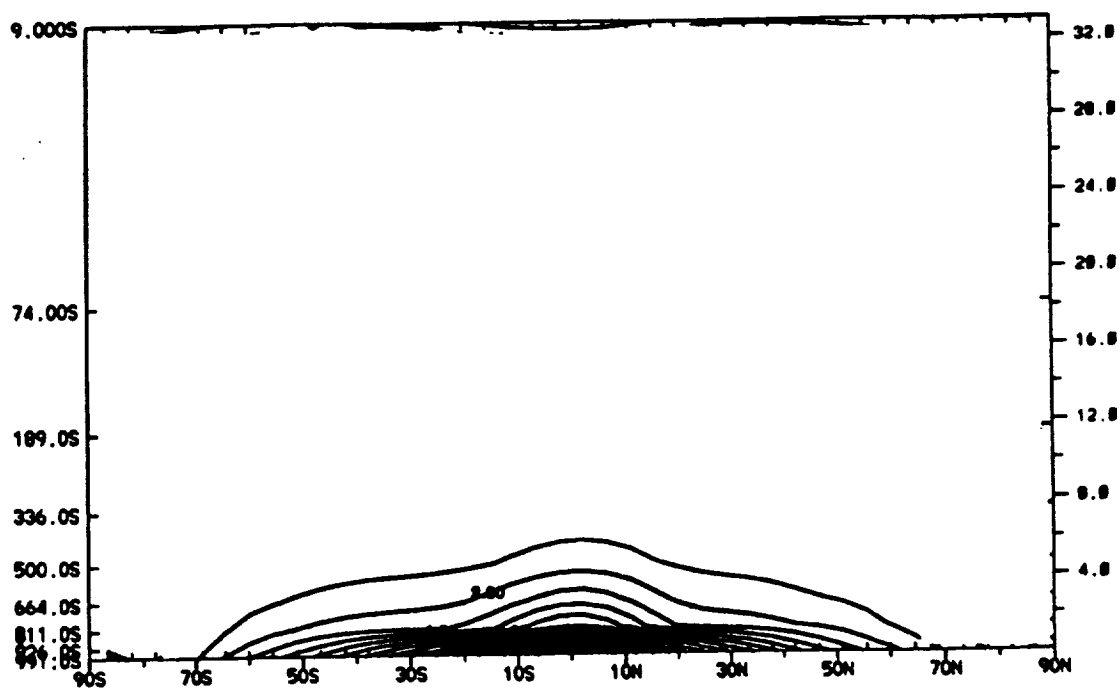
(b) Simulated meridional streamfunction. Contour interval: $1 \times 10^{10} \text{ kg s}^{-1}$

Figure 2.5: Latitude-height distribution of zonal wind and streamfunction. (a) zonal wind; (b) streamfunction.



(a) Observed water-vapor mixing ratio. Units: g kg^{-1} (Oort and Peixóto, 1983).



(b) Simulated water-vapor mixing ratio. Units: g kg^{-1} .

Figure 2.6: Tropospheric distribution of mixing ratio. (a) observed; (b) simulated.

Simulated zonal cloud fraction versus observation

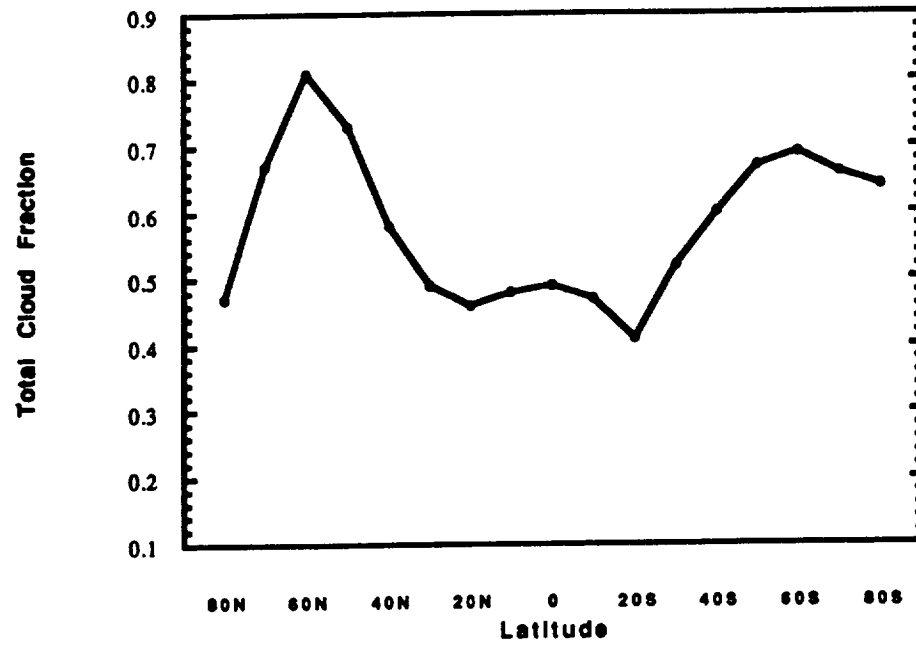
The zonally averaged cloud fraction is shown in Figure 2.7 with the observed data (Thompson and Barron, 1981). A comparison of the simulated data with the observed indicates that the model cannot represent very well the observed cloud distribution. This is apparent in high latitudes; nonetheless, the model does capture some features of the low latitudes, with a peak in cloud fraction near the equator and a minimum in the subtropics. The exclusion of cloud microphysics is the main cause of the poorly simulated cloud field. Globally observed and simulated total cloud fractions are shown in Table 2.1.

Simulated zonally averaged precipitation versus observation

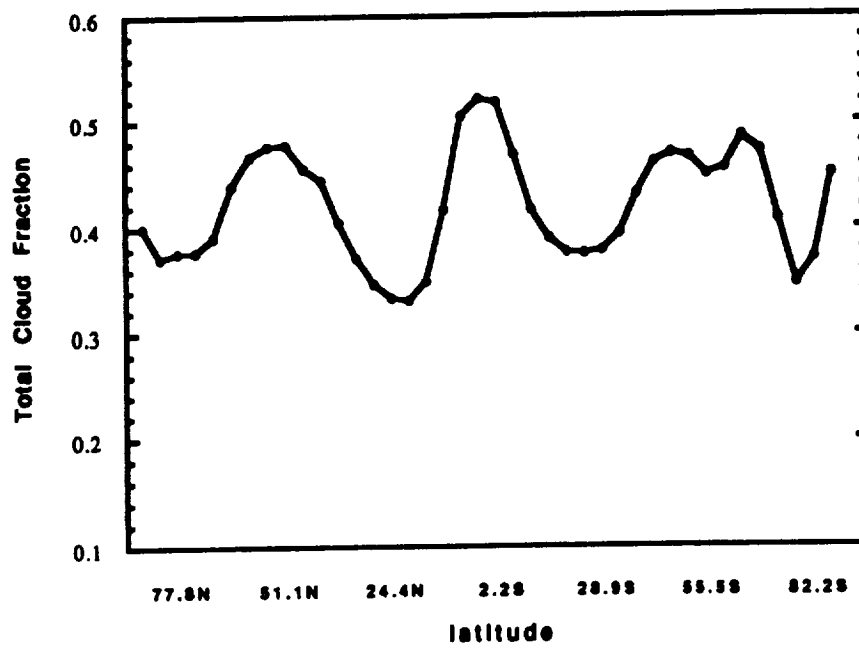
Zonally averaged precipitation is shown in Figure 2.8. The observed data (Sellers, 1965) are compared to the simulated values. The structure of the precipitation pattern is captured by the model, but the model overestimates precipitation at most latitudes. The differences are modest in the equatorial and polar regions. Both the convective-adjustment scheme and the cloud scheme, which allows for precipitation with cloud formation, are responsible for the larger-than-observed precipitation rates. Globally averaged precipitation rates for the observed and simulated data are given in Table 2.1.

2.4 CO₂-Induced Climate Change

CO₂ makes up .03% of the total atmospheric components by volume and, therefore, is considered a trace gas. CO₂, a greenhouse gas because of its absorption properties in the infrared regions, has major absorption bands at 4.3, 9.4, 10.4, and 15.2 μm .

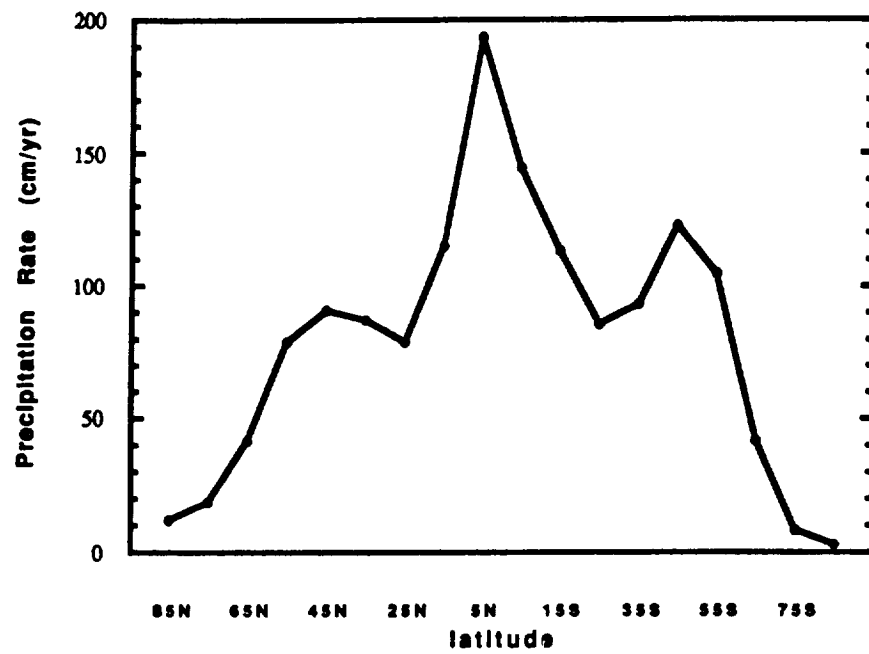


(a) Observed cloud fraction (Thompson and Barron, 1981).

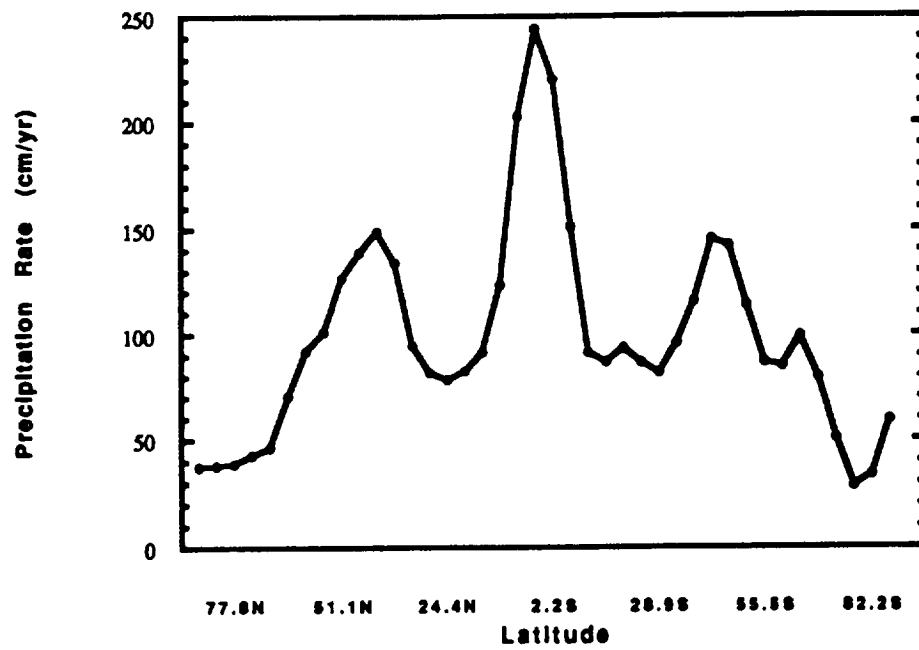


(b) Simulated cloud fraction.

Figure 2.7: Zonally averaged total cloud fraction. (a) observed; (b) simulated.



(a) Observed precipitation rates. Units: cm yr^{-1} (data from Sellers, 1965).



(b) Simulated precipitation rates. Units: cm yr^{-1} .

Figure 2.8: Zonally averaged annual precipitation. (a) observed; (b) simulated.

The net effect of increased CO_2 concentrations from the surface of the earth is warmer tropospheric temperatures. Climate models indicate that globally averaged surface temperature increases 2 to 5 K for doubled CO_2 concentrations (Schlesinger and Mitchell, 1987). Much of the warming occurs in the high latitudes with melting of snow and sea ice, thereby lowering the surface albedo. The lower surface albedo allows more absorption of solar radiation which heats up the surface. In addition, GCMs indicate regional warming from doubled CO_2 concentrations. This warming is related to changes in clouds, precipitation, surface pressure, and soil moisture.

The greenhouse effect refers to the trapping of infrared radiation. The term, "trapping," is not completely correct. The atmosphere naturally absorbs infrared radiation emitted from the warmer surface below and reemits the infrared radiation into space at an atmospheric temperature that is lower than the surface. A net reduction in the infrared radiation emitted from the surface results. When additional greenhouse gases, such as CO_2 , are added to the atmosphere, more absorption of infrared radiation results. The additional absorption of infrared radiation takes place throughout the entire troposphere. The infrared radiation is then radiated into space at a temperature locally colder than normal because the effective emitting layer is now higher in the troposphere. This leads to an even larger reduction in the infrared radiation emitted from the surface into space. The stratosphere also emits infrared radiation into the upper troposphere to cause some warming.

2.5 Planned Experiments

Climatic factors, such as rotation rate, carbon dioxide, lower solar luminosity, and zero land fraction are simulated in chapter 3. The influence of each climatic factor on the present climate is investigated and the climatic factors are combined in a set of sensitivity experiments in order to gain information about climatic conditions of the Archean.

In section 3.1, the influence of faster rotation rate on present-day climate is explored with two experiments—a present-day climate control and an experiment corresponding to a 14-hr earth day. Present-day topography and continental distribution are assumed. Both the control and experiment (denoted FastL) are integrated for 300 days. For all rotation-rate experiments, a 20-min time step is used to ensure model stability. The last 100 days of the integration are time-averaged. The effects of rotation rate on temperature, zonal wind, clouds, precipitation, and other atmospheric variables are explored.

In section 3.2, the role of reduced land fraction and lower solar luminosity is investigated with a control and two experiments. The first experiment (denoted Glocean) represents a global ocean in which sea-surface temperatures are calculated everywhere using the energy balance equation. Glocean has no topography and is integrated for 450 days. The last 200 days of the integration are time averaged. The longer integration time is needed because the starting point of the integration is from a winter boundary condition. In the second experiment, (ColdO) a global ocean condition is once again used, but the solar luminosity is reduced by 10% from 1370 to 1233 W m^{-2} . ColdO is integrated for 300 days and compared to the present-day climate control. The last 100 days are time averaged. The goal of this experiment is to determine if an ice-albedo catastrophe can be avoided. In both experiments, changes in atmospheric variables such as temperature and clouds are noted.

In section 3.3, the role of reduced land fraction, lower solar luminosity, higher carbon-dioxide concentrations and faster rotation rate is explored through four experiments: (1) ColdO (the global ocean with a 10% reduction in the solar luminosity), (2) 4ColdO (carbon dioxide is increased in experiment ColdO by 4 times the present amount—330 ppm), (3) 8ColdO (then by 8 times the present-day concentrations), and (4) 14hrColdO (experiment ColdO is considered with a faster rotation rate corresponding to a 14-hr earth day). Both 4ColdO and 14hrColdO experiments

are integrated for 150 days, with the last 50 days for time averaging. Experiment 8ColdO is integrated for 300 days and the last 90 days are time averaged. Particular attention in these experiments is given to sea-ice distribution, sea-surface temperature and dynamics.

In section 3.4, the combined roles of reduced land fraction, higher carbon-dioxide concentrations, higher rotation rate, and lower solar luminosity are investigated with three experiments: (1) an experiment with 8 times present carbon-dioxide concentrations, a rotation rate corresponding to a 14-hr earth day, zero land fraction, and a 10% reduction in the solar constant (denoted Ice1), (2) the same factors as (1) except the solar constant is reduced by 15% (denoted Ice2) and (3) the same conditions as (1) and (2) except the solar constant is reduced by 20% (denoted Ice3). The equatorward movement of sea ice, along with radiative and dynamical changes, is noted in these experiments.

CHAPTER III

ARCHEAN CLIMATE SIMULATIONS

3.1 The Effects of Faster Rotation Rate on the Climate System

Introduction

In this section I explore the effect of a faster rotation rate on the climate system. The present-day climate simulation (control) has a rotation rate of $7.292 \times 10^{-5} \text{ s}^{-1}$. In the fast rotation rate simulation (FastL—L stands for land), a rotation rate is changed to $1.23964 \times 10^{-4} \text{ s}^{-1}$ (values are from Kuhn et al., 1989; Figure 1.4). These experiments contain present-day smoothed topography and land distribution. Both the control and FastL are integrated for 300 days, with the last 100 days used as the averaging period.

Temperature

Faster rotation rates cause colder polar regions and warmer temperatures elsewhere. Figure 3.1 shows the zonally averaged surface temperatures for FastL and the control. Poleward of 65° , in both hemispheres, the surface temperature decrease

is caused by less efficient heat transport of eddy motions. The reduced efficiency of heat transport by eddies is caused by a decrease in the horizontal scale of atmospheric eddies demonstrated in dishpan experiments (Fultz, 1959). As the rotation rate increases, the transient and stationary eddies become smaller. This result for stationary waves is obtained if the Rossby frequency equation is used. It is given by the following formulation:

$$L_s = 2\pi \sqrt{\frac{u}{\beta}} \quad (3.1)$$

β is given by

$$\beta = \frac{\partial f}{\partial y} = \frac{\partial(2\Omega \sin \phi)}{a \partial \phi} = \frac{2\Omega \cos \phi}{a}$$

$u \equiv$ Mean wind at 500 mb

$L_s \equiv$ Wavelength of stationary waves

For a mean winter values of $u = 15 \text{ m s}^{-1}$ at 45° :

$$L_{s24} = 6046 \text{ km}$$

$$L_{s14} = 4640 \text{ km}$$

For model results at .5S (near 500 mb), 42.2°N :

$$U_{24} = 15.79 \text{ m s}^{-1}$$

$$U_{14} = 5.575 \text{ m s}^{-1}$$

$$L_{s24} = 6203 \text{ km}$$

$$L_{s14} = 2829 \text{ km}$$

The increase in the number of stationary troughs for FastL is evident from the 300 mb geopotential heights in the Northern Hemisphere (Figure 3.2). The global mean surface temperature is shown in Table 3.1. The 2 K increase for FastL is caused by a decrease in the total cloud fraction (Figure 3.11). FastL exhibits a steeper meridional temperature gradient in middle and high latitudes, thus creating an environment for greater baroclinic activity.

The faster rotation rate is responsible for warmer temperatures near the surface and in the upper troposphere and cooler temperatures in the middle troposphere and

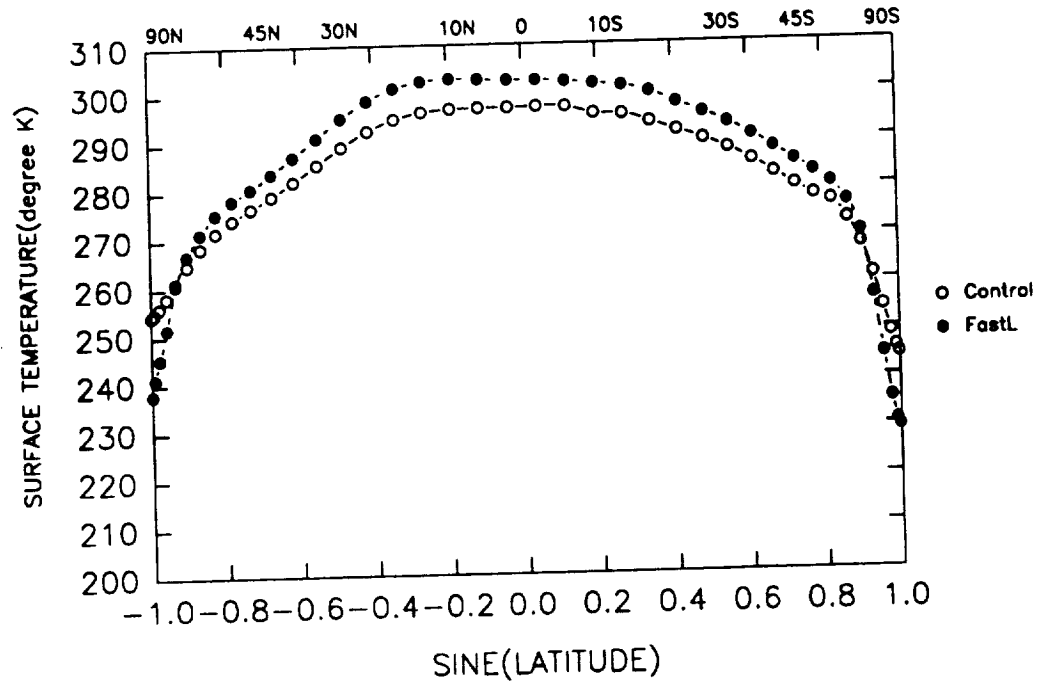
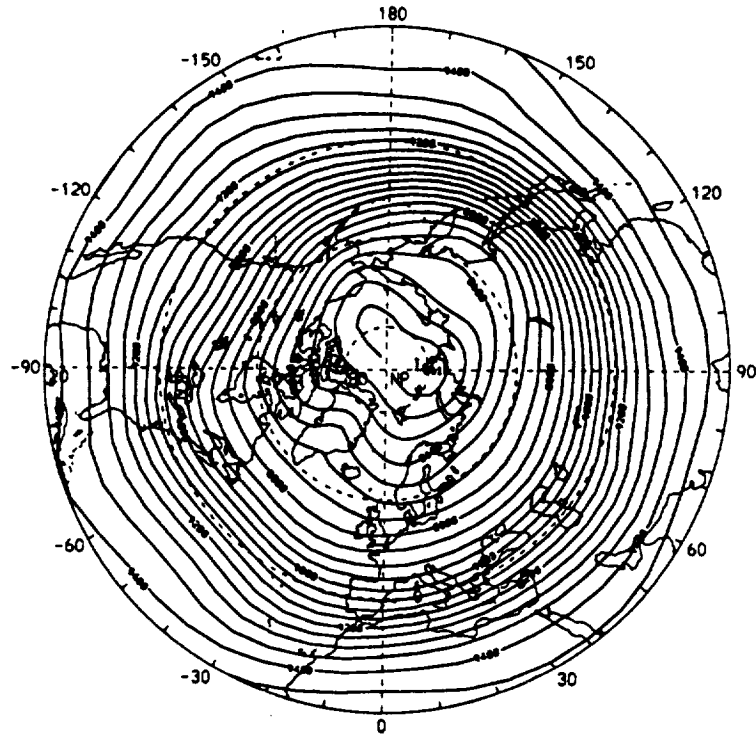


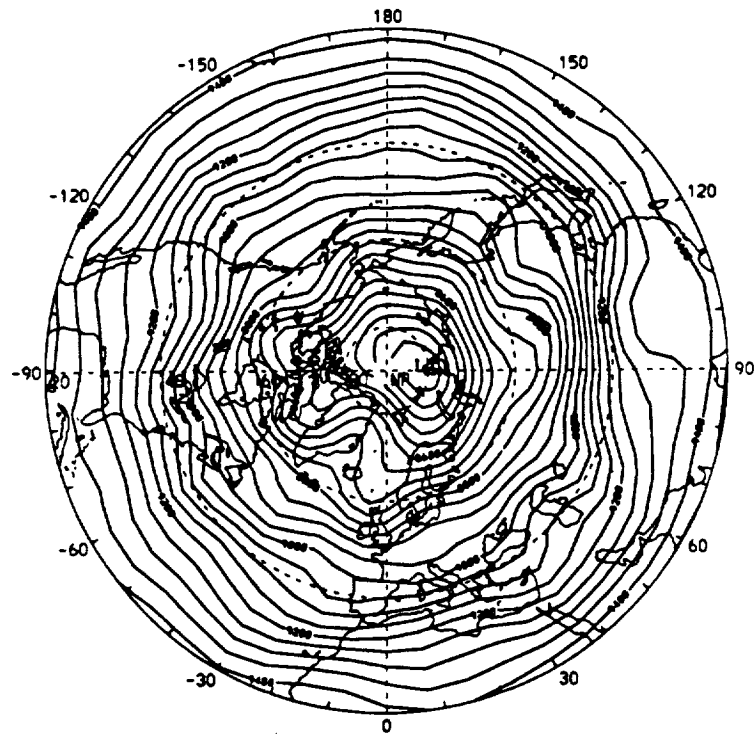
Figure 3.1: Zonally averaged surface temperature in degrees Kelvin.

Variable	Control	FastL
T_{air} K	284.96	287.22
Cloud fraction	0.423	0.331
Precipitation (cm yr^{-1})	114.2	118.3
$F_{TopIR} \uparrow$ (W m^{-2})	230.01	240.28
$F_{SurfIR} \downarrow$ (W m^{-2})	295.1	298.1
$F_{SurfIR} \uparrow$ (W m^{-2})	373.9	385.9
$F_{Surfsolar} \downarrow$ (W m^{-2})	188.09	198.08

Table 3.1: Global mean values for the control and FastL.



(a) Geopotential heights for the control.



(b) Geopotential heights for FastL.

Figure 3.2: 300-mb Northern Hemisphere geopotential heights. (a) control; (b) FastL. Units: meters

lower troposphere in polar regions. Figure 3.3 shows the difference in the latitude height temperature field between FastL and the control simulation. Cooling occurs in the polar regions of the lower troposphere and in the middle troposphere near 30°N and 30°S. Cooling in the polar regions is a result of the decrease in transport of sensible heat by eddy motions, while the cooling trend in the subtropics is due to less subsidence at the poleward edge of the Hadley cell. This decrease in subsidence causes less adiabatic warming and a cloud increase (Figure 3.12). The warming trend near the polar tropopause is caused by increases in the heat transport of both transient and stationary eddies (Figure 3.7). Equatorial tropopause temperatures for FastL increase slightly compared to the control.

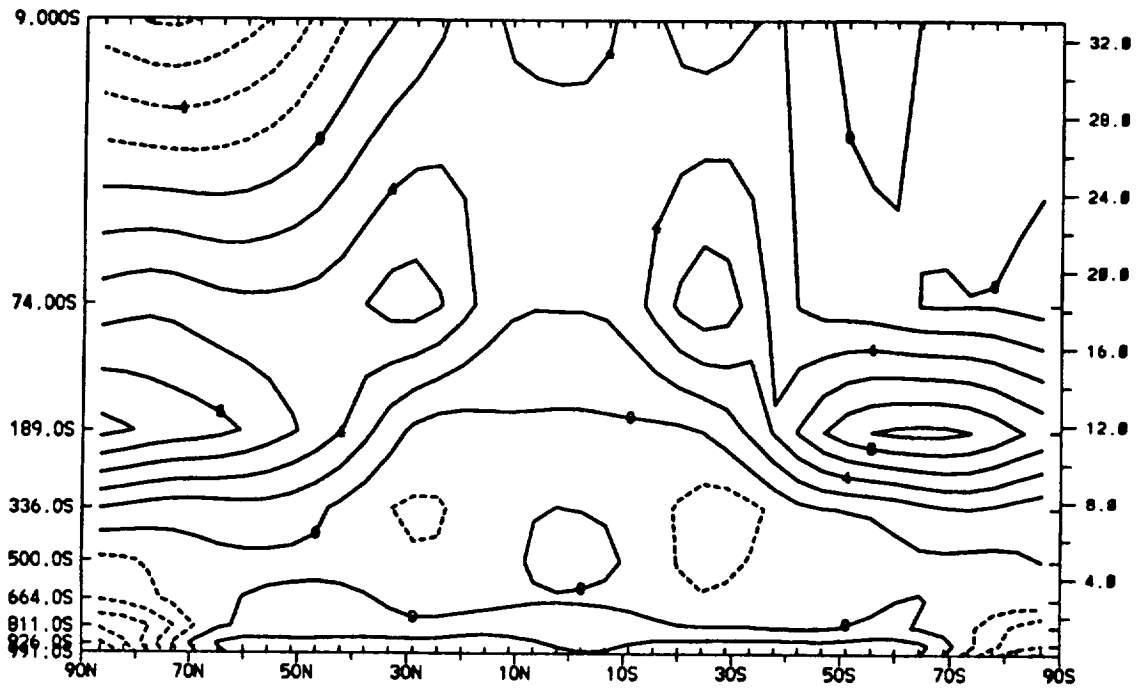


Figure 3.3: Atmospheric temperature difference in degrees Kelvin.
FastL minus control.

Zonal winds

Faster rotation rates allow the westerly jet to decrease and move equatorward.

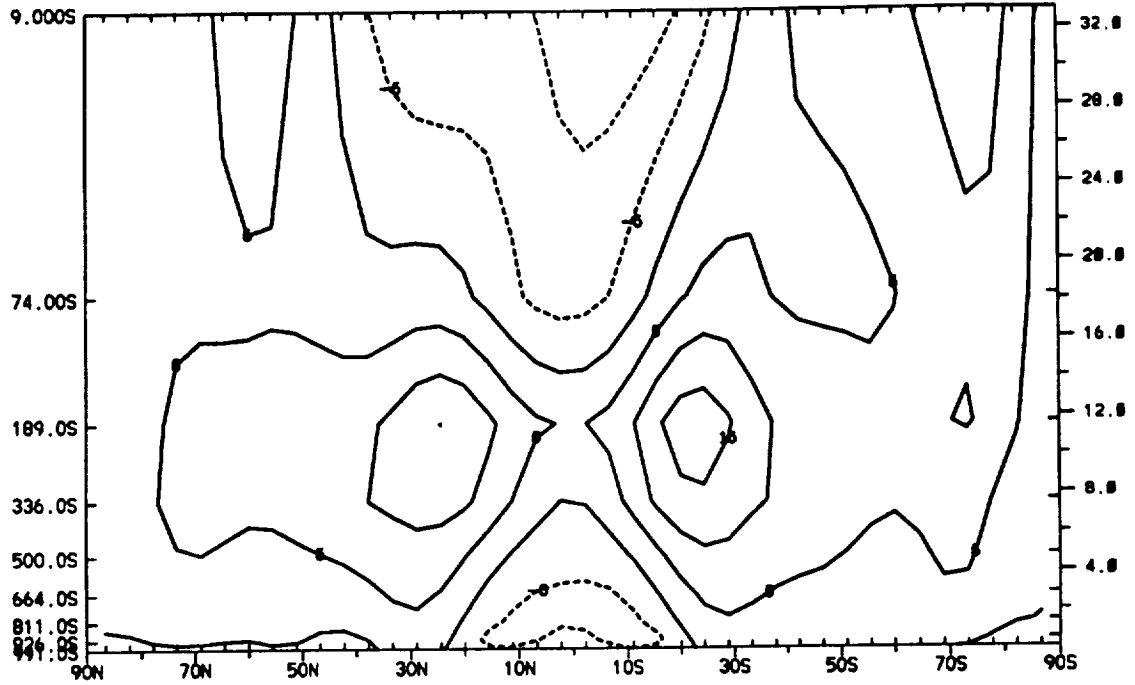
FastL shows a decrease in the mean annual jet of 10 m s^{-1} compared to the control (Figure 2.5) in Figure 3.4. There are weaker tropical easterlies in the lower and upper troposphere. The low-level polar easterly winds in the Northern Hemisphere extend nearly to 35° because of the topography of the Northern Hemisphere; this effect is not observed in the Southern Hemisphere. The jets show an equatorial shift of approximately 10° in position. Larger vertical shear is predicted from the thermal wind equation and is noted in the jet cores of FastL.

Streamfunction

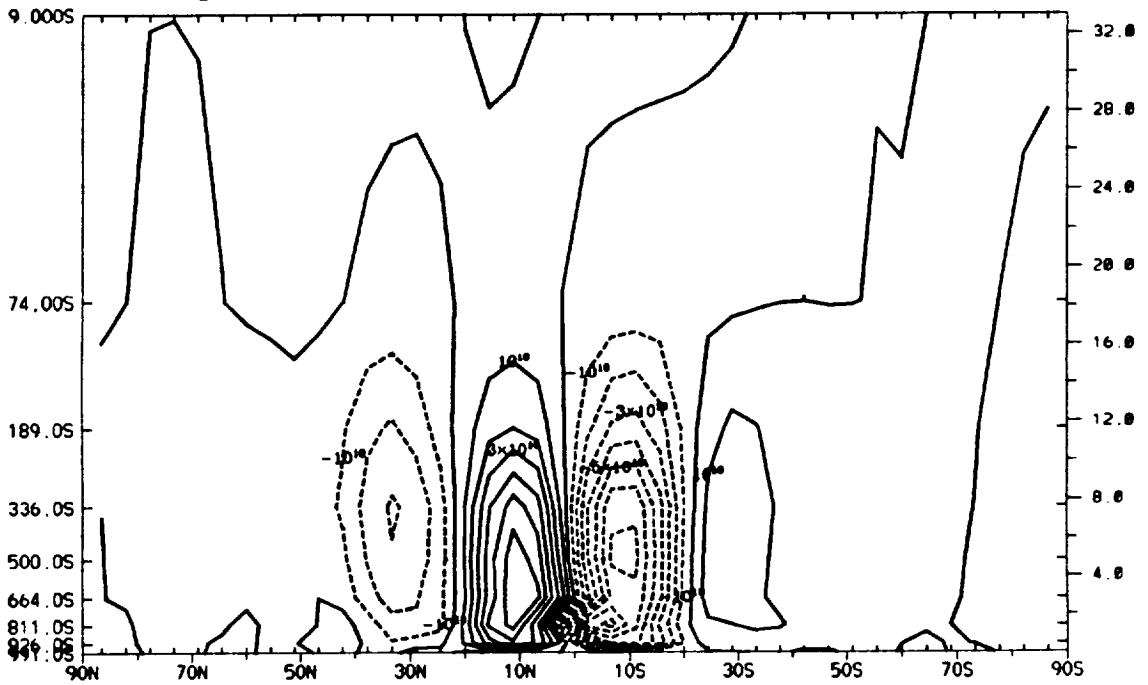
A weaker Hadley cell is confined to low latitudes with a faster rotation rate. FastL (Figure 3.4) exhibits a weaker Hadley cell narrower in latitudinal width than the control (Figure 2.5). The indirect Ferrel cells have not changed much in magnitude except in the Southern Hemisphere, but they have shifted equatorward. The shift in the Hadley and Ferrel cells is approximately 10° . The shift in the indirect Ferrel cell indicates that much of the baroclinic activity has also shifted equatorward and is apparent in the precipitation field (Figure 3.15) which shows the equatorward shift. The intensity of the Hadley cell has decreased by factors of 1.5 and 1.2 for FastL in the Northern and Southern Hemispheres, respectively. The Southern Hemisphere indirect Ferrel cell in FastL has decreased by a factor of 1.8 compared to the control.

Transient and stationary eddy heat transport

Faster rotation rates allow a decrease in midlatitude heat transport by transient eddies. An equatorial shift in the heat transport distribution of the upper troposphere however, allows areas of increases. The latitude-height transient eddy heat transport for FastL shows significant changes with respect to the control simulation (Figure 3.5). The maximum transient heat transport in the upper troposphere shows an



(a) Zonal wind. Contour interval: 5 m s^{-1} .



(b) Mean meridional streamfunction. Contour interval; $1 \times 10^{10} \text{ kg s}^{-1}$

Figure 3.4: (a) Zonal wind distribution; (b) mean meridional streamfunction for FastL.

equatorial shift of 10° when compared to the control. In the lower troposphere, the transient heat transport is less than the control with the maximum heat transport in FastL shifting poleward to approximately 60° in the Northern Hemisphere and between 60° and 70° in the Southern Hemisphere. This leads to large changes when differences between the FastL and the control are compared (Figure 3.7a).

The entire atmosphere in Figure 3.7a shows increases in heat transport in the middle and upper troposphere and decreases in the lower troposphere. The control simulation has both poleward and equatorward heat transport in the middle and upper troposphere, whereas FastL shows mainly northward heat transport.

To demonstrate the increase in the heat transport of the upper troposphere, consider the geographical distribution of heat transport by transient eddies near 200 mb over North America. Observations (Oort, 1983), the control, and FastL are shown in Figures 3.8 and 3.9. The simulated equatorial heat transport is somewhat different in magnitude and direction from the observed in some regions. The control simulation shows equatorward and poleward heat transport, whereas FastL shows little or no equatorward heat transport. The heat transport in FastL appears to be less organized, thus supporting the idea of smaller eddies.

Faster rotation alters the stationary heat transport in latitudes where topography occurs. These latitudes include (1) 30° – 40° N (site of the Rocky and Himalaya Mountains), (2) near 75° N (Greenland), and (3) poleward of 80° S (Antarctica).

The stationary heat transport in FastL carries a distribution similar to the control (Figure 3.6), but the magnitudes of the equatorward and poleward heat transports have changed significantly. The heat transport has changed as follows: (1) Near 75° N, the equatorward heat transport near .5s has increased. (2) In midlatitudes between 30° – 40° N, near .5S the heat transport has increased by a factor of two. (3) Only poleward heat transport near 70° S is noted in the midtroposphere of FastL. (4) Only poleward heat transport in southern polar regions near .189S is displayed in FastL.

(5) The poleward heat transport near the surface in the northern polar regions has increased in FastL. (6) The poleward heat transport in the upper troposphere and lower stratosphere in the control centered near 30°N and .74s does not appear in FastL.

The differences in the stationary heat transport are shown in Figure 3.7b and reflect the changes above. The largest changes occur in the polar regions of the Southern Hemisphere.

Spectral kinetic energy

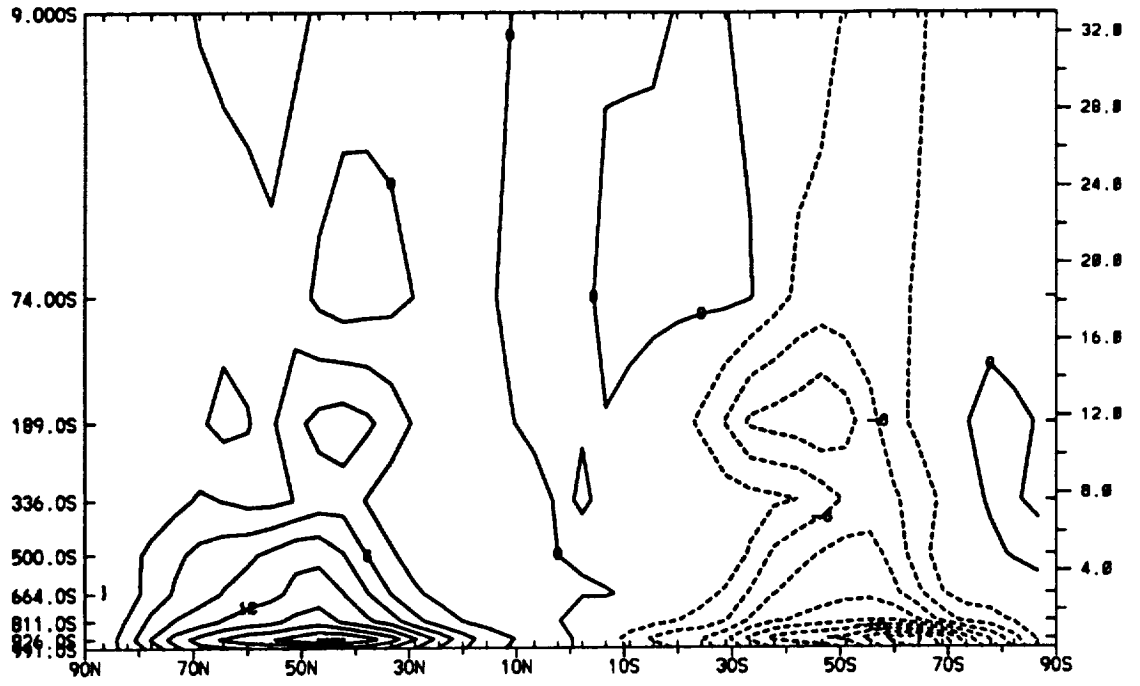
Kinetic energy increases in smaller-sized baroclinic waves with faster rotation rates. The spectral kinetic energy for FastL and control is shown in Figure 3.10. The two-dimensional wavenumber is given by

$$K = \frac{2\pi r \cos \phi}{L} \quad (3.1)$$

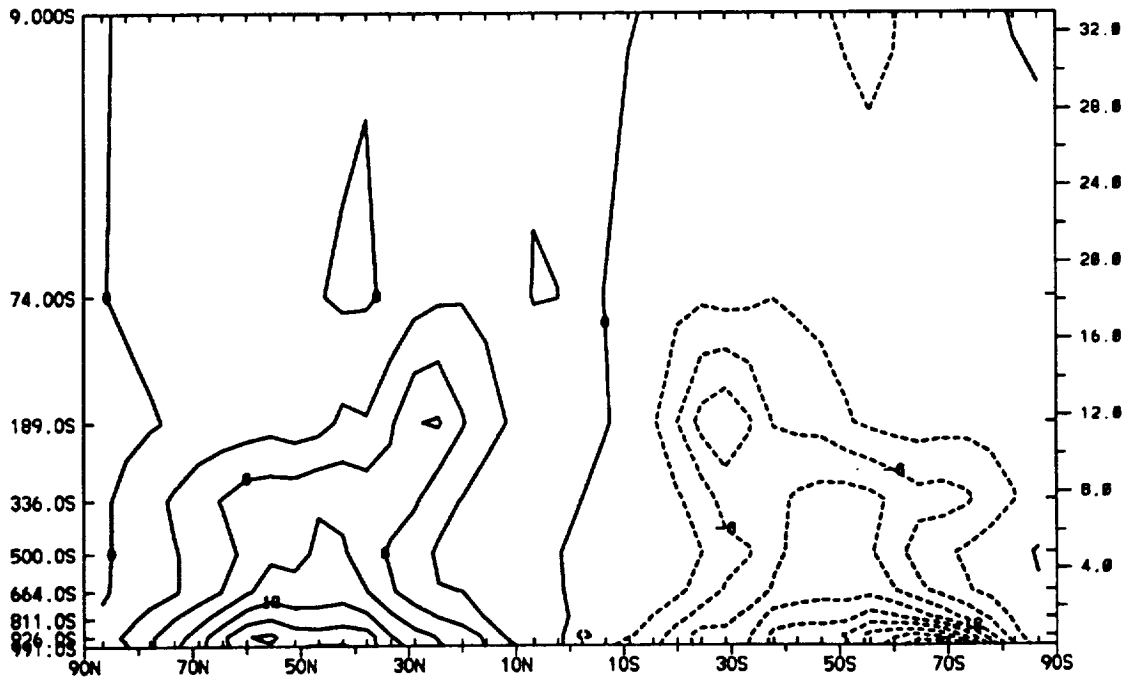
where r is the earth's radius, L longitudinal wavelength, and ϕ latitude. FastL indicates that energy is being shifted to larger wavenumbers with a peak at roughly wavenumbers 13–15. The peak occurs near the truncation value of the model (wavenumber 15). The wavelength shifts from approximately 3145 km for the control to 2177 km for FastL at 45°. Both cases reflect that the -3 power law is in effect. The values in Figure 3.10 represent the global value of specific kinetic energy at .5S (near 500 mb).

Clouds

When the rotation rate is increased, the total cloud fraction is substantially reduced. FastL shows a large decrease for zonally averaged total cloud fraction, compared to the control (Figure 3.11) simulation. The largest change in the total cloud

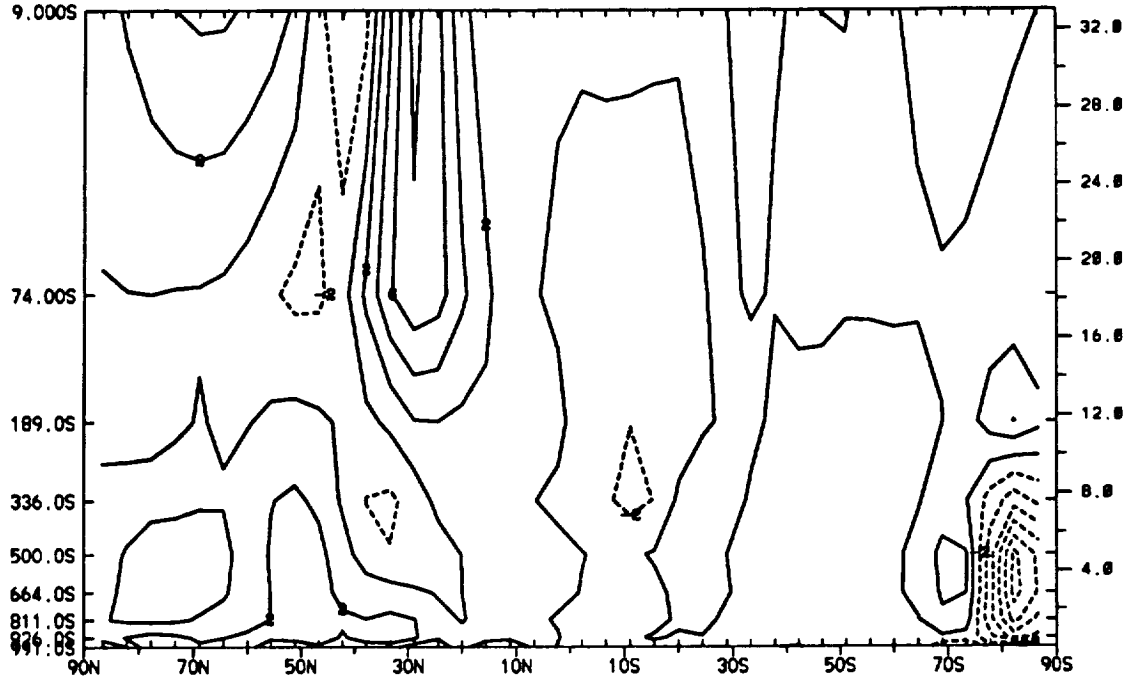


(a) Control.

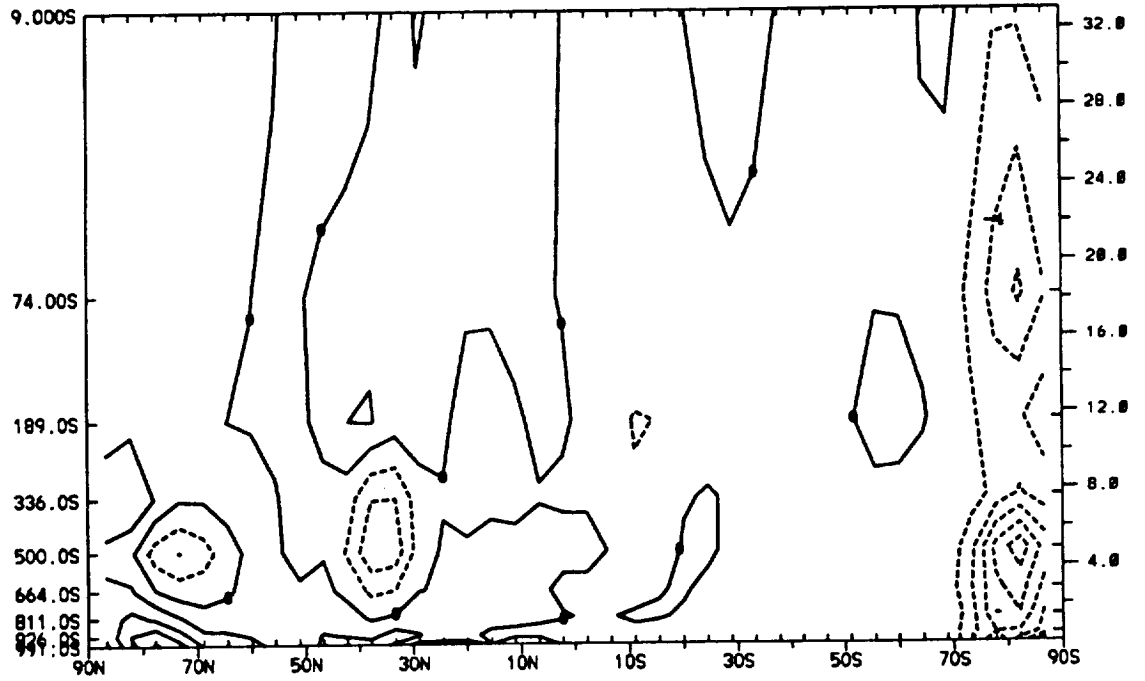


(b) FastL.

Figure 3.5: Transient eddy heat transport for the control and FastL.
 (a) control; (b) FastL. Contour interval: 3 K m s^{-1}

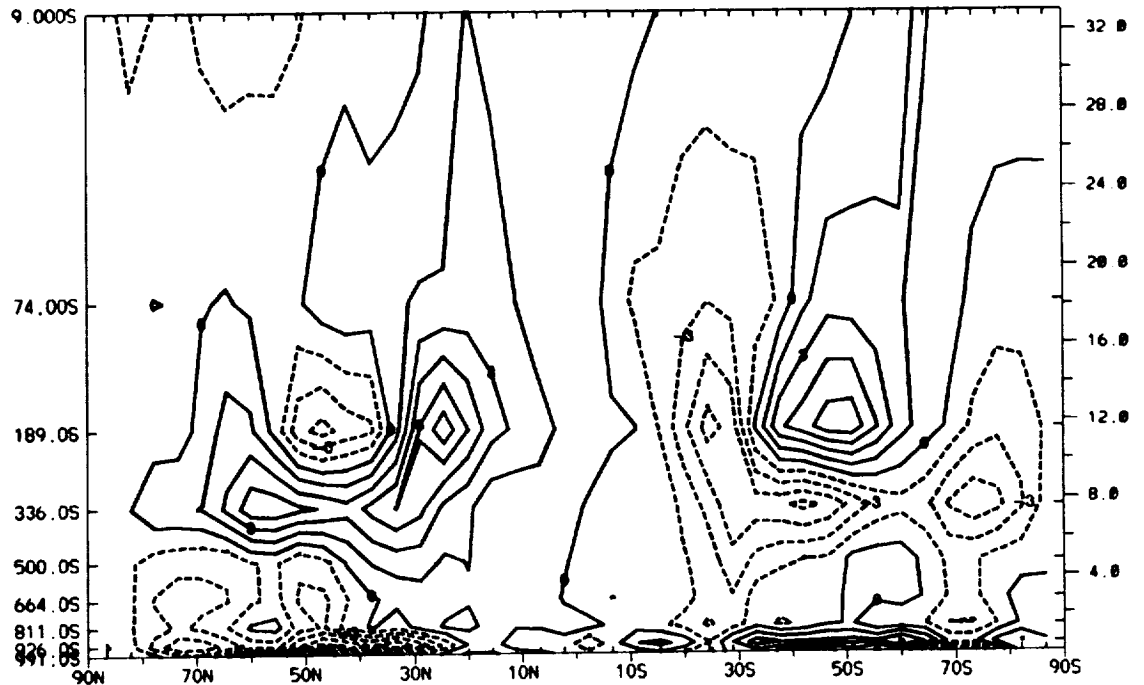


(a) Control.

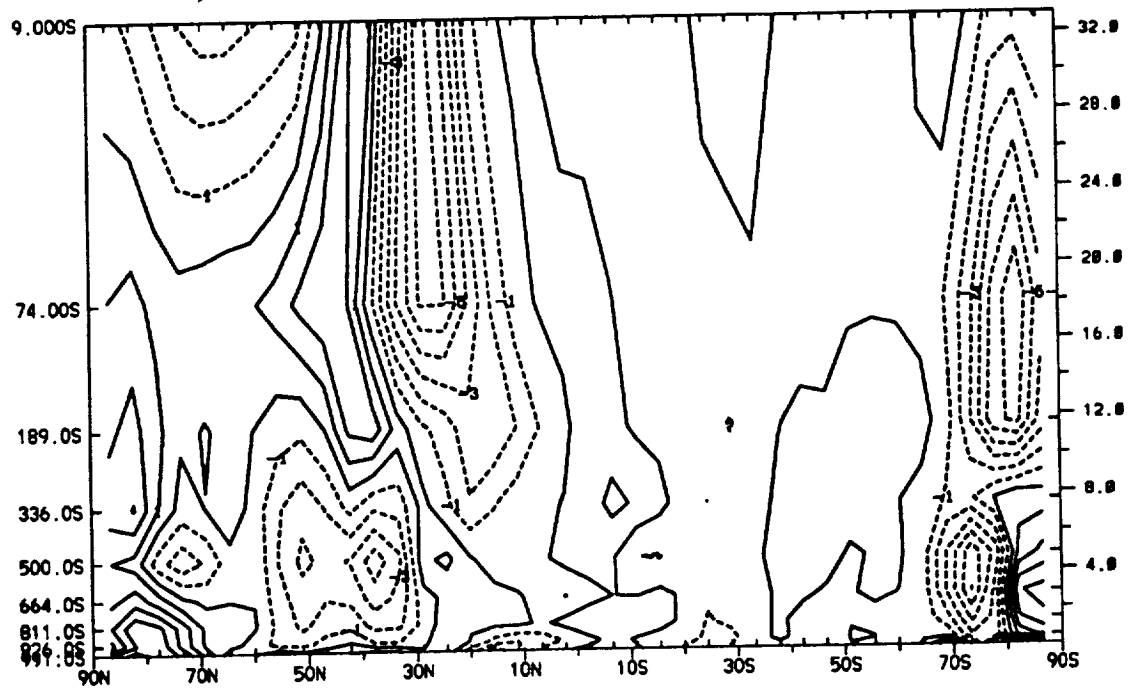


(b) FastL.

Figure 3.6: Stationary eddy heat transport for the control and FastL.
 (a) control; (b) FastL. Contour interval: 2 K m s^{-1}



(a) Difference in transient eddy heat transport. Contour interval: 1.5 K m s^{-1} .



(b) Difference in stationary eddy heat transport. Contour interval: 1.0 K m s^{-1} .

Figure 3.7: Difference in eddy heat transport. (a) transient; (b) stationary: FastL minus control.

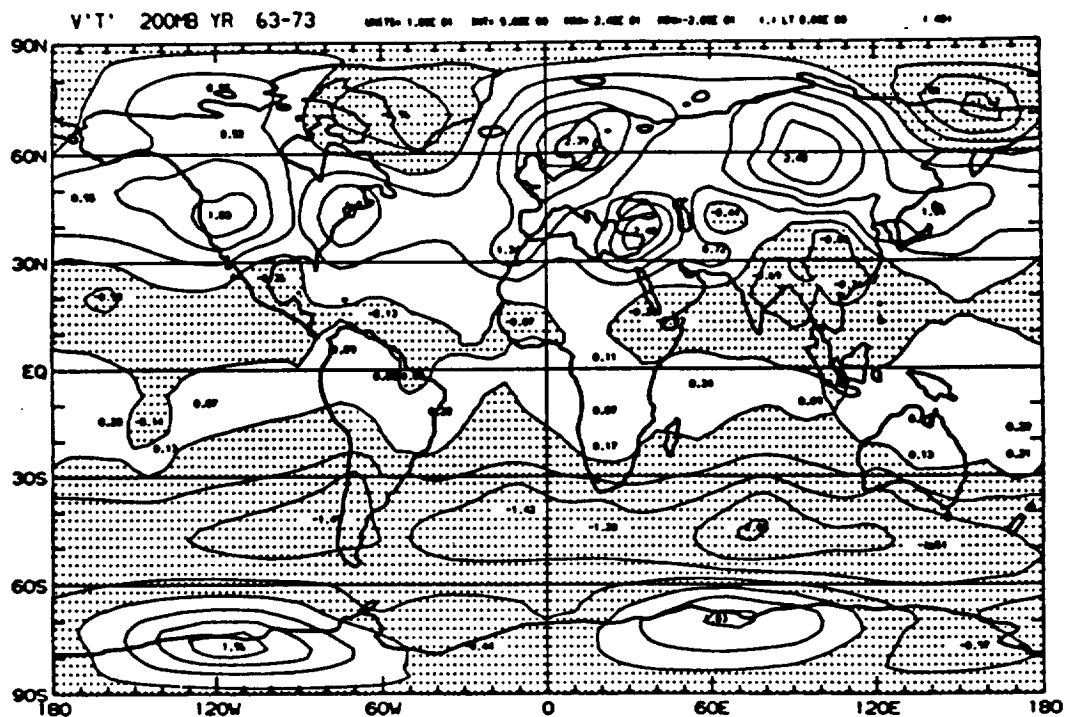
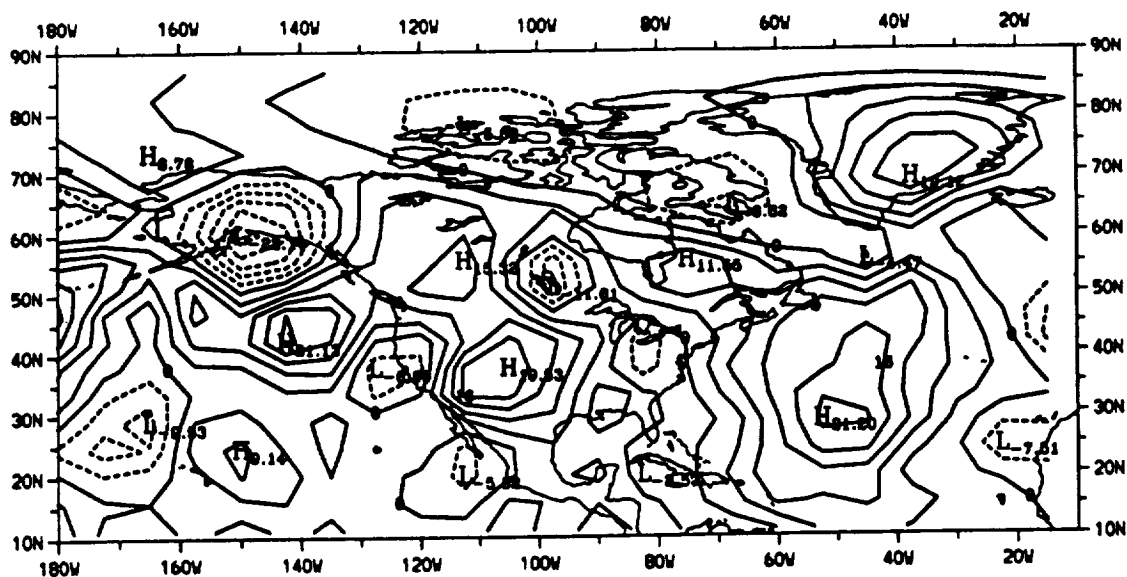


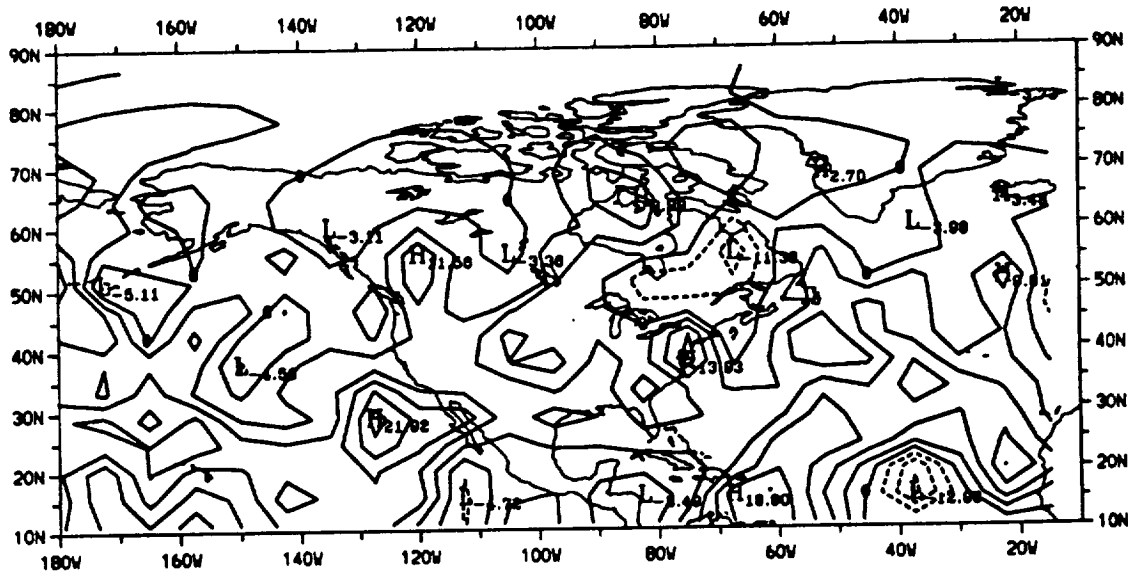
Figure 3.8: Observed distribution of transient eddy heat transport at 200 mb. Units: K m s^{-1} .

fraction occurs in the equatorial and polar regions. The latitude-height difference in clouds (Figure 3.12) shows that clouds decrease at all atmospheric levels and at all latitudes in the FastL compared to the control, except in the tropics. The only regions of increase are near 30°N and 30°S in the middle troposphere. A 21% decrease in global mean cloud field for FastL is noted in Table 3.1. The decrease in clouds is caused by a decrease in relative humidity (Figure 3.12) which indicates that the atmosphere is either warmer or drier. The difference in mixing ratio (Figure 3.13) shows a drier atmosphere in the tropics and polar regions, while Figure 3.3 shows a warmer atmosphere in many regions throughout the troposphere.

The warmer atmosphere drives down relative humidity because of the larger saturation vapor pressure which increases exponentially with temperature. The temperature increase in the mid- to upper troposphere and lower stratosphere is the primary cause for the cloud decrease. This temperature increase (Figure 3.3) is caused by

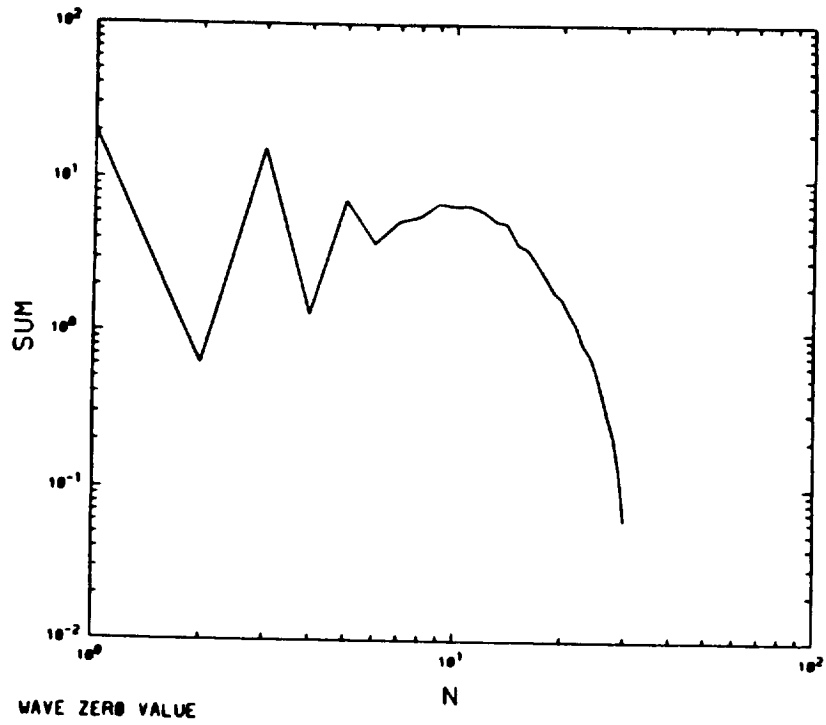


(a) Control. Units: K m s^{-1} .

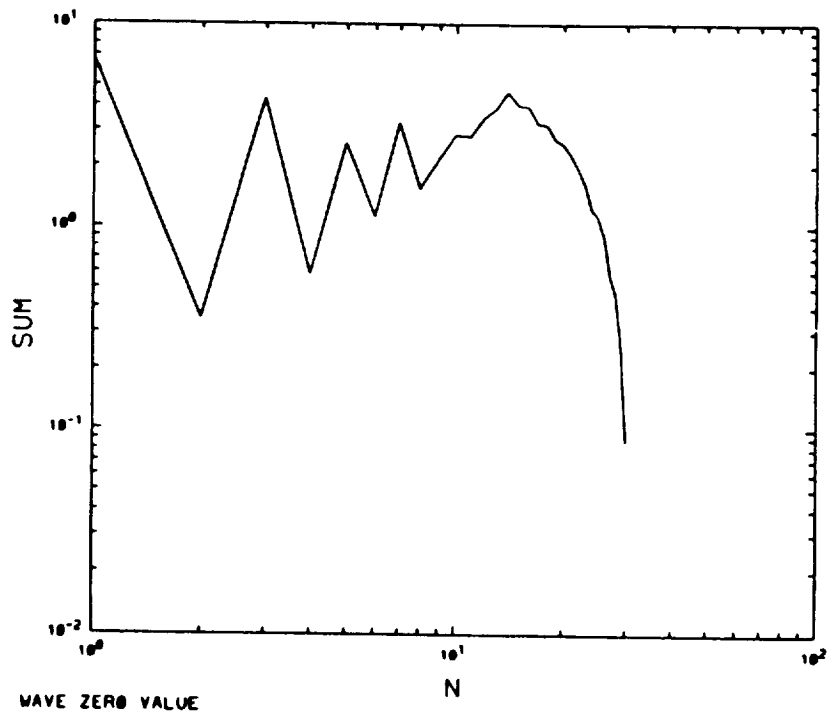


(b) FastL. Units: K m s^{-1} .

Figure 3.9: Geographical transient heat at .189S (near 200mb) over North America. (a) control; (b) FastL.



(a) Control.



(b) FastL.

Figure 3.10: Spectral kinetic energy. (a): control; (b): FastL. Units: J kg^{-1} .

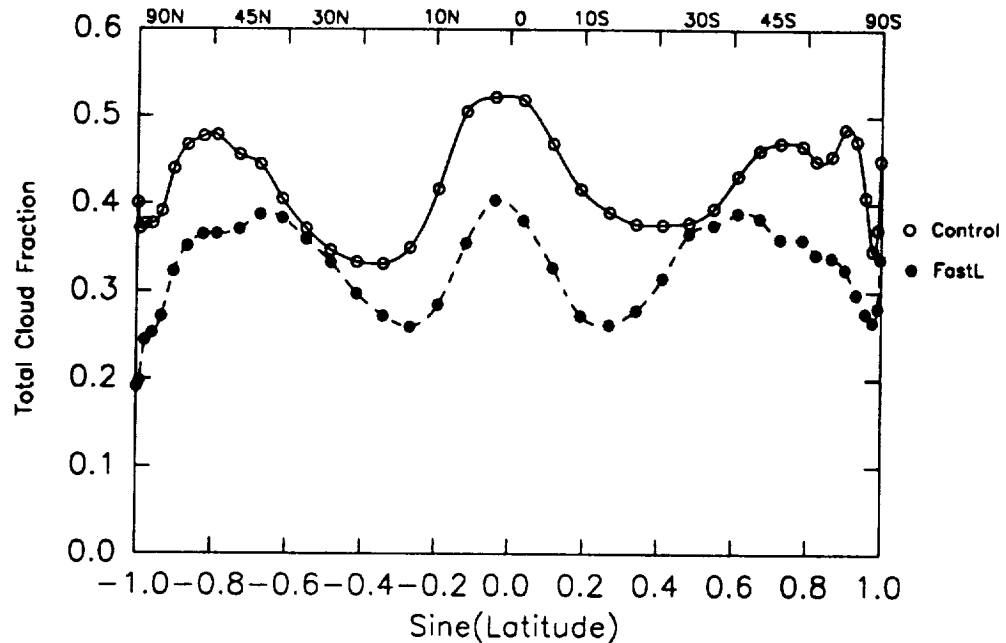
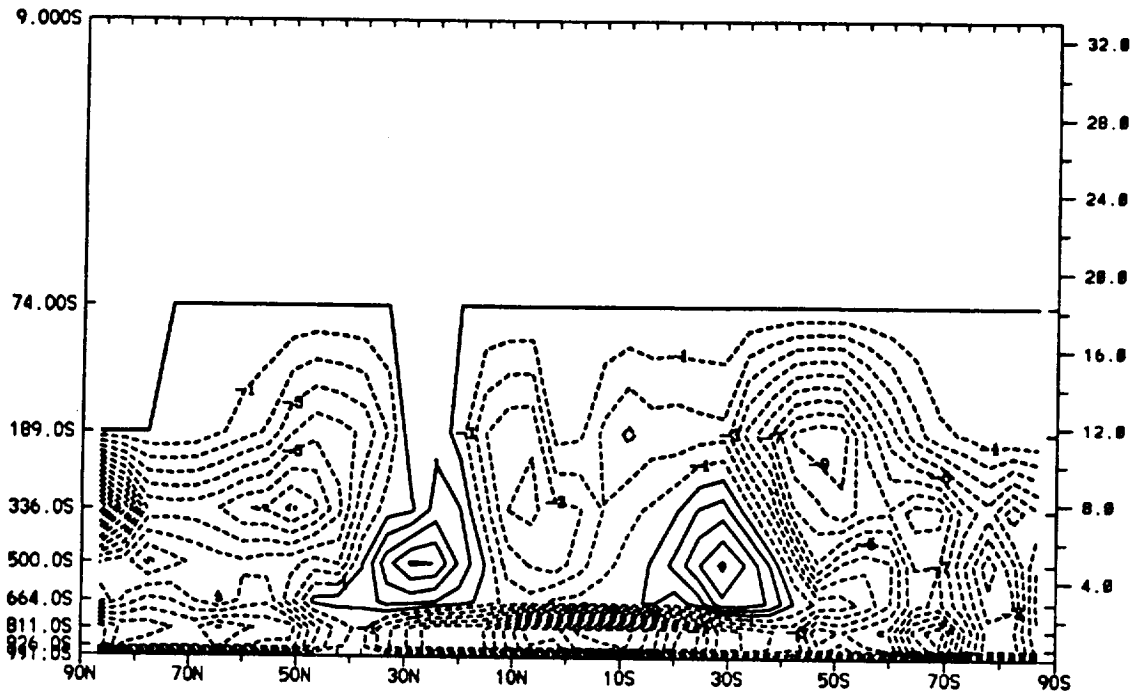


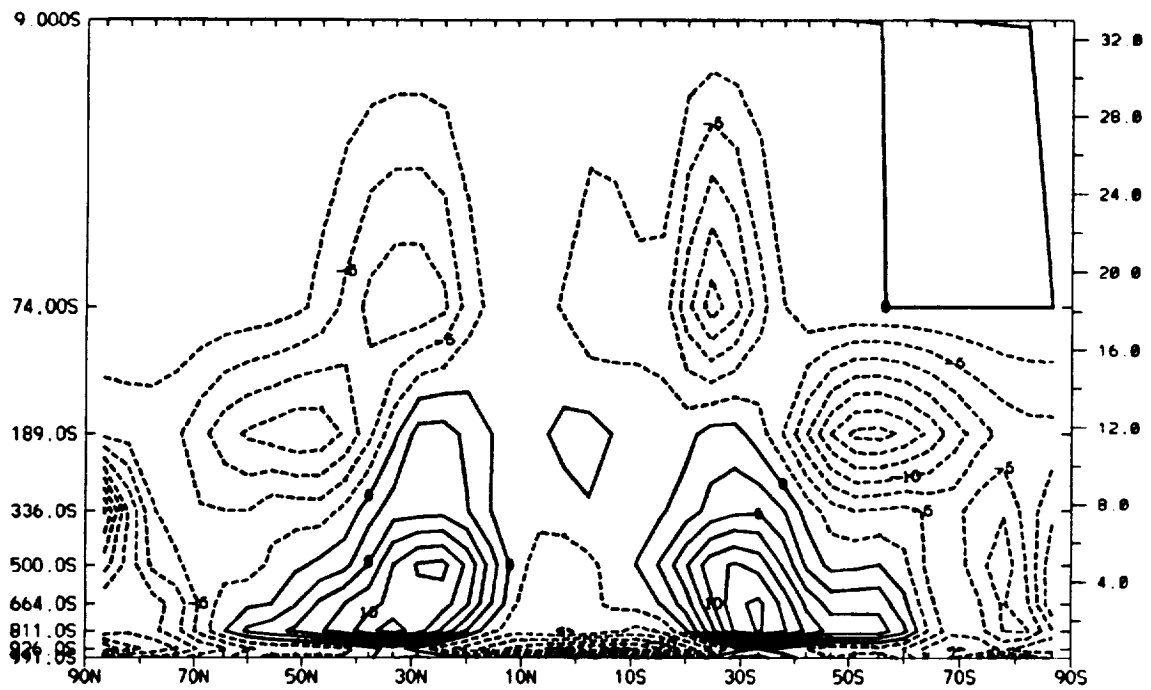
Figure 3.11: Total cloud fraction.

increased stationary and transient heat transport in regions depicted in Figure 3.7. The increase in clouds near 30°N and 30°S in the midtroposphere is caused by the equatorial shift in the Hadley cell. The equatorward movement of the Hadley cell in FastL causes less sinking and more rising motions near the poleward edge of the Hadley cell in the control allowing a temperature decrease. This increases relative humidity.

The decrease in relative humidity with a faster rotation rate, causes in convective and nonconvective clouds to decrease. The interactive cloud scheme (Figure 2.1) of the CCM makes all clouds dependent on relative humidity; if the relative humidity falls below 80% clouds dissipate. This effect is largest for the nonconvective clouds which assume a much larger cloud fraction than convective clouds. Figure 3.14 depicts the difference in nonconvective and convective clouds between FastL and the control. The changes in nonconvective clouds reflect the changes of the total cloud



(a) Cloud difference. Units: percent.



(b) Relative humidity difference. Units: percent

Figure 3.12: Difference in (a) cloud field; (b) relative humidity. FastL minus control.

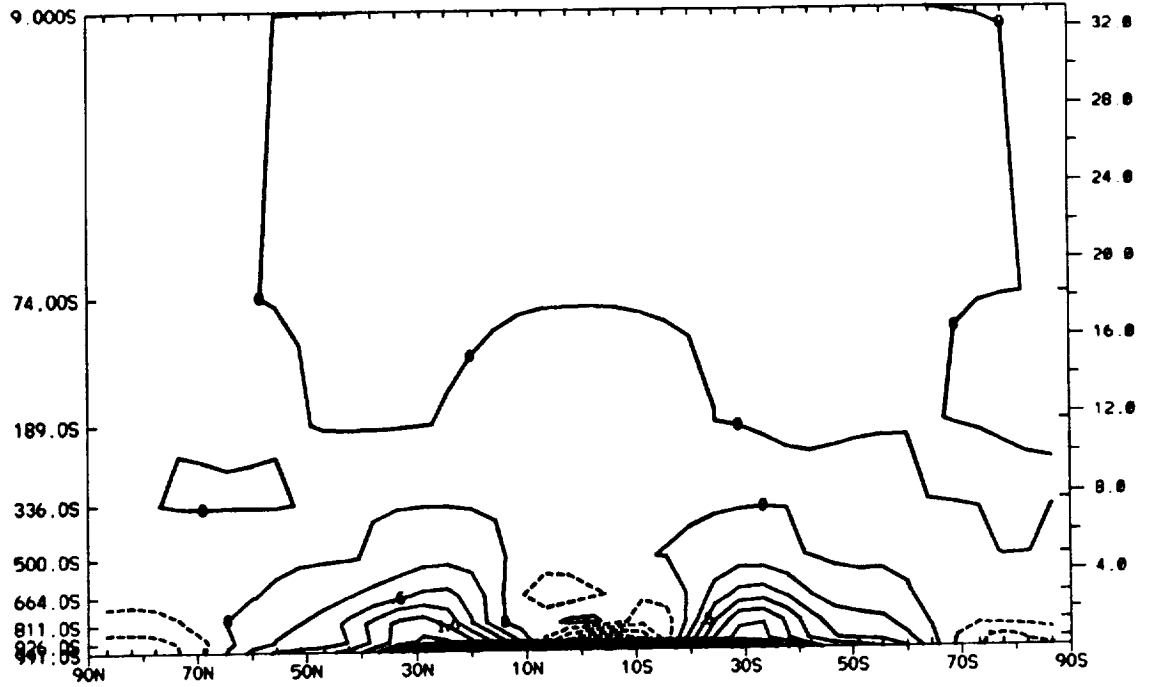
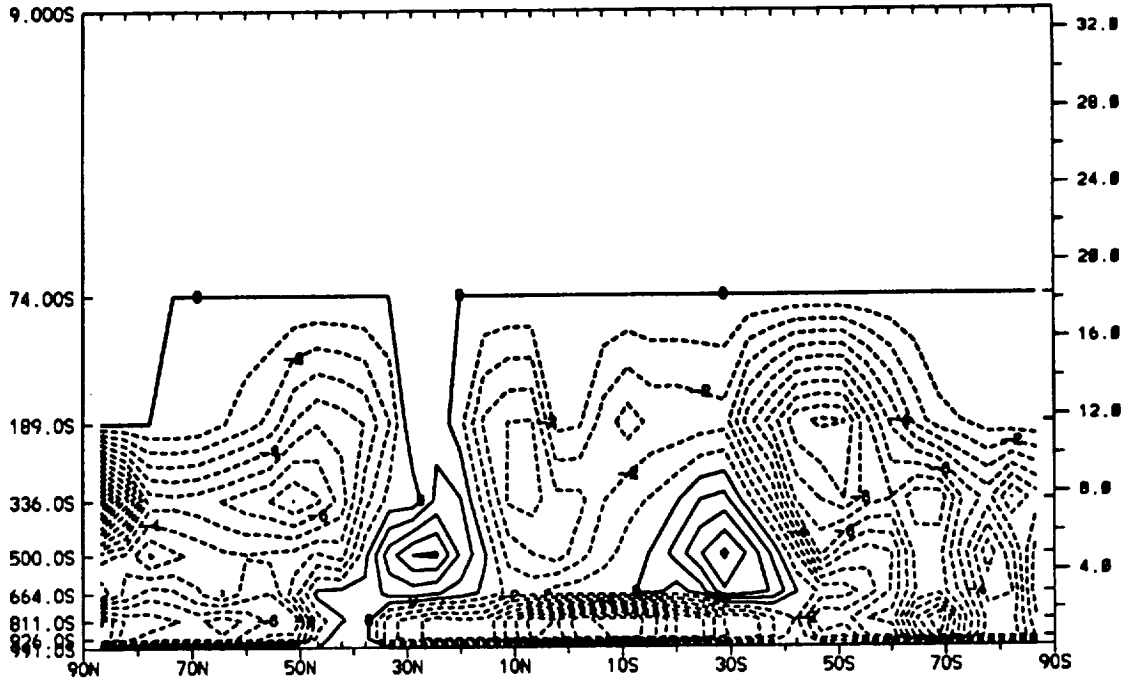


Figure 3.13: Difference in mixing ratio: FastL minus control. Units: g kg^{-1} .

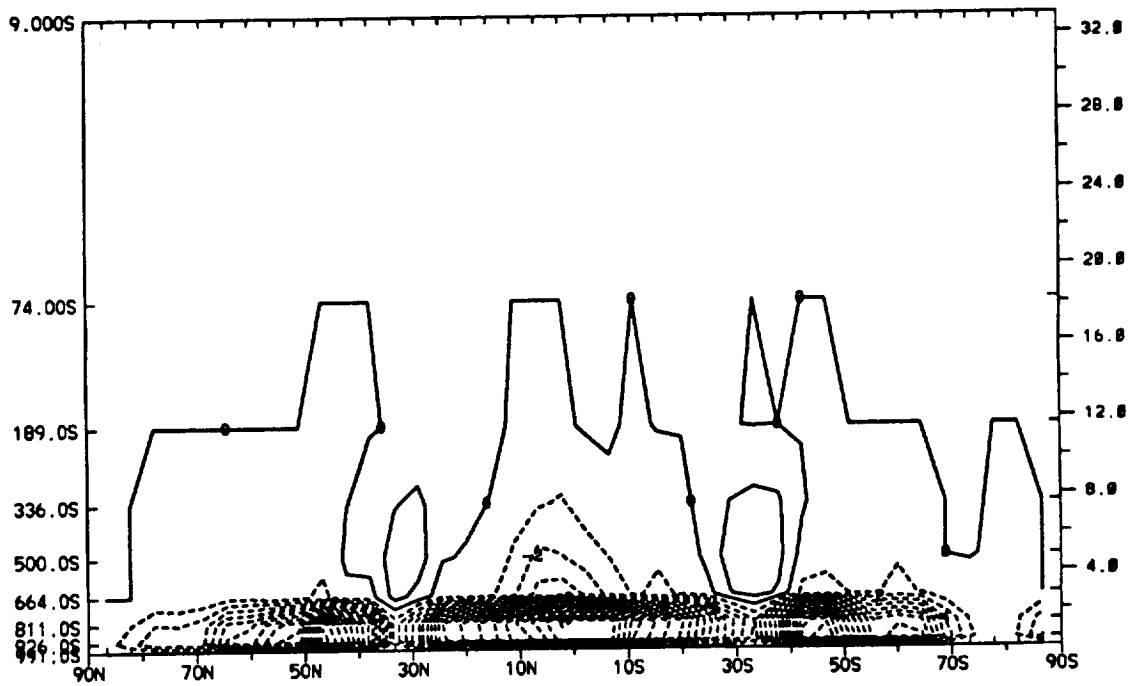
field (Figure 3.12) because of its larger cloud fraction. Convective clouds are largely affected in equatorial and midlatitude regions. There are some indications that the small disorganized baroclinic systems have less clouds associated with them.

Precipitation

With faster rotation, the midlatitude precipitation field is shifted equatorward and subtropical precipitation increases (Figure 3.15). A decrease in equatorial precipitation is noted because of a decrease in rising motions. A decrease in precipitation for FastL is noted in the midlatitudes with small changes elsewhere, except near 60°S – 70°S , the region of the circumpolar current (a decrease in precipitation is noted here). Global mean precipitation shows a slight increase in precipitation for FastL (Table 3.1).



(a) Convective-cloud difference. Units: percent.



(b) Nonconvective-cloud difference. Units: percent

Figure 3.14: Difference in clouds. FastL minus control. (a) convective;
(b) nonconvective. Units: percent

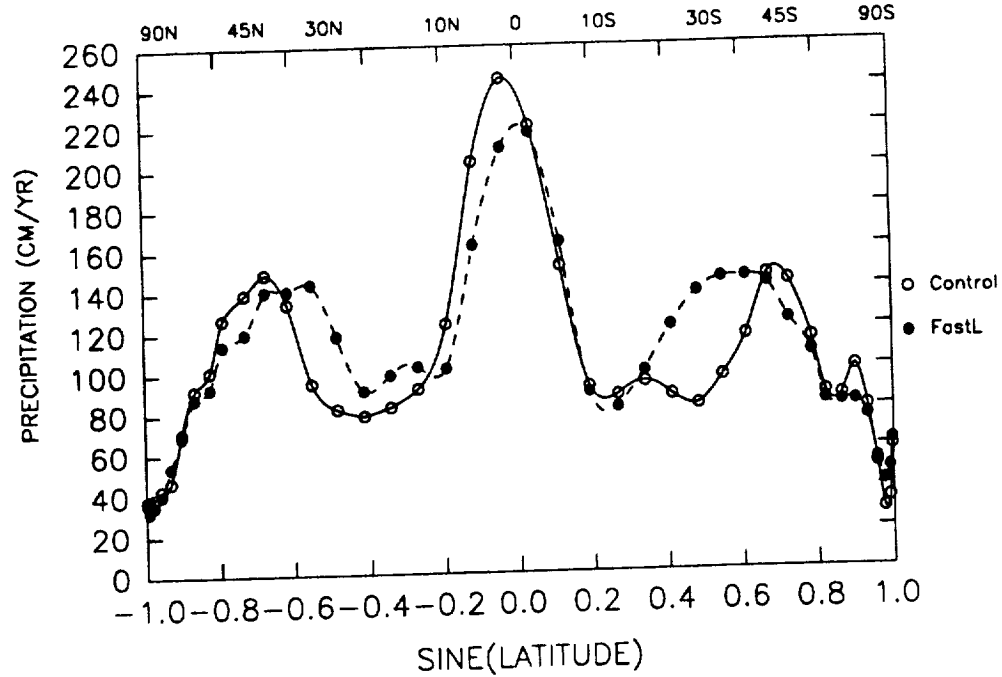


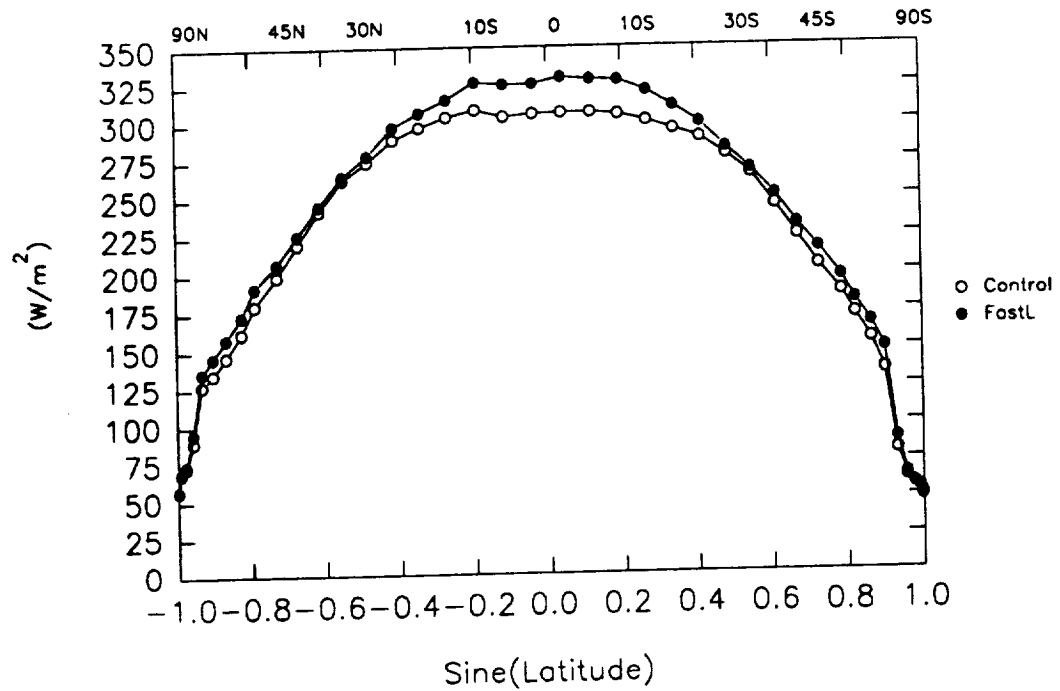
Figure 3.15: Zonally averaged precipitation cm yr^{-1} .

Absorbed solar and outgoing longwave radiation (OLR)

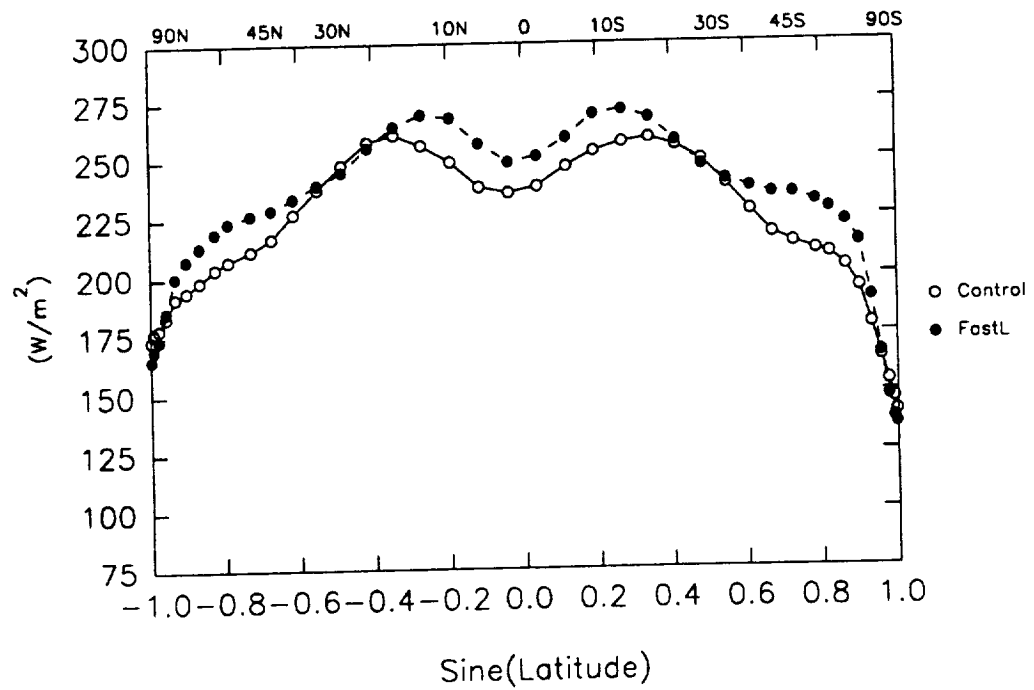
The large cloud decreases associated with the faster rotation rates allow more solar radiation to be absorbed by the surface. FastL absorbs more solar radiation by the earth-atmosphere system compared to the control simulation (Figure 3.16). This increase in solar radiation occurs in equatorial and midlatitude regions where clouds show the largest decreases (Figure 3.11). The smallest increase in absorbed solar radiation occurs near 30°N and 30°S and is associated with the cloud increase in the middle troposphere (Figure 3.12).

Larger amounts of longwave radiation are emitted into space because of the cloud decrease associated with faster rotation. FastL allows more OLR at the top of the model atmosphere (Figure 3.16). Once again, the cloud field is closely related to the increase in OLR because of the smaller cloud fraction (Figure 3.11) allowing for more longwave radiation from the surface to escape into space. At 30°N and 30°S , the OLR

decreases slightly. The increase in middle troposphere clouds (Figure 3.12) captures more of the OLR than the control and radiates OLR at its local temperature, which is colder than the surface. The increase in water vapor (Figure 3.13) also absorbs the surface-emitted longwave radiation, thereby radiating at its local temperature (which is lower than the surface) and reducing the amount of OLR near 30°N and 30°S. The large temperature increase located near the polar tropopause (Figure 3.3) has little effect on the amount of OLR at the top of the model. The global mean OLR indicates a 10 W m^{-2} increase for FastL (Table 3.1).



(a) Absorbed solar radiation by earth-atmosphere system.



(b) Outgoing longwave radiation.

Figure 3.16: (a) Absorbed solar radiation; (b) OLR. Units: $W\ m^{-2}$.

3.2 Zero Land Fraction and Lower Solar Luminosity Experiments

Introduction

These experiments explore the effects of a landless planet and lower solar luminosity on the climate. As described by Kuhn et al. (1989), the earth may have contained only small fractions of land in the early Archean. Continental Cratons in the form of embryotic islands may have been the predominate land masses on this young planet. Three experiments are presented in this section a control experiment, a global ocean simulation (Glocean), and a global ocean simulation with a 10% reduction in the solar constant (ColdO). EBM studies indicate that a frozen planet is possible after a few percent decrease in the solar constant (Budkyo, 1969; Sellers, 1969). More recent studies with 1DRC models (Kasting, 1987) and EBMs continue to indicate the need for introducing large amounts of CO₂ into the early earth's atmosphere to avoid a completely frozen planet. Wetherald and Manabe (1975) used a GCM to test the effects of the solar constant on atmospheric circulation and found sizable changes in precipitation, surface temperature, and eddy kinetic energy, etc. But a completely frozen earth did not result from a 4% decrease in the solar constant.

The control experiment that represents the present-day climate is integrated for 300 days, the last 100 days used as the average with one-day time samples. The global ocean experiment is integrated for approximately 450 days with the last 200 days as the time average. There is a two-day time sample in Glocean. Because Glocean was started from a wintertime tape with no mountains, a longer run time was needed to bring the experiment to near-equilibrium. ColdO is integrated for 300 days with the last 100 days used as the average.

Temperature

When geography is removed, considerable warming takes place at the surface. Reducing the solar constant by 10Figure 3.17 displays the zonally averaged surface temperature for the three experiments. Glocean has the warmest temperatures, while ColdO has the coldest zonally averaged surface temperatures. The equator-to-pole temperature difference is the smallest for Glocean and largest for ColdO. The polar temperatures in both hemispheres for Glocean are near the freezing point of sea ice (272.1 K), and equatorial temperatures are just above 300 K. ColdO has polar temperatures around 230 K and equatorial temperatures near 285 K. Global mean surface temperatures are shown in Table 3.2.

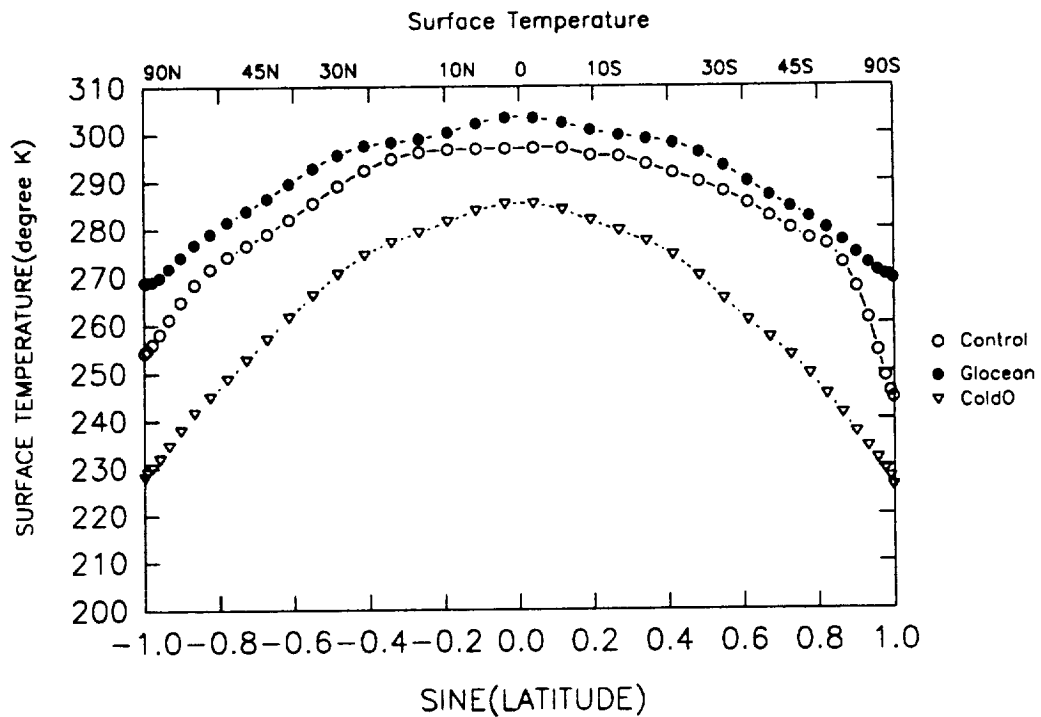
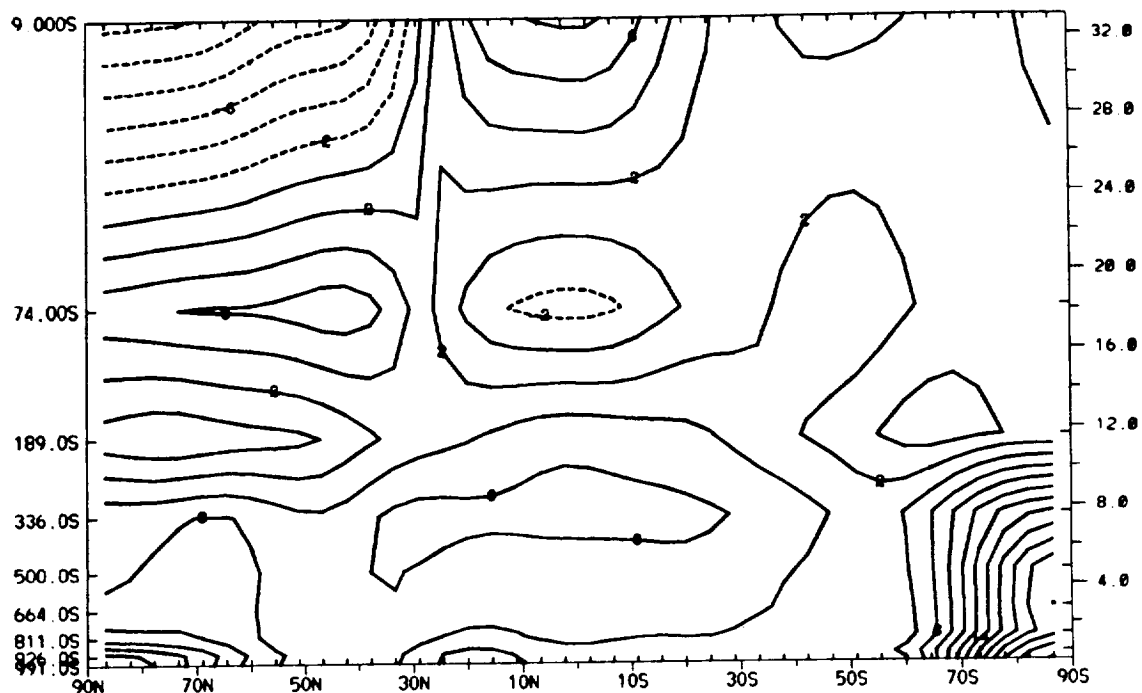
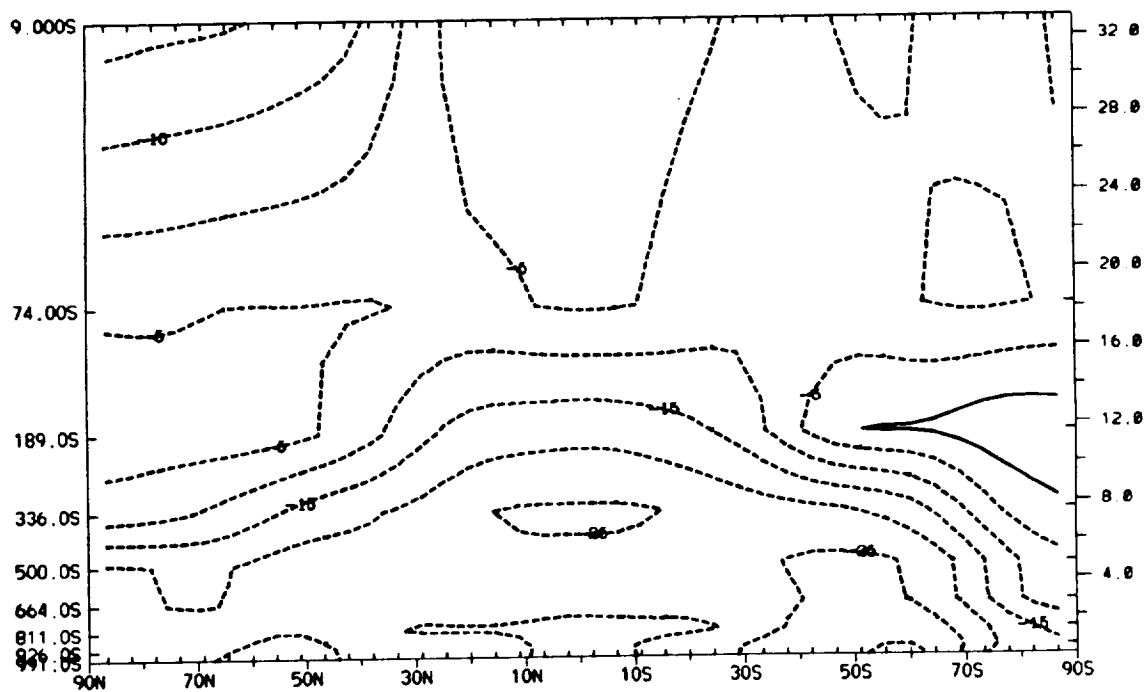


Figure 3.17: Zonally averaged surface temperature (degrees Kelvin).

The removal of land causes tropospheric and stratospheric temperatures to increase. Figure 3.18 shows the difference in the latitude-height temperature field



(a) Glocean minus control.



(b) ColdO minus control.

Figure 3.18: Temperature difference (degrees Kelvin). (a) Glocean minus control; (b) ColdO minus control.

Variable	Control	Glocean	ColdO
$T_{surface}$ K	287.22	291.3	264.72
Cloud fraction	0.423	0.407	0.409
Precipitation (cm yr ⁻¹)	114.2	135.15	57.3
$F_{TopIR} \uparrow$ (W m ⁻²)	230.01	240.76	182.52
$F_{SurfIR} \downarrow$ (W m ⁻²)	295.1	331.1	187.65
$F_{SurfIR} \uparrow$ (W m ⁻²)	373.9	408.27	278.44
$F_{Surfsolar} \downarrow$ (W m ⁻²)	188.09	195.75	165.15

Table 3.2: Global mean values for control, Glocean, and ColdO.

between Glocean and the control simulation. The troposphere has warmer temperatures with the greatest increases in the Southern Hemisphere polar regions. The large increase is due to the removal of the Antarctic ice sheets. A similar pattern exists in the Northern Hemisphere polar regions but the warming is not so intense. The warming is related to a strong ice-albedo feedback. Barron and Washington (1984) have shown that a considerable amount of the heating in the Southern Hemispheric polar regions is due to heat-transport convergence when the topography is removed. Temperatures decrease in the Northern Hemispheric stratosphere as a result of a decrease in the amount of stationary heat transported poleward. A slight decrease in temperature is noted at the equatorial tropopause.

With a lower solar constant, both tropospheric and stratospheric temperatures decrease. Figure 3.18 shows the difference in latitude-height temperature field between ColdO and the control simulation. Large decreases in temperature occur throughout the troposphere and stratosphere, and the largest decrease occurs very close to the surface and near the middle troposphere over the equator. There is a

slight temperature increase near the southern polar tropopause.

Sea ice

Zero land fraction with the present-day solar constant inhibits sea-ice formation except in the highest latitudes. On the other hand, a 10% reduction in the solar constant allows sea ice to form in subtropical regions. The geographical distribution of sea ice is shown in Figure 3.19 with a 1 m contour. This contour more closely corresponds to the freezing point of sea ice from the analysis of temperature, sea ice, and albedo fields. The control shows that much of the sea ice is confined to the high latitudes. Glocean indicates that sea ice is confined to even higher latitudes than the control. On the other hand, ColdO shows sea ice extending down to 30° in both hemispheres.

Zonal wind

The swamp global ocean allows for stronger westerly jets even though the surface equator-to-pole temperature difference is smaller. Figure 3.20 shows zonal wind for Glocean. The global ocean experiment shows a greater intensity at the jet stream maximum in comparison to the control (Figure 2.5) simulation. The mean temperature for the layer between 200 and 500 mb displays a larger equator-to-pole difference in comparison to the control, even though the opposite holds true at the surface. There is little difference in the altitude of the jet-stream maximum winds. The tropical low-level easterly winds in Glocean are weaker than in the control simulation. Weak low-level easterly winds in the high latitudes persist for the global ocean.

A lower solar constant gives rise to slightly weaker westerly jets which are shifted slightly equatorward. The zonal wind for ColdO is shown in Figure 3.20. ColdO

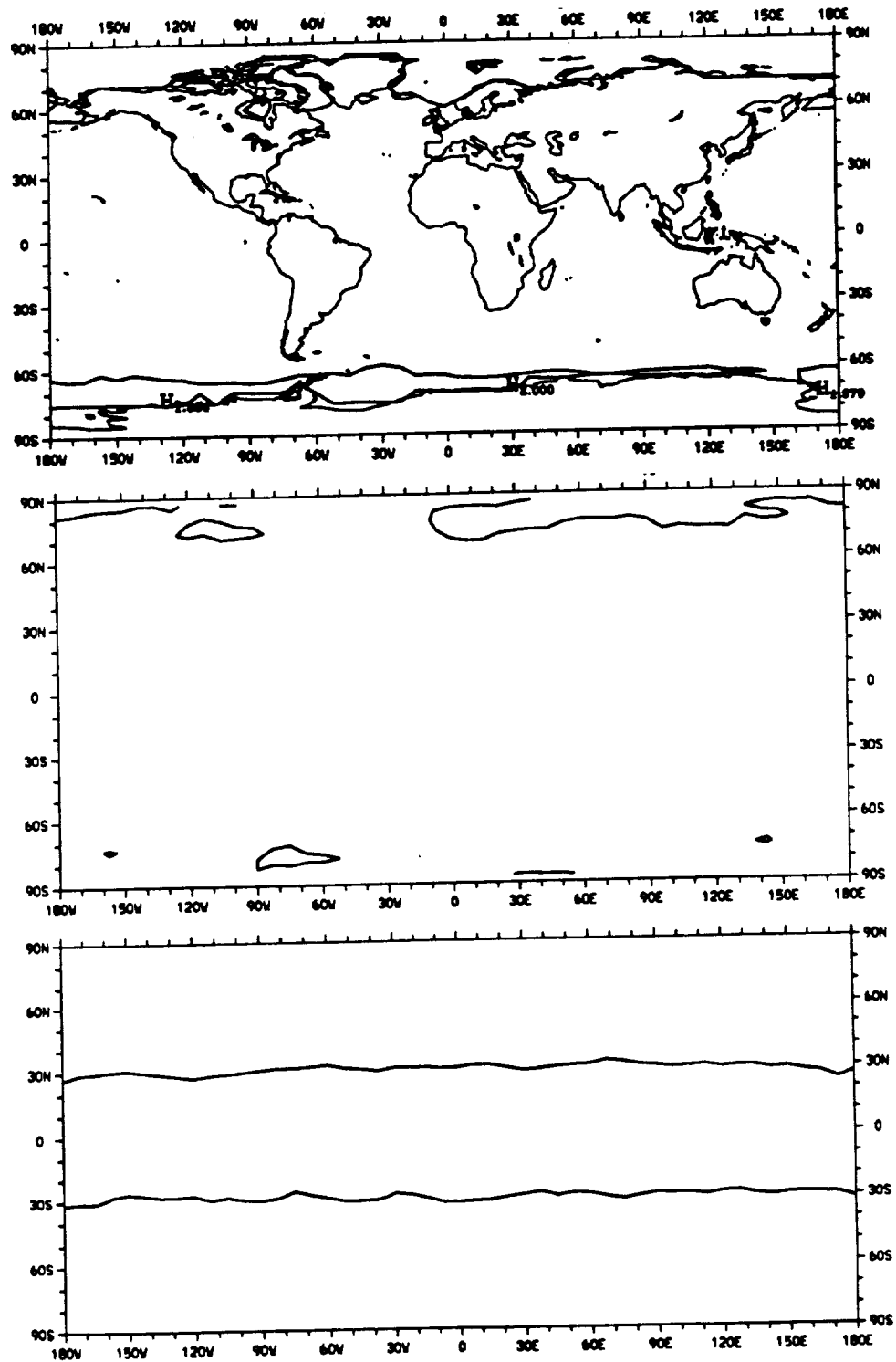
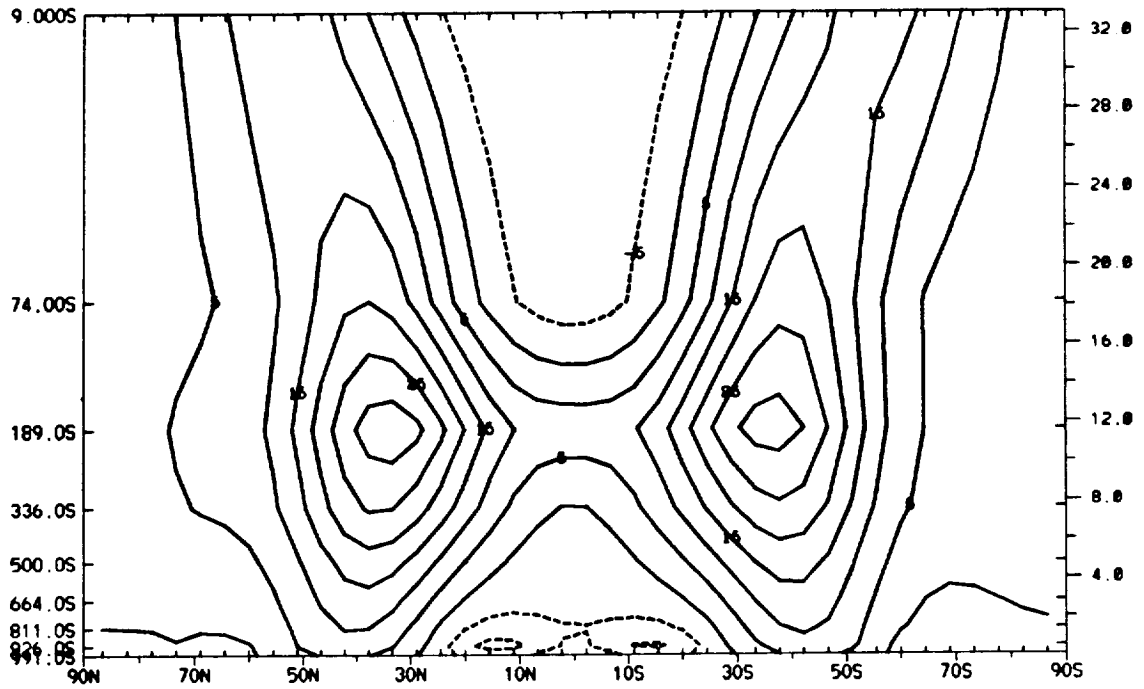
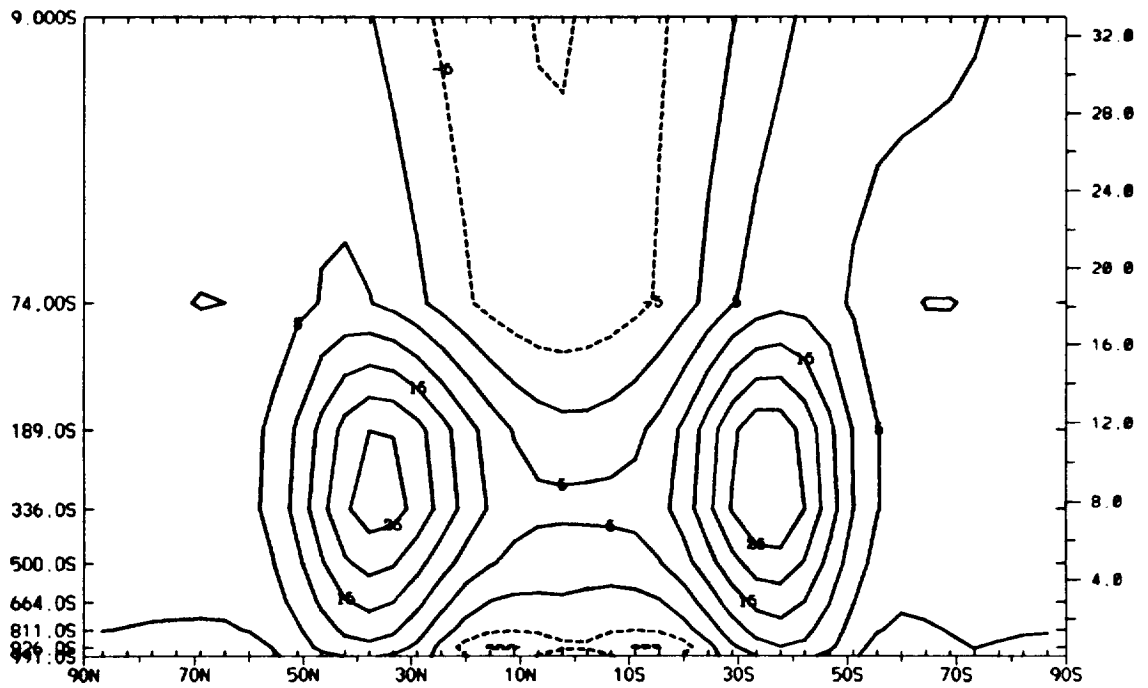


Figure 3.19: Geographical sea-ice distribution. Top: control; middle: Glocean; bottom: ColdO. Units: meters



(a) Glocean. Contour interval: 5 m s^{-1} .



(b) ColdO. Contour interval: 5 m s^{-1} .

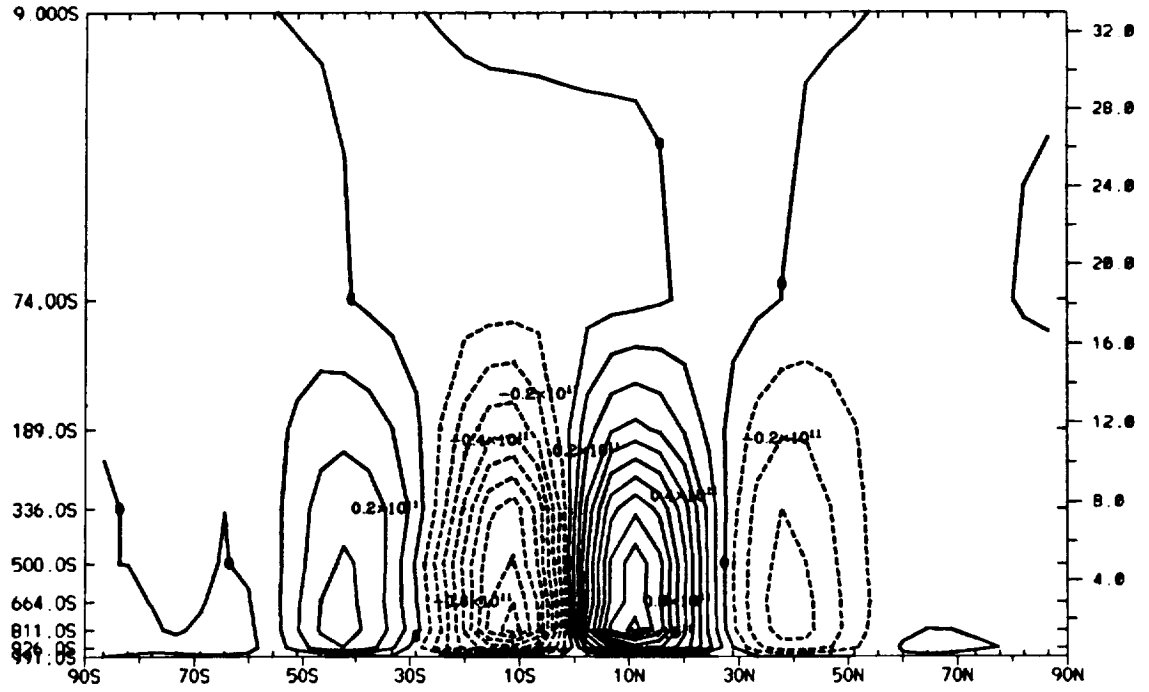
Figure 3.20: Zonal wind distribution. (a) Glocean; (b) ColdO.

shows a jet that is narrower in latitudinal width than the control simulation. In addition, the jet has been shifted equatorward by a few degrees which is more apparent from the meridional streamfunction (Figure 3.21b). The polar easterly winds in ColdO have a greater equatorial extent than the control, extending to near 50° in each hemisphere. This equatorward shift in easterly wind allows more transfer of angular momentum from the ground to the atmosphere.

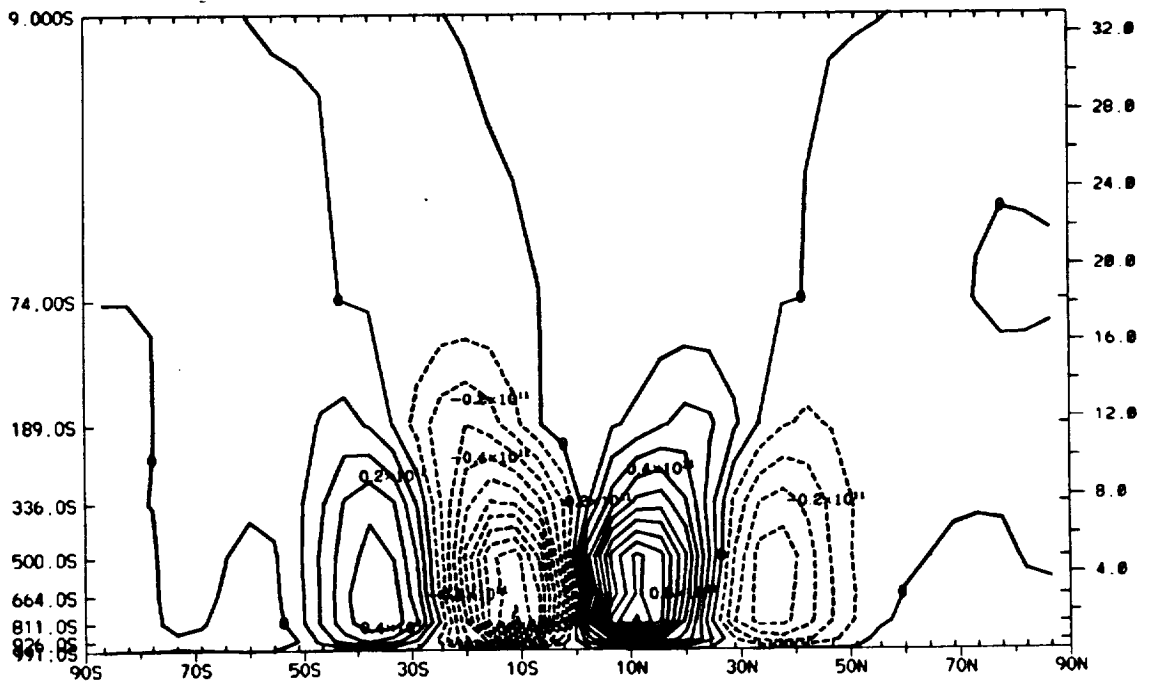
Sea ice has migrated into the subtropics (Figure 3.19) creating a greater sink for angular momentum. Sea ice has a larger drag coefficient than ocean and creates greater surface stress. The stress creates a larger torque and, hence, will cause any changes in the angular momentum over time. The high latitudes have easterlies over a larger area, thus generating a larger source for angular momentum for the atmosphere and compensating for the loss in the midlatitudes. The ice line in ColdO is creating a greater source in the low and high latitudes and a greater sink of momentum in middle latitudes. The jet cores for ColdO extend from 8–12 km as compared to the 8–10 km range in the control. The equatorial easterlies are somewhat stronger in ColdO, occupying a slightly smaller latitudinal area than the control (Figure 2.5).

Streamfunction

Removal of land brings about nearly symmetric Hadley and Ferrel cells. Figure 3.21 shows the mean meridional streamfunction for Glocean which is more symmetric than the control (Figure 2.5) due to nonexistent continents. The maximum mass flow occurs near 850 mb for the Hadley cell in Glocean. The Northern Hemisphere Hadley cell transports more mass than the control while the converse is true in the Southern Hemisphere. The indirect Ferrell cells show transport of the same order of magnitude between the two cases. No other significant direct or indirect cells are noted in Glocean.



(a) Glocean. Contour interval: $1 \times 10^{10} \text{ kg s}^{-1}$.



(b) ColdO. Contour interval: $1 \times 10^{10} \text{ kg s}^{-1}$.

Figure 3.21: Mean meridional streamfunction. (a) Glocean; (b) ColdO.

Lower solar luminosity brings forth Hadley and Ferrel cells that have stronger mass flow and are shifted a few degrees equatorward. Figure 3.21b shows the mean meridional streamfunction for ColdO. ColdO has both Hadley and Ferrel cells that have stronger mass transport than the present-day climate control (Figure 2.5). The Ferrel cell shows the greatest increase in mass transport for ColdO. There is a small equatorial shift in the Hadley cell of 2–5° which is reflected in the cloud field. The stronger Ferrel cell indicates stronger baroclinic systems in ColdO.

Heat transport by eddies

The global ocean simulation carries a transient eddy heat transport distribution similar to that of the Southern Hemisphere in the control simulation. The transient heat transport for both Glocean and ColdO is shown in Figure 3.22. The stationary eddy heat transport is very small due to lack of topography and continents. Therefore, the total heat transport is very nearly the same as the transient eddy heat transport for both Glocean and ColdO. The transient heat transport is compared to that of the transient eddies for the control in Figure 2.7. The difference in total eddy heat transport between the control, Glocean, and ColdO is shown in Figure 3.23.

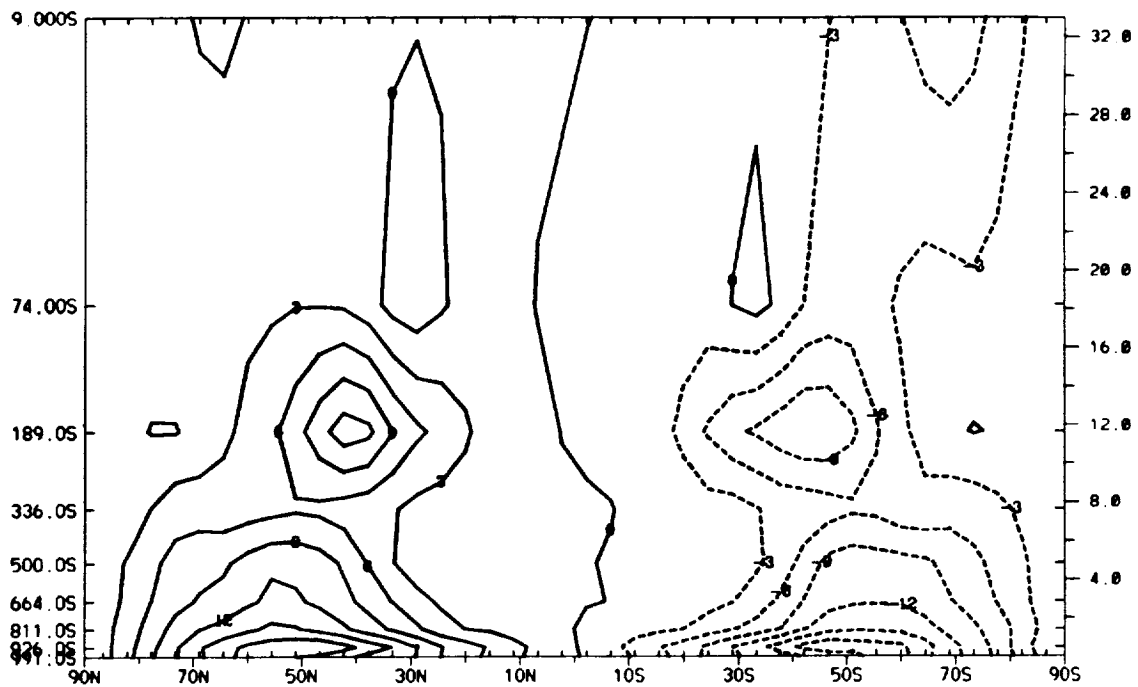
In the lower troposphere of the Northern Hemisphere, Glocean shows the maximum heat transport displaced poleward in contrast to the control distribution. This displacement leads to an increase poleward of 50°N and a decrease equatorward of this latitude (Figure 3.23). In the Southern Hemisphere, Glocean shows that the maximum heat transport in the lower troposphere displaced equatorward in contrast to the control (Figure 3.5a). Other changes include an increase in heat transport centered near 70°S at roughly 4 km and 40°N at .189S. The latter increase occurs because of topography and continents. The transient heat transport in the Southern Hemisphere of the control is very similar to that of Glocean except in high latitudes.

Lowering the solar constant allows maximum transient heat transport to occur near the sea ice edge. ColdO has maximum heat transport in the lower troposphere near 40° (Figure 3.22). This is approximately 10° equatorward of the control in the Northern Hemisphere and 25° in the Southern Hemisphere and leads to increased heat transport equatorward of 70° in the Northern Hemisphere and 55° in the Southern Hemisphere (Figure 3.23). Poleward of these regions, the heat transport decreases. The maximum heat transport in the mid- to upper troposphere occurs lower in the troposphere for ColdO, resulting in a slight decrease in heat transport in the Northern Hemisphere and a larger decrease in the Southern Hemisphere just above $.189\text{S}$ (Figure 3.23).

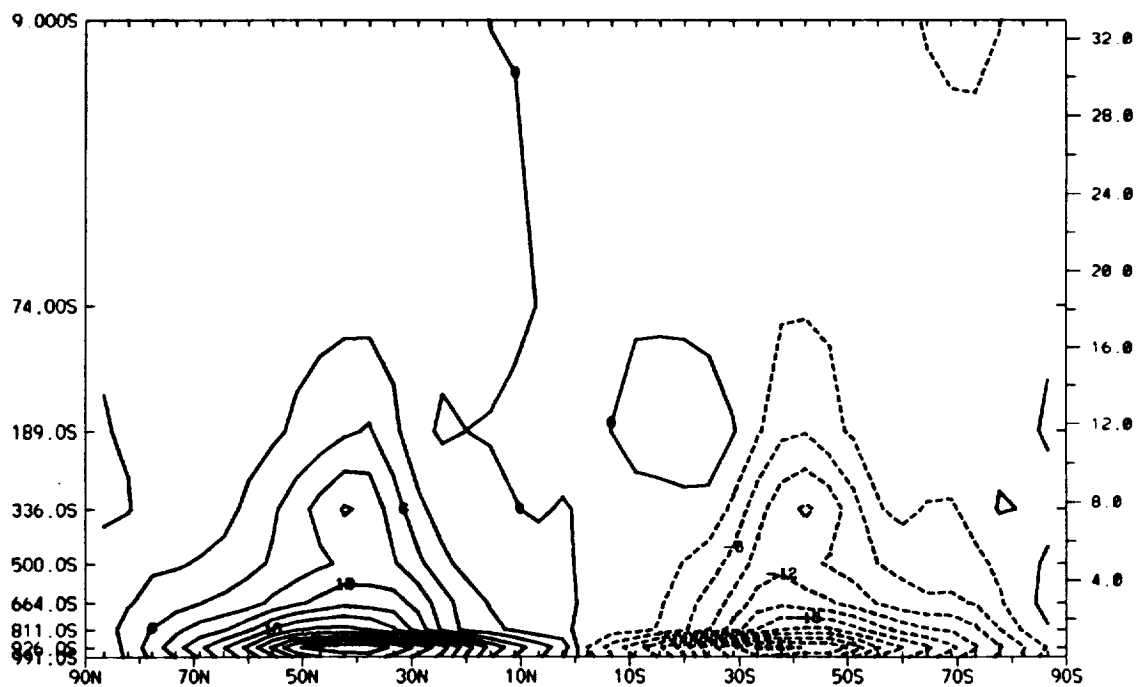
Clouds

The removal of land causes zonally averaged total clouds to increase in high latitudes and decrease slightly in middle and low latitudes (Figure 3.24). Glocean shows the largest cloud fraction in the high latitudes; present-day climate control shows the largest cloud fraction in the equatorial regions, while ColdO has the highest zonally averaged cloud fraction in the midlatitudes. ColdO shows a large reduction in high latitude clouds. Table 3.2 contains global mean values.

Clouds increase in the upper troposphere at nearly all latitudes, while decreasing in the lower and middle troposphere equatorward of 55° with the removal of geography. Figure 3.25a shows the difference in the latitude-height cloud field for Glocean and the control. Clouds are decreasing in the middle-to-low latitudes and up to the middle troposphere. The Southern Hemisphere shows a decrease in clouds between 60°S and 60°S due to circulation changes in the circumpolar current. Clouds increase in the high latitudes and in the upper troposphere. Some clouds decrease for Glocean because the atmosphere is warmer, drier, and convectively more unstable in contrast to the control. Nonconvective clouds then switch to convective clouds

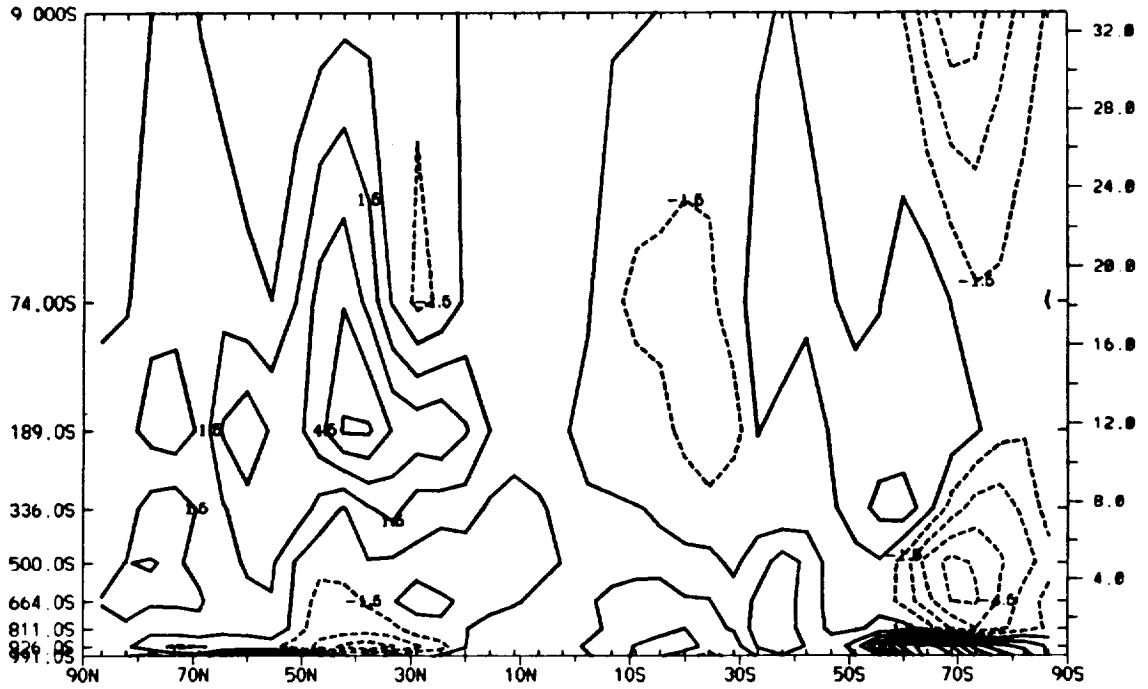


(a) Glocean. Contour interval: 3 K m s^{-1} .

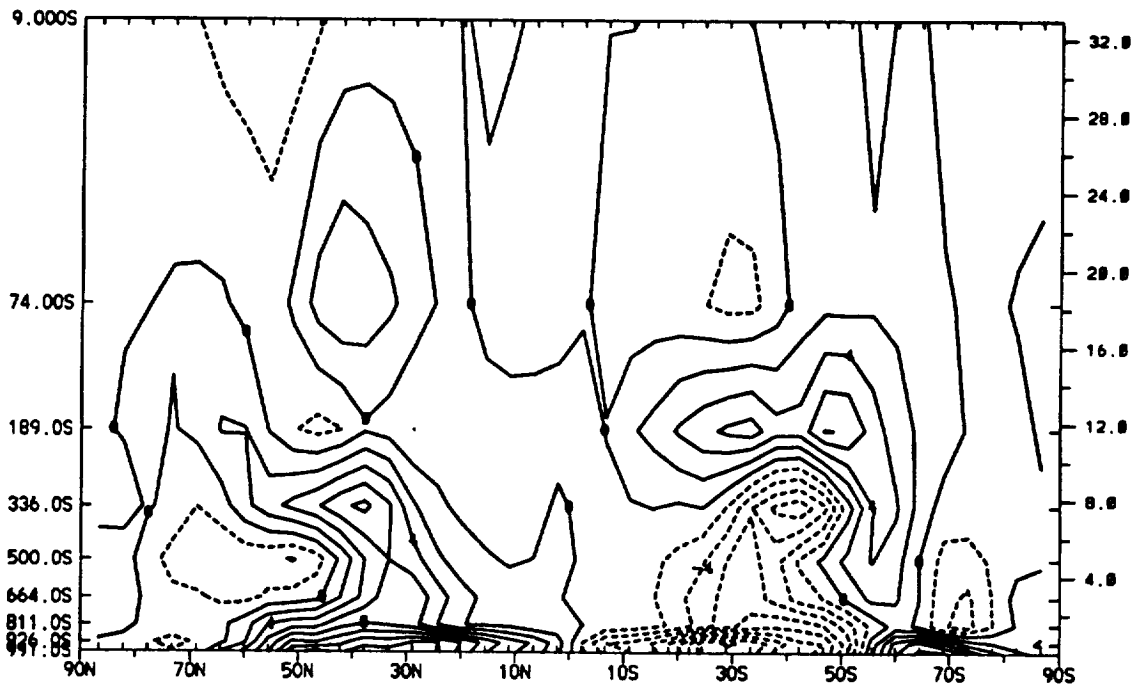


(b) ColdO. Contour interval: 3 K m s^{-1} .

Figure 3.22: Transient eddy heat transport. (a) Glocean; (b) ColdO.



(a) Glocean minus control. Contour interval: 1.5 K m s^{-1} .



(b) ColdO minus control. Contour interval: 1.5 K m s^{-1} .

Figure 3.23: Difference in transient eddy heat transport. (a) Glocean minus control; (b) ColdO minus control.

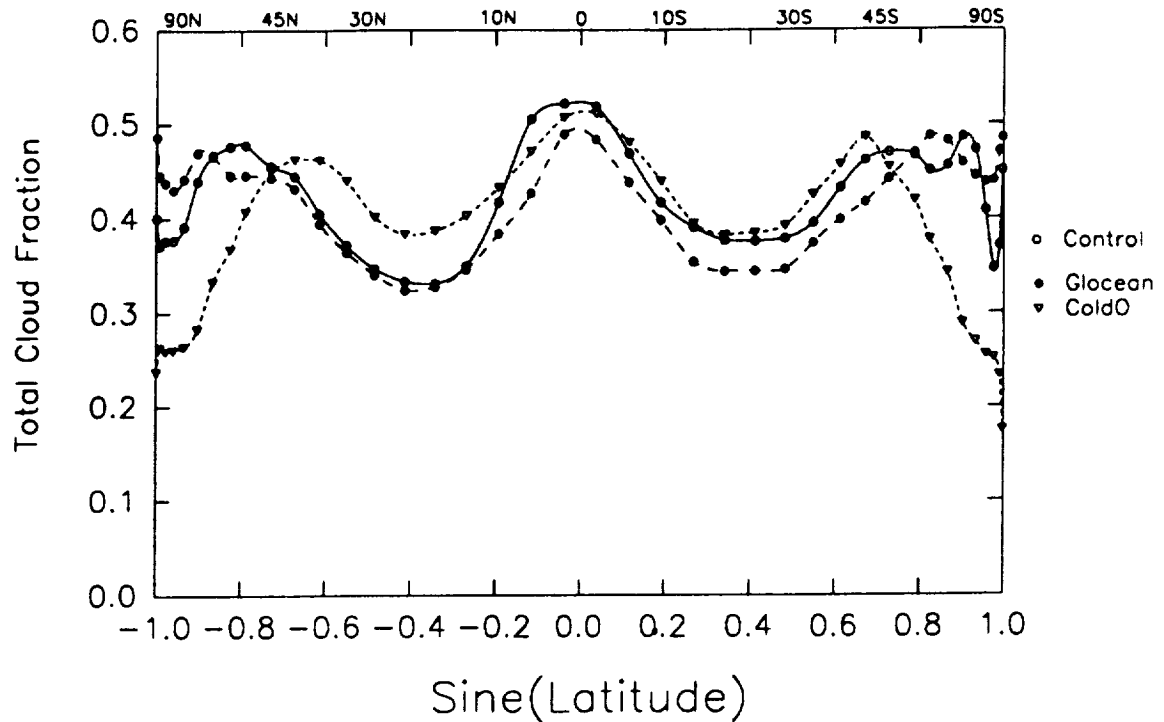
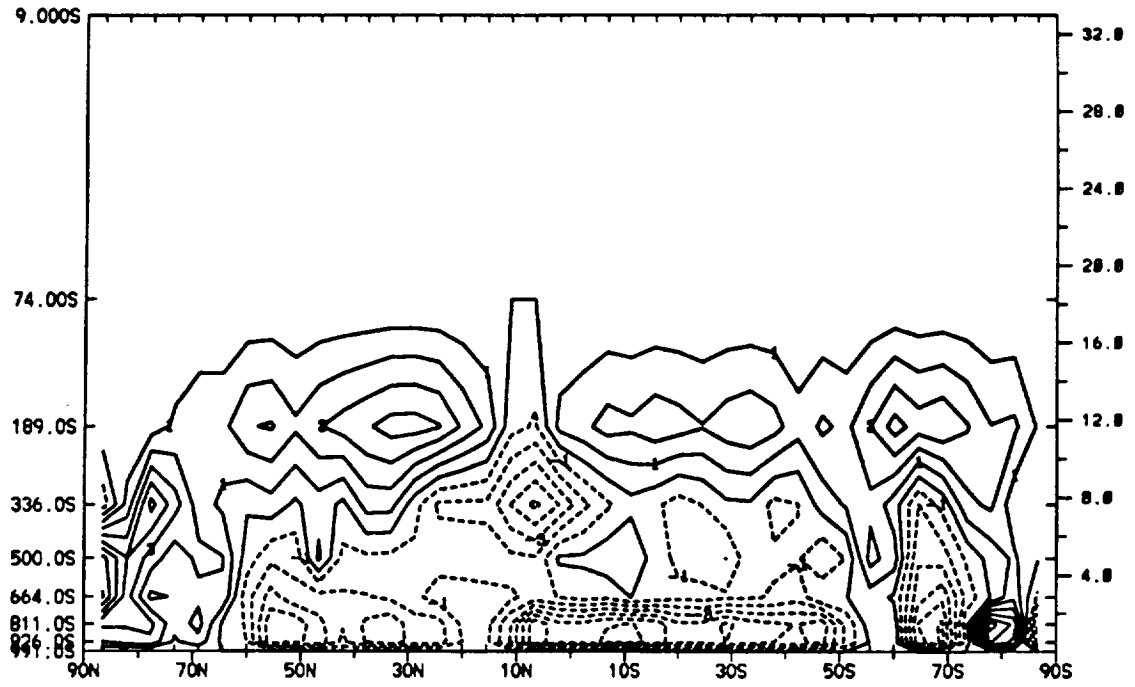


Figure 3.24: Zonally averaged total cloud fraction.

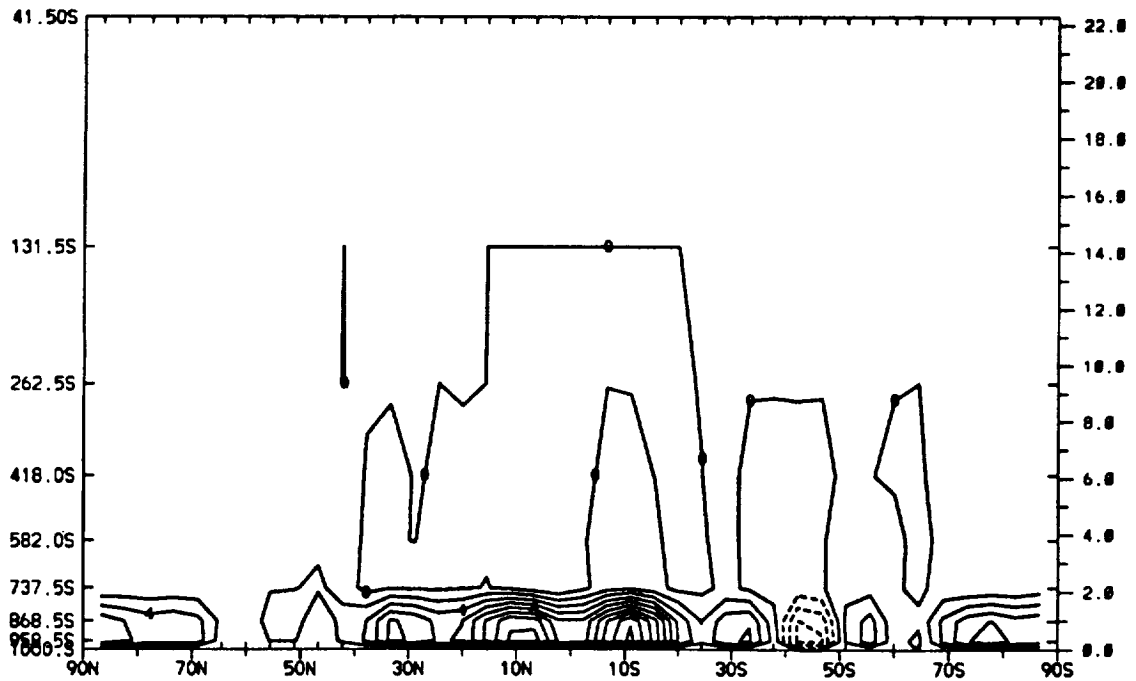
(Figure 2.1) which have a smaller cloud fraction. This effect is noted in much of the lower troposphere (Figure 3.25). Other changes in clouds occur because of changes in relative humidity that are influenced by temperature and water-vapor increases.

The lower solar constant reduces high-latitude clouds, while increasing clouds in the lower latitudes (Figure 3.26a). The difference in latitude-height clouds for ColdO and the present-day climate control shows a decrease in high-latitude and altitude clouds which occurs primarily because of decreased relative humidity (Figure 3.26b). The reduction in relative humidity is caused by a substantial decrease in atmospheric water vapor (Figure 3.28b).

In the middle latitudes, the increase in clouds is due primarily to a slight equatorward shift in the Hadley cell. Less sinking and more rising motions are noted for ColdO at the poleward edge of the Hadley cell in the control. This allows for less adiabatic compression and some adiabatic expansion in the air column. Cooling



(a) Cloud field difference. Units: percent.



(b) Convective cloud field difference. Units: percent.

Figure 3.25: Latitude-height difference in cloud field. Glocean minus control. (a) all clouds; (b) convective clouds.

occurs, the relative humidity increases, and clouds form. Global mean values for both ColdO and Glocean are shown in Table 3.2.

Precipitation

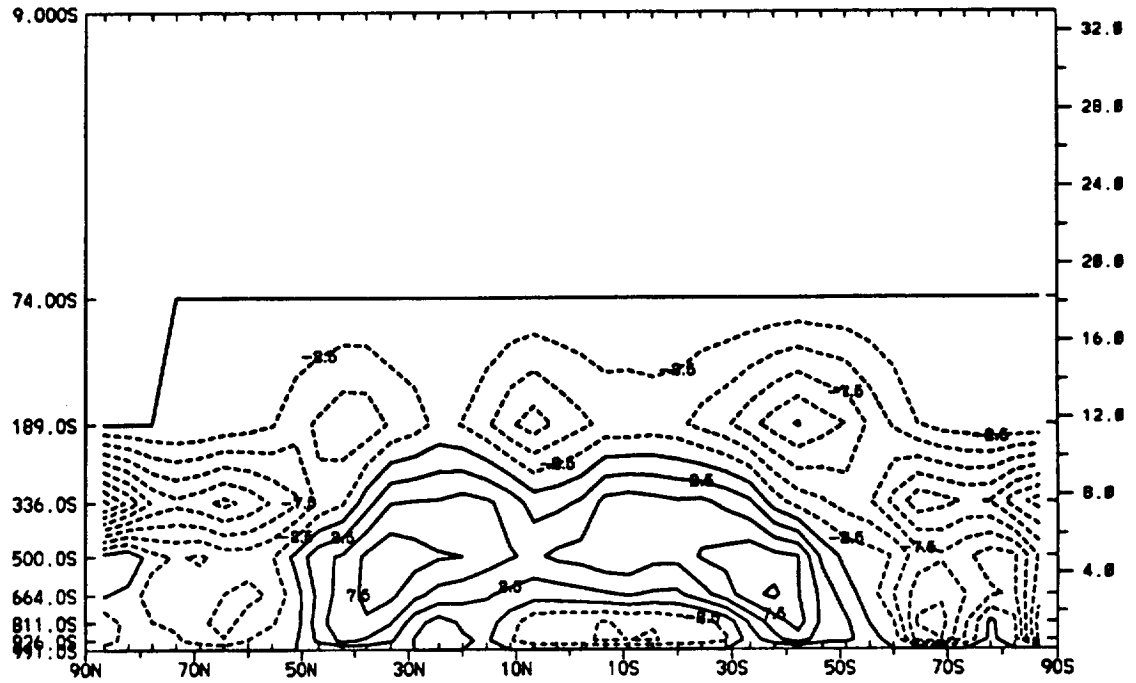
Zonally averaged precipitation rates increase with the removal of land (Figure 3.27). Glocean shows more precipitation at most latitudes compared to the control because the swamp ocean makes water vapor available from its saturated surface. An area of decreasing precipitation occurs near the circumpolar current; the removal of the Antarctica ice sheets causes the circumpolar current to disappear. The circumpolar current is a region of high precipitation in the control.

A lower solar constant causes a meaningful decrease in precipitation rates. ColdO shows a large decrease in precipitation. Compared to the other experiments, water-vapor has significantly decreased (Figure 3.28) since sea ice isolates the swamp ocean from the atmosphere and drives down evaporation. Global mean precipitation rates reflect the smaller precipitation rates for the lower solar constant (Table 3.2).

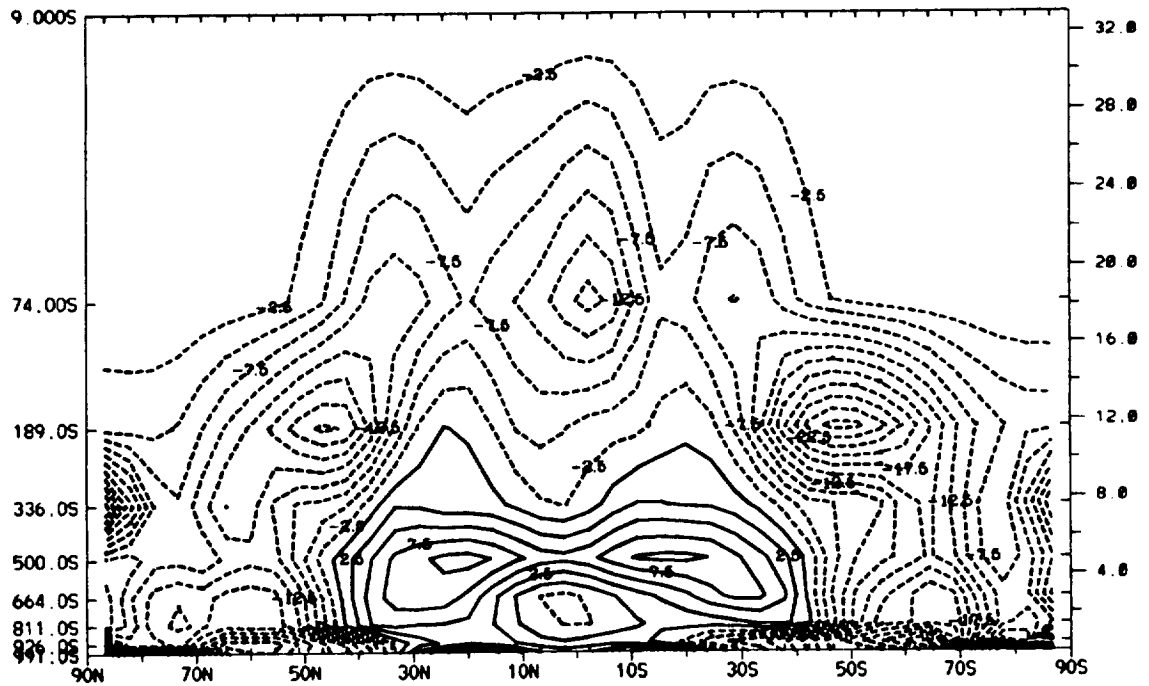
Water-vapor mixing ratio

The global ocean provides plentiful water vapor to the atmosphere. The warmer atmospheric temperatures (Figure 3.18) can hold larger amounts of water vapor. The difference in the latitude-height mixing ratio between Glocean and the control is illustrated in Figure 3.28 with an increase in water vapor noted everywhere in the middle and lower troposphere. This increased water vapor reflects the significant increase in surface evaporation for Glocean (Figure 3.29).

On the other hand, water vapor is reduced with lower solar constant conditions. ColdO shows a significant reduction in the atmospheric water vapor relative to the



(a) Cloud field difference. Units: percent.



(b) Relative humidity difference. Units: percent.

Figure 3.26: Latitude-height differences. ColdO minus control. (a) clouds; (b) relative humidity.

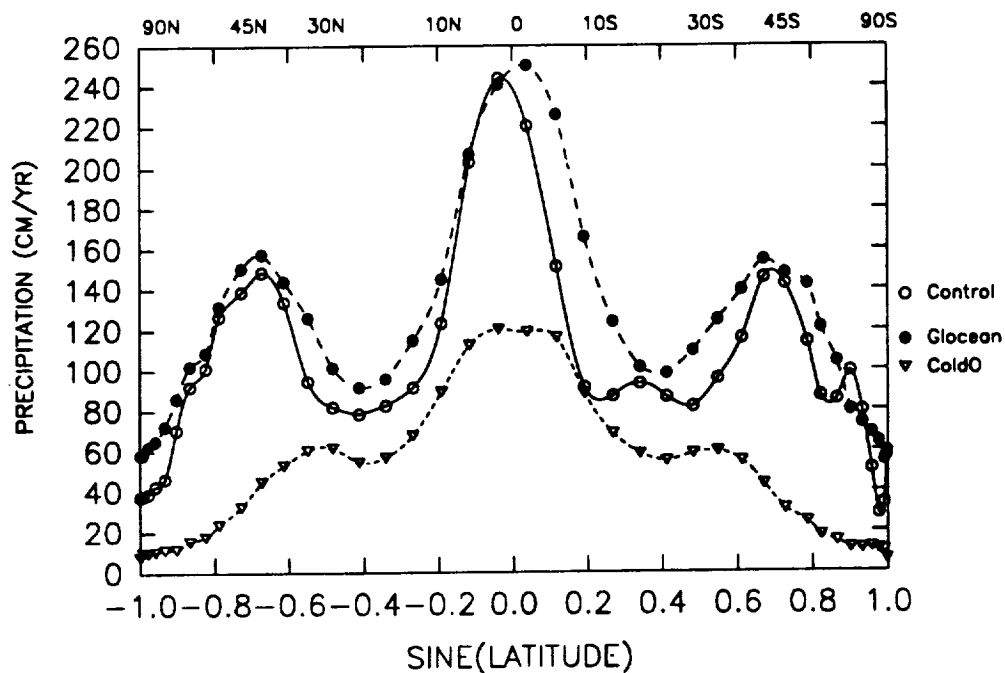


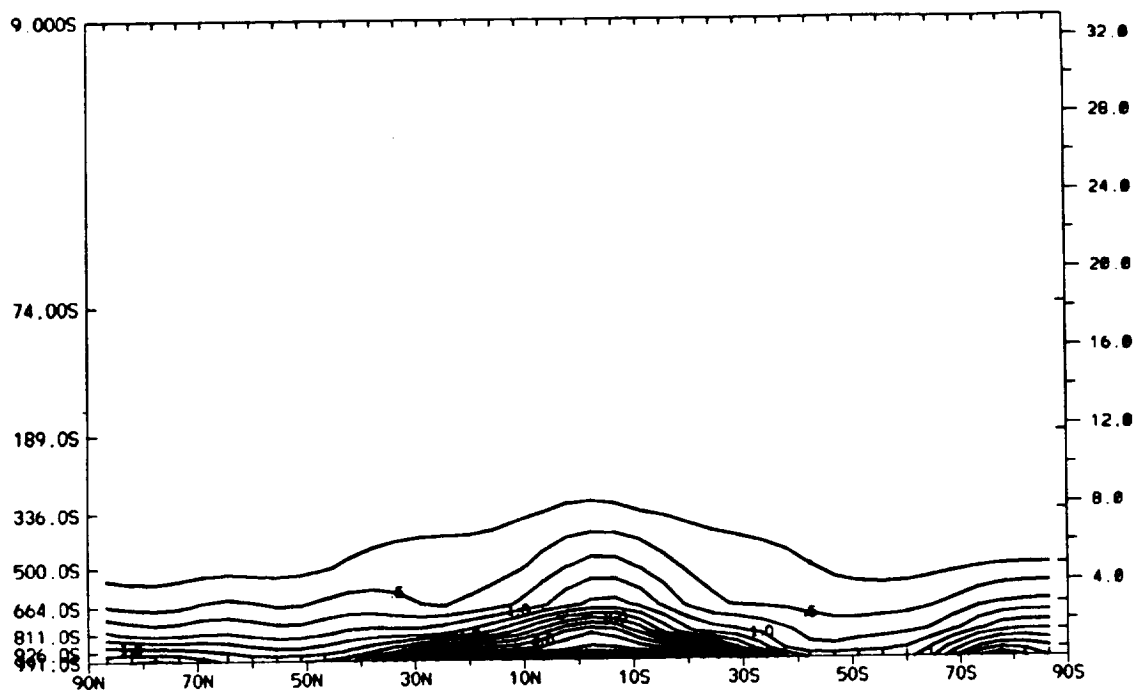
Figure 3.27: Zonally averaged precipitation rates (cm yr^{-1}).

control (Figure 3.28). Sea ice cuts off the swamp ocean's water supply and the water-vapor pressure decreases. The large decrease in evaporation for ColdO compared to the present-day climate control is shown in Figure 3.29.

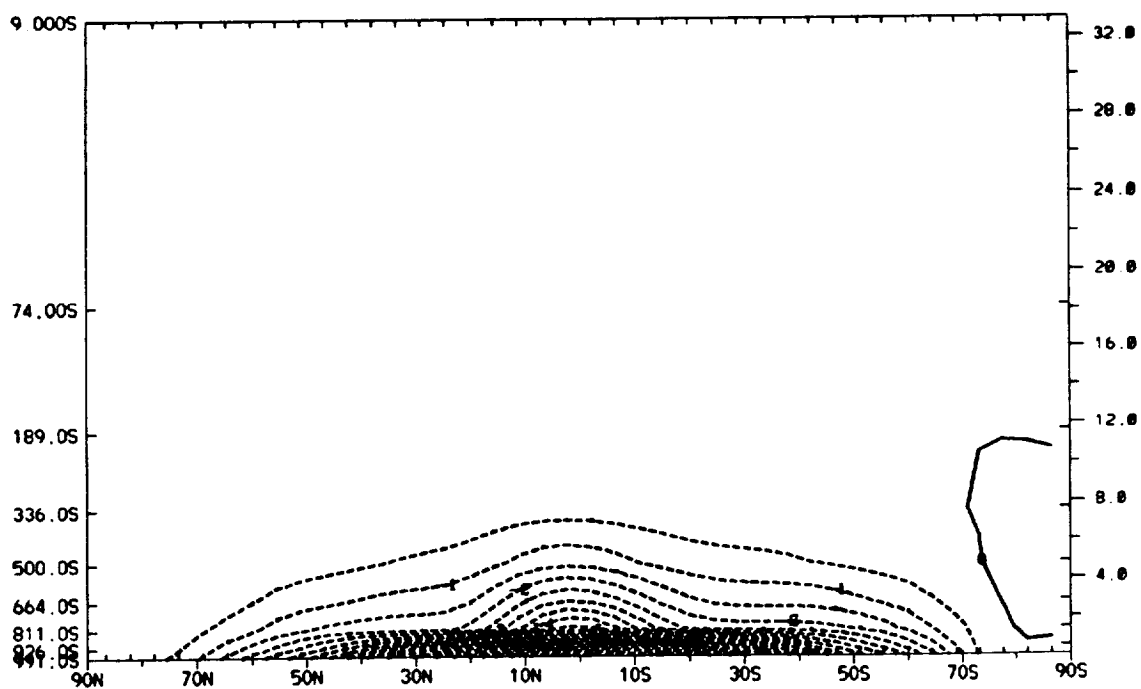
Outgoing longwave radiation

The removal of land allows greater amounts of longwave radiation to be emitted to space because of the warmer surface. The OLR for the three simulations is shown in Figure 3.30. Glocean emits the greatest OLR and ColdO the least. Glocean emits more OLR primarily because of a warmer surface and warmer atmosphere. The smaller increases located near 70°S are related to the decrease in total clouds and smaller changes in surface temperatures due to the already oceanic areas of the circumpolar current in the control.

Longwave radiation is reduced because of much colder surface temperatures with



(a) Mixing-ratio difference. Glocean minus control. Units: g kg^{-1} .



(b) Mixing-ratio difference. ColdO minus control. Units: g kg^{-1} .

Figure 3.28: Latitude-height difference for water-vapor mixing ratio
(a) Glocean minus control; (b) ColdO minus control.

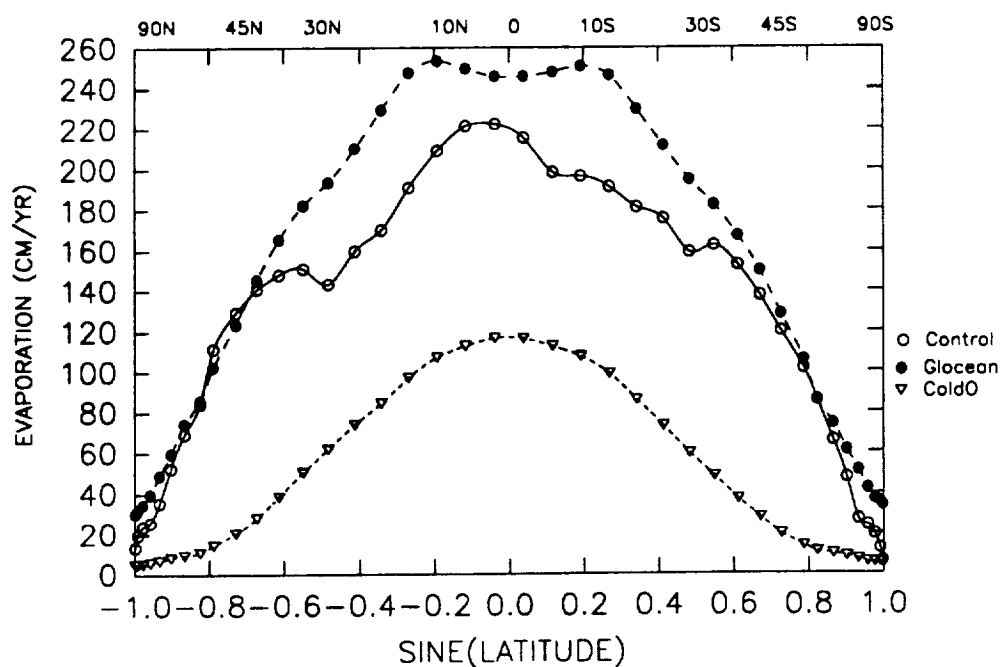


Figure 3.29: Surface evaporation (cm yr^{-1}).

a lower solar constant. ColdO has much colder surface temperatures and atmospheric temperatures than the present-day climate control which is the primary cause for the reduction in OLR compared to the control. Global mean values for OLR are shown in Table 3.2.

Absorbed solar radiation by the earth-atmosphere system

The global ocean conditions allow greater amounts of solar radiation to be absorbed at the surface and in the atmosphere. Figure 3.31 shows the zonally averaged absorbed solar radiation by the earth-atmosphere system. The results demonstrate that Glocean absorbs more solar radiation by the atmosphere-earth system. Much of the increase is at the surface because of the lower surface albedo of Glocean. The largest increases in the absorbed solar radiation occur in the polar regions where snow and sea ice have been replaced by ocean; an increase of 40 W m^{-2} is noted

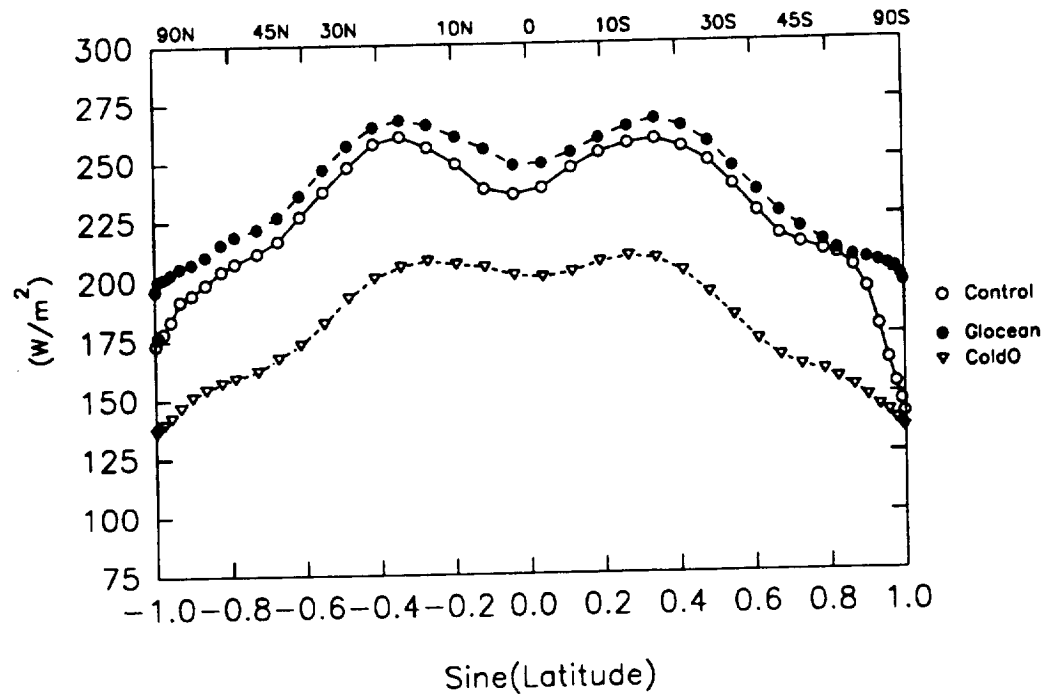
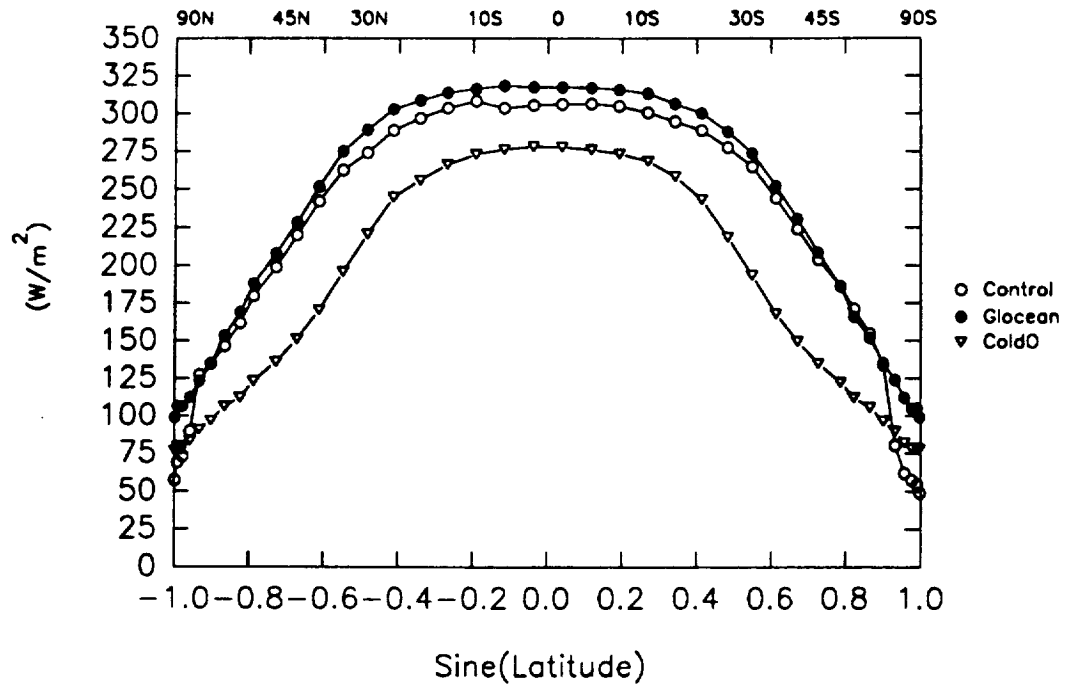


Figure 3.30: Outgoing longwave radiation. Units: W m^{-2} .

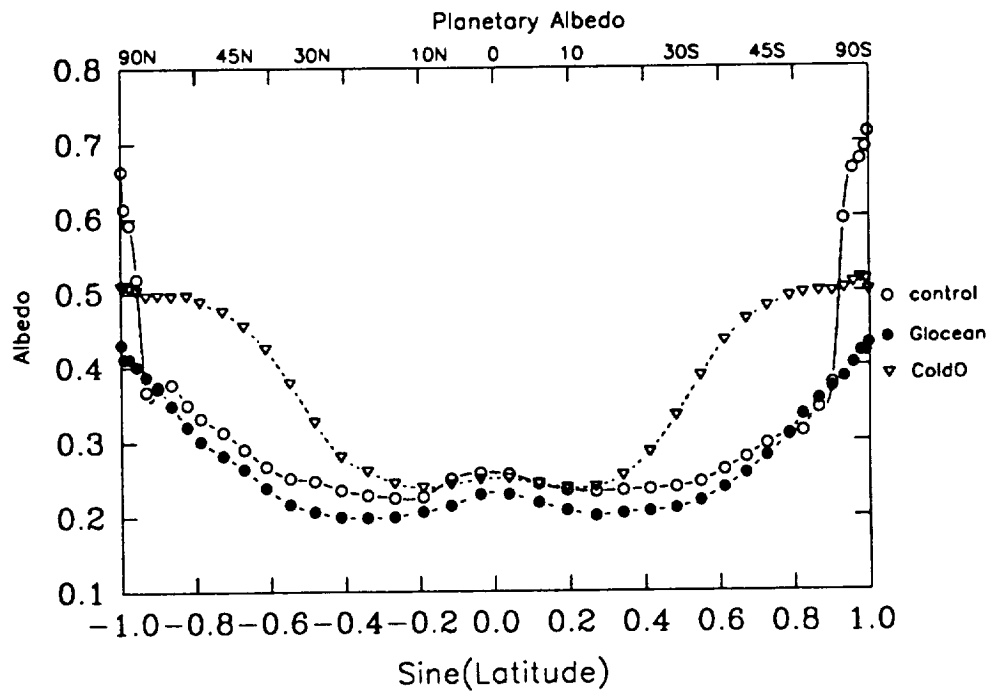
there. Further, a large increase in the absorbed solar radiation is noted equatorward of 30° because of the lower surface albedo and a decrease in the total cloud field (Figure 3.24).

A significant reduction in absorbed solar radiation occurs with the lower solar constant conditions, with ColdO showing the smallest amounts of absorbed solar radiation by the earth-atmosphere system (in contrast to the control). The decreased energy from the sun (lower solar constant) and the increased surface albedo are the primary causes of the reduction of absorbed solar radiation. An interesting feature occurs in the polar regions where ColdO shows more absorption by the earth-atmosphere system than the present-day climate control. This increases even in the face of colder polar temperatures and lower water values for ColdO (Figure 3.18b and 3.28b). The large decreases in clouds of the polar regions, however, allow for penetration of solar radiation to the surface. Planetary albedo decreases (Figure

3.31) for the highest latitudes for ColdO and is due to the fact that the highest albedo allowed for the ocean simulations is .7 while it is .8 for the land experiments. This difference in maximum surface albedo results from no-snow conditions in the ocean simulations, whereas fixed snow is prescribed over the Arctic, Greenland, and Antarctica for the control simulation. The decreased planetary albedo for ColdO in high latitudes is also due to decreased clouds.



(a) Absorbed solar radiation. Units: W m^{-2} .



(b) Planetary albedo.

Figure 3.31: (a) Absorbed solar radiation by the earth-atmosphere system; (b) planetary albedo.

3.3 CO₂ and Rotation Rate under Lower Solar Luminosity Conditions

Introduction

Larger CO₂ concentrations and faster rotation-rate conditions are explored when external boundary conditions of zero land fraction and a 10% reduction in solar luminosity are introduced. CO₂ is increased by four and eight times the control concentrations (330 ppm). The rotation rate is increased to correspond to a 14-hr earth day. The CO₂ experiments are denoted 4ColdO and 8ColdO—4 and 8 times the amount of CO₂ in experiment ColdO. Recall that ColdO represents an experiment in which solar luminosity has been reduced by 10%. The fast-rotation-rate experiment is denoted 14hrColdO. All experiments are run with zero land fraction and are compared to ColdO. 4ColdO and 14hrColdO have been integrated for 150 days with the last 50 days for time averaging. 8ColdO is integrated for 300 days with the last 95 days for the time averaging. The integration times were limited for 4ColdO and 14hrColdO because of computational cost.

Temperature

Higher CO₂ concentrations increase surface temperatures when compared to ColdO (Figure 3.32a). The surface temperature increases at all latitudes in both 4ColdO and 8ColdO, with 8ColdO showing the largest increase in surface temperature. Latitudinally, the greatest increase in temperature occurs in the mid-latitudes, while the smallest temperature increases occur in high latitudes. Midlatitude surface temperatures have risen by 15 K, whereas equatorial and polar surface temperatures have risen by approximately 10 K. The increased midlatitude temperatures are greatest because of the melting of sea ice in these latitudes. Equatorial surface

Variable	ColdO	4ColdO	8ColdO	14hrColdO
$T_{surface}$ K	264.72	269.6	276.6	271.3
Cloud fraction	0.409	0.423	0.43	0.328
Precipitation (cm yr ⁻¹)	57.3	71.6	90.7	80.7
$F_{TopIR} \uparrow$ (W m ⁻²)	182.52	185.4	196.1	216.5
$F_{SurfIR} \downarrow$ (W m ⁻²)	187.65	215.2	253.8	209.2
$F_{SurfIR} \uparrow$ (W m ⁻²)	278.44	299.4	331.7	307.2
$F_{Surfsolar} \downarrow$ (W m ⁻²)	166.15	166.59	168.90	178.54

Table 3.3: Global values for ColdO, 4ColdO, 8ColdO and 14hrColdO.

temperatures in 8ColdO hover around 293 K. Global mean values are shown in Table 3.3.

Colder polar and warmer middle and lower latitudes are brought about by a faster rotation rate when compared to ColdO (Figure 3.32b). Poleward of 60°, the surface temperature decreases and results from smaller-sized eddies that transport heat less efficiently. A larger equator-to-pole temperature difference, with a steeper gradient in the midlatitudes, exists in 14hrColdO and enhances baroclinic instability. Equatorial temperatures in 14hrColdO are near 293 K, while polar temperatures are about 220 K. Midlatitude temperatures show the largest increases compared to ColdO. Increases of roughly 15 K are noted because sea ice has migrated poleward. Global mean surface temperatures are in Table 3.3.

When higher CO₂ concentrations are added, tropospheric temperatures increase and stratospheric temperatures decrease in comparison to ColdO (Figure 3.33). 8ColdO shows the largest changes in atmospheric temperature with an increase of 15

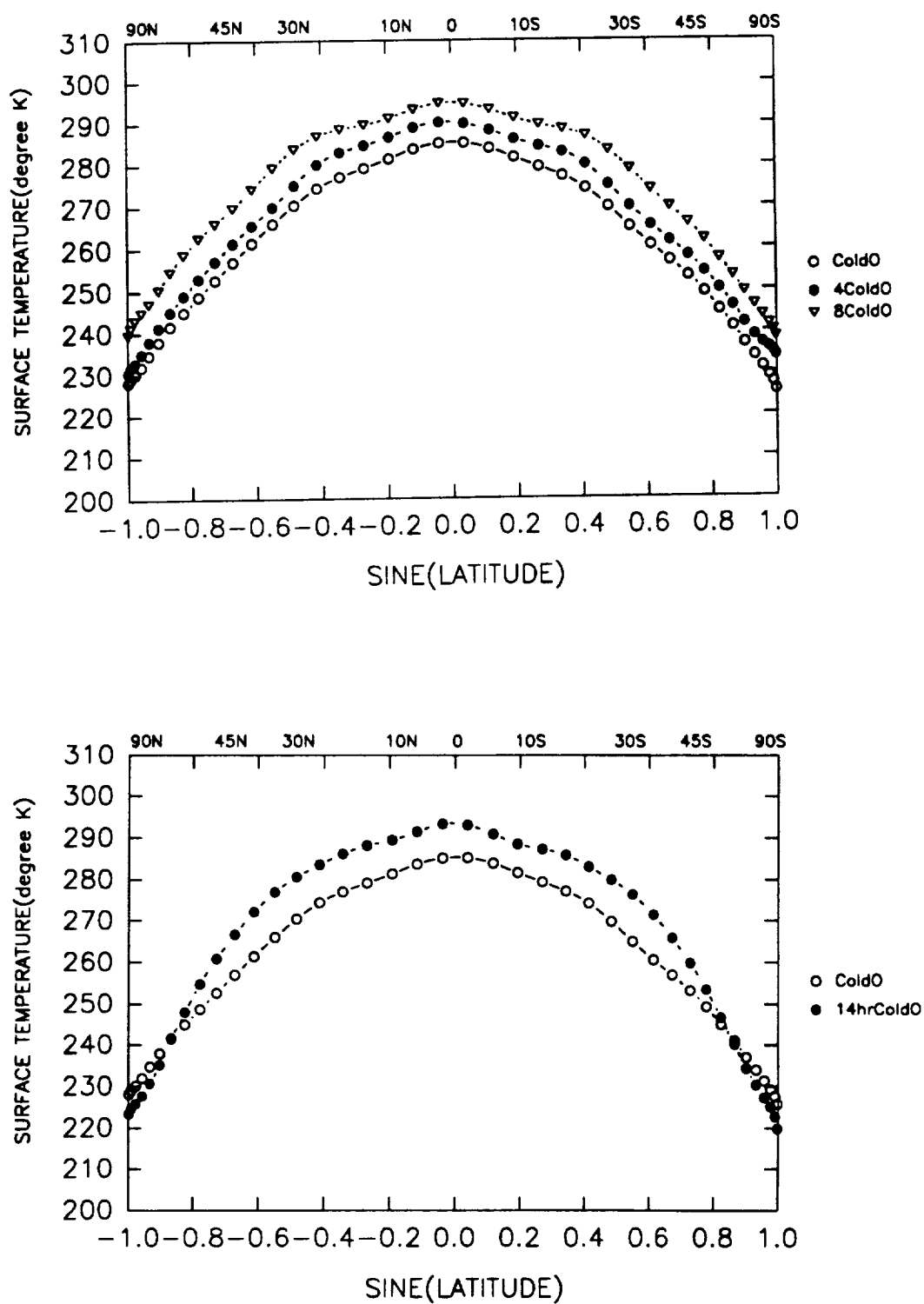


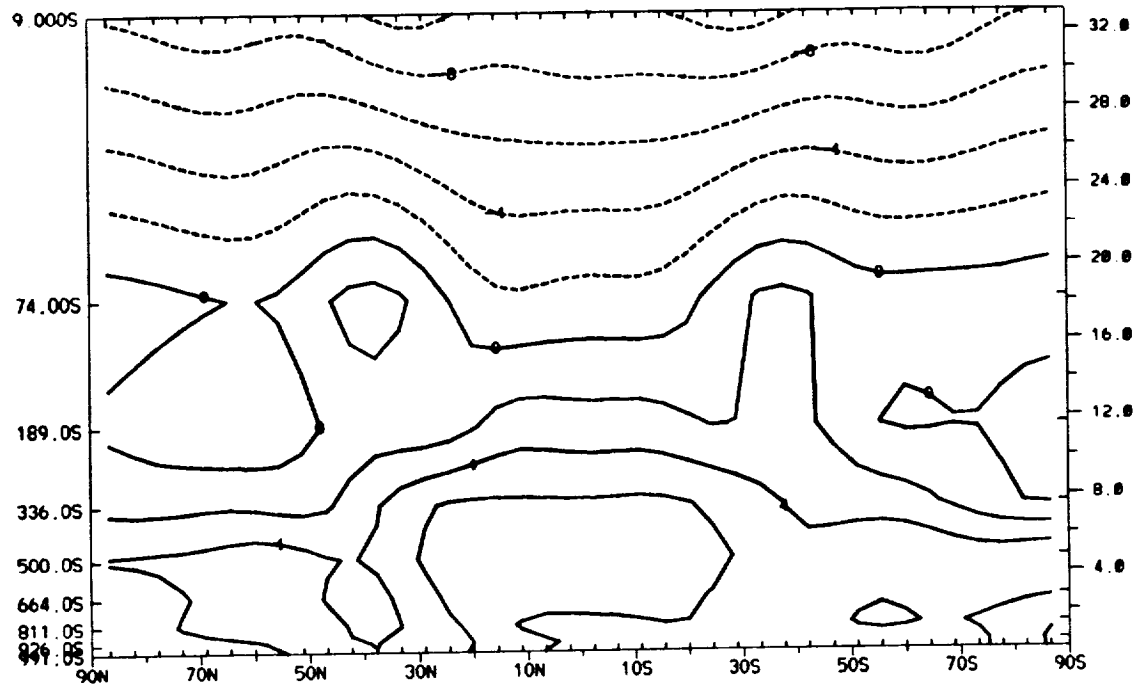
Figure 3.32: Zonally averaged surface temperature. Units: degrees Kelvin.

K in the midtroposphere (near .5S) of the equator, while a temperature decrease of 12 K occurs in the stratosphere (.009S (10mb)) in the equatorial region. The equatorial and polar tropopause show little change in temperature. Polar tropopause showing a slight decrease in temperature when compared to ColdO. The atmospheric temperature changes are similar to those predicted when CO₂ is doubled for present-day conditions (Washington and Meehl, 1983).

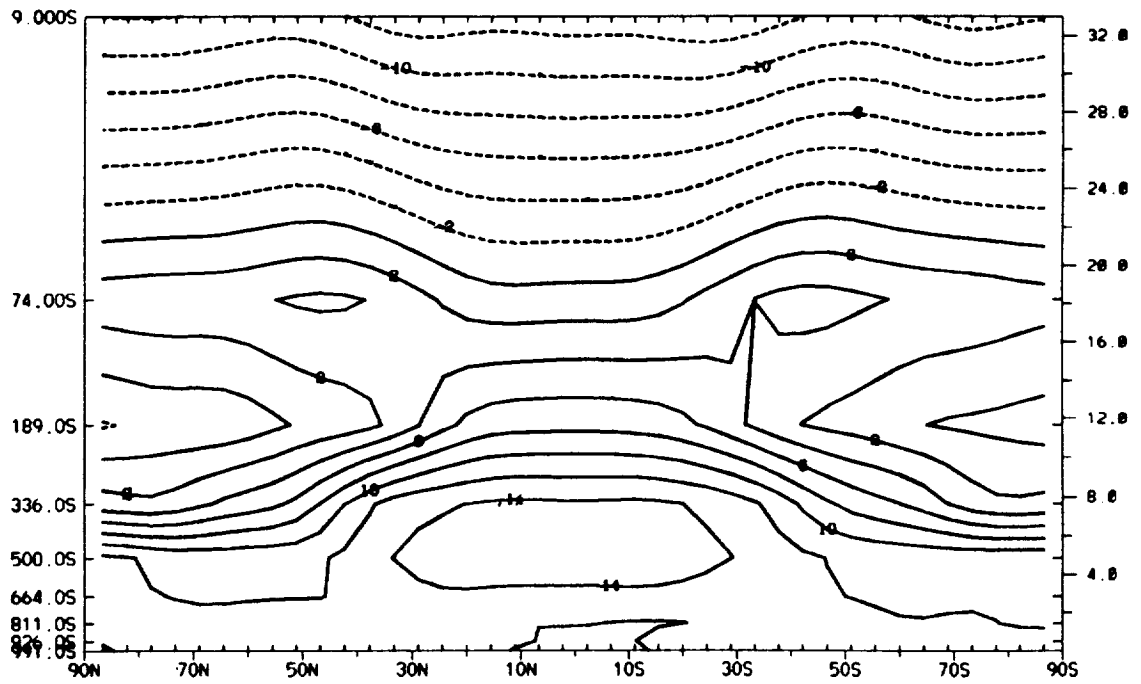
A faster rotation rate produces increased atmospheric temperatures in the troposphere and stratosphere when compared to ColdO (Figure 3.34). Lower atmospheric temperatures are confined to small areas poleward of 70° in the lower troposphere with a maximum cooling of 4 K. The lower polar atmospheric temperatures are expected because of less efficient eddies, but the overall warming of the troposphere and stratosphere is not expected. The warming comes from increased atmospheric latent heat that is transported by transient eddies (Figure 4.2). A temperature increase of 10 K is noted near .336S and roughly 60° of latitude in both hemispheres, over the equator, and near the surface at approximately 30° in both hemispheres. The stratosphere also shows two areas of temperature increase of about 6 K centered around 18 km and 30° of latitude in both hemispheres.

Zonal wind

Higher CO₂ concentrations steepen the midtropospheric temperature gradient and cause the westerly jets to speed up. On the other hand, faster rotation rates cause the jets to move equatorward and weaken. 4ColdO (not shown) and 8ColdO (Figure 3.35) show increases in the jet, while 14hrColdO (Figure 3.35) indicates a significant decrease in the mean annual jet with respect to ColdO (Figure 3.20). 8ColdO jet intensity increases by 5-6 m s⁻¹. The vertical shear is greater in 8ColdO which is in agreement with the larger latitudinal temperature gradient in the temperature field. Stronger equatorial easterlies are noted for 8ColdO. The 14hrColdO jet weakens by



(a) 4ColdO minus ColdO. Units: degrees Kelvin.



(b) 8ColdO minus ColdO. Units: degrees Kelvin.

Figure 3.33: Difference in atmospheric temperatures. (a) 4ColdO minus ColdO; (b) 8ColdO minus ColdO.

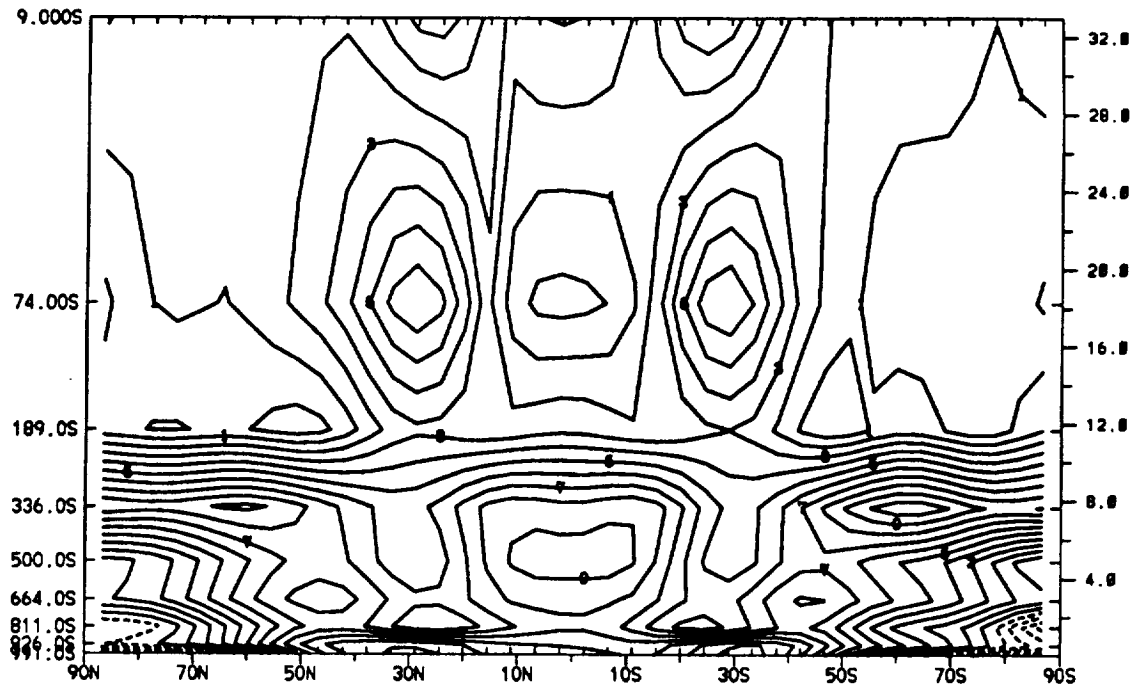
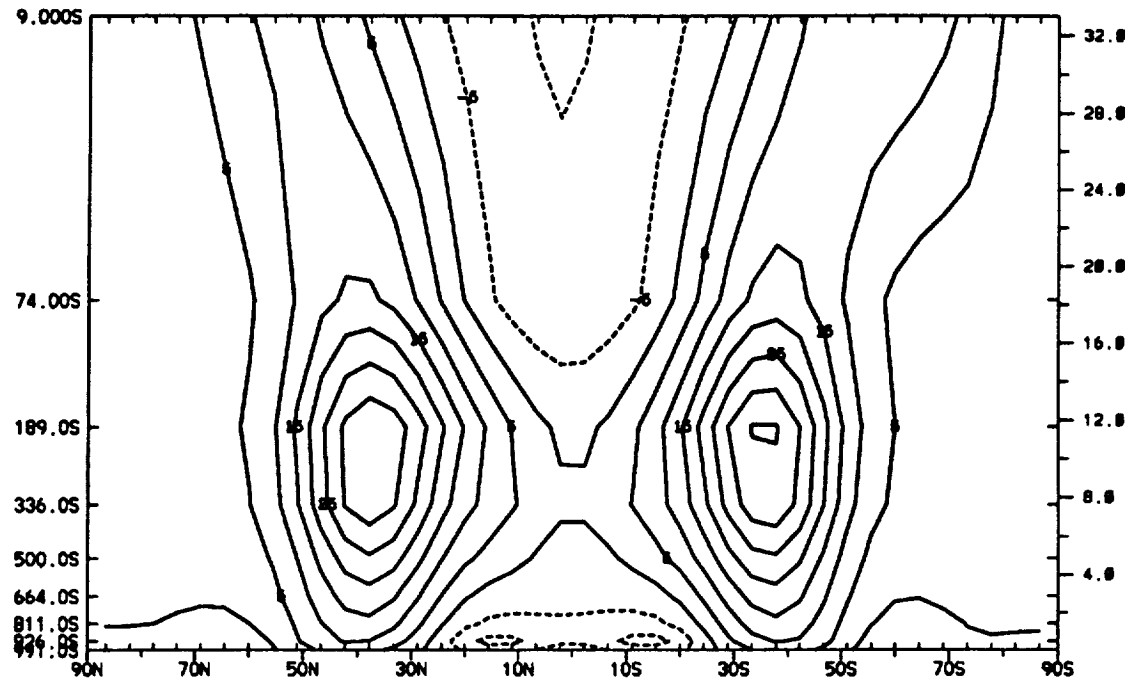


Figure 3.34: Difference in atmospheric temperatures (degrees Kelvin).
14hrColdO minus ColdO.

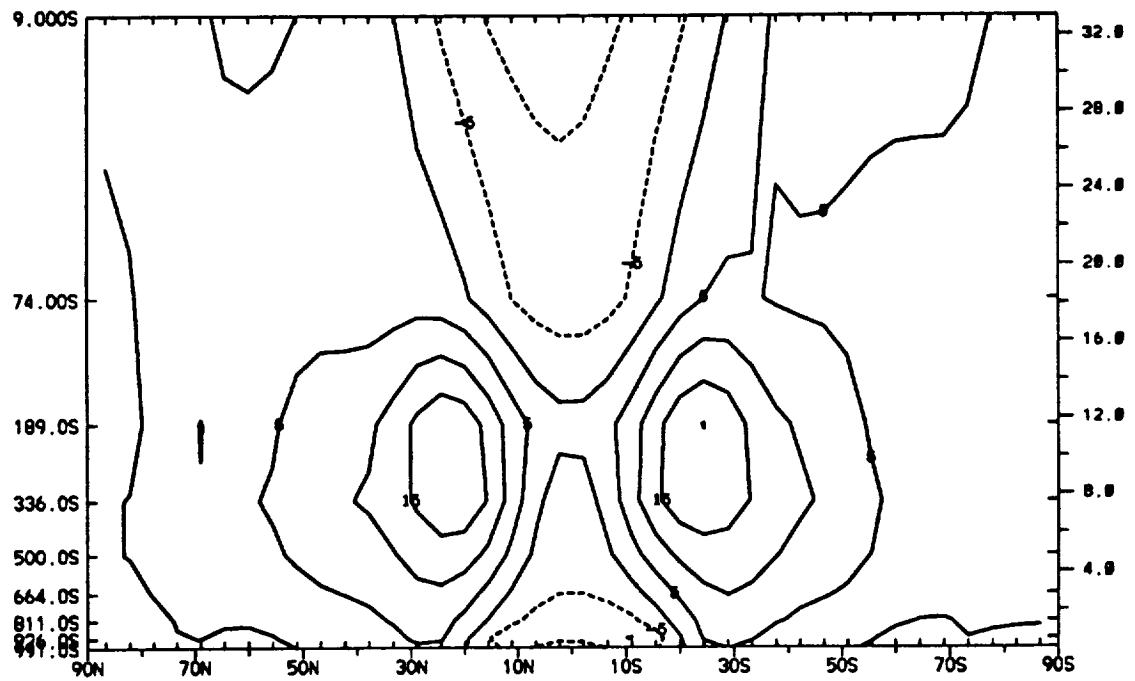
roughly 10 m s^{-1} relative to ColdO (Figure 3.20) and shows an equatorial shift of approximately 10° .

Mean meridional streamfunction

Higher CO_2 concentrations under lower solar constant conditions allow for a slightly stronger Hadley cell. The Hadley cell in 8ColdO (Figure 3.36) has slightly larger mass flow than ColdO (Figure 3.21). This maximum mass flow occurs in the midtroposphere which is approximately the same altitude as ColdO. The Ferrel cell is roughly the same order of magnitude in 8ColdO as ColdO (Figure 3.21). An additional cell appears in 4ColdO (not shown) poleward of 50° . This cell has mass flowing into polar regions. This feature is not shown in 8ColdO and is a function of the shorter integration time of 4ColdO which had not come to an equilibrium state.

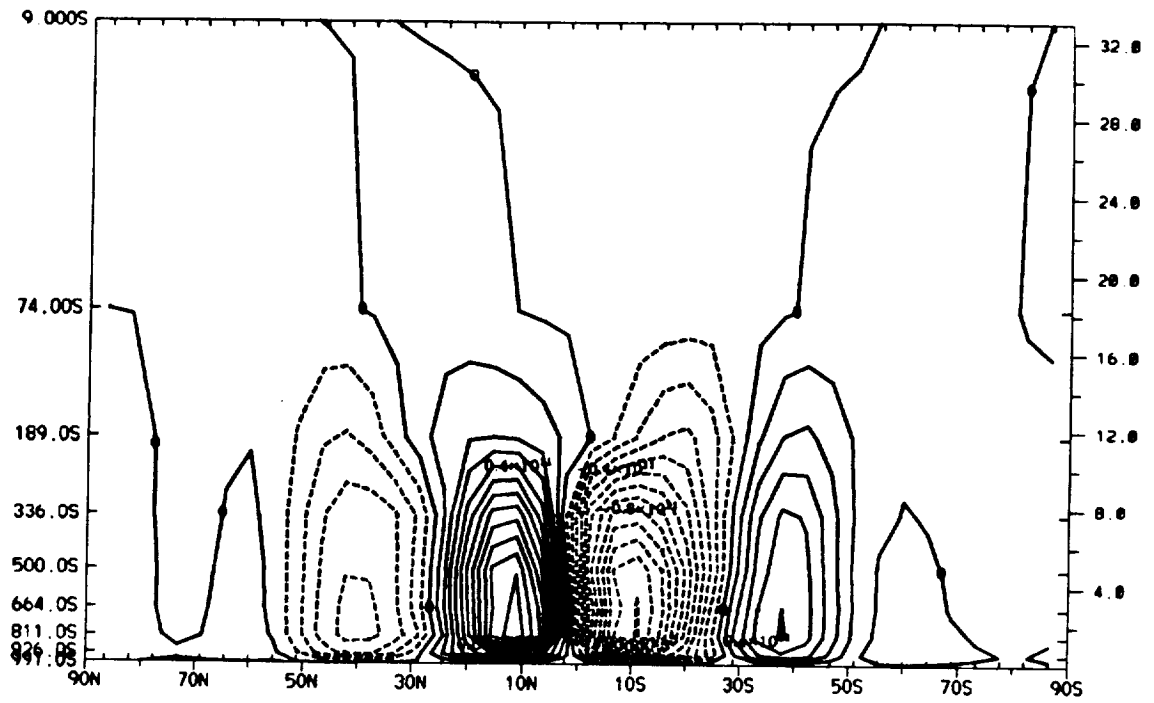


(a) Zonal wind for 8ColdO. Contour interval: 5 m s^{-1} .

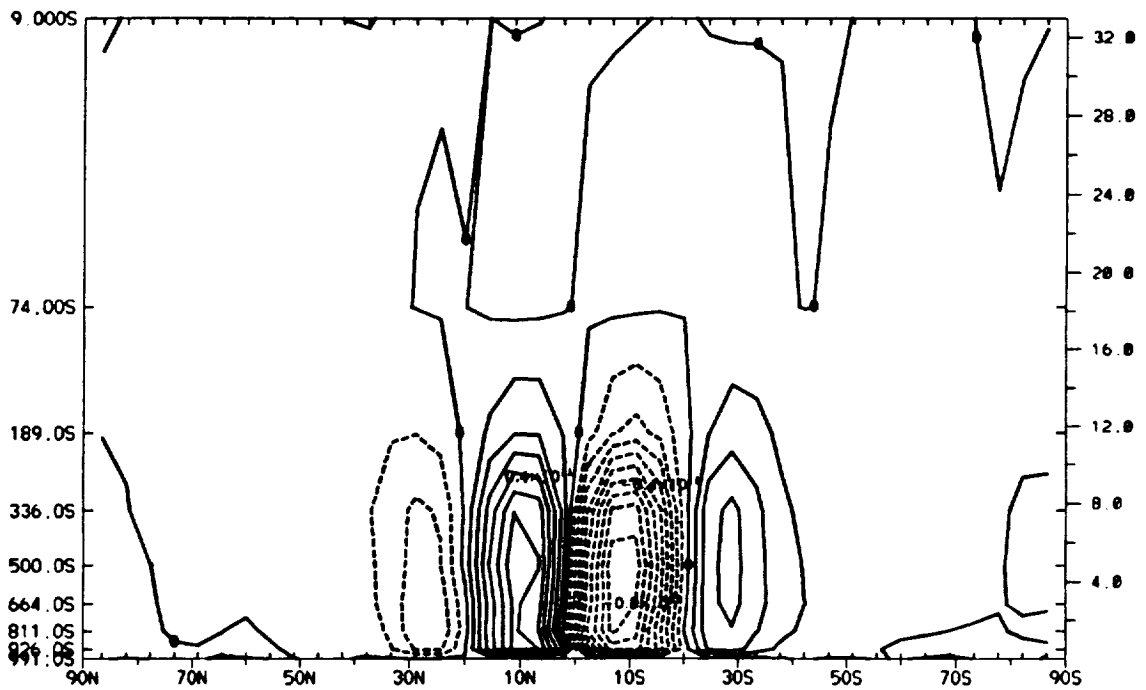


(b) Zonal wind for 14hrColdO. Contour interval: 5 m s^{-1} .

Figure 3.35: Zonal wind. (a) 8ColdO; (b) 14hrColdO.



(a) 8ColdO. Contour interval: $1 \times 10^{10} \text{ kg s}^{-1}$.



(b) 14hrColdO. Contour interval: $1 \times 10^{10} \text{ kg s}^{-1}$.

Figure 3.36: Mean meridional streamfunction. (a) 8ColdO; (b) 14hrColdO.

Faster rotation rates cause a weaker Hadley cell to be confined to tropical regions (Figure 3.36). When compared to ColdO, the intensity of the Hadley cell is roughly 30-50% smaller in 14hrColdO. The magnitudes of the mass flow in 14hrColdO Northern and Southern Hemispheres of 14hrColdO are not similar and suggest that a longer time integration is needed. The same is true of the Ferrel cell. The Ferrel cells in 14hrColdO are about 58% weaker in the Northern Hemisphere and 30% weaker in the Southern Hemisphere than in ColdO. The qualitative properties of the streamfunction are similar to those noted in section 3.1.

Heat transport by transient eddies

Only small changes in the heat-transport distribution by transient eddies occur for higher CO₂ concentrations, with much of the change occurring in the subtropics. The transient heat transport for 8ColdO (Figure 3.37a) shows striking similarities to that of ColdO (Figure 3.22). The difference in transient heat transport indicate that a decrease equatorward of 50° occurs for 8ColdO (Figure 3.38a). An increase occurs poleward of this latitude, and an increase is noted at .189S which is just above the maximum heat transport in ColdO (Figure 3.22b).

A faster rotation rate causes an equatorial shift in the heat-transport maximum associated with the jet. 14hrColdO shows a shift in the maximum heat transport in the upper troposphere (Figure 3.37b). The equatorward shift in the heat transport for 14hrColdO in the upper troposphere allows for an increase in the heat transport equatorward of 30°, with a decrease occurring just poleward of this position (Figure 3.38b). In the lower troposphere, a decrease occurs in the subtropics, with smaller decreases in the polar regions. A slight increase in poleward heat transport occurs between 30° and 50° near the surface in both hemispheres.

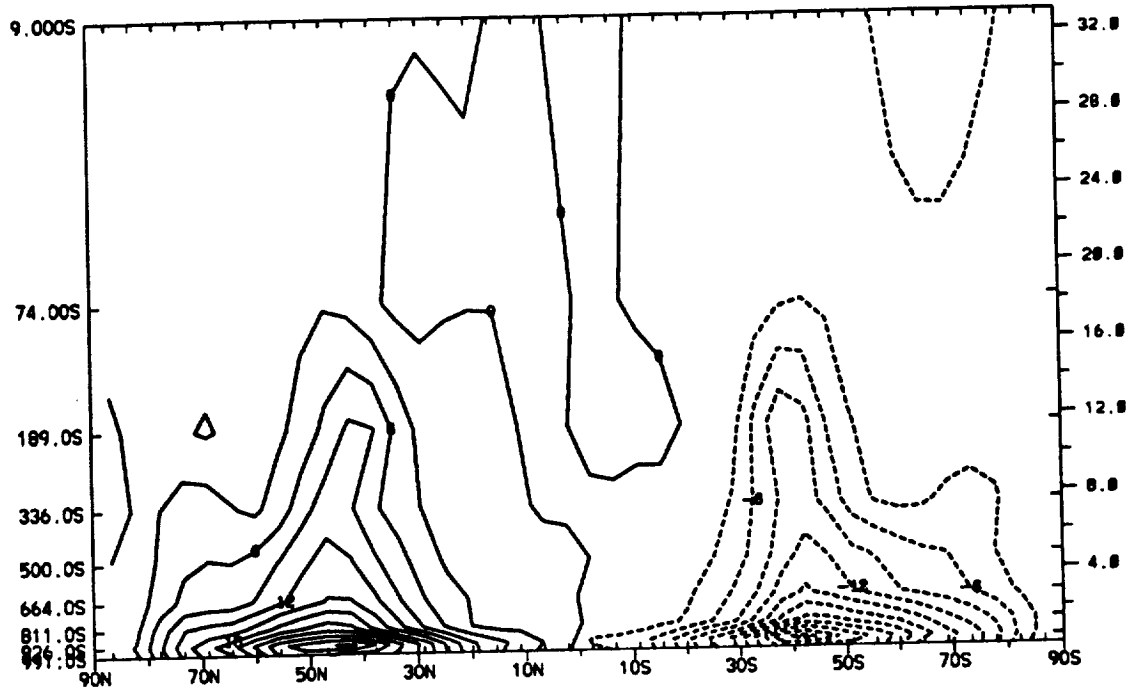
Spectral Kinetic Energy

Kinetic energy is shifted to larger wavenumbers with faster rotation rates under lower solar constant conditions. 14hrColdO has energy cascading to higher wavenumbers compared to ColdO (Figure 3.39). The faster rotation rate causes smaller baroclinic eddies which contain less kinetic energy. The peaks in 14hrColdO near spherical wavenumber 15 indicate that subgrid-scale processes may be important. Higher model resolution could show the importance of the subgrid-scale processes.

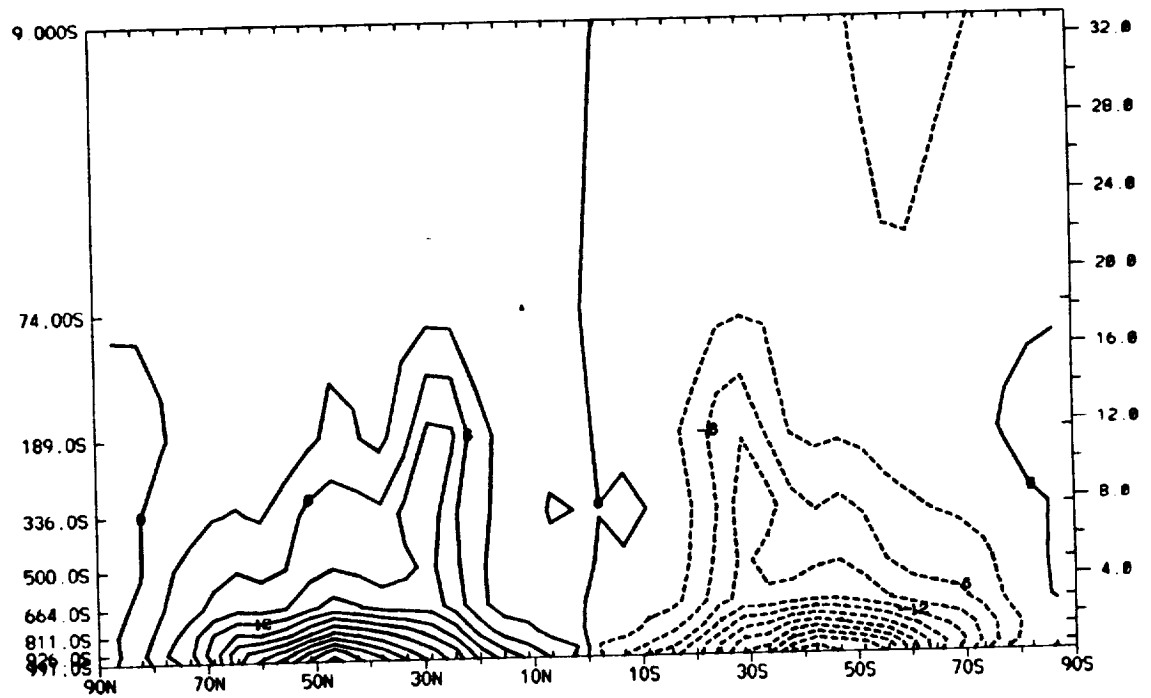
Clouds

Zonally averaged total clouds have increased with larger CO₂ concentrations under the lower solar constant conditions—an increase at the equator and poleward of 45° and a decrease in the subtropics (Figure 3.40). Only a slight increase in clouds for 4ColdO is noted at most latitudes, although a modest increase is noted near 40°. The difference in the latitude-height cloud distribution for 4ColdO and 8ColdO when compared to ColdO is shown in Figure 3.41. 4ColdO shows an increase in high-altitude clouds and a decrease in low-altitude clouds, with an increase in clouds at all levels near 40° of latitude. 8ColdO shows a trend similar to that of 4ColdO, except that the decrease in low-altitude clouds of the troposphere is confined mainly to latitudes equatorward of 40°. The decrease in clouds in both experiments appears to be correlated to increases and decreases in the relative humidity field (Figure 3.42). The increase in relative humidity in the upper troposphere and lower stratosphere is consistent with the change in the temperature field (Figure 3.33).

The cooler temperatures (Figure 3.33) in the upper troposphere and lower stratosphere at higher CO₂ concentrations decrease saturation vapor pressure, thus increasing relative humidity. The opposite is true, however, in the lower troposphere where the temperature increases. The amount of water vapor in the troposphere is also

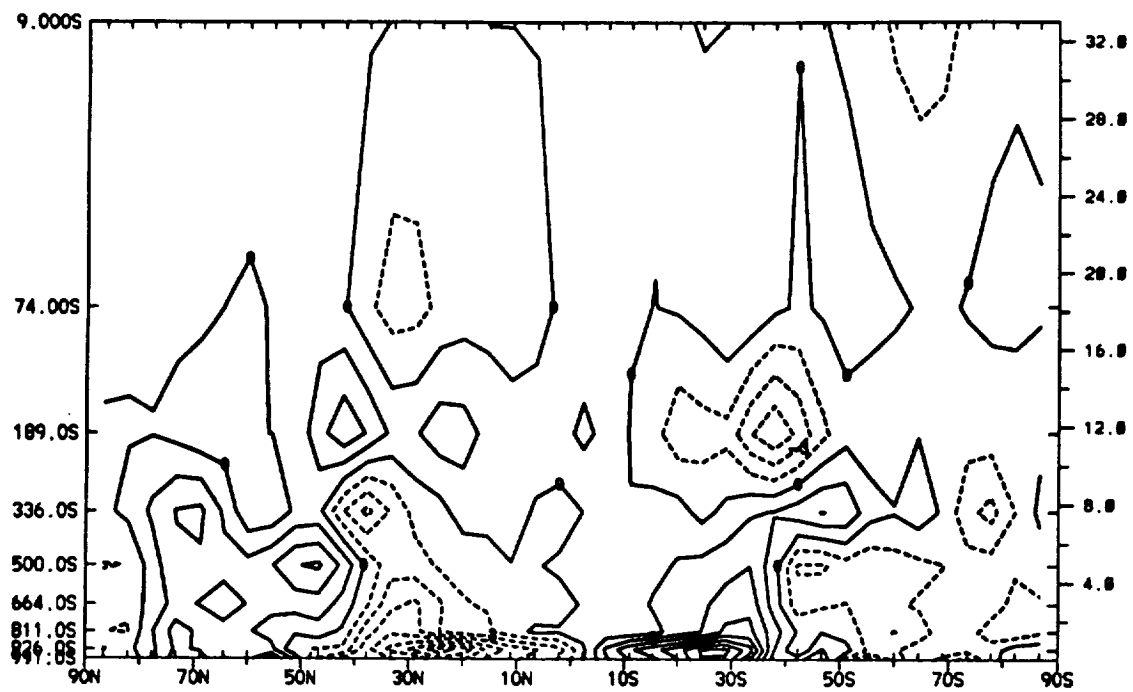


(a) 8ColdO. Contour interval: 3 K m s^{-1} .

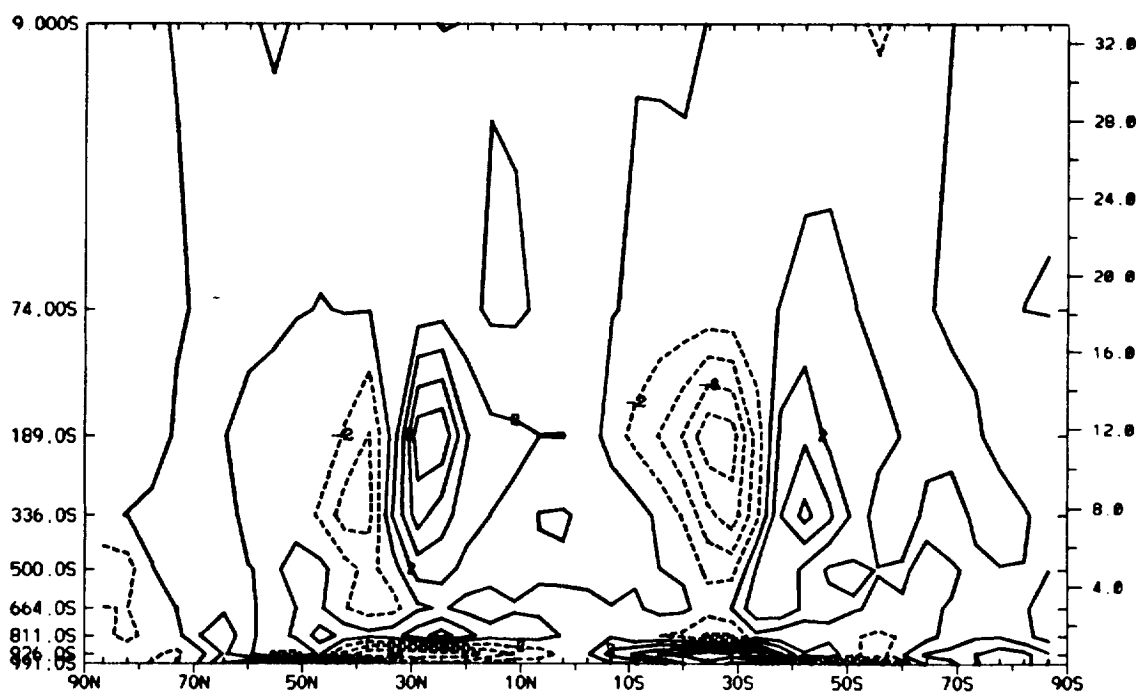


(b) 14hrColdO. Contour interval: 3 K m s^{-1} .

Figure 3.37: Transient eddy heat transport. (a) 8ColdO; (b) 14hrColdO.

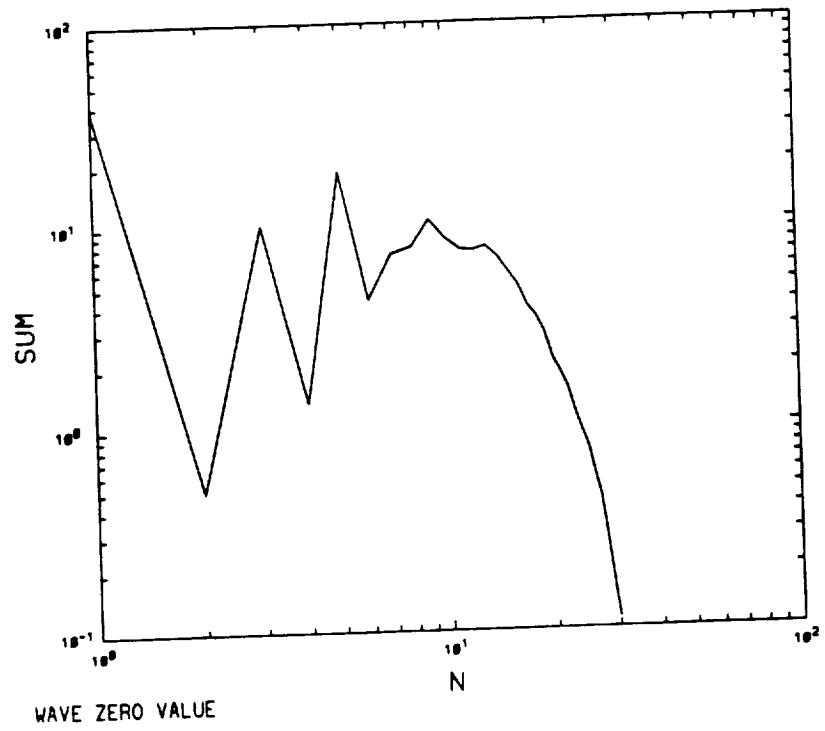


(a) 8ColdO minus ColdO. Contour interval: 1.5 K m s^{-1} .

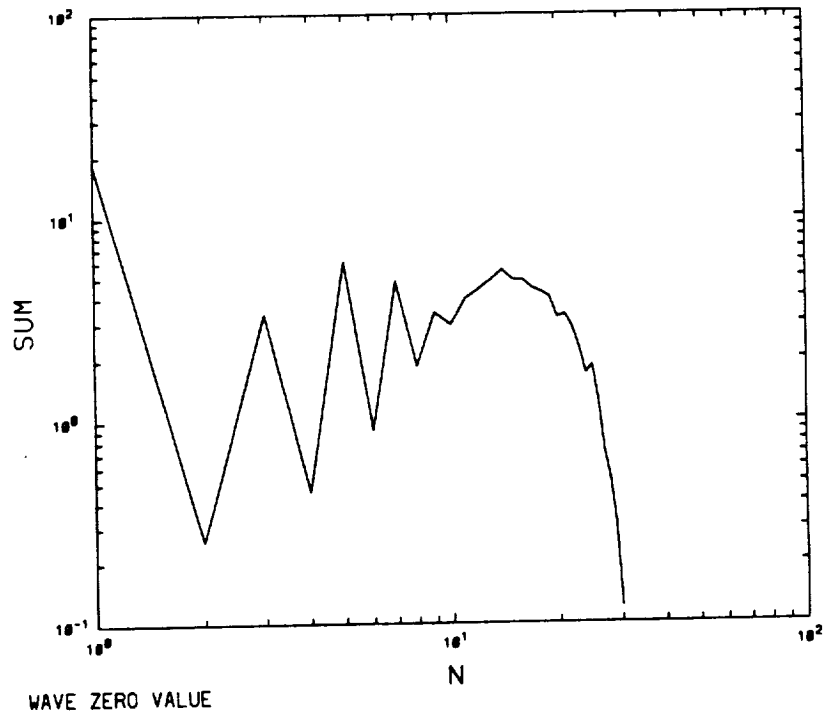


(b) 14hrColdO minus ColdO. Contour interval: 1.5 K m s^{-1} .

Figure 3.38: Difference in transient eddy heat transport. (a) 8ColdO minus ColdO; (b) 14hrColdO minus ColdO.



(a) ColdO.



(b) 14hrColdO.

Figure 3.39: Spectral kinetic energy. (a) ColdO; (b) 14hrColdO.
Units: J kg^{-1} .

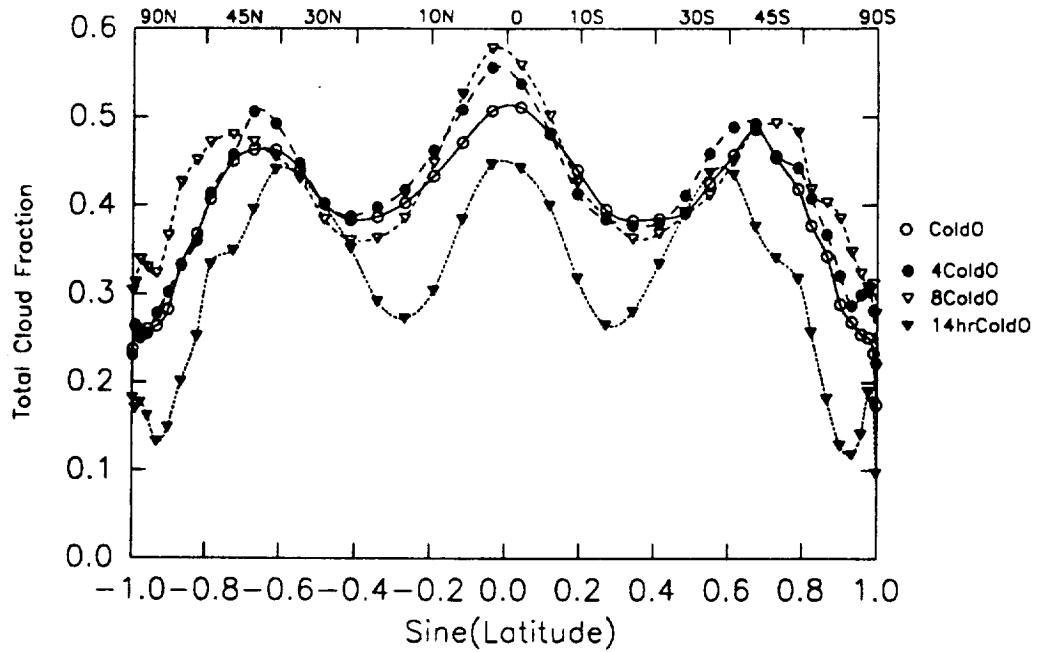
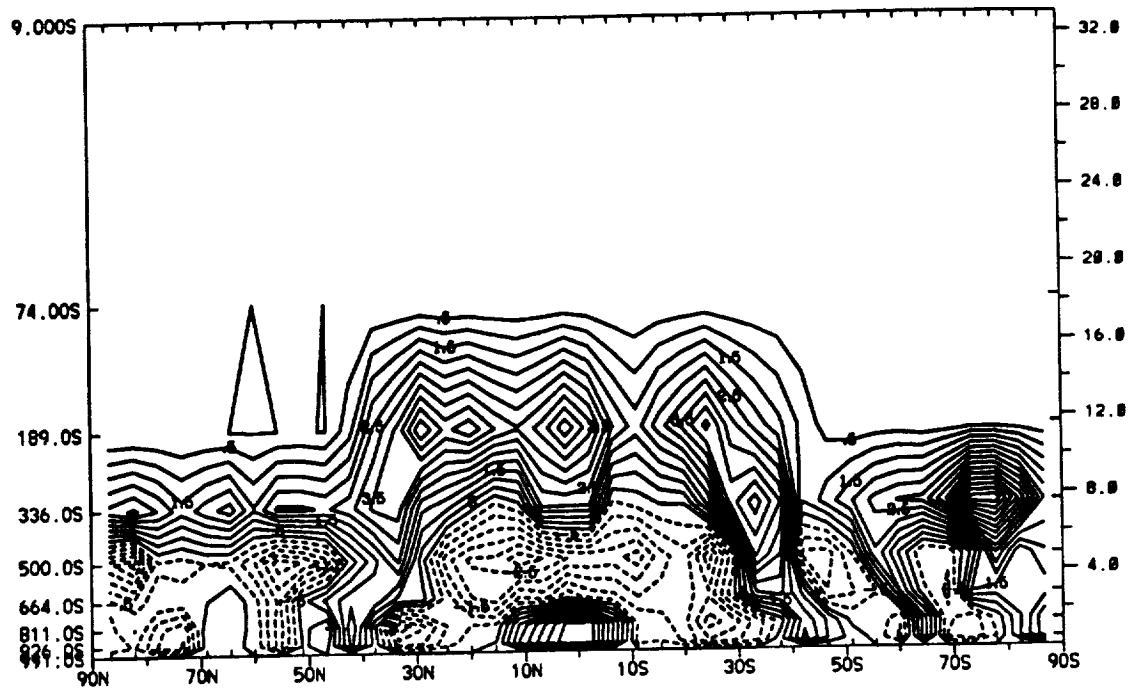


Figure 3.40: Zonally averaged cloud field.

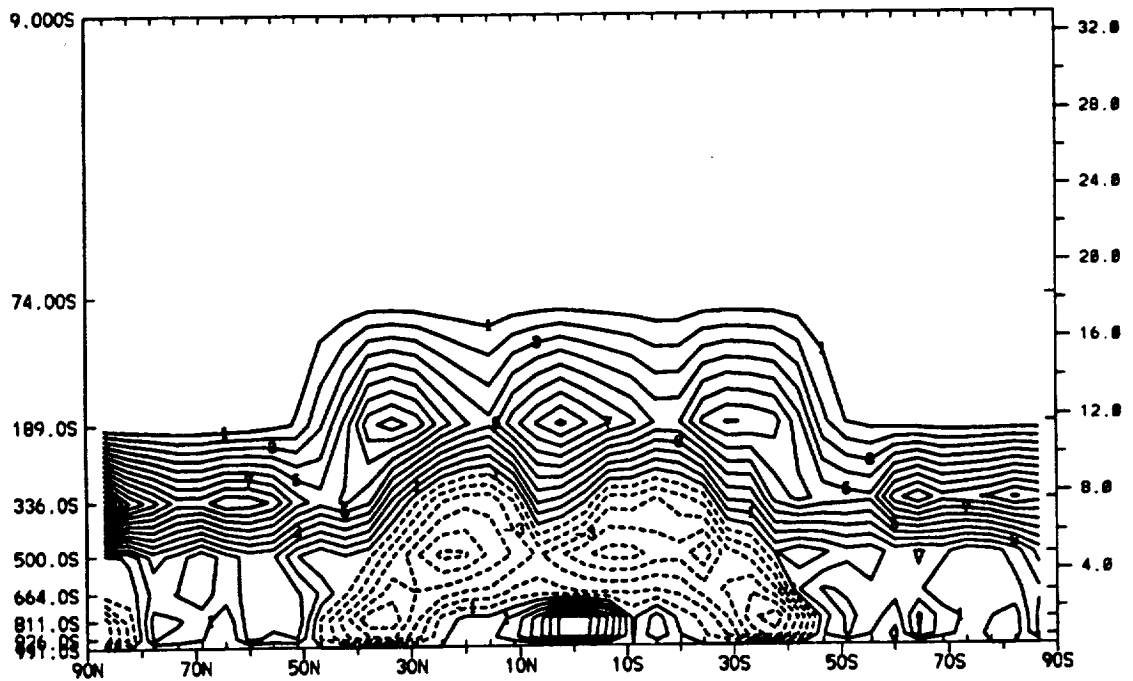
important because if it has increased significantly, the relative humidity may not decrease even in a warmer atmosphere. This appears to be the case for 8ColdO (Figure 3.42b). The mixing ratio has increased in the troposphere when compared to ColdO (Figure 3.43) for both 4ColdO and 8ColdO.

Increases in the condensed moisture field occur in 8ColdO when compared to ColdO (Figure 3.44) which leads to additional heating from latent-heat releases in these regions and helps to decrease relative humidity at 30°N and 30°S. The warmer surface temperatures in 8ColdO lead to increased convective clouds near 50°N and 50°S (Figure 3.44). The increase is correlated with larger upward motion at the poleward edge of the Ferrel cell (Figure 3.45b).

Zonally averaged total clouds have decreased significantly for 14hrColdO (Figure 3.38) and are similar to the results obtained for the same rotation rate under present-day conditions (Fig. 3.11). Changes in the latitude-height cloud distribution (Figure

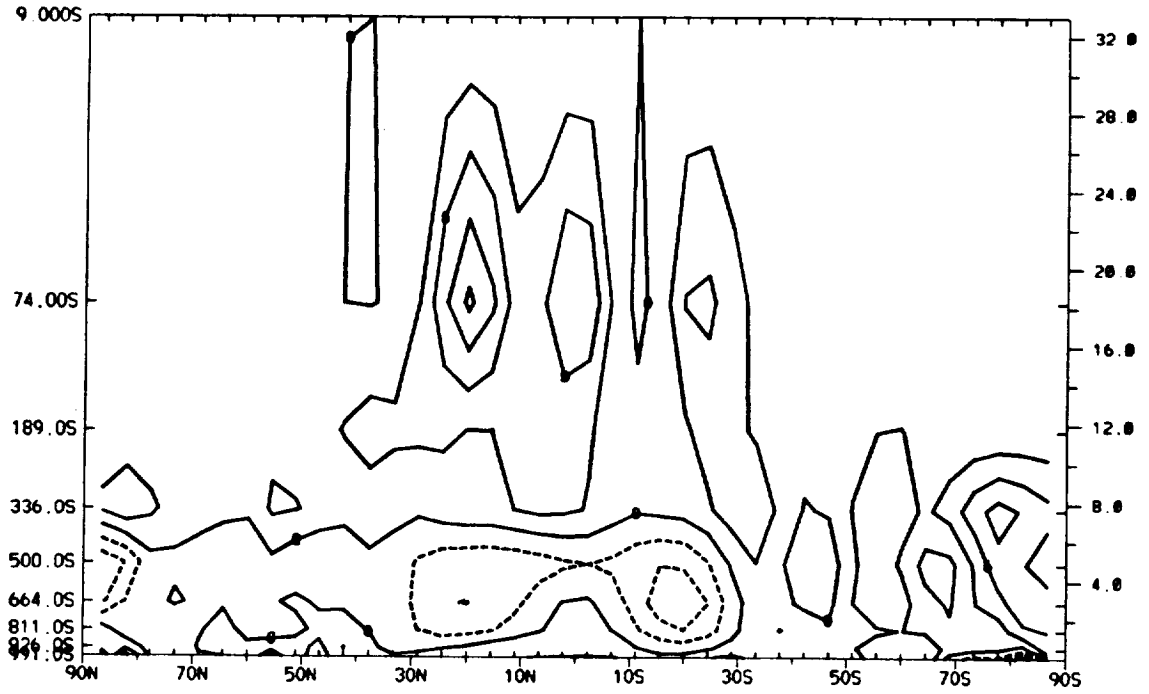


(a) Cloud difference. 4ColdO minus ColdO . Units: percent.

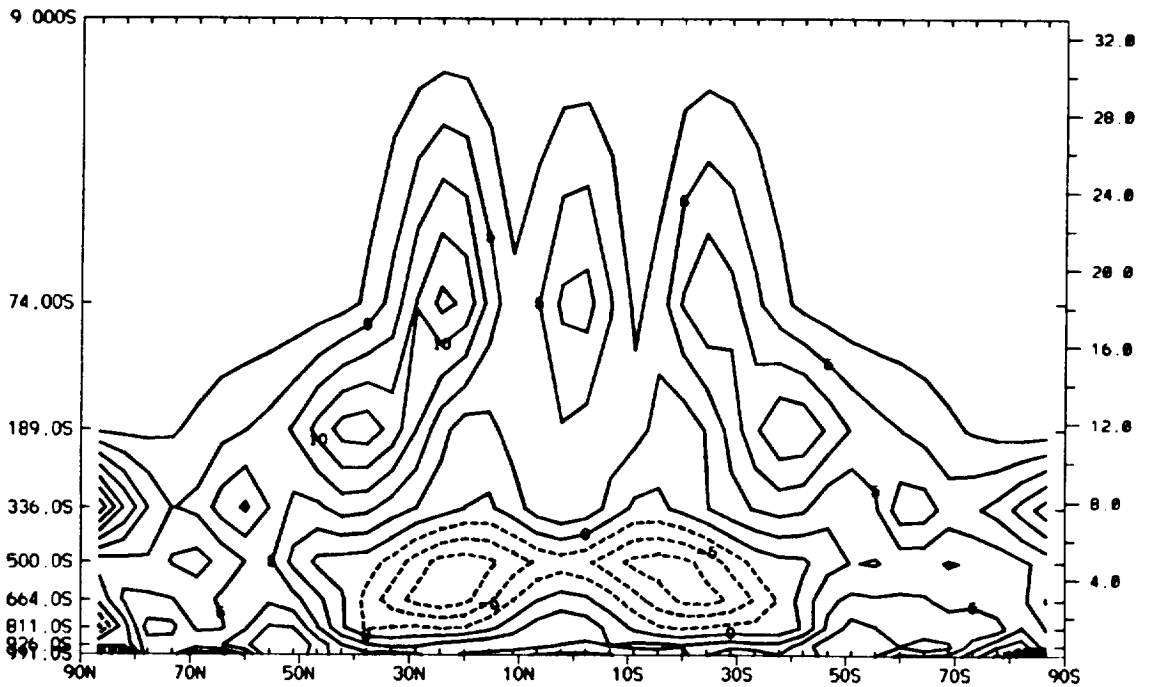


(b) Cloud difference. 8ColdO minus ColdO . Units: percent.

Figure 3.41: Latitude-height difference in clouds. (a) 4ColdO minus ColdO ; (b) 8ColdO minus ColdO .

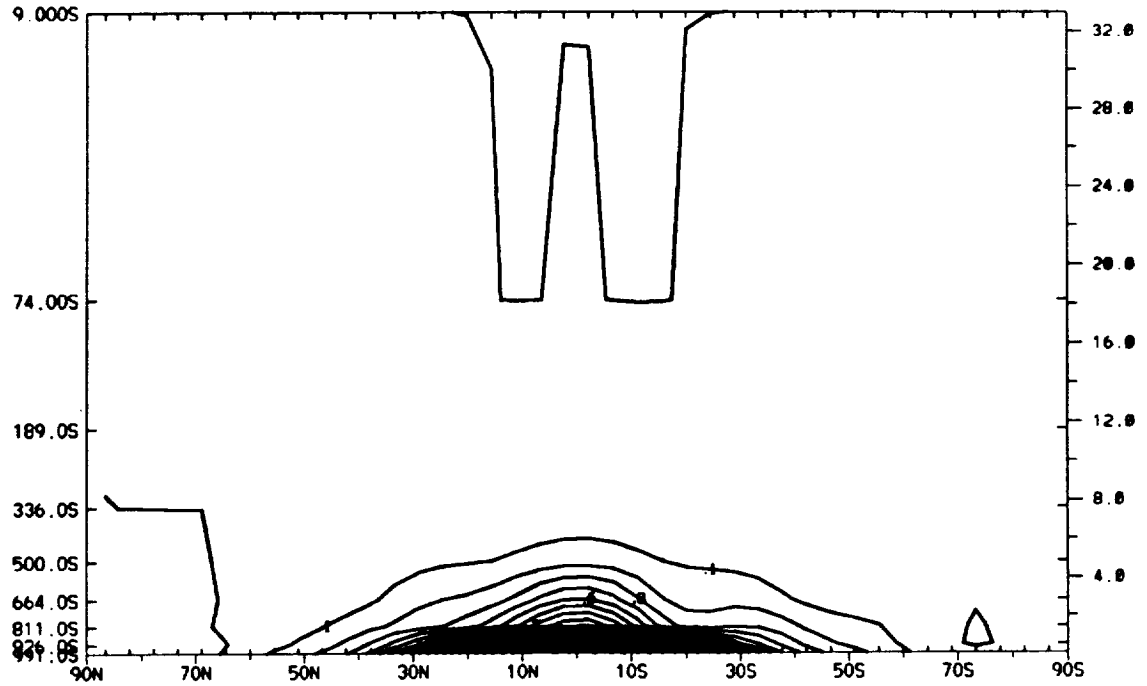


(a) Relative humidity difference. 4ColdO minus ColdO. Units: percent.

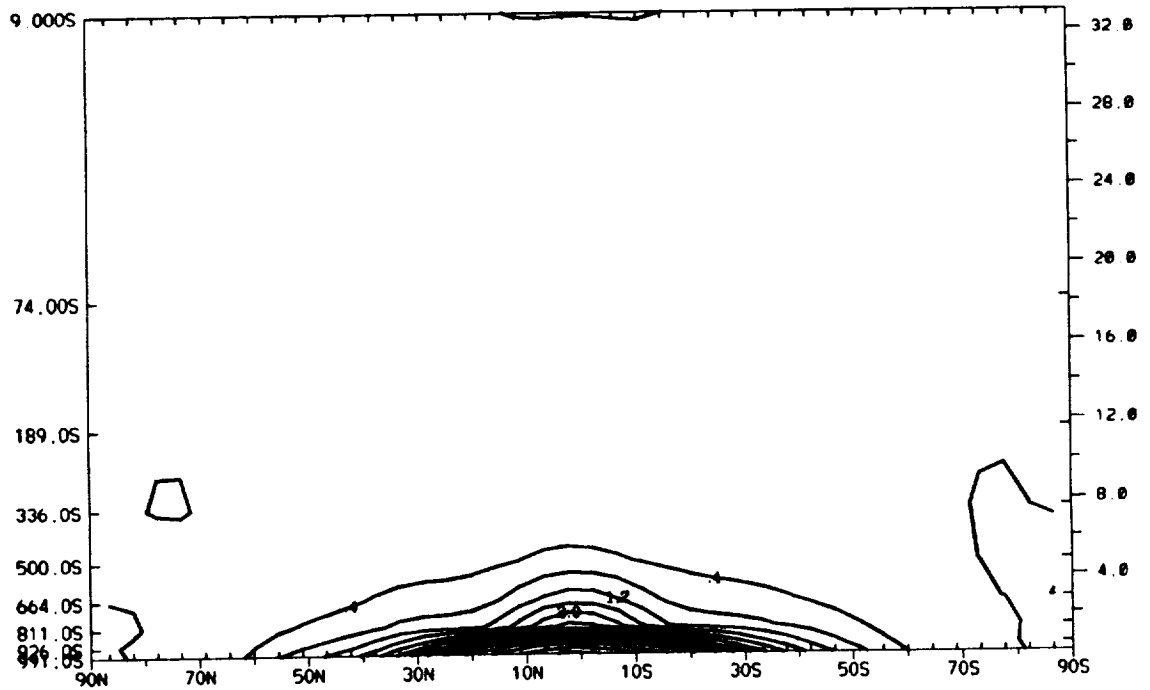


(b) Relative humidity difference. 8ColdO minus ColdO. Units: percent.

Figure 3.42: Latitude-height difference of relative humidity. (a) 4ColdO minus ColdO; (b) 8ColdO minus ColdO.

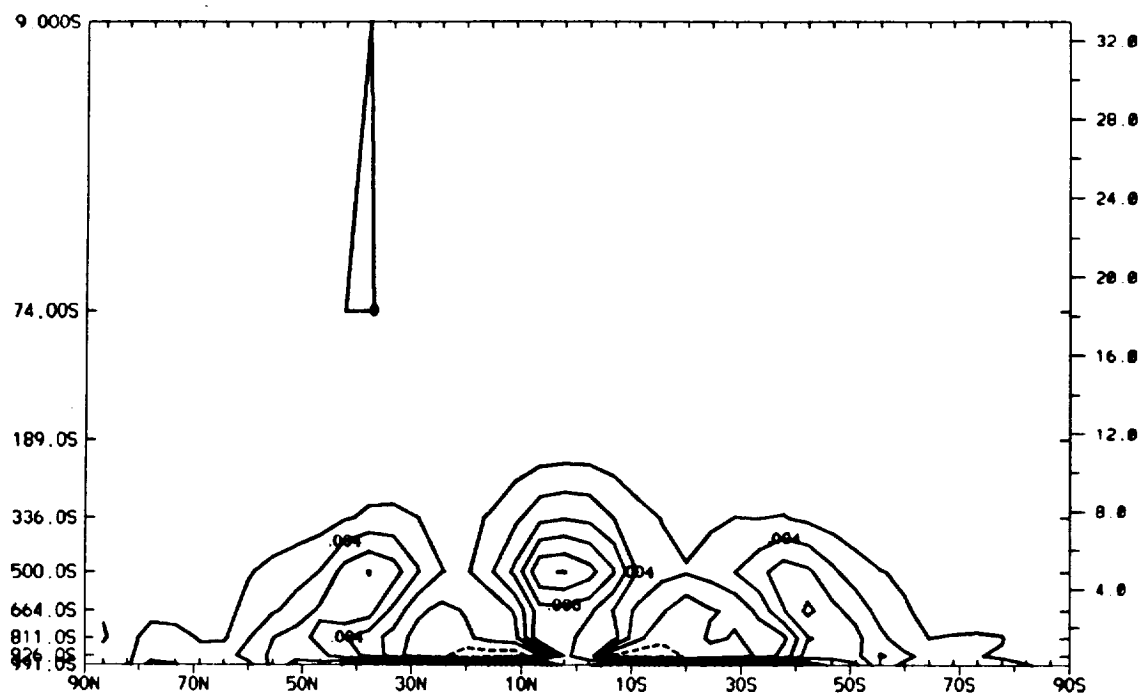


(a) Mixing-ratio difference. $4\text{ColdO} - \text{ColdO}$. Units: g kg^{-1} .

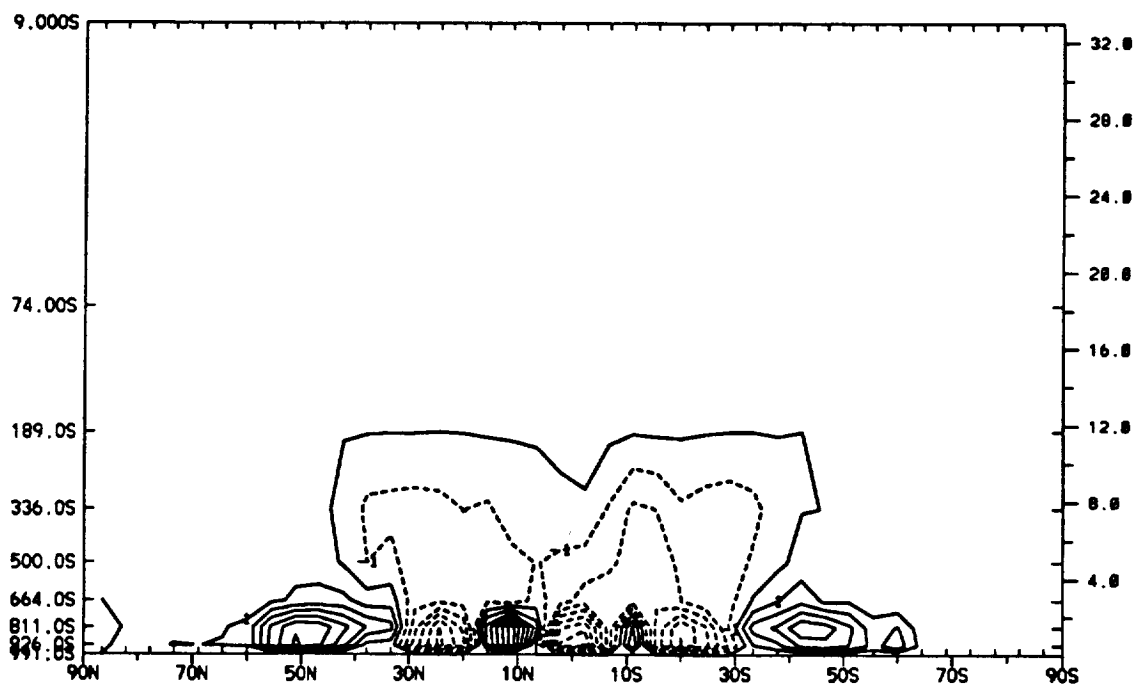


(b) Mixing-ratio difference. $8\text{ColdO} - \text{ColdO}$. Units: g kg^{-1} .

Figure 3.43: Latitude-height difference of mixing ratio. (a) $4\text{ColdO} - \text{ColdO}$; (b) $8\text{ColdO} - \text{ColdO}$

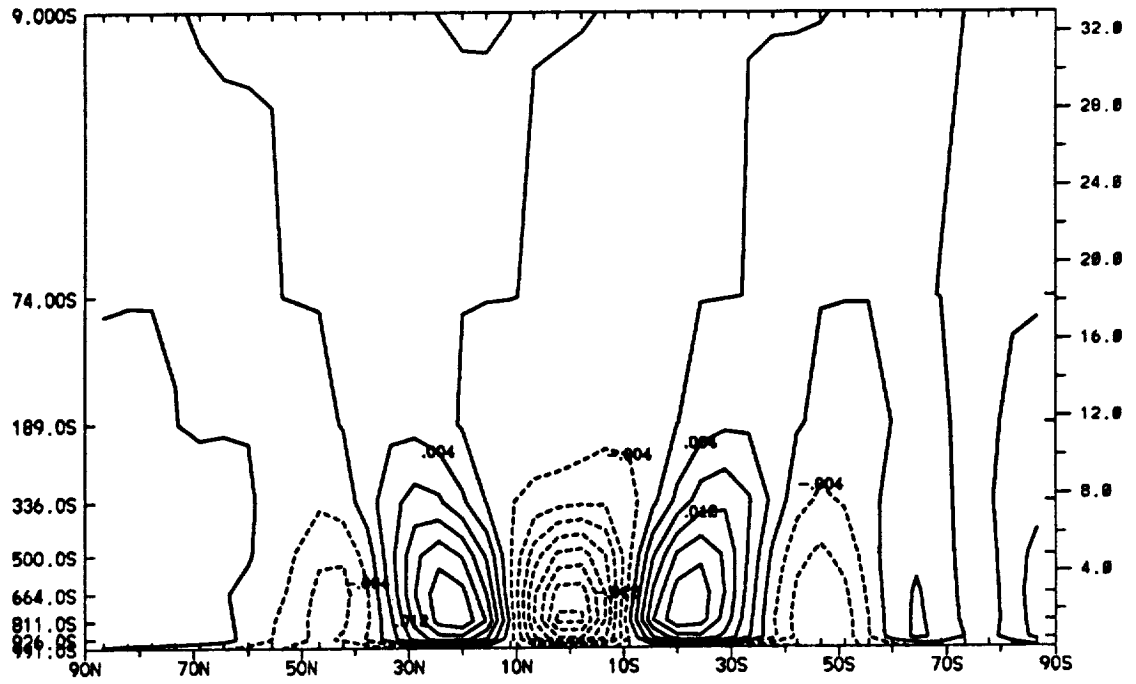


(a) Condensed moisture difference. 8ColdO minus ColdO. Units: millimeters.

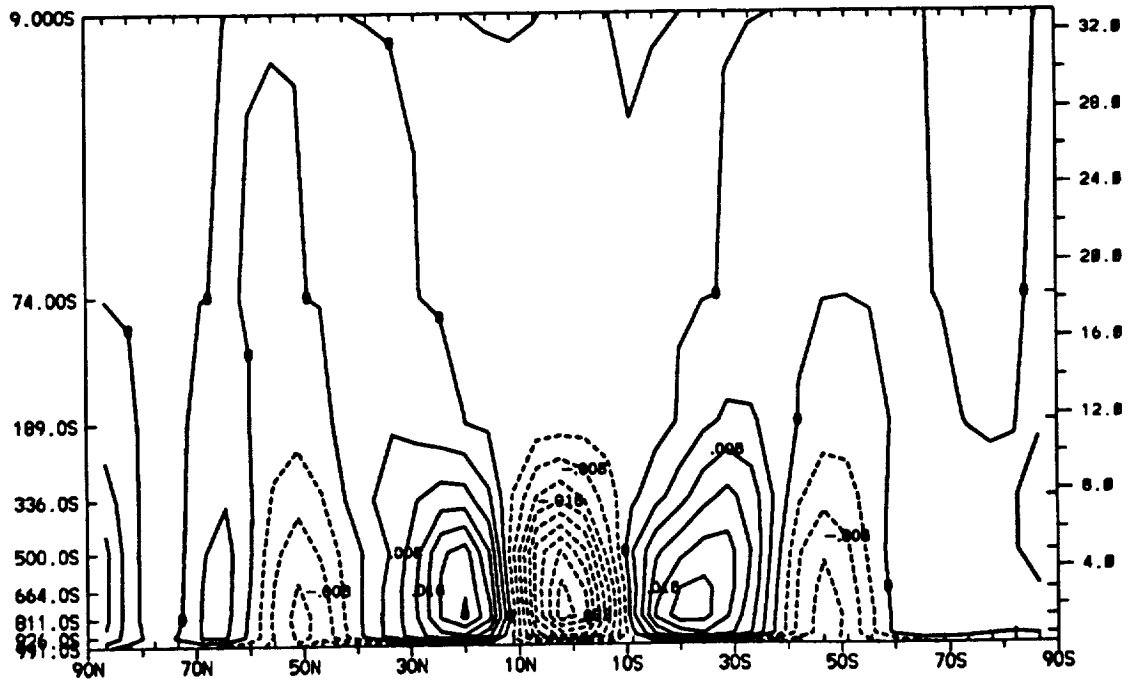


(b) Convective cloud difference. 8ColdO minus ColdO. Units: percent.

Figure 3.44: (a) Latitude-height difference of condensed moisture; (b) convective cloud difference. 8ColdO minus ColdO.



(a) Vertical velocity for ColdO. Contour interval: $4 \times 10^{-3} \text{ mb s}^{-1}$.



(b) Vertical velocity for 8ColdO. Contour interval: $4 \times 10^{-3} \text{ mb s}^{-1}$.

Figure 3.45: Vertical velocity. (a) ColdO; (b) 8ColdO.

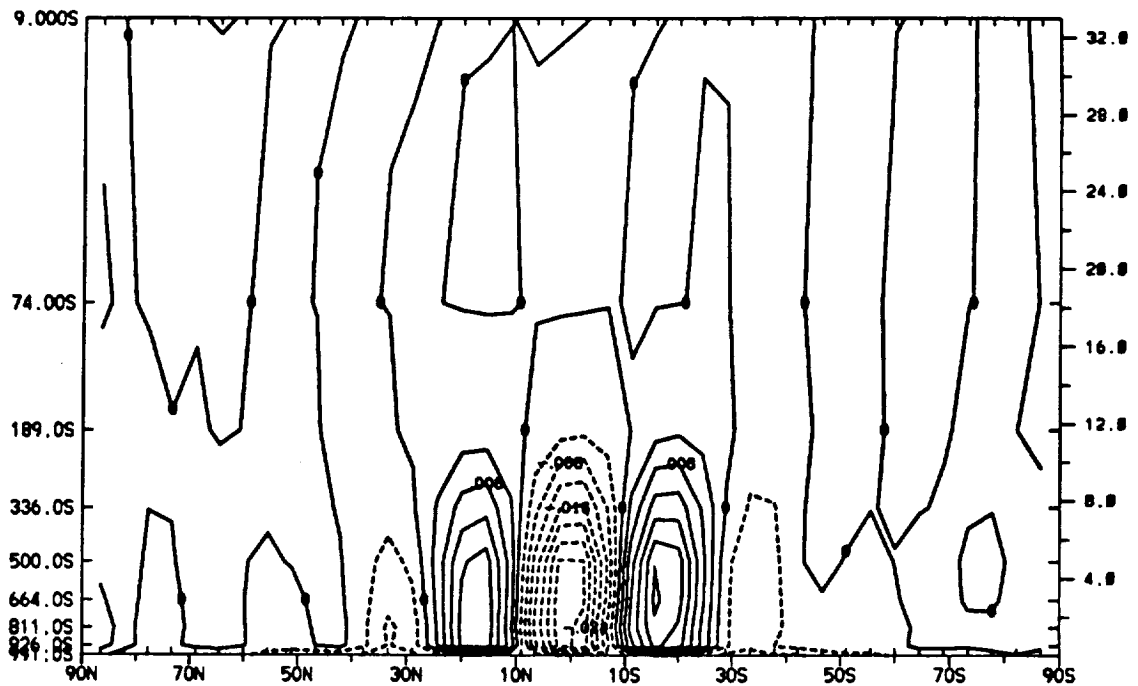
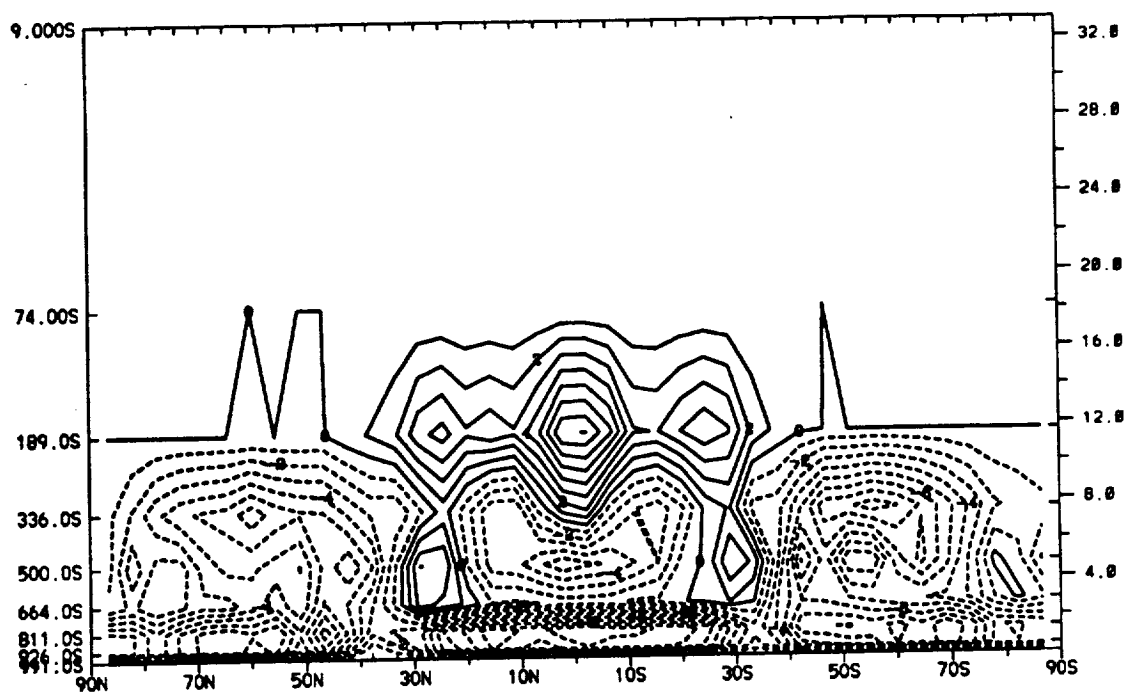


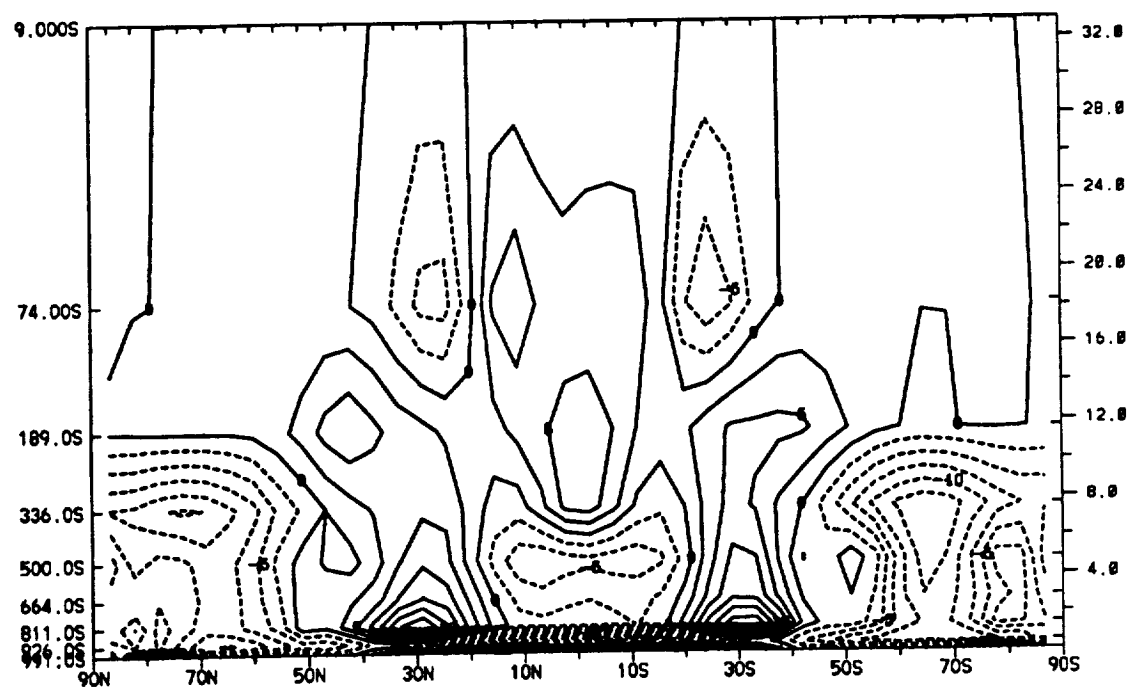
Figure 3.46: Vertical velocity for 14hrColdO. Contour interval: $4 \times 10^{-3} \text{ mb s}^{-1}$.

3.47) indicate a decrease throughout much of the troposphere, except for a small region just below the tropopause in equatorial regions and in the middle troposphere near 30°N and 30°S . The increases and decreases in clouds are highly correlated to increases and decreases in relative humidity (Figure 3.47), with the general trend of decreasing relative humidity for most of the troposphere.

The decreased relative humidity is caused by warmer atmospheric temperatures in 14hrColdO (Figure 3.34), thereby driving up the saturation vapor pressure. Clouds and relative humidity increase near 30°N and 30°S because of the equatorial shift at the poleward-edge Hadley cell. Rising motions occur in 14hrColdO at the poleward edge of the Hadley cell in ColdO thus allowing greater relative humidities and cloud formation. Only a slight increase in convective clouds is noted (Figure 3.48a) in this region, while nonconvective clouds have nearly a 2% increase in this region (Figure 3.48b).



(a) Cloud difference. 14hrColdO minus ColdO. Units: percent.



(b) Relative humidity difference. 14hrColdO minus ColdO. Units: percent.

Figure 3.47: (a) Difference in cloud field; (b) difference in relative humidity. 14hrColdO minus ColdO. Units: percent.

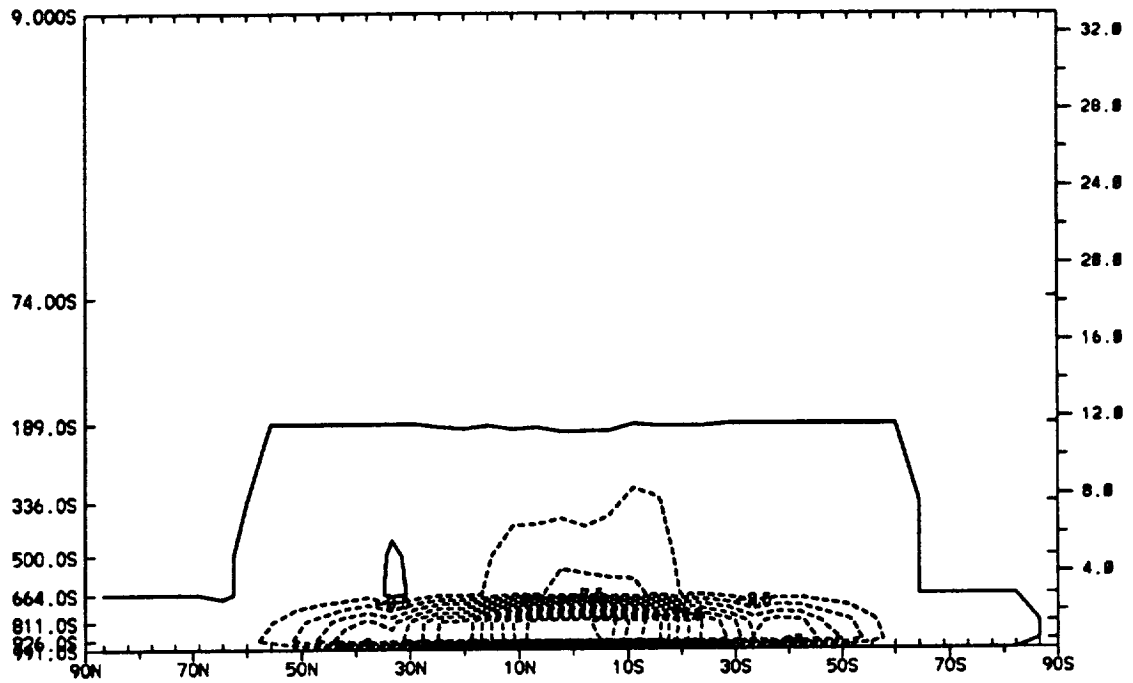
An increase in nonconvective clouds just below the equatorial tropopause is noted and is associated with larger upward vertical velocities in 14hrColdO compared to ColdO (Figure 3.46). Variations in the subsidence patterns between 14hrColdO and ColdO causes increased clouds between 10° and 20° near .189s.

Precipitation

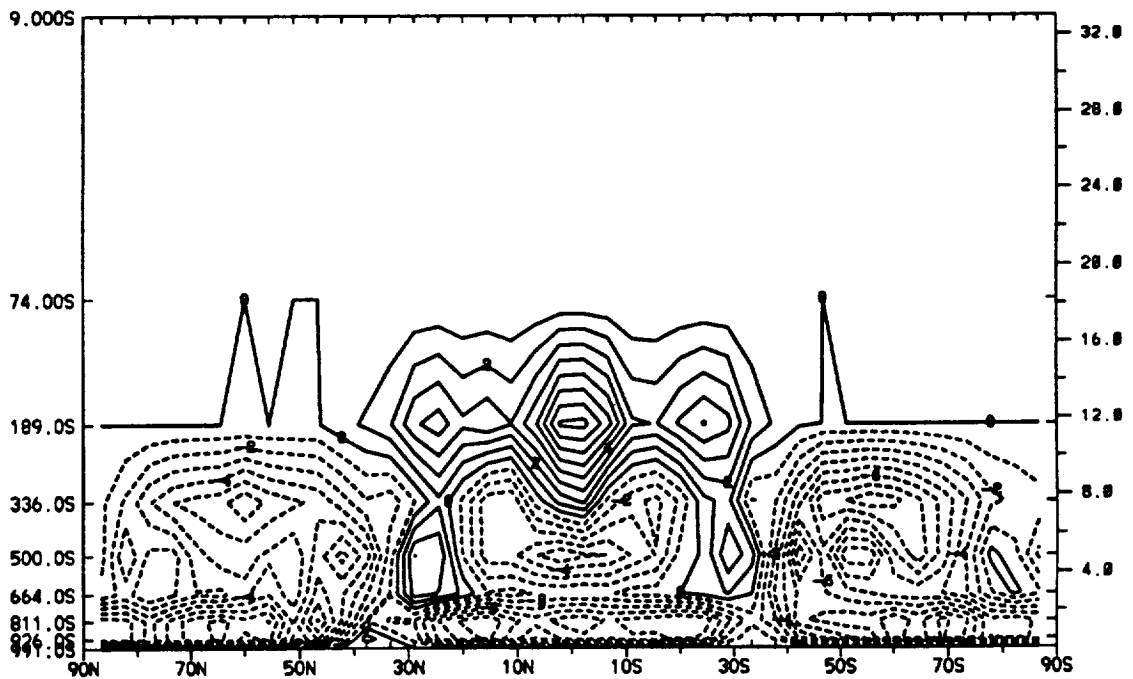
Zonally averaged precipitation increases with higher CO_2 concentration and faster rotation rate (Figure 3.49). Experiments 4ColdO and 8ColdO show largest increases in precipitation in the midlatitudes and over the equator with 8ColdO having the largest increase in precipitation of the three cases. This precipitation increase is consistent with more water vapor being available at higher CO_2 concentrations (Figure 3.43). The condensed moisture field (Figure 3.44) also indicates that more water vapor is condensed in the CO_2 experiments. 14hrColdO shows more precipitation at all latitudes when compared to ColdO (Figure 3.49). More water vapor is available equatorward of 50° (Figure 3.50) from the melting of sea ice which exposes the open water for more evaporation. A slight equatorial shift in subtropical precipitation is noted, which is consistent with a shift in the Hadley cell. The global mean values of precipitation are given in Table 3.3.

Evaporation

The zonally averaged surface evaporation increases with higher CO_2 concentrations and faster rotation rates with large increases for 8ColdO and 14hrColdO in tropical regions compared to ColdO. At the same time, a slight decrease in evaporation in 4ColdO is noted (Figure 3.50b) because of weaker winds. The large increases in both 8ColdO and 14hrColdO are caused by an increase in the vertical gradient of



(a) Convective cloud difference. 14hrColdO minus ColdO. Units: percent.



(b) Nonconvective difference. 14hrColdO minus ColdO. Units: percent.

Figure 3.48: Difference in cloud field. (a) convective; (b) nonconvective. 14hrColdO minus ColdO.

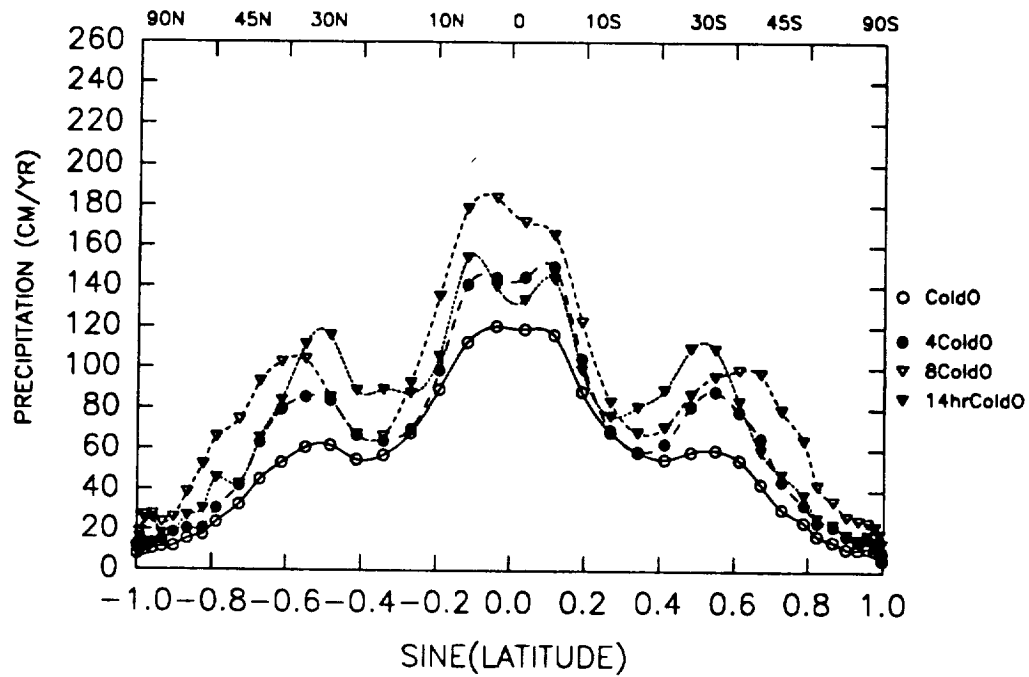
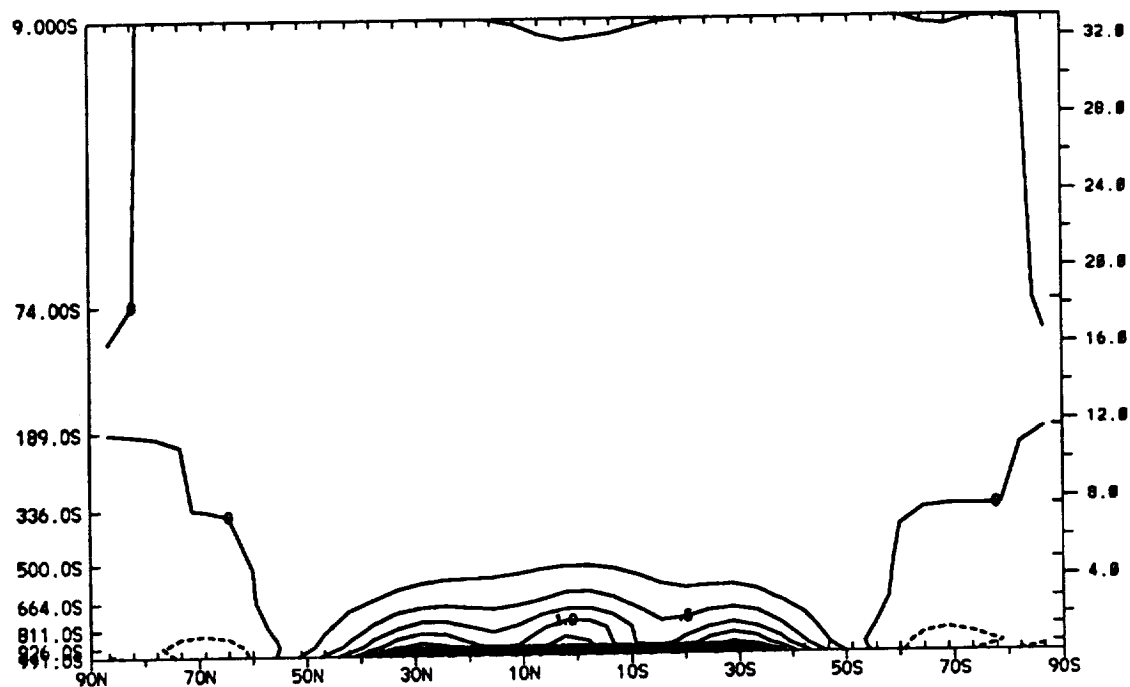


Figure 3.49: Zonal averaged precipitation. Units: cm yr^{-1} .

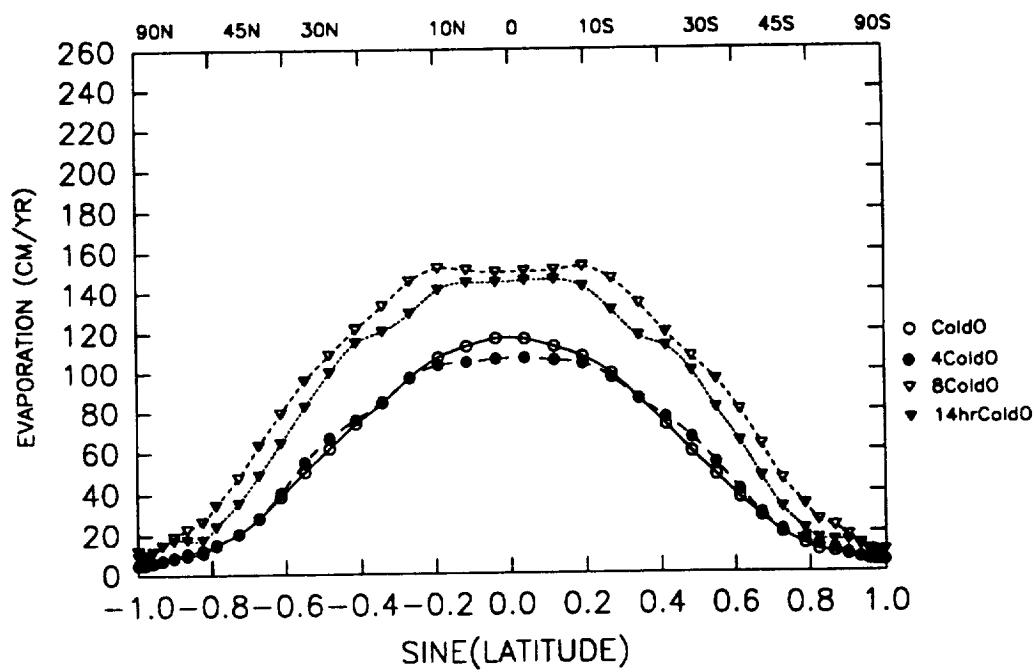
mixing ratio (Figures 3.43 and 3.50a) and an increase in wind magnitude in low latitudes in comparison to ColdO. Outside the tropics, the evaporation rates for 4ColdO are similar to ColdO, while both 8ColdO and 14hrColdO show larger values.

Solar absorbed radiation by the earth-atmosphere system

Because of a decrease in clouds with faster rotation (Figure 3.40), more solar radiation amounts is absorbed at the surface. 14hrColdO shows the largest solar absorbed radiation by the earth-atmosphere system in the tropics (Figure 3.51). In addition, increases are noted at all latitudes when compared to ColdO. Because of larger water-vapor amounts, 4ColdO and 8ColdO show increases in absorbed solar radiation throughout most of the subtropics and midlatitudes.



(a) Mixing-ratio difference. 14hrColdO minus ColdO. Units: g kg^{-1} .



(b) Surface evaporation. Units: cm yr^{-1} .

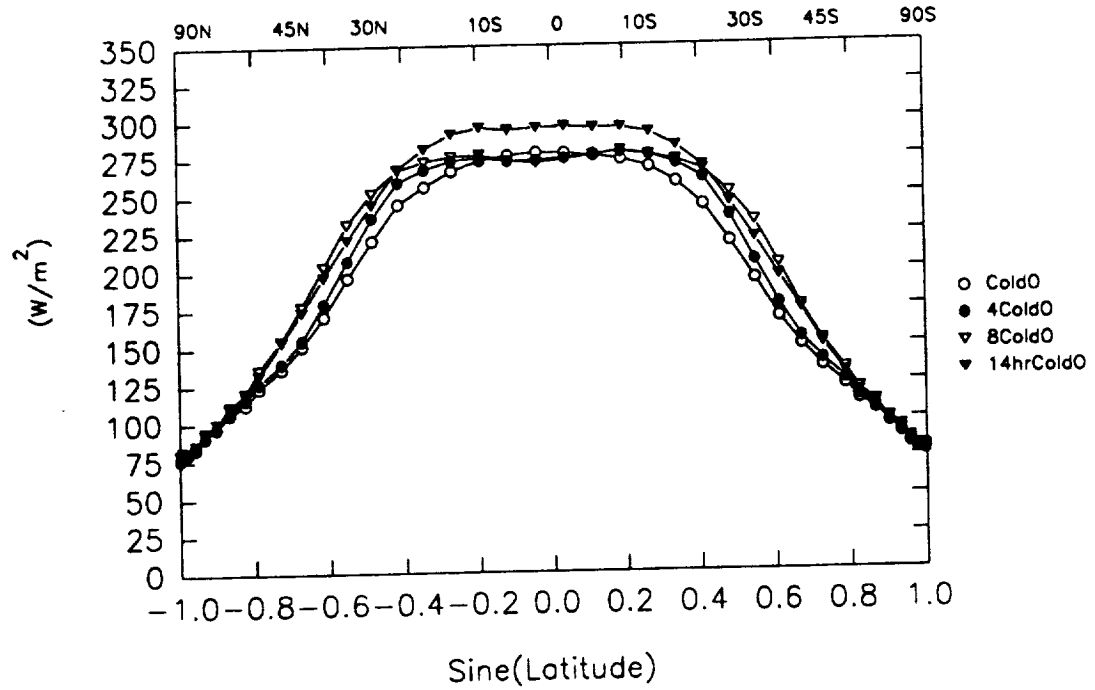
Figure 3.50: (a) Difference in mixing ratio. 14hrColdO minus ColdO;
(b) Zonally averaged evaporation rates.

Outgoing longwave radiation

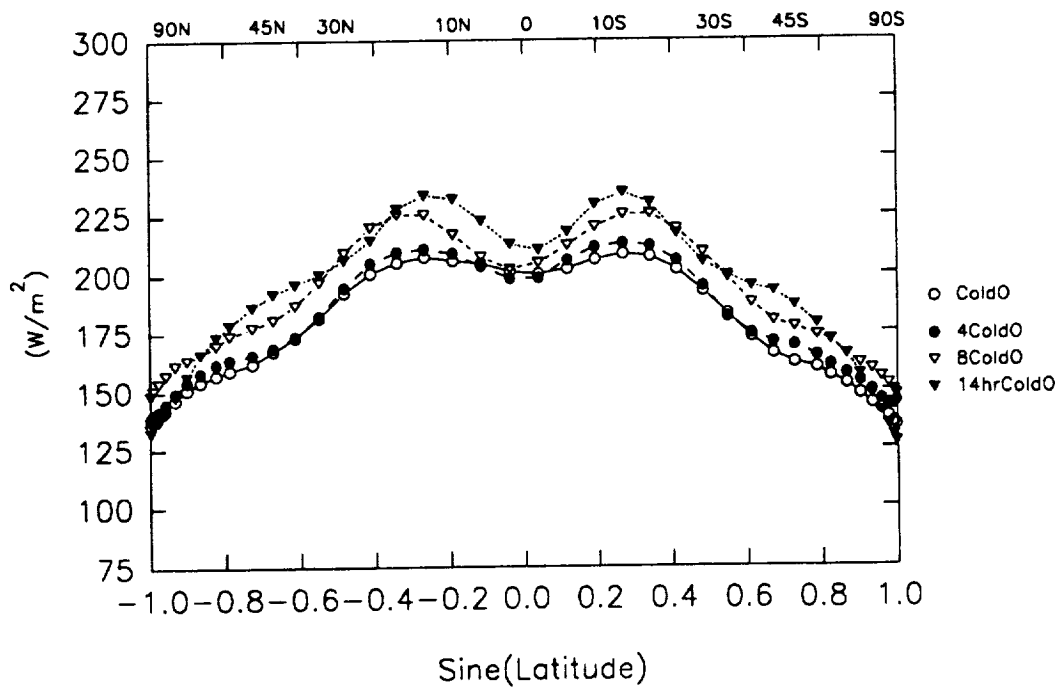
Higher CO₂ concentration and a faster rotation rate increase emitted longwave radiation into space (Figure 3.51). 14hrColdO shows the largest OLR, except in the polar regions. Both 4ColdO and 8ColdO show increases in the OLR, with the largest changes occurring in the subtropics in comparison to ColdO. A slight decrease in OLR is noted near the equator for the CO₂ experiments because of an increase in high-altitude clouds in equatorial regions which reduce the OLR. The warmer surface temperatures for 14hrColdO, 4ColdO, and 8ColdO contribute significantly to the OLR. The large decrease in clouds in 14hrColdO allow radiation to escape that would otherwise be captured by the clouds and radiated out to space at lower temperatures. Warmer atmospheric temperatures also contribute to larger OLR values, but the larger water-vapor amounts for the three cases reduce the amount of OLR. Global mean values are noted in Table 3.3, with 14hrColdO showing a sizable increase in OLR.

Sea ice

Higher CO₂ concentrations and a faster rotation rate cause the sea-ice edge to shift poleward (Figure 3.52). ColdO shows that the sea-ice line extends to near 25°, but when CO₂ is added, sea ice melts and retreats poleward. 4ColdO indicates that the sea ice edge is near 35°, while 8ColdO shows the sea ice edge near 45°. The increase in downward longwave radiation contributes to sea-ice melting (Table 3.3). When a faster rotation rate is introduced the sea-ice line is near 40°. Much of the sea-ice melting is caused by the great decrease in clouds (Figure 3.40) which allows more solar radiation to reach the surface and melt sea ice. A secondary cause for the sea-ice melt is the larger downward longwave radiation from the increased atmospheric water-vapor amounts (Figure 3.50a).



(a) Absorbed solar radiation by earth-atmosphere system. Units: W m^{-2} .



(b) Outgoing longwave radiation. Units: W m^{-2} .

Figure 3.51: Zonally averaged absorbed solar radiation and outgoing longwave radiation.

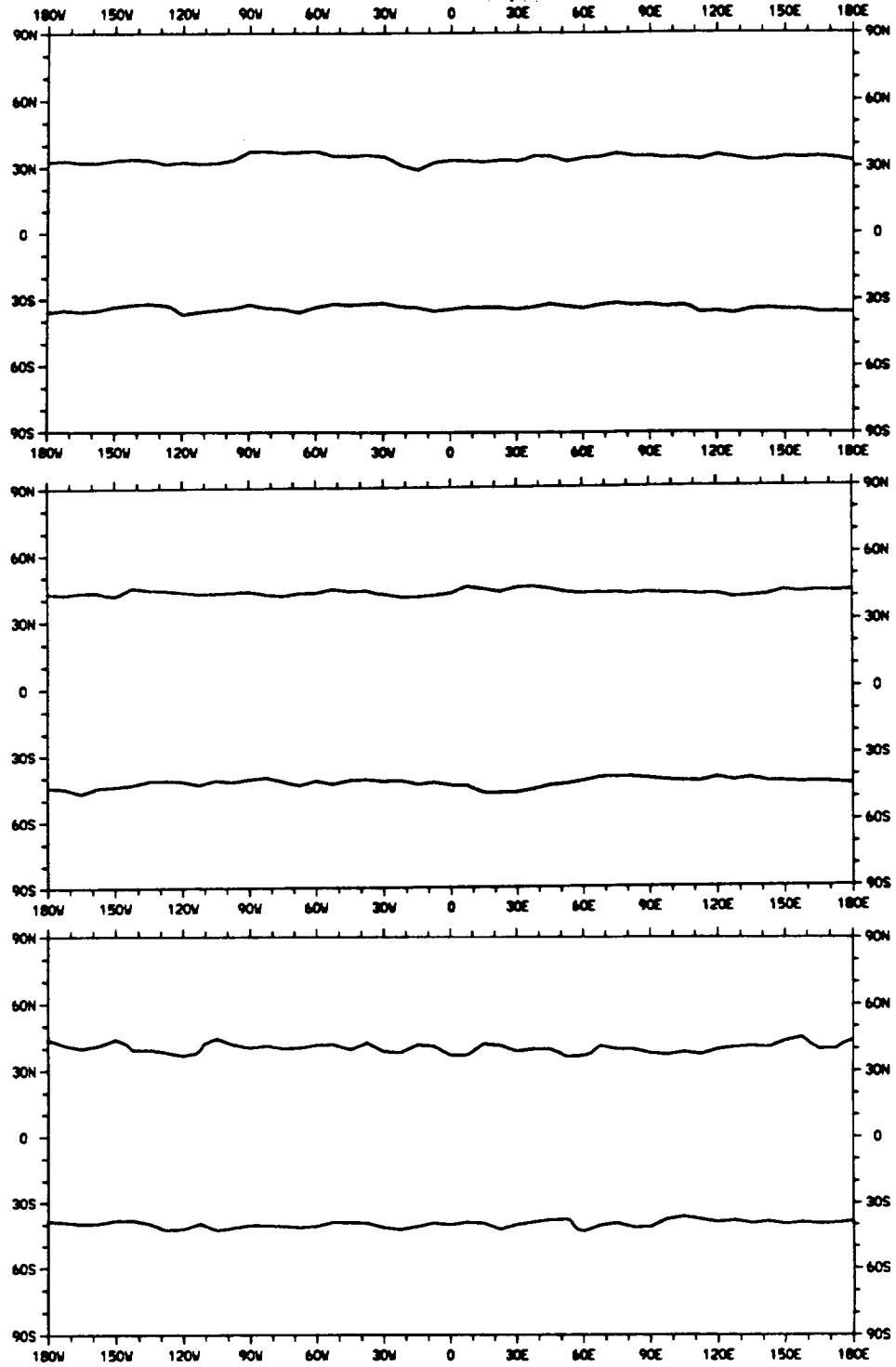


Figure 3.52: Geographical sea ice distribution: Top: 4ColdO; middle: 8ColdO; bottom: 14hrColdO. Units: meters.

3.4 Sensitivity Experiments with Combined Climatic Factors

Introduction

The combined effects of faster rotation rate, higher CO_2 concentrations, zero land fraction, and lower solar luminosity are explored in this section. The rotation rate is set to correspond to a 14-hr day. The CO_2 concentration is raised to eight times the control concentration. Several values of the solar constant are assumed: (1) The solar luminosity is reduced by 10% (Ice1). (2) The solar luminosity is reduced by 15% (denoted as Ice2). (3) The solar luminosity is reduced by 20% (Ice3). All of these experiments are compared to the global ocean experiment with present-day solar luminosity (Glocean). This experiment is used because of its simple surface which eliminates the effects of continents and topography and makes the analysis simpler.

Surface temperature

As the solar luminosity is reduced by up to 20% relative to the present, the surface temperature is reduced significantly (Figure 3.53) in comparison to Glocean. Surface temperatures above the freezing point of sea ice exist only at the equator for Ice3. The temperature gradient increases significantly with lower solar luminosity, and Ice2 exhibits the largest meridional temperature gradient at the surface. The global mean surface temperatures are shown in Table 3.4.

The geographical distribution of surface temperatures shows that the temperature is above the freezing point of water for all experiments (Figure 3.54). Ice1 has equatorial temperatures that are hovering near 300 K, while the equatorial temperatures of Ice3 are just above freezing. The temperatures above freezing in Ice3 are confined

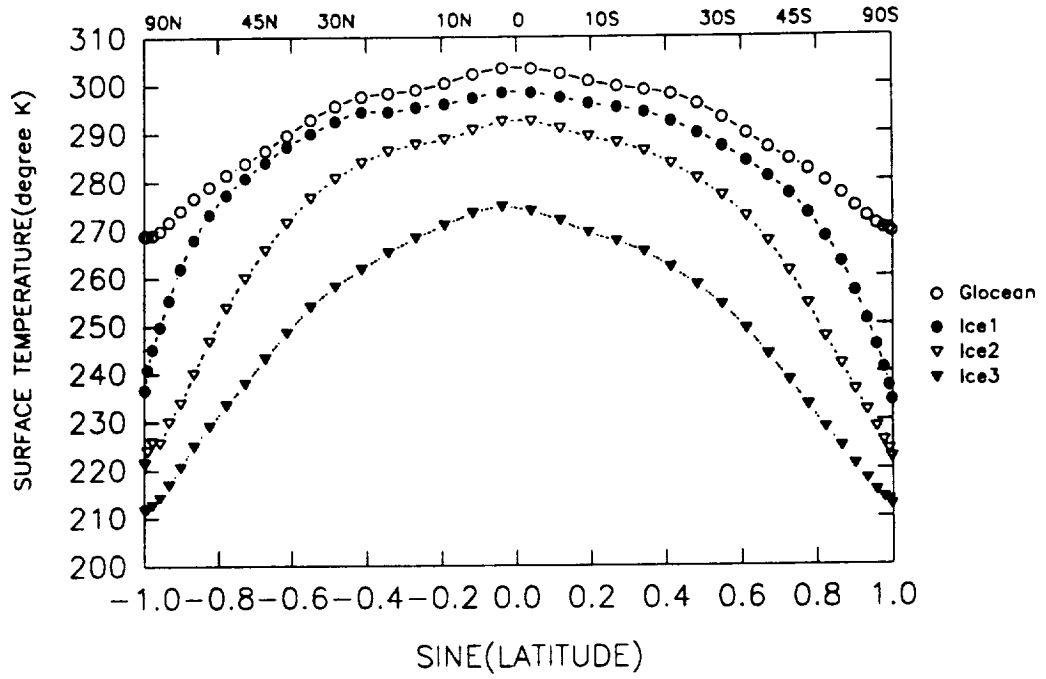


Figure 3.53: Zonally averaged surface temperature. Units: degrees Kelvin

Variable	Ice1	Ice2	Ice3
$T_{surface} \text{ } ^\circ K$	283.2	271.3	251.6
Cloud fraction	0.318	0.323	0.301
Precipitation (cm yr^{-1})	106.6	77.8	28.3
$F_{TopIR} \uparrow (\text{W m}^{-2})$	244.9	190.63	157.7
$F_{SurfIR} \downarrow (\text{W m}^{-2})$	277.5	216.4	133.87
$F_{SurfIR} \uparrow (\text{W m}^{-2})$	364.7	307.3	227.3
$F_{Surfsolar} \downarrow (\text{W m}^{-2})$	182.68	167.38	138.46

Table 3.4: Global mean values for Ice1, Ice2, and Ice3.

to areas equatorward of 10° . The steepest temperature gradient in Ice1, Ice2, and Ice3 occurs in the midlatitudes, with Ice2 showing the greatest temperature gradient (Figure 3.54).

When the solar luminosity is lower by 10%, 8 times the present CO_2 concentration is added, and a rotation rate corresponding to a 14-hr day is introduced (Ice1) and compared to Glocean, significant changes in atmospheric temperature are shown. A decrease occurs everywhere except near the polar and equatorial tropopause (Figure 3.55b). The largest temperature decreases occur in the polar regions near the surface, where a decrease of 31 K is noted. The latitude-height temperature field for Ice1 shows an inversion in the lowest levels of the troposphere in polar regions (Figure 3.55a) which is caused by smaller amounts of longwave cooling at the surface than in the air above.

Ice2 shows an inversion in the polar regions in the lower troposphere (Figure 3.56a) caused by less longwave cooling rates at the surface. Furthermore, large decreases in atmospheric temperatures occur when compared to Glocean (Figure 3.56b). The largest temperature decrease occurs in polar regions where a temperature decrease of 44 K is noted. Large decreases in the stratospheric temperature also occur monotonically as the height increases. The only increase in temperature occurs at the equatorial tropopause.

Ice3 has the largest atmospheric temperature decreases with respect to Glocean (Figure 3.57b). A temperature decrease of 56 K occurs in polar regions. The only area of increase is at the equatorial tropopause. The temperature distribution of Ice3 indicates that the polar tropopause has dropped down to 500 mb (Figure 3.57a).

Sea ice

The sea-ice edge migrates toward the equator as the solar constant is reduced. Figure 3.58 shows the geographical distribution of sea ice for Ice1, Ice2, and Ice3,

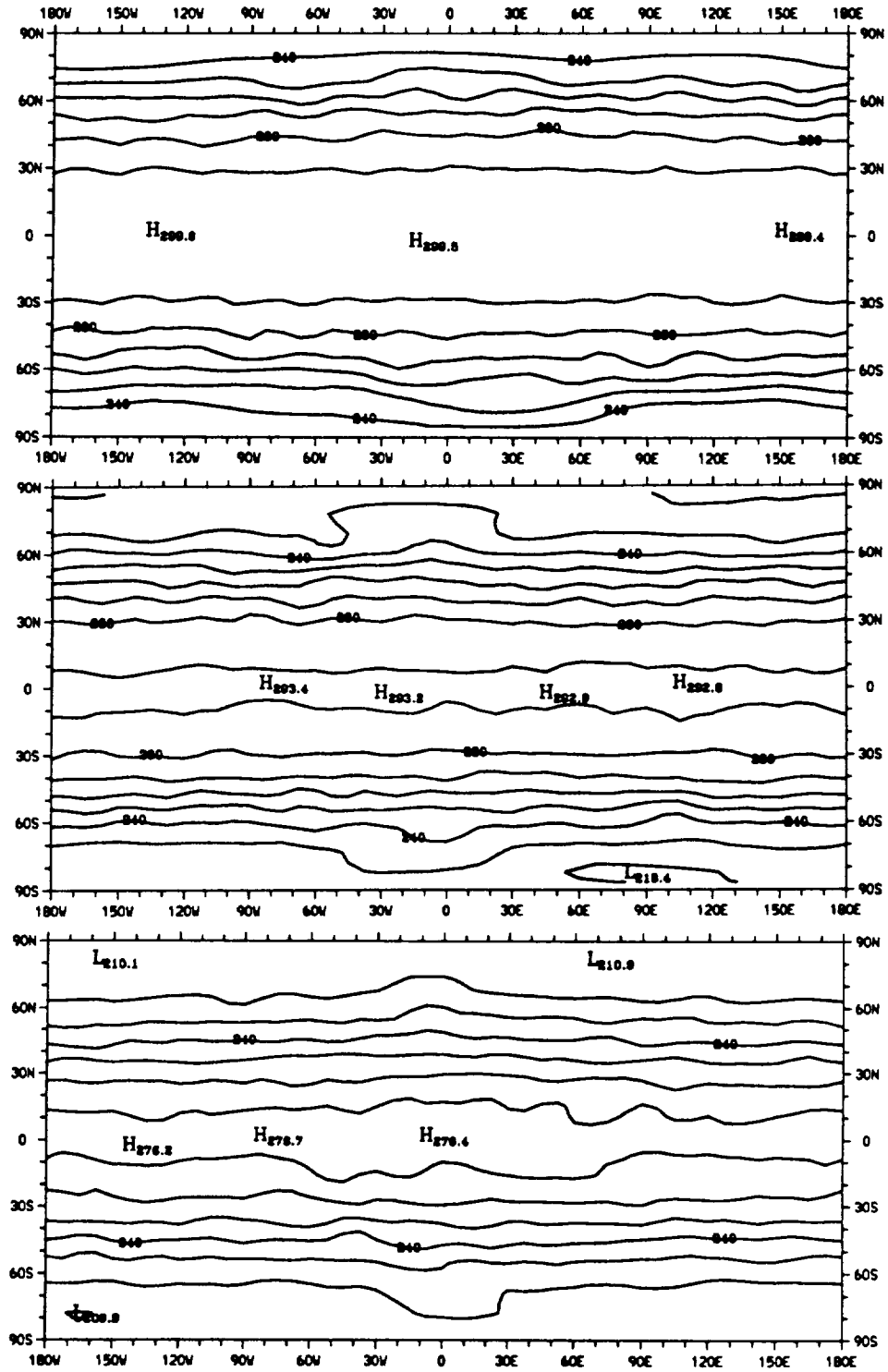
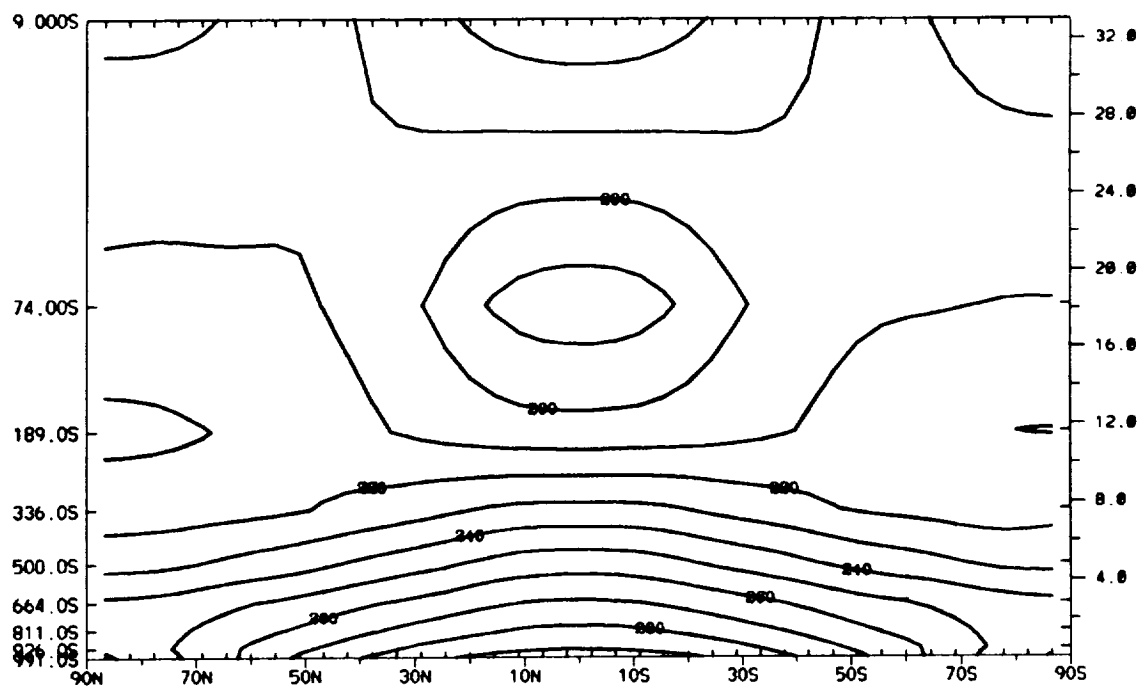
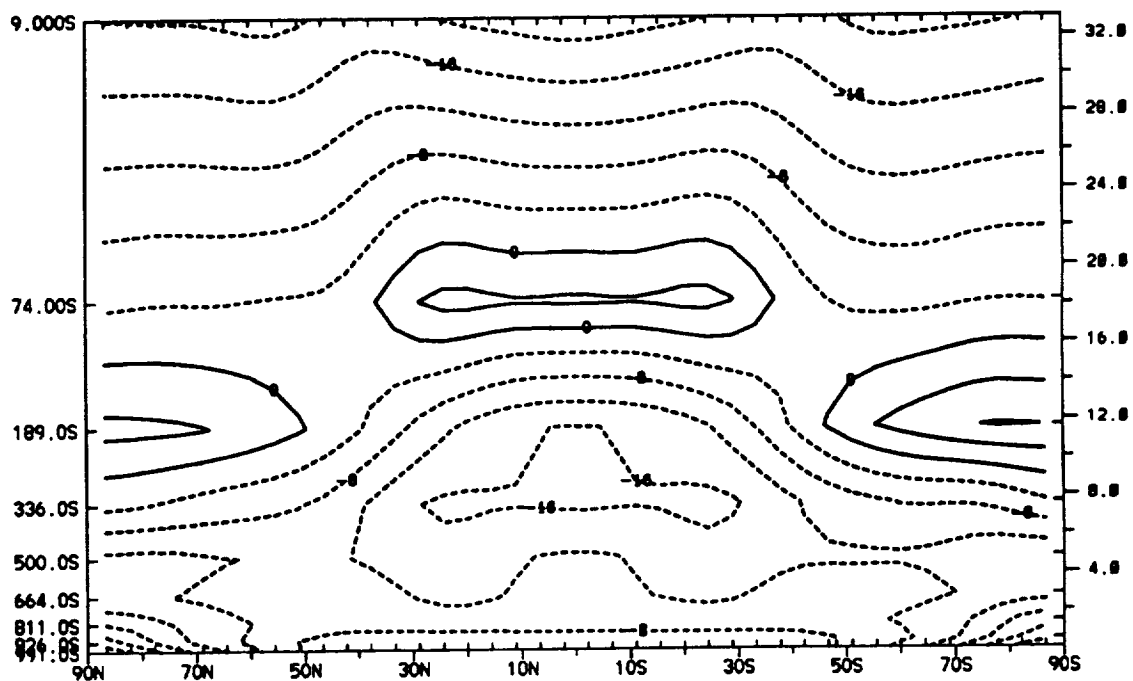


Figure 3.54: Geographical surface temperature: Top: Ice1; middle: Ice2; bottom: Ice3. Units: degrees Kelvin.

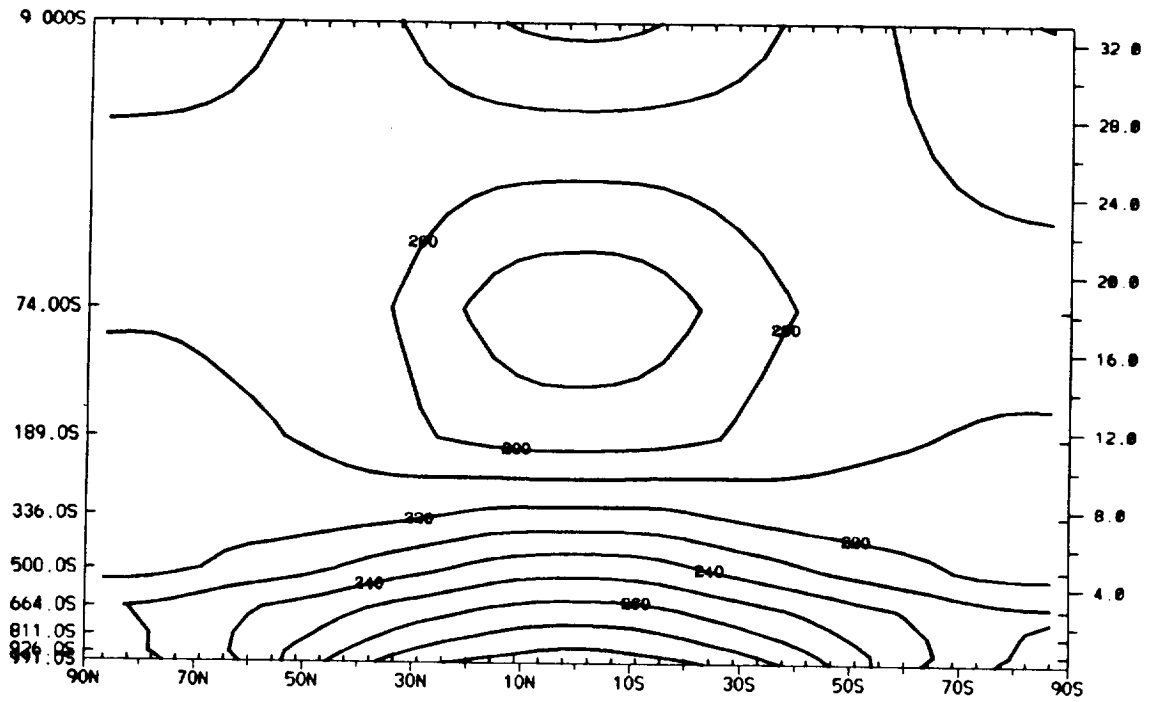


(a) Temperature distribution for Icel. Units: degrees Kelvin.

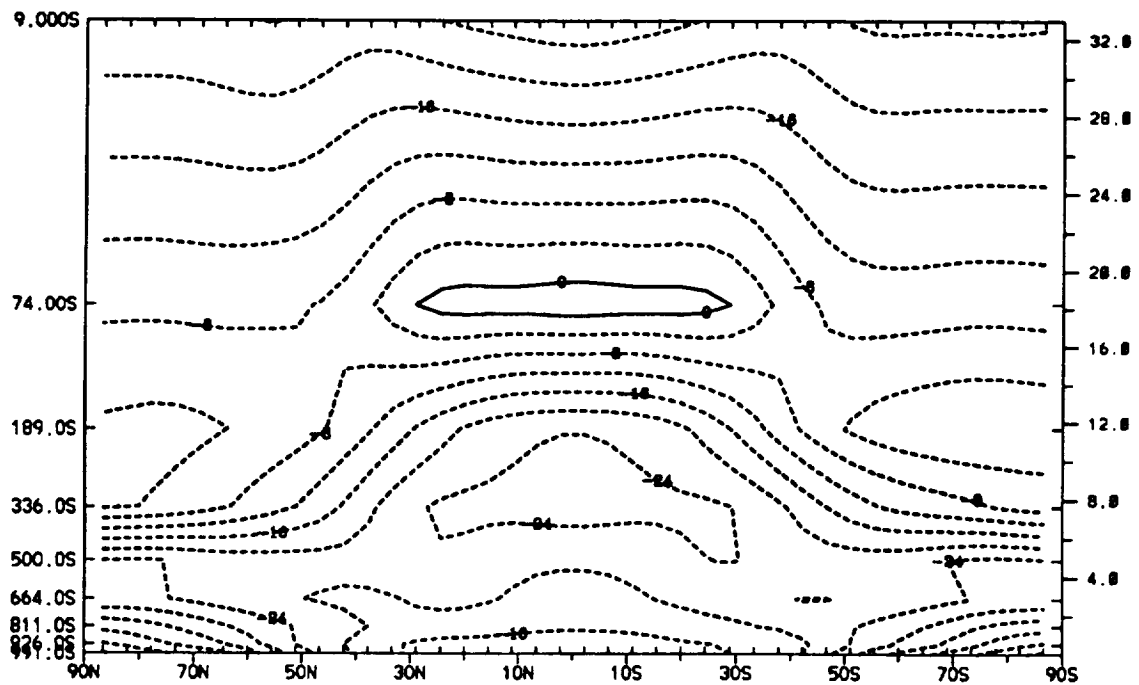


(b) Temperature difference. Icel minus Glocean. Units: degrees Kelvin.

Figure 3.55: Atmospheric temperatures. (a) Icel; (b) temperature differences: Icel minus Glocean. Contour interval: 4 K.

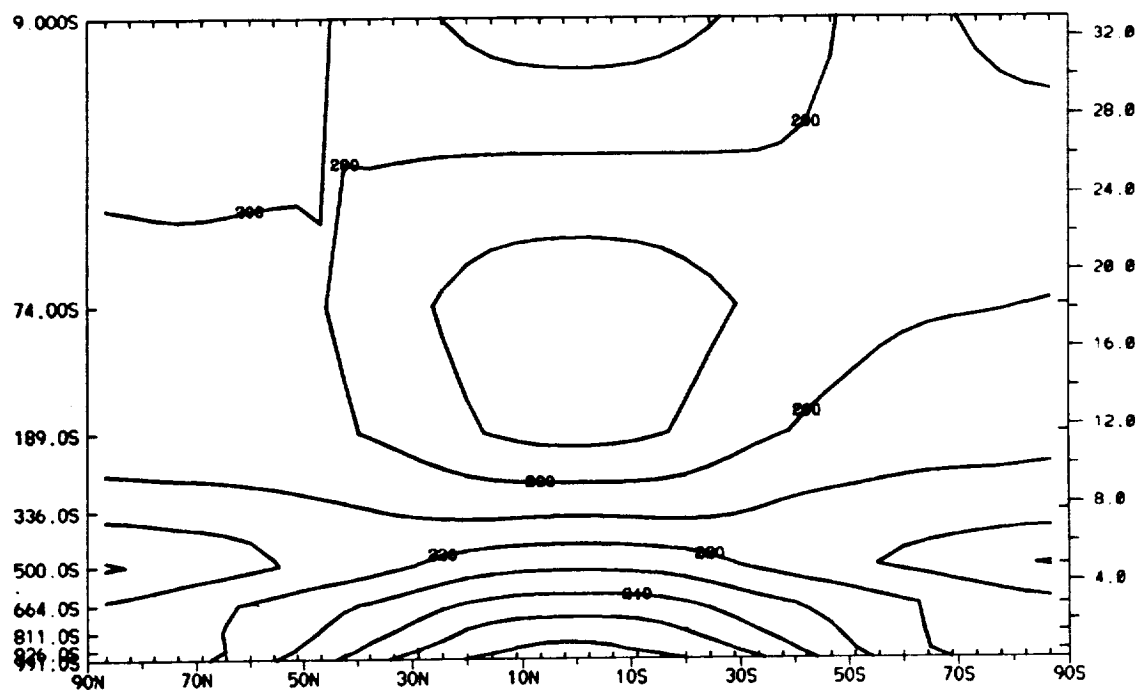


(a) Temperature distribution for Ice2. Units: degree K.

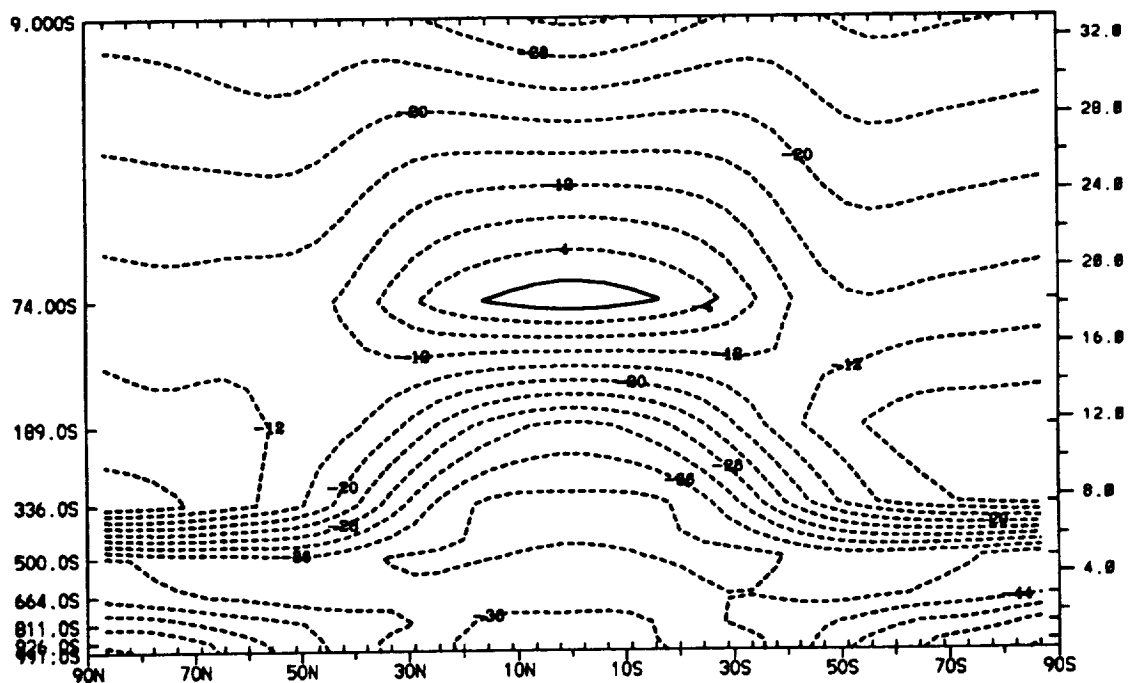


(b) Temperature difference. Ice2 minus Glocean. Units: degree K.

Figure 3.56: Atmospheric temperatures. (a) Ice2; (b) temperature differences: Ice2 minus Glocean. Contour interval: 4 K.



(a) Temperature distribution for Ice3. Units: degrees Kelvin.



(b) Temperature difference. Ice3 minus Glocean. Units: degrees Kelvin.

Figure 3.57: Atmospheric temperatures. (a) Ice3; (b) temperature differences: Ice3 minus Glocean. Contour interval: 4 K.

with Ice3 having sea ice extending nearly to the equator. This equatorward extent of ice causes significant changes in the angular momentum budget, because of the larger surface stress from the sea ice. Ice1 indicates that sea ice extends from the poles down to about 50° , and Ice2 has sea ice extending down to roughly 40° of latitude.

Zonal wind

Weaker westerly jets are noted in each Ice experiment in comparison to the global ocean simulation. The zonal wind for Ice1 and Ice2 is shown in Figure 3.59. Because of the faster rotation rate, the jet core is weaker and confined to lower latitudes for all ice simulations. The jet cores in Ice1 and Ice2 (Figure 3.59) are centered near 25° and near $.189\text{S}$, although Ice2 has an elongated jet core (Figure 3.59b). Equatorial regions display easterlies that extend from the surface into the stratosphere for Ice1 and Ice2. Polar easterlies extend down to the midlatitudes in both simulations.

Ice3 shows three jet cores—two subtropical and one equatorial jet (Figure 3.60) which have similar wind speed of approximately 15 m s^{-1} . In addition, the jet cores are lower in the troposphere and centered between $.336\text{S}$ and $.5\text{S}$. The equatorial jet core is formed from the additional angular momentum that is imparted to the atmosphere from the extensive surface easterlies and the smaller area of surface westerly winds. In equatorial regions, easterly winds blow in the lower troposphere near the surface and above the equatorial tropopause. Polar easterlies extend down to near 40° in both hemispheres, imparting more angular momentum to the atmosphere.

Mean meridional streamfunction

Weaker Hadley cells are confined to equatorial regions with a faster rotation rate, higher CO_2 concentrations, and lower solar-constant values. The Hadley cell is confined to areas equatorward of 20° for Ice1, Ice2, and Ice3 (Figures 3.61 and 3.62).

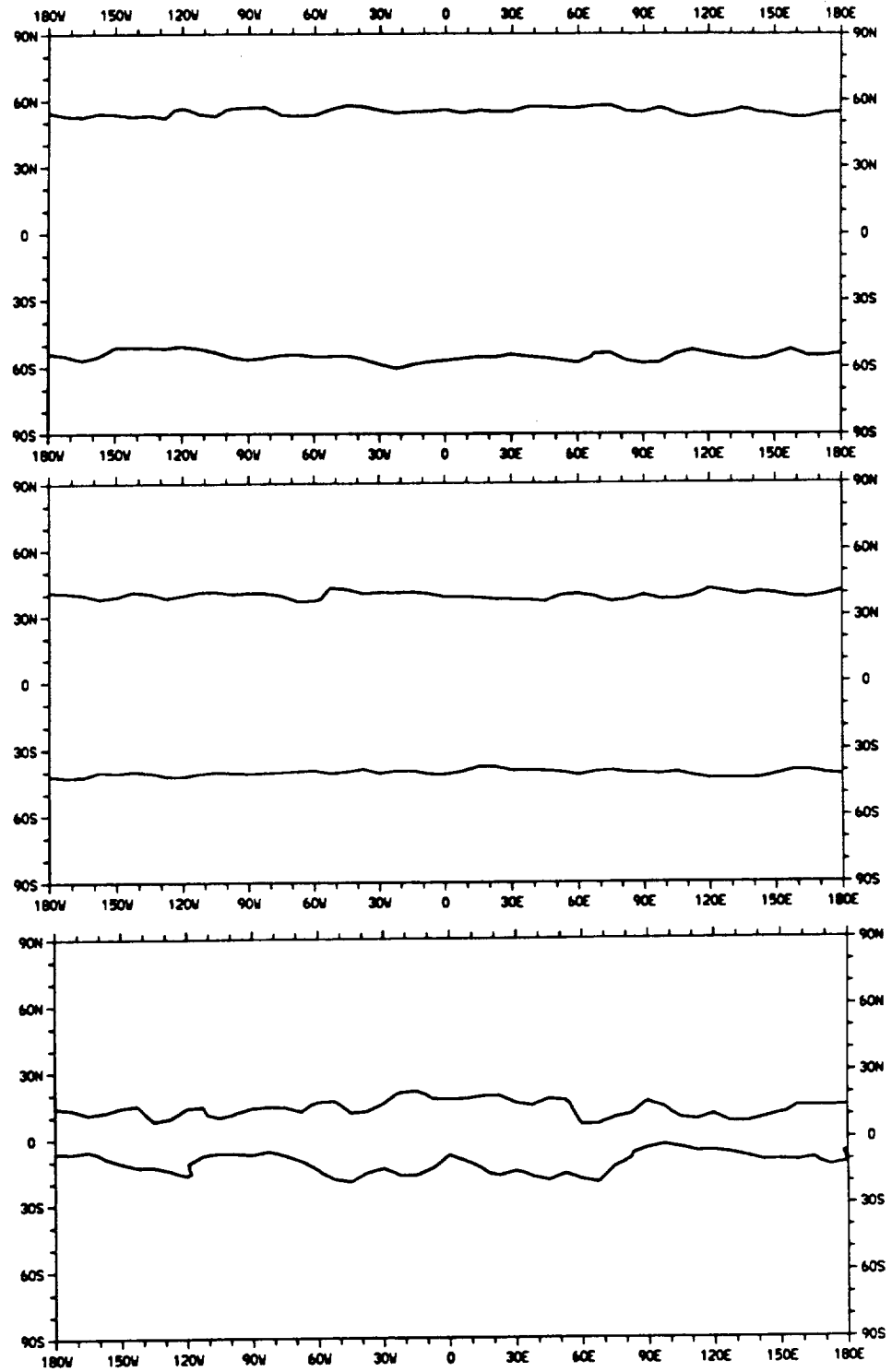
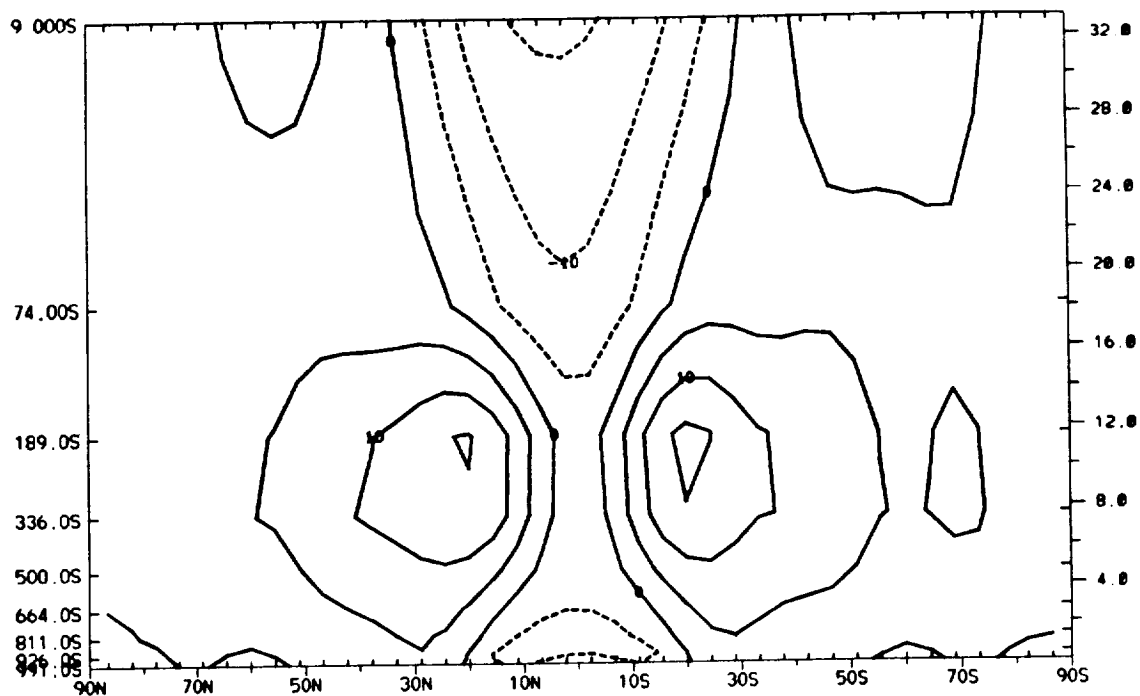
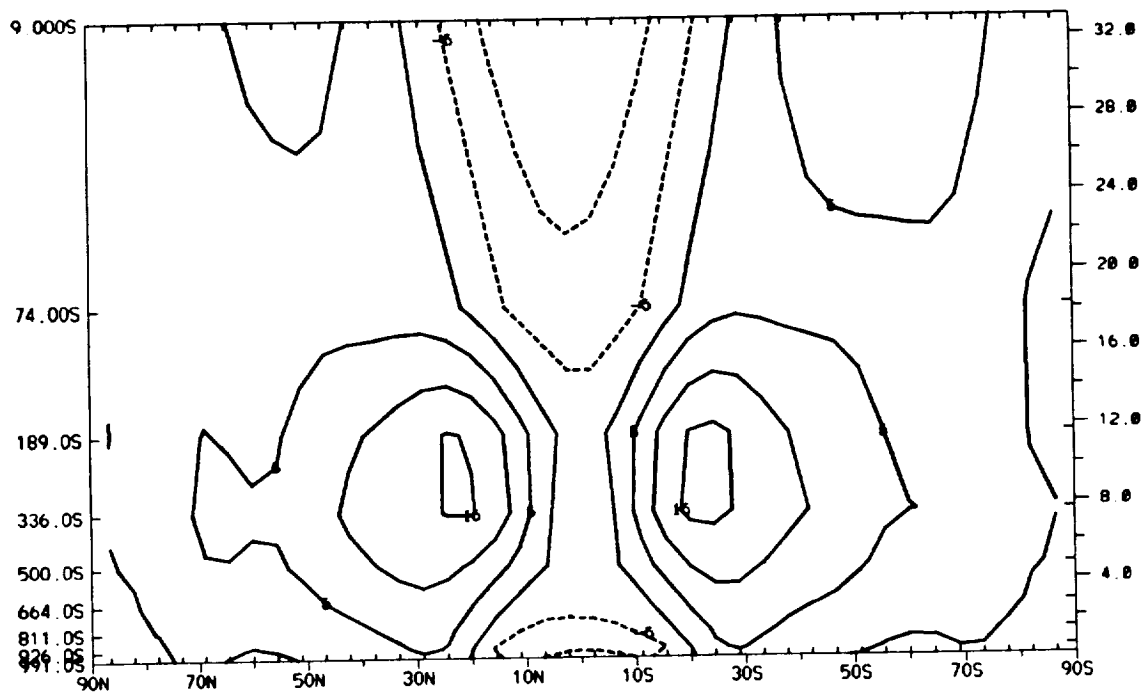


Figure 3.58: Geographical sea ice distribution: Top: Ice1; middle: Ice2; bottom: Ice3. Units: meters



(a) Zonal wind distribution for Ice1. Contour interval: 5 m s^{-1} .



(b) Zonal wind distribution for Ice2. Contour interval: 5 m s^{-1} .

Figure 3.59: Zonal wind distribution: (a) Ice1; (b) Ice2.

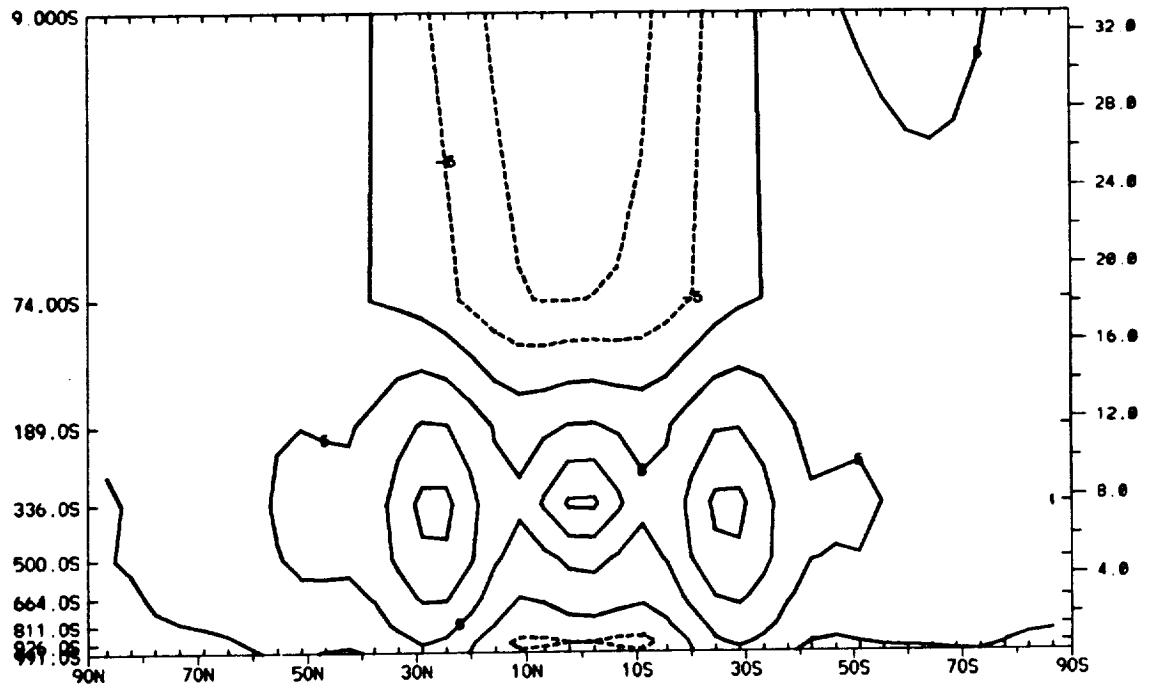


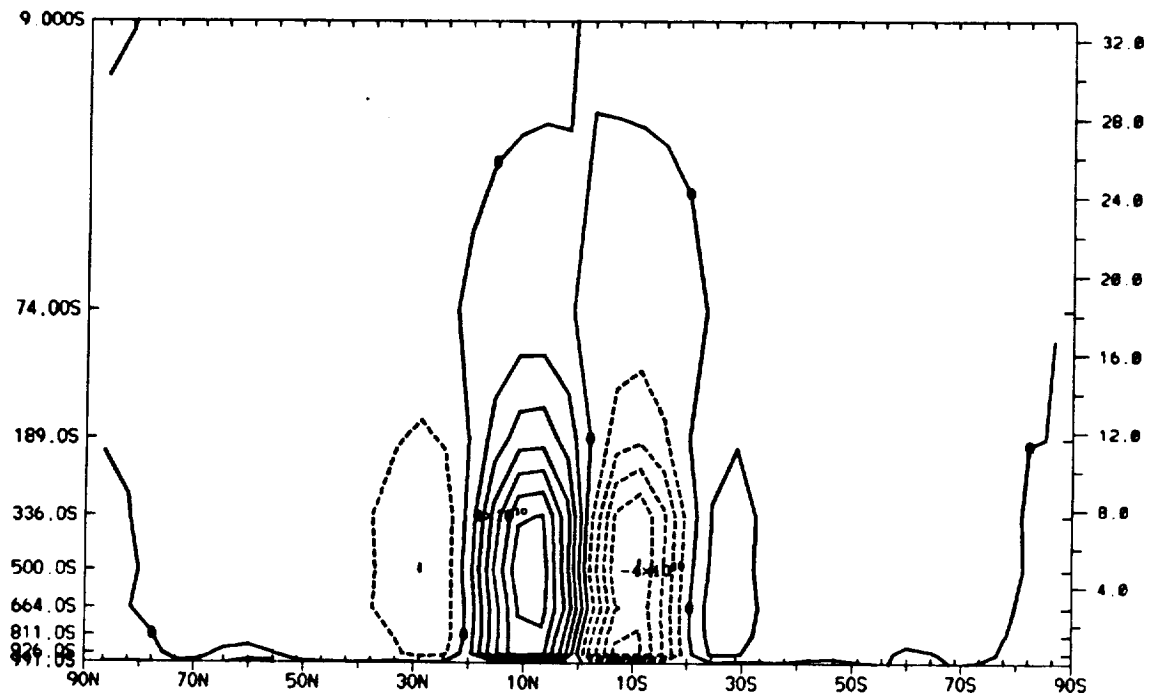
Figure 3.60: Zonal wind distribution. Ice3. Contour interval: 5 m s^{-1} .

The Hadley cell is weakest for Ice3 (Figure 3.62) and is confined to lower altitudes with respect to Ice1 and Ice2 (Figure 3.61). The weaker Hadley cell in Ice3 is caused by smaller surface evaporation (Figure 3.76) in the subtropics that brings moisture to the Hadley cell.

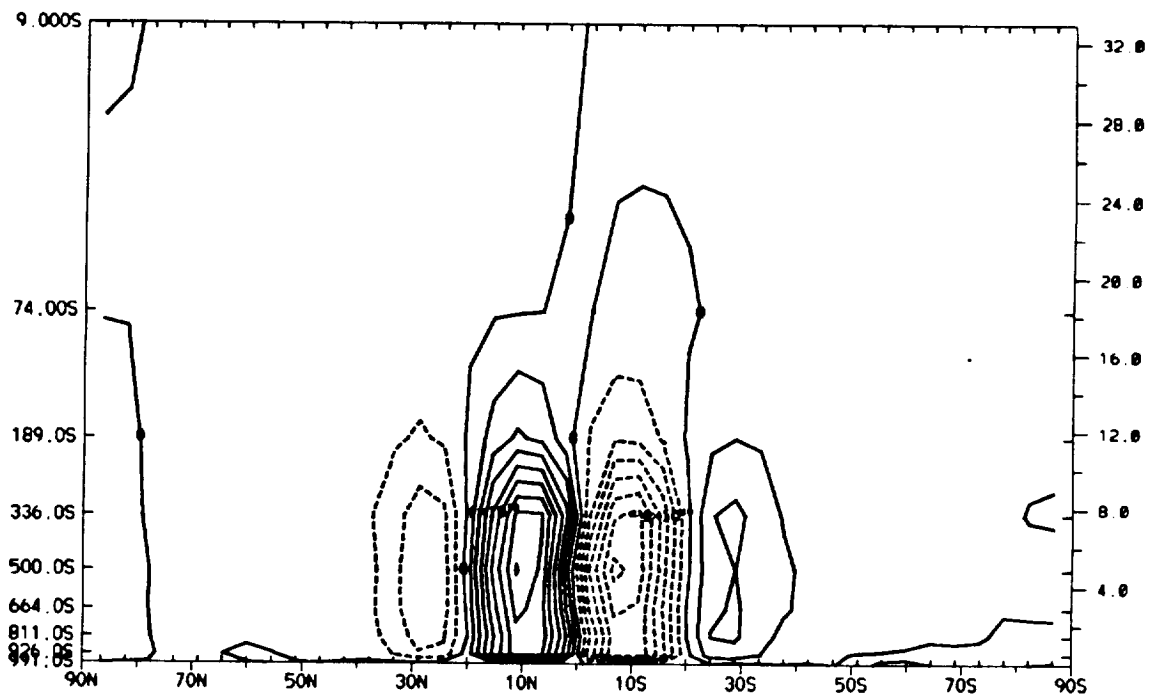
Ice2 has the strongest Hadley and Ferrel cells in comparison to Ice1 and Ice3. The Ferrel cells are confined to lower latitudes and appear to occupy smaller latitudinal areas between 20° and 40° , while in Glocean the Ferrel cell is restricted to areas between 30° and 50° (Figure 3.21a). Cells other than the Hadley and Ferrel cells are not observed for the Ice simulations.

Transient eddy heat transport

Ice1 shows an equatorial shift in the transient heat transport maximum of the upper troposphere (Figure 3.63a). This feature, relates to the equatorial shift in



(a) Meridional streamfunction for Ice1. Contour interval: $1 \times 10^{10} \text{ kg s}^{-1}$.



(b) Meridional streamfunction for Ice2. Contour interval: $1 \times 10^{10} \text{ kg s}^{-1}$.

Figure 3.61: Mean meridional streamfunction: (a) Ice1; (b) Ice2.

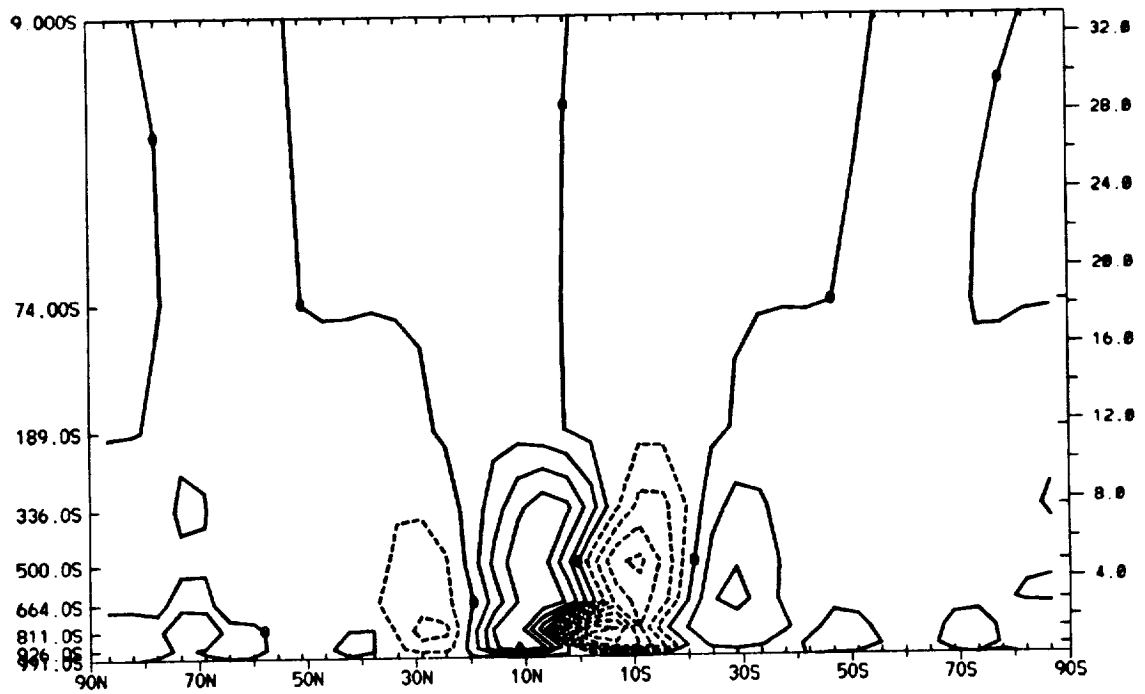
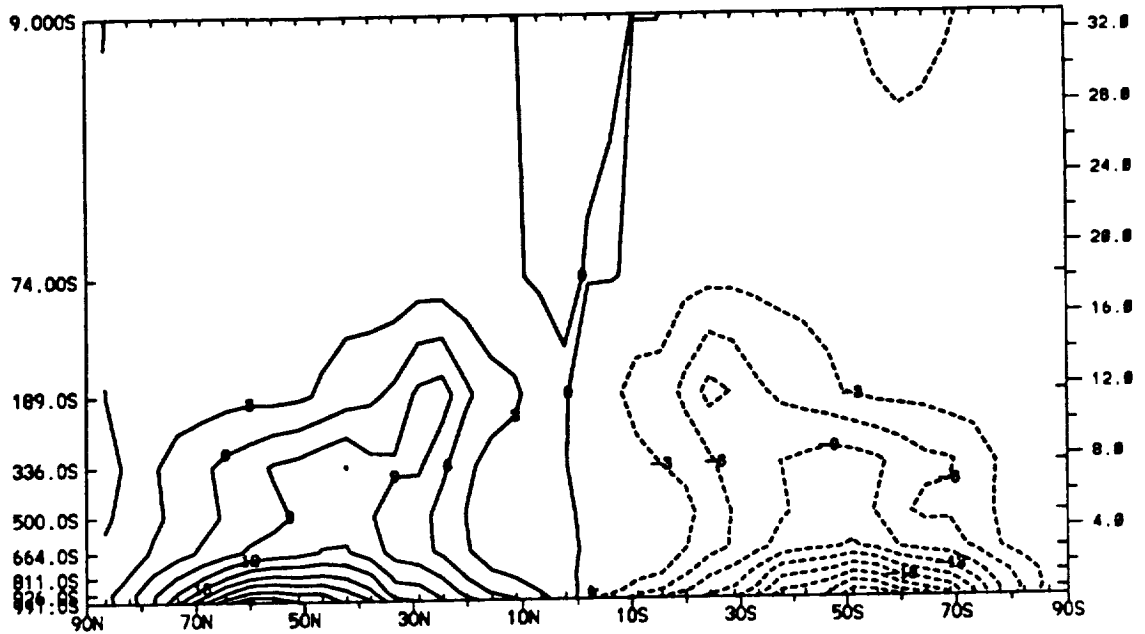


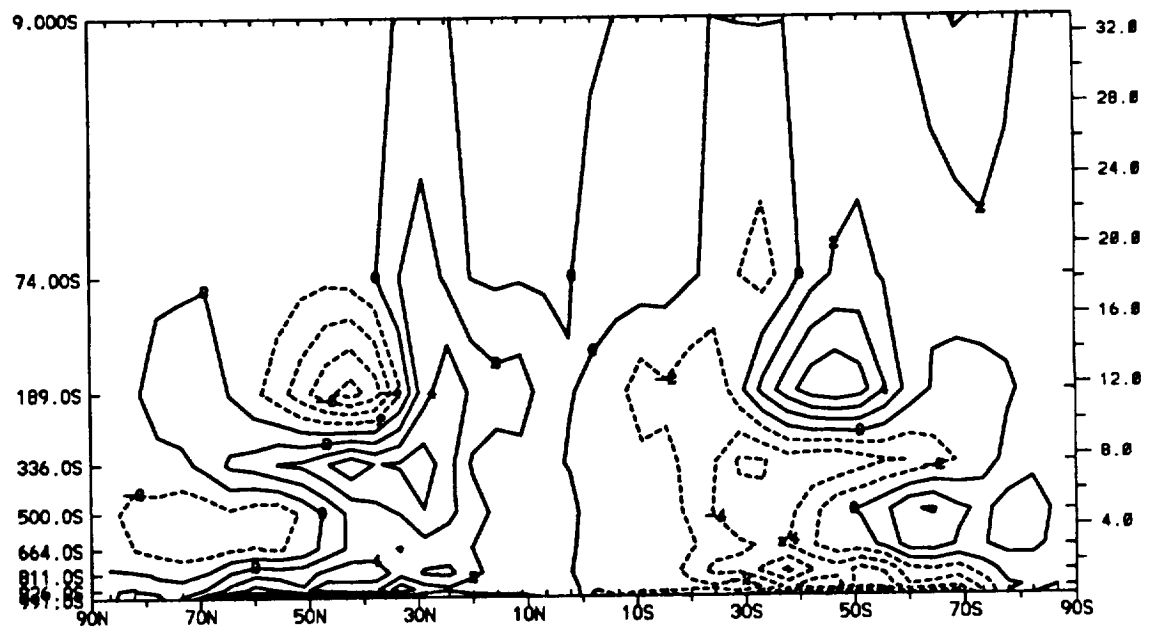
Figure 3.62: Mean meridional streamfunction for Ice3. Contour interval: $1 \times 10^{10} \text{ kg s}^{-1}$.

the Hadley cell when a faster rotation rate is introduced and is shown in other fast-rotation experiments. The shift leads to an increased heat transport near 30° centered near $.336\text{S}$, and a decrease occurs poleward of this position near 50° at $.189\text{S}$ (Figure 3.63b). Ice1 has increased heat transport in the lower troposphere from the equator well into polar regions in both hemispheres, with decreased heat transport in the middle troposphere poleward of 50° (Figure 3.63b). Near the surface, the maximum heat transport occurs near the sea-ice edge.

Ice2 displays an equatorial shift of heat transport in the upper troposphere, with the maximum heat transport in the lower troposphere between 40° and 50° at the surface (Figure 3.64a) which closely corresponds to the sea-ice edge (Figure 3.58). When compared to Glocean, an increase is noted near 30° at $.336\text{S}$ in the middle-to-upper troposphere (Figure 3.64b), while poleward of this region heat transport decreases. In the lower troposphere, heat transport increases equatorward of 65° ,



(a) Transient eddy heat transport for Icel. Contour interval: 3 K m s^{-1} .



(b) Transient heat difference. Icel minus Glocean. Contour interval: 2 K m s^{-1} .

Figure 3.63: Transient eddy heat transport. (a) Icel; (b) difference in heat transport: Icel minus Glocean.

with a decrease poleward of this region.

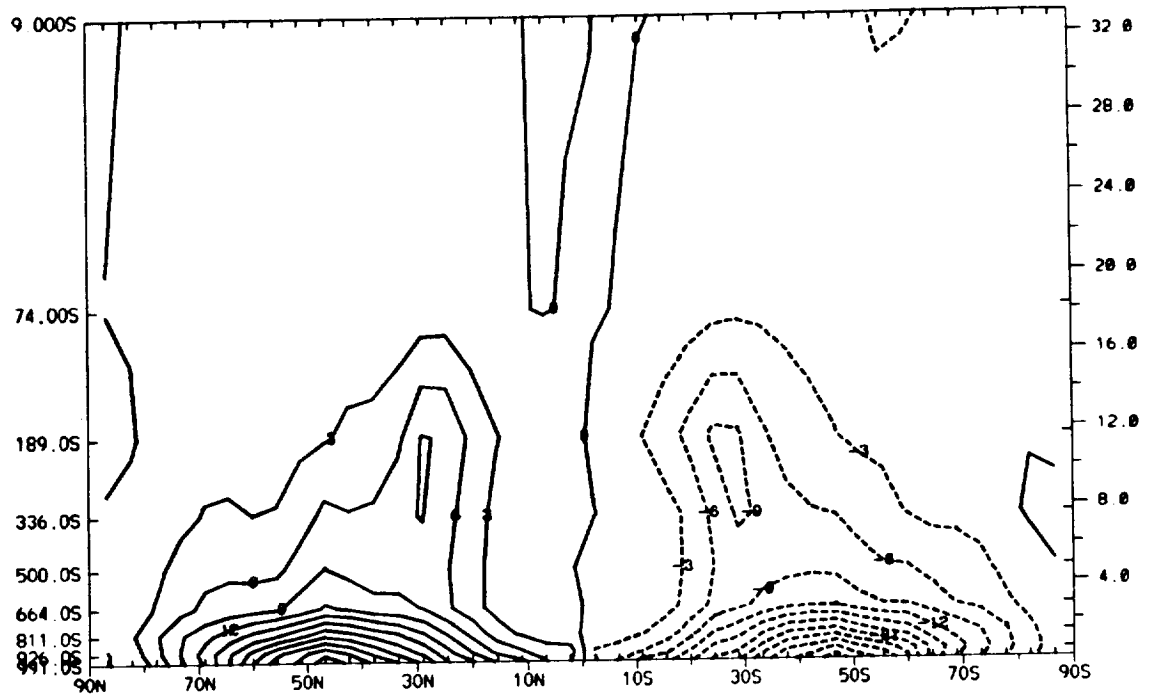
Finally, Ice3 (Figure 3.65a) shows a pattern similar to Ice1 and Ice2, but the maximum heat transport does not correspond to the sea-ice edge. It is located between 30° and 40° , whereas the sea-ice edge is confined to equatorial regions (Figure 3.58). The difference in the transient heat transport between Glocean and Ice3 show that heat transport increases from the equator to near 45°, extending from the surface to the upper troposphere (Figure 3.65b). Poleward of this area, a decrease in heat transport is noted, with the largest decrease at 45° centered near .189S.

Spectral kinetic energy

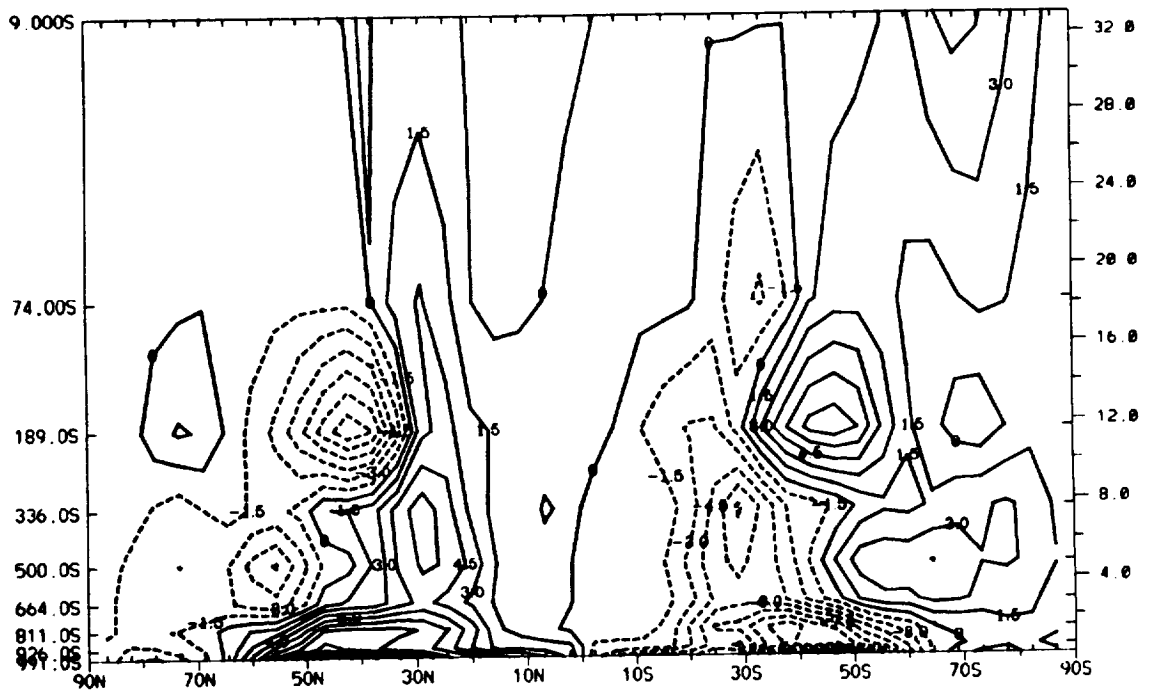
Kinetic energy is displaced into smaller scales with a faster rotation rate, higher CO₂ concentrations, and lower solar constant values. The spectral kinetic energy diagram at .5S is shown in Figures 3.66 and 3.67. As with all of the faster rotation-rate simulations, Ice1, Ice2, and Ice3 show a spectral peak near wavenumber 15 which represents the small-sized eddies associated with a faster rotation rate. All three simulations show similar trends, although Ice3 shows smaller kinetic energy at wavenumber 3.

Clouds

Zonally averaged total clouds decrease with a faster rotation rate, higher CO₂ concentrations, and lower solar constant values. A major decrease in zonally averaged clouds is noted for Ice1, Ice2, and Ice3 in areas poleward of 45° relative to Glocean (Figure 3.68). A decrease in clouds is noted near the equator because of smaller atmospheric water-vapor amounts (Figures 3.73 and 3.74). When the rotation rate

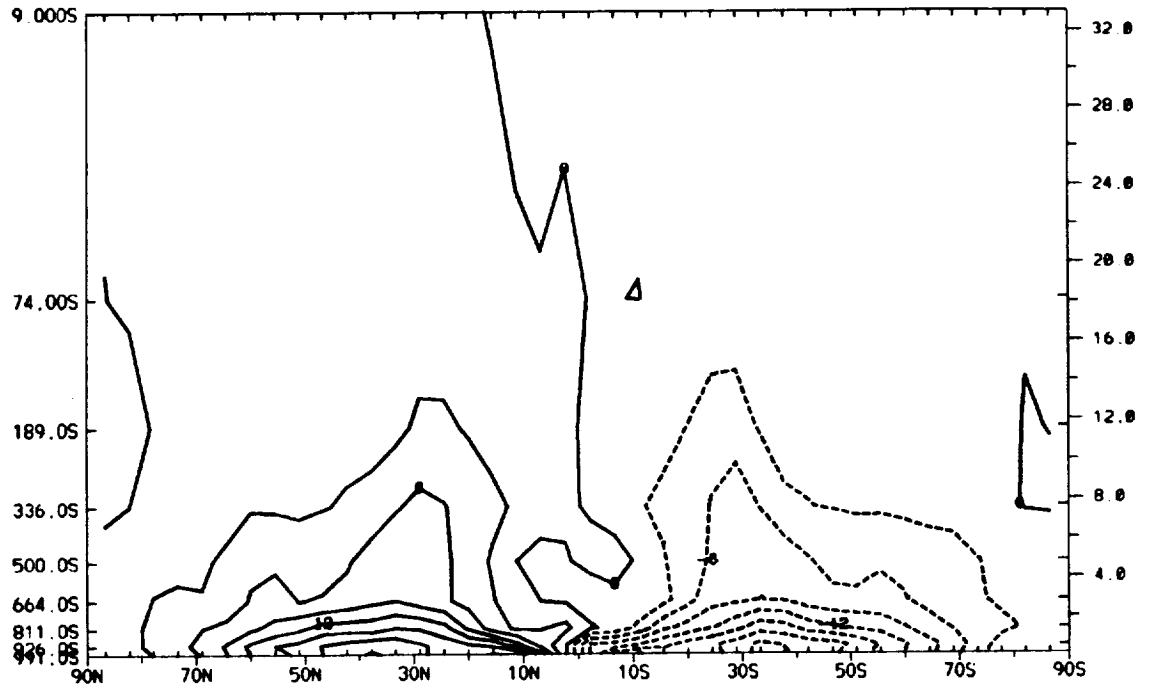


(a) Transient eddy heat transport for Ice2. Contour interval: 3 K m s^{-1} .

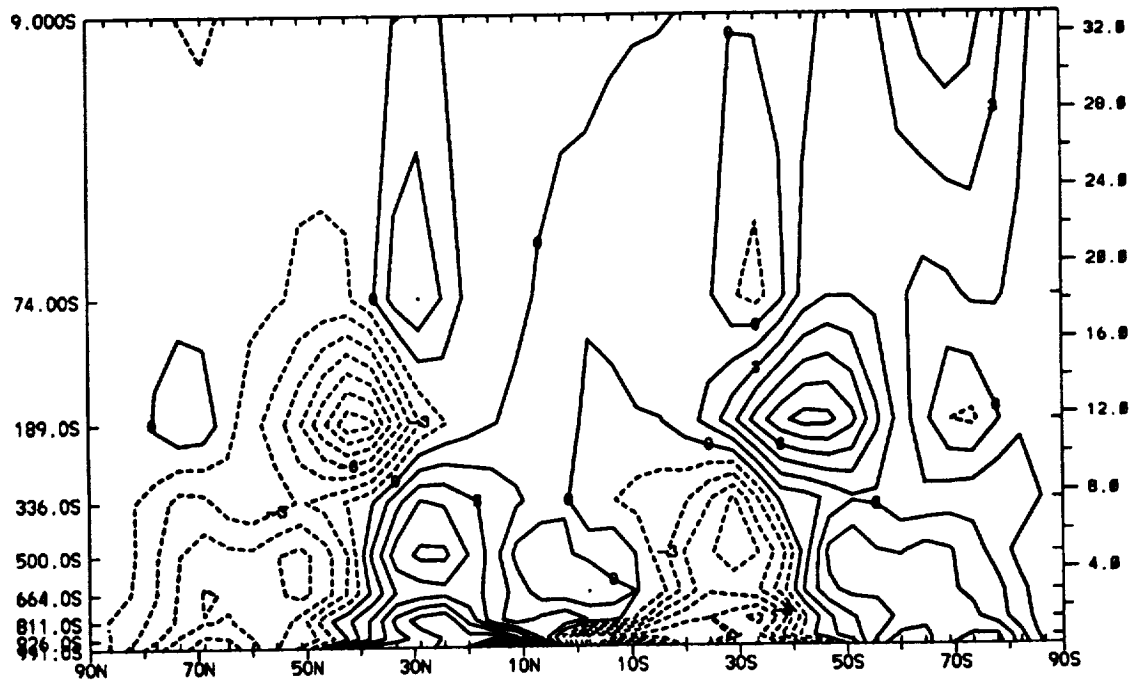


(b) Transient heat difference. Ice2 minus Glocean. Contour interval: 1.5 K m s^{-1} .

Figure 3.64: Transient eddy heat transport. (a) Ice2; (b) difference in heat transport: Ice2 minus Glocean.

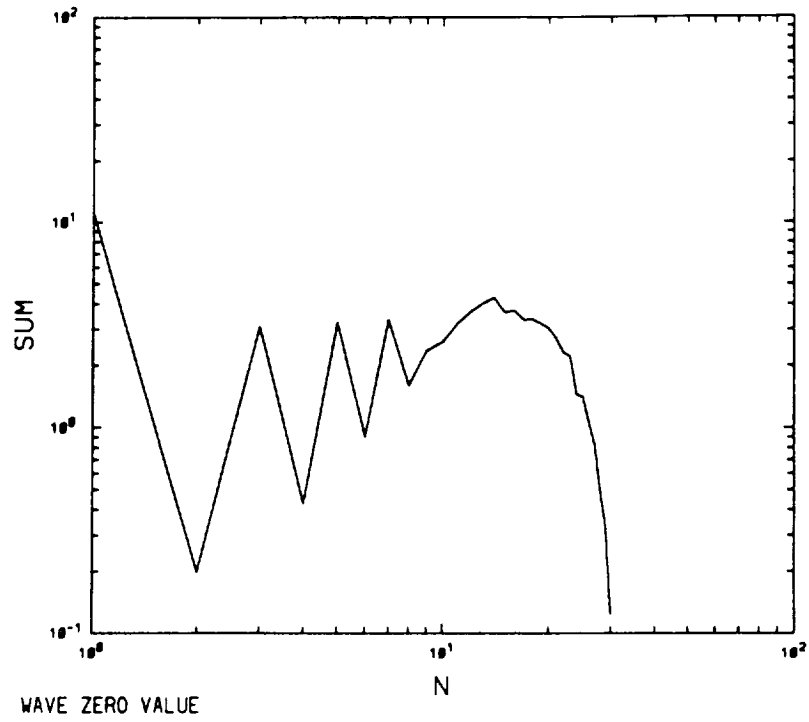


(a) Transient eddy heat transport for Ice3. Contour interval: 3 K m s^{-1} .

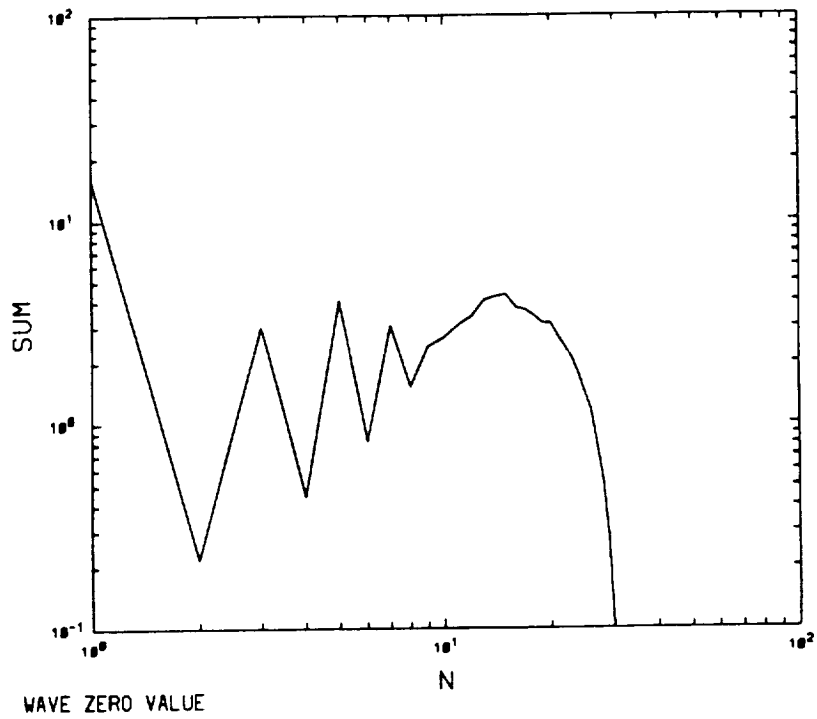


(b) Transient heat difference. Ice3 minus Glocean. Contour interval: 1.5 K m s^{-1} .

Figure 3.65: Transient eddy heat transport. (a) Ice3; (b) difference in heat transport: Ice3 minus Glocean.



(a) Ice1.



(b) Ice2.

Figure 3.66: Spectral kinetic energy. (a) Ice1; (b) Ice2. Units: J kg^{-1} .

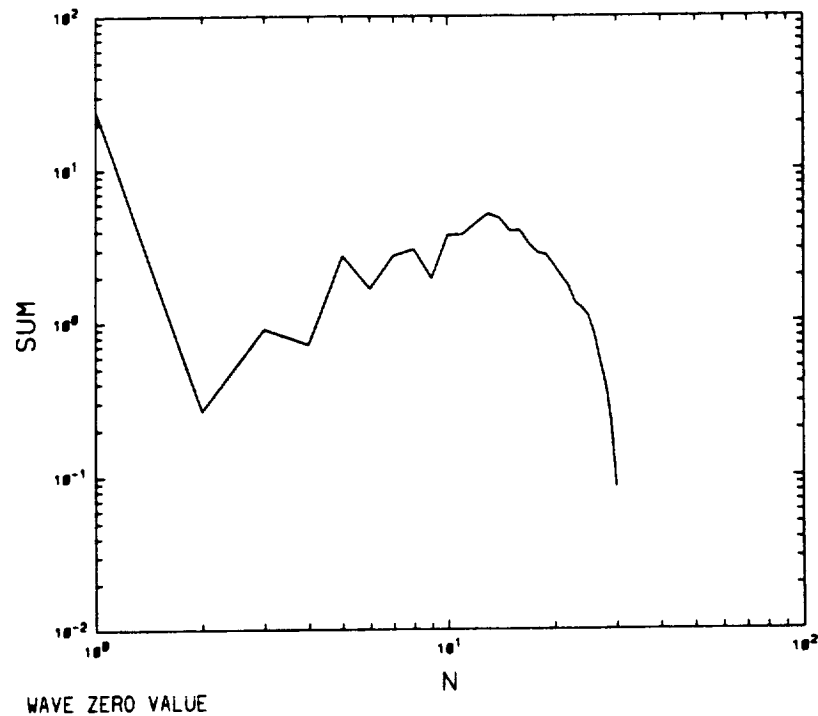


Figure 3.67: Spectral kinetic energy. Ice3. Units: J kg^{-1} .

is increased, clouds increase for Ice2 and Ice3 in the subtropics due to the equatorial shift in the Hadley cell.

The differences in the latitude-height cloud distribution display a decrease in clouds at most latitudes because of decreased relative humidity for the three simulations (Figures 3.71 and 3.72). The much colder atmosphere (Figures 3.55–3.57) has a lower saturation-vapor pressure which should lead to increased relative humidity. However, the water-vapor pressure of the atmosphere for Ice1, Ice2 and Ice3 also significantly decreases (Figures 3.73 and 3.74). Therefore, relative humidity is controlled by water-vapor amounts and not by its temperature-dependency. The lower relative humidities inhibit the formation of clouds with only areas of cloud increase in the three simulations centered near 30° , as a consequence of rising motions in the Ice experiments in contrast to the sinking motions at the poleward-edge of the Hadley cell in Glocean.

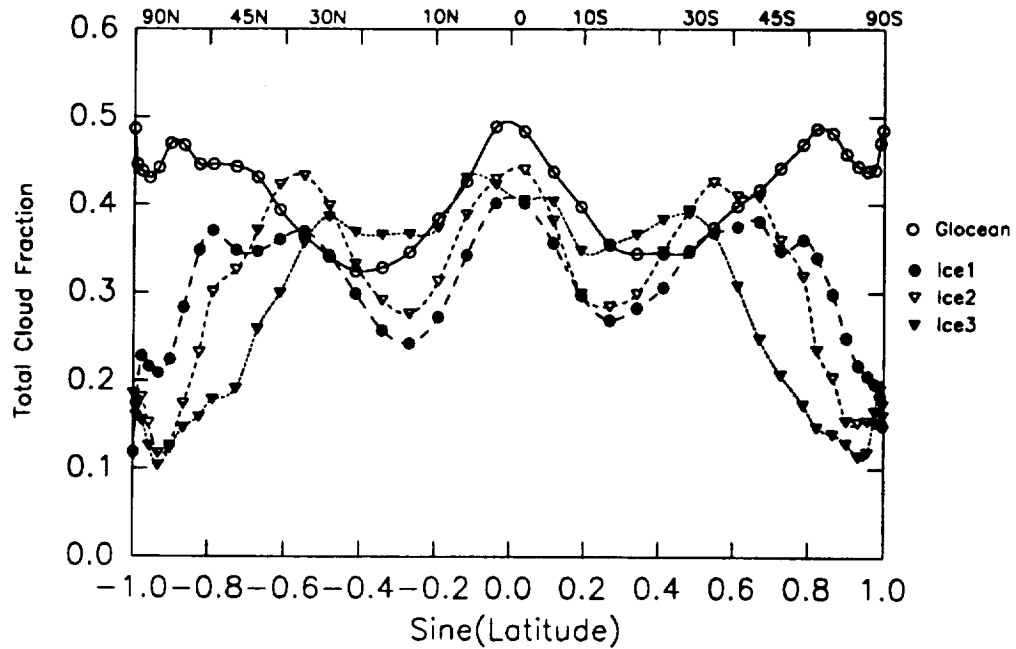


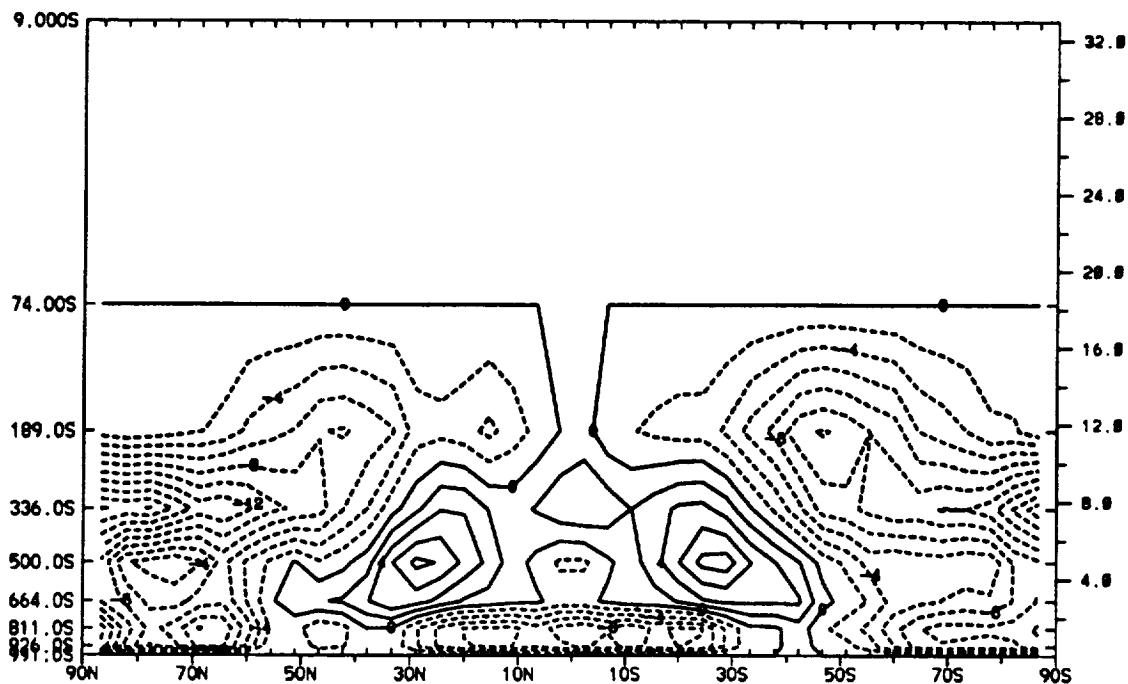
Figure 3.68: Zonally averaged cloud field.

Precipitation

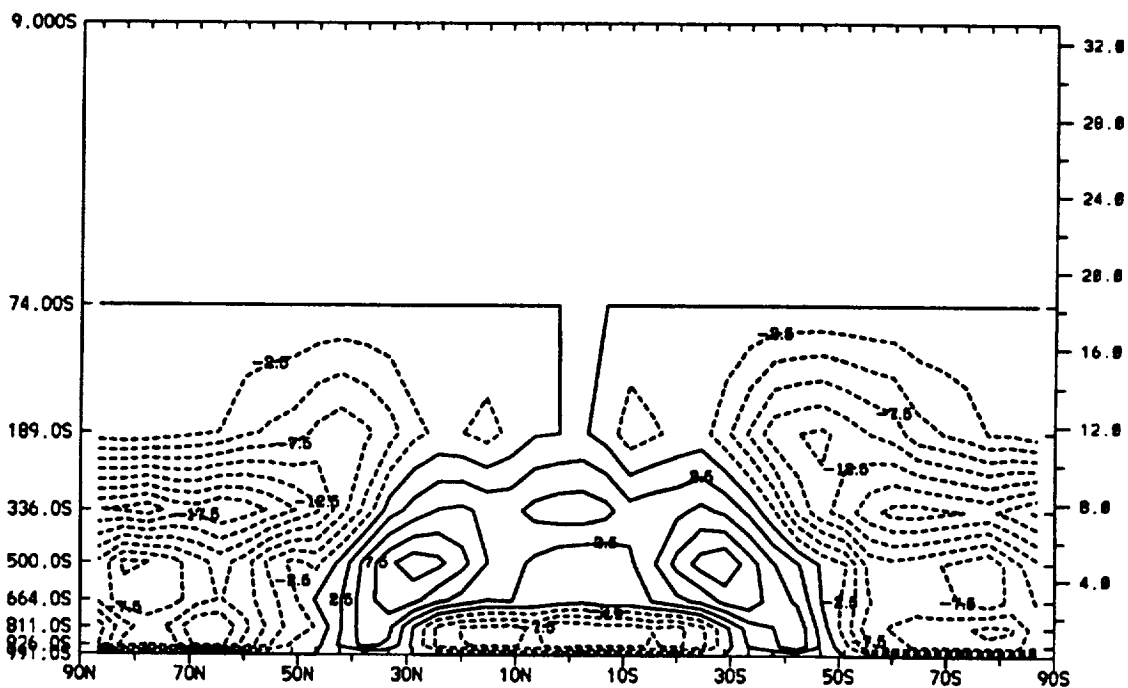
Precipitation is significantly reduced with faster rotation rates, higher CO_2 concentrations, and lower solar constant values (Figure 3.75). Ice1 and Ice2 show increased precipitation in subtropical regions due to an equatorial shift in the baroclinic zone. Ice3 shows a major reduction in precipitation, which is reflected in the global mean of precipitation rates (Table 3.4).

Evaporation

As with the precipitation field, zonally averaged evaporation decreases significantly when solar luminosity is reduced (Figure 3.76). The largest changes in evaporation occur for Ice3, where the sea ice extends down to near the equator (Figure 3.58). The primary reason for the decreased evaporation is the large reduction of

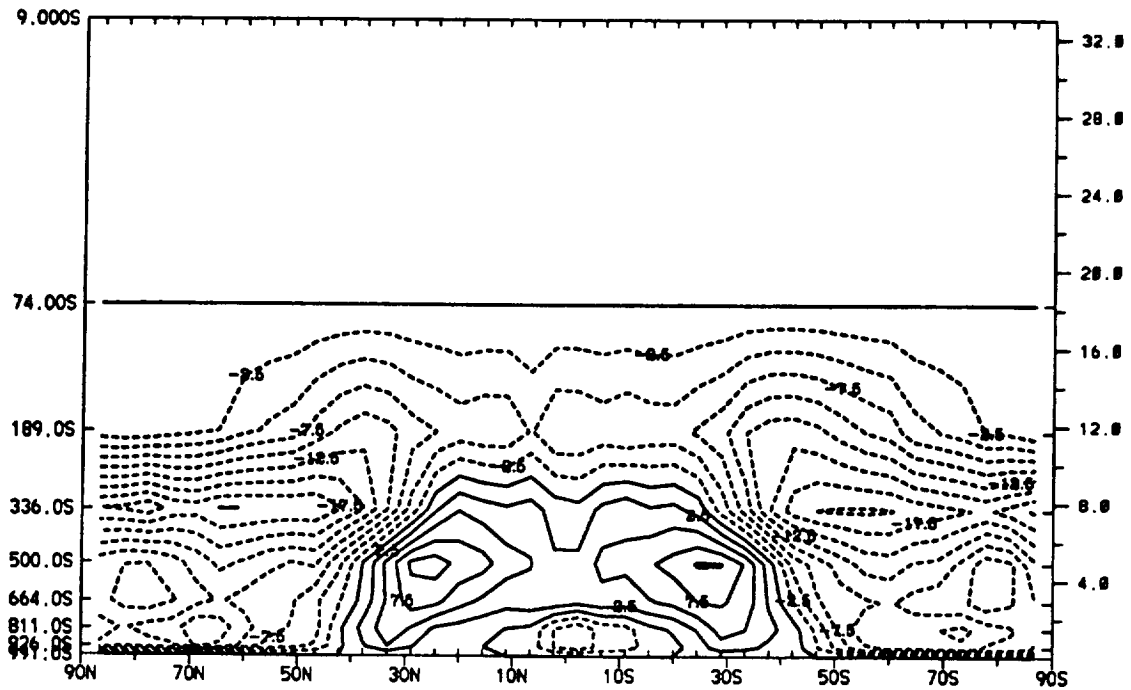


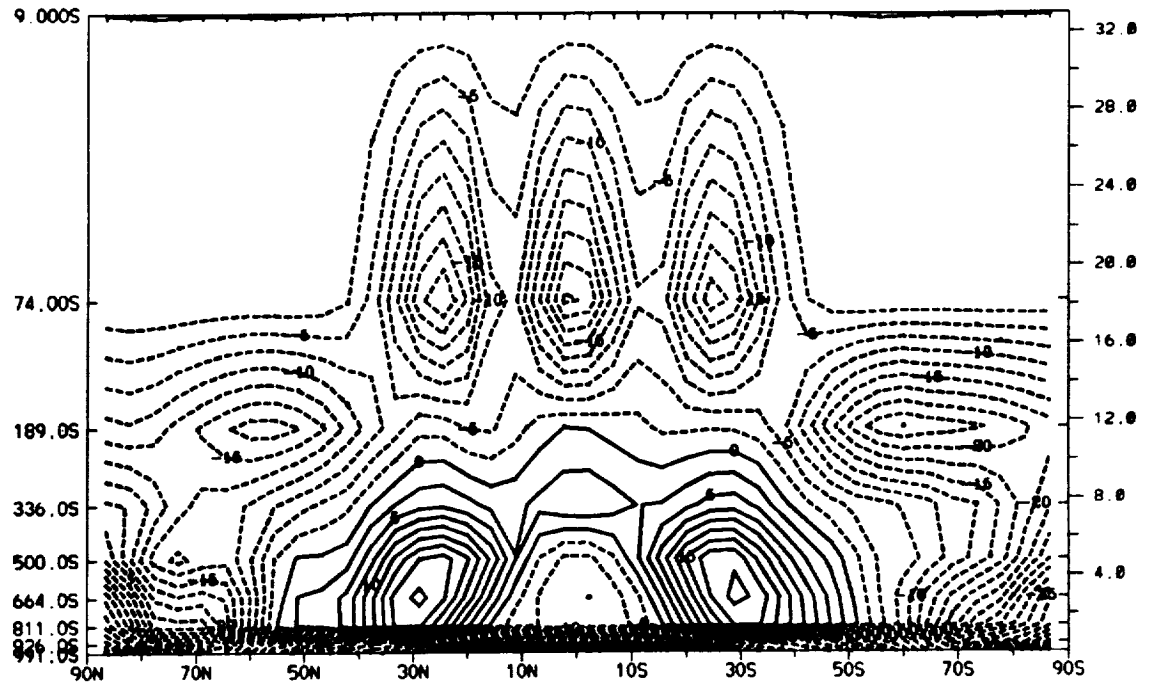
(a) Cloud field difference. Icel minus Glocean. Units: percent.



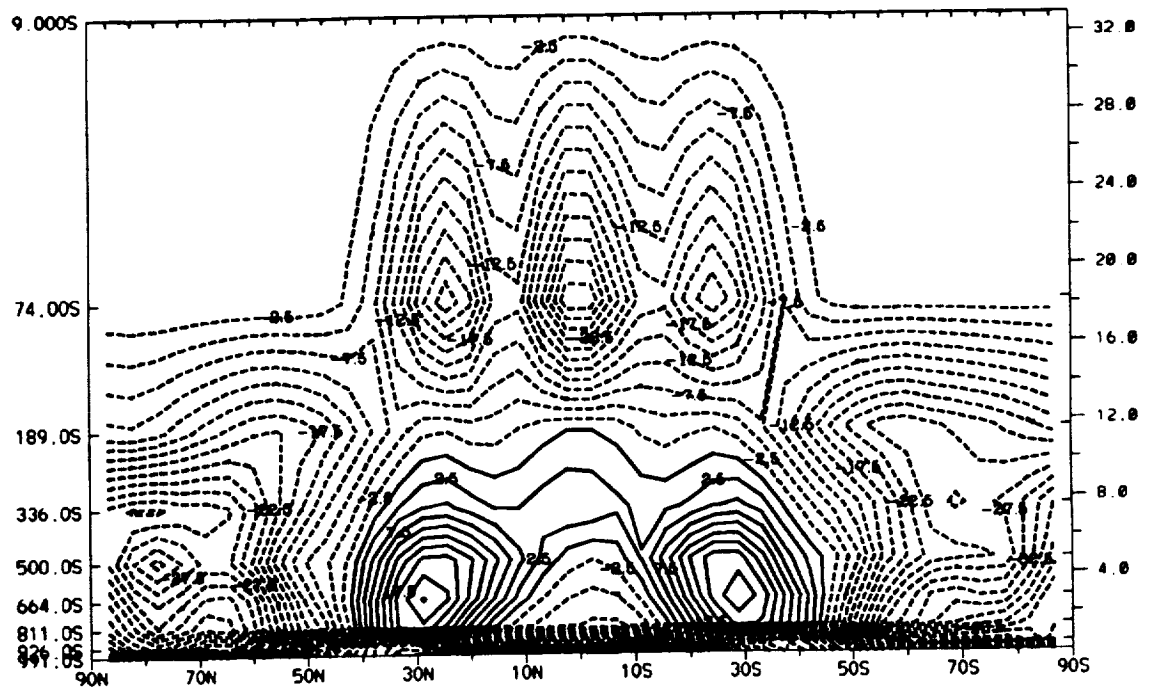
(b) Cloud field difference. Ice2 minus Glocean. Units: percent.

Figure 3.69: Latitude-height difference in clouds. (a) Icel minus Glocean; (b) Ice2 minus Glocean.





(a) Relative humidity difference. Icel minus Glocean. Units: percent.



(b) Relative humidity difference. Ice2 minus Glocean. Units: percent.

Figure 3.71: Latitude-height difference of relative humidity. (a) Icel minus Glocean; (b) Ice2 minus Glocean.

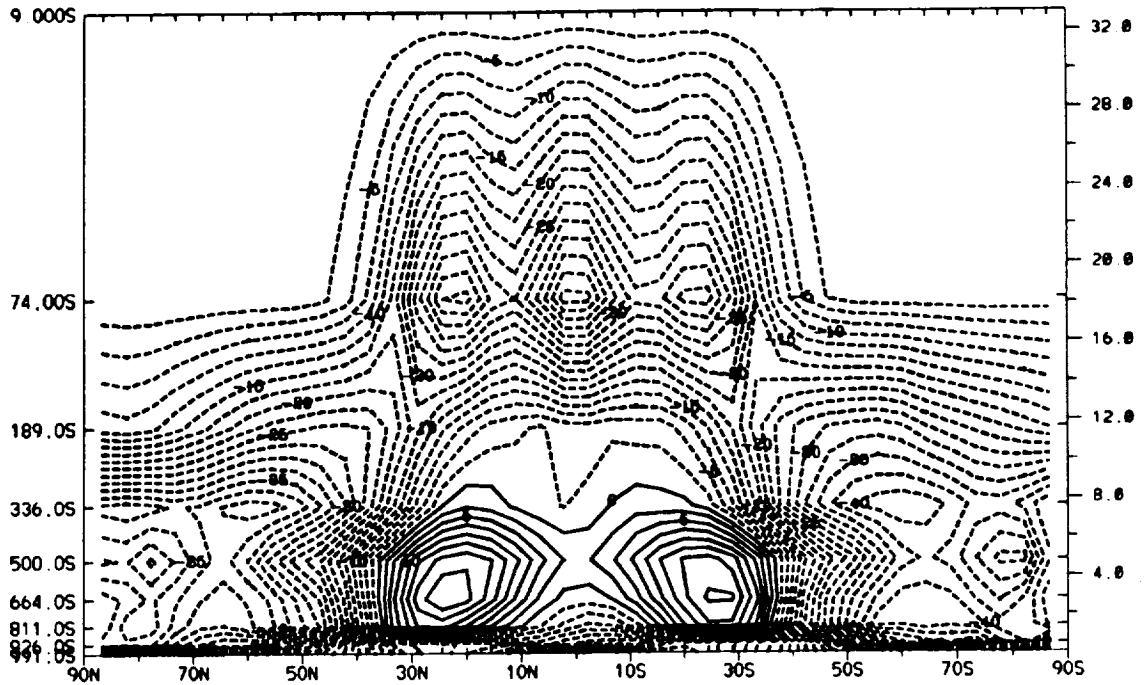
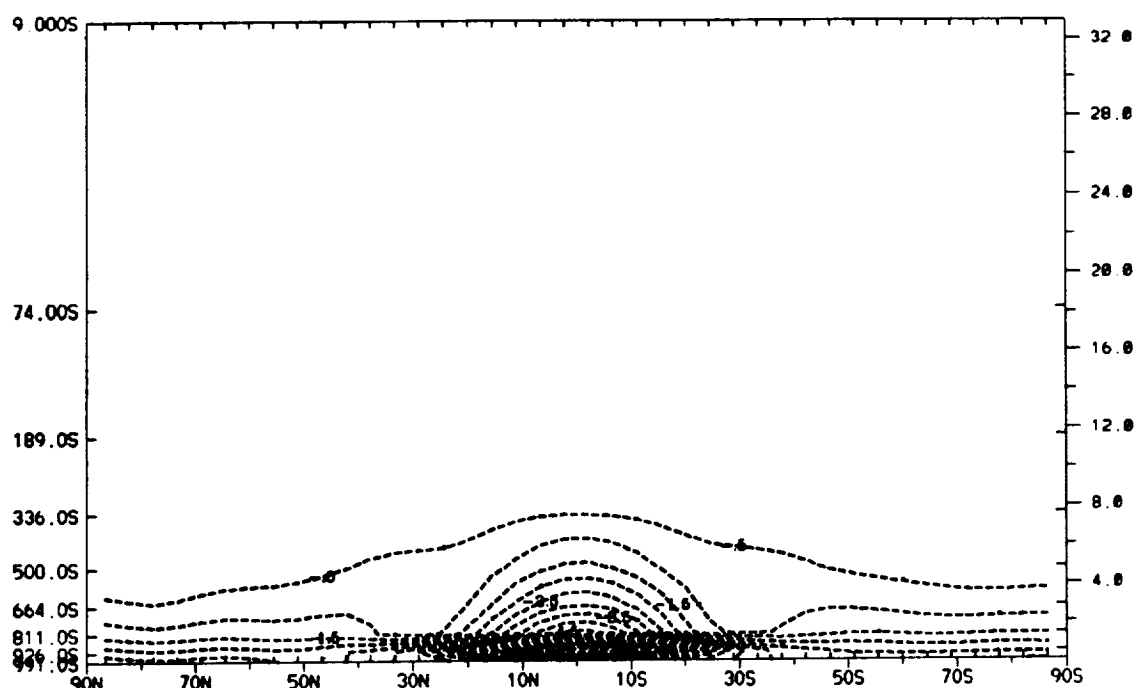


Figure 3.72: Latitude-height difference in relative humidity. Ice3 minus Glocean. Units: percent

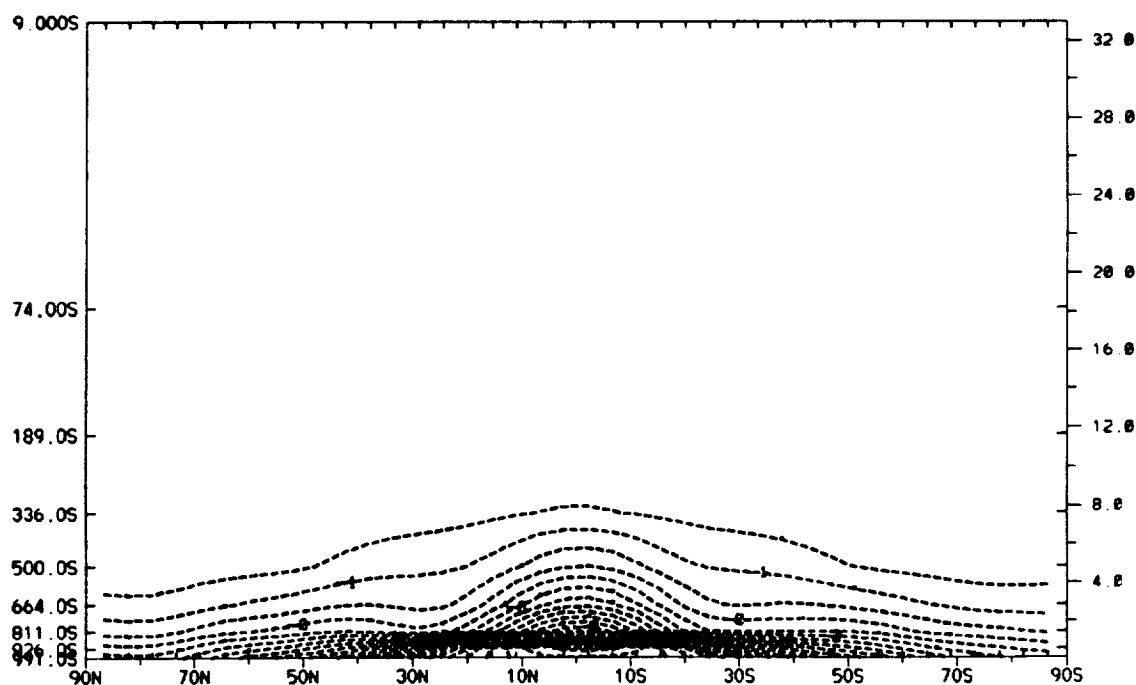
along with the higher surface albedo.

Outgoing longwave radiation

Decreasing solar luminosity requires that less radiation leave the earth's atmosphere (Figure 3.78). The reduction is primarily caused by colder surface and atmospheric temperatures and larger CO_2 concentrations for Ice1, Ice2, and Ice3 (Figure 3.53). The factors that keep the OLR larger than if there were no other feedbacks include less water vapor (Figures 3.73 and 3.74) and smaller cloud amounts (Figure 3.68).



(a) Mixing-ratio difference. Icel minus Glocean. Units: g kg^{-1} .



(b) Mixing-ratio difference. Ice2 minus Glocean. Units: g kg^{-1} .

Figure 3.73: Latitude-height difference of mixing ratio. (a) Icel minus Glocean; (b) Ice2 minus Glocean.

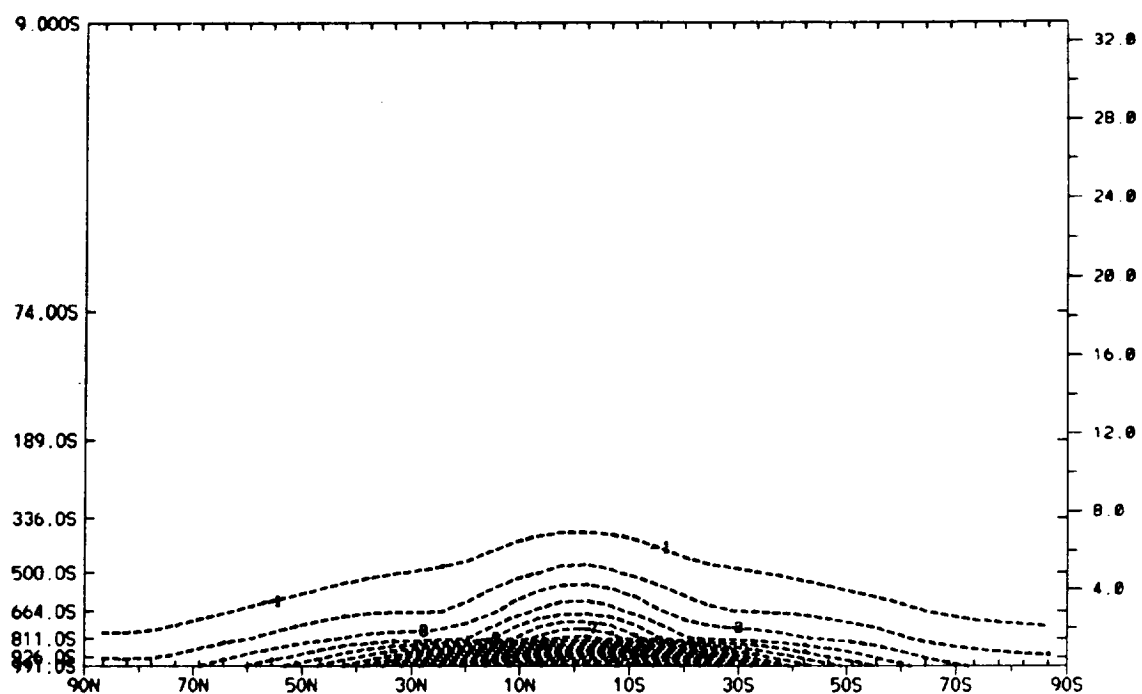


Figure 3.74: Latitude-height difference in mixing ratio. Ice3 minus Glocean. Units: g kg^{-1} .

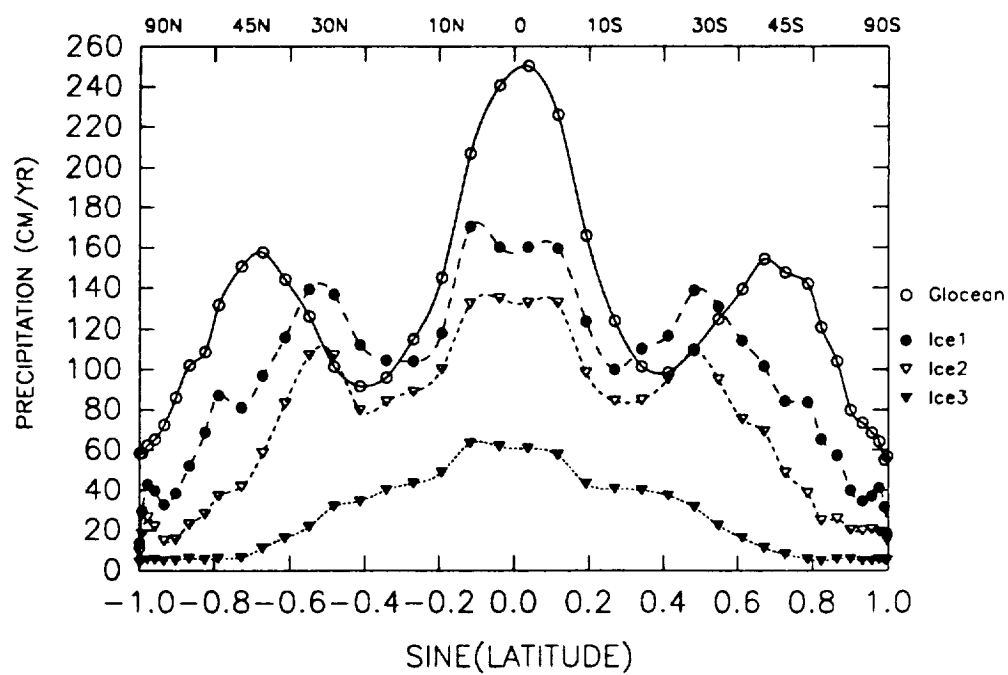


Figure 3.75: Precipitation. Units: cm yr^{-1} .

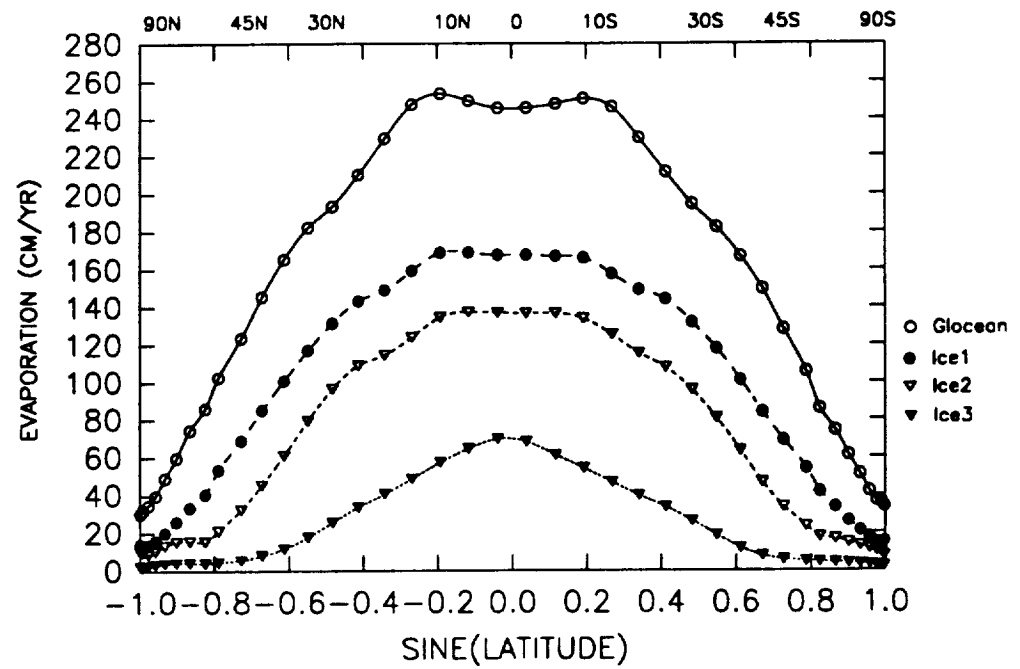


Figure 3.76: Surface evaporation. Units: cm yr⁻¹.

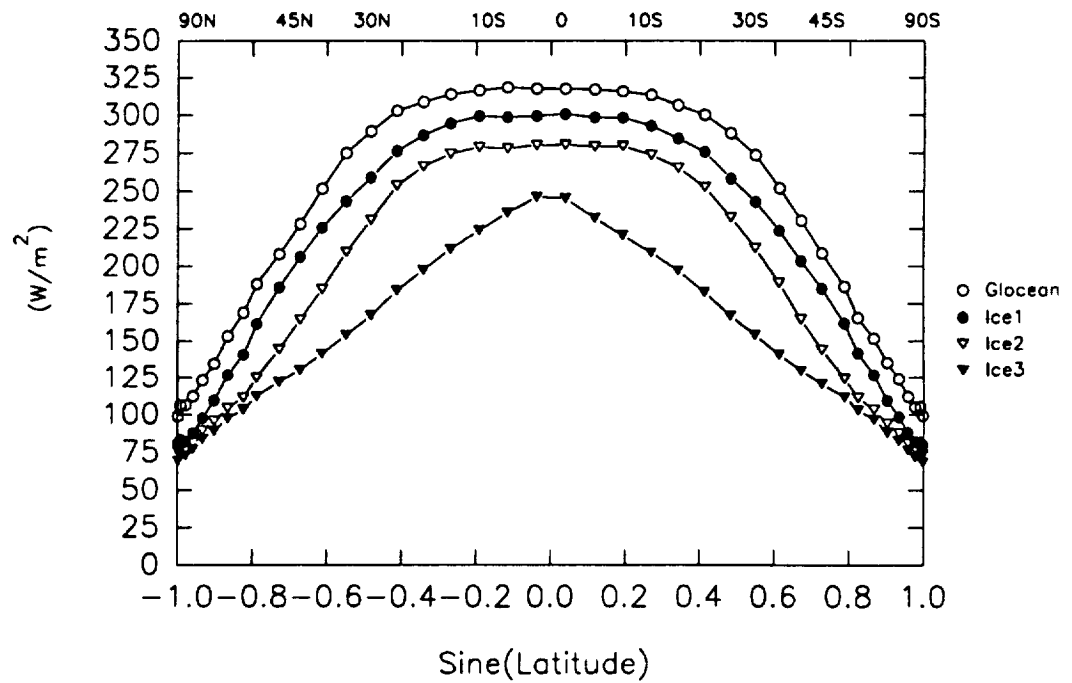


Figure 3.77: Absorbed solar radiation. Units: W m⁻².

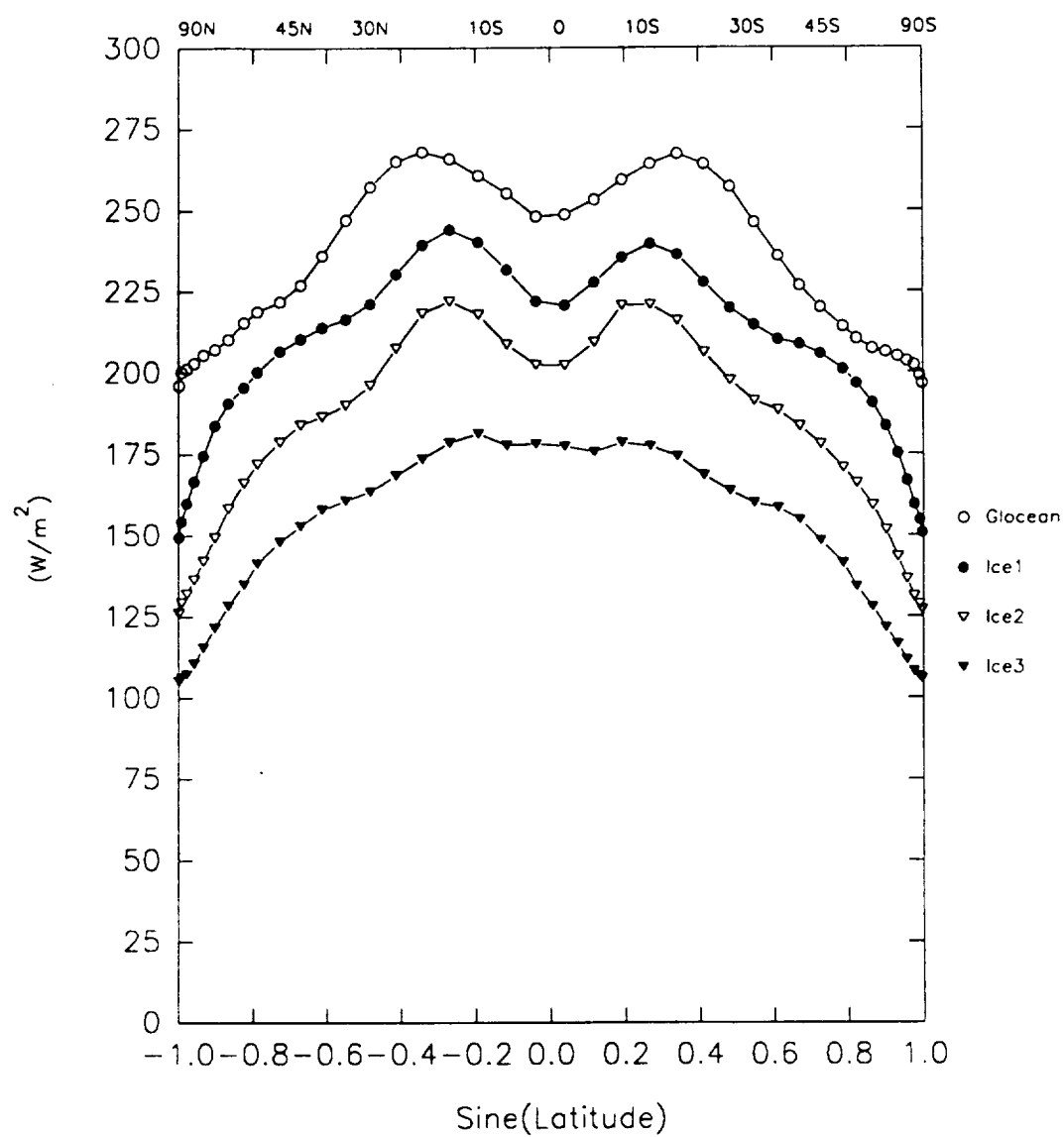


Figure 3.78: Outgoing longwave radiation. Units: $W m^{-2}$.

CHAPTER IV

DISCUSSION

By means of nine simulations and a control experiment we explored the climate of the early earth. The simulations include several geophysical factors that may have played a crucial role in the climate of the Archean (2.5 to 3.8 Ga)—rotation rate of the earth, land fraction, CO₂ concentrations, and solar luminosity. In the simulations we, first considered each factor separately and then their combined effects. In the following sections we discuss the results from the simulations and their implications for the Archean climate.

4.1 Rotation Rate

In section 3.2, the role of a faster rotation rate under present-day climate conditions was examined. Present-day topography, continental distribution, and solar luminosity were assumed. In sections 3.3 and 3.4 the role of a faster rotation rate under different solar forcing and zero land fraction was explored. The rotation rate was equal to a 14-hr earth day in all experiments.

Earlier studies by Hunt (1979) and Williams (1988) used a GCM. Hunt used a hemispheric GCM with no topography, fixed surface albedo, clouds, ozone, and water vapor. Williams, on the other hand, used a global GCM with a swamp surface that

had no continents, no topography, no ice-albedo feedback, and fixed clouds. Hunt (1979) assumed a rotation rate of 5 times the present (which corresponds to a 5-hr earth day and, therefore, does not have much relevance to the Archean) (Figure 1.7). Williams (1988) assumed a rotation rate of 2 times the present (which corresponds to approximately a 12-hr day). This value is within reasonable limits for the early Archean. Using an EBM, Kuhn et al. (1989) considered the influence of a faster rotation rate by parameterizing the heat transport as a function of the Coriolis parameter, thereby taking into account the change of rotation rate over geologic time.

A faster rotation rate in all simulations of this study creates: (1) cooler polar temperatures and a steeper temperature gradient in middle and high latitudes, (2) a shift of kinetic energy out to smaller wavelengths, (3) an equatorial shift in the Hadley Cell, (4) a decrease in clouds, and (5) an equatorial shift in the eddy heat transport of the middle troposphere.

The most notable feature associated with faster rotation rates from dishpan (Fultz, 1959) and GCM experiments (Hunt, 1979; Williams, 1988) is its effect on heat transport. Faster rotation rates decrease the size of transient and stationary eddies, while breaking down mean meridional circulation. The smaller eddies transport heat less effectively to the middle and high latitudes causing decreased polar temperatures, while the meridional circulations are weaker and confined to lower latitudes. The amounts of vertically integrated sensible and latent heat transported by the eddies are smaller in middle latitudes of FastL and larger in the subtropics (Figure 4.1), which is in agreement with the results of Hunt (cf. Figure 17, 1979) in the middle latitudes. But, contrary to the earlier GCM studies, larger heat transport by transient eddies occurs in the upper troposphere in this study.

The larger heat transport by transient eddies is associated with the equatorial shift of the jet. A maximum in the transient eddy heat transport is noted poleward

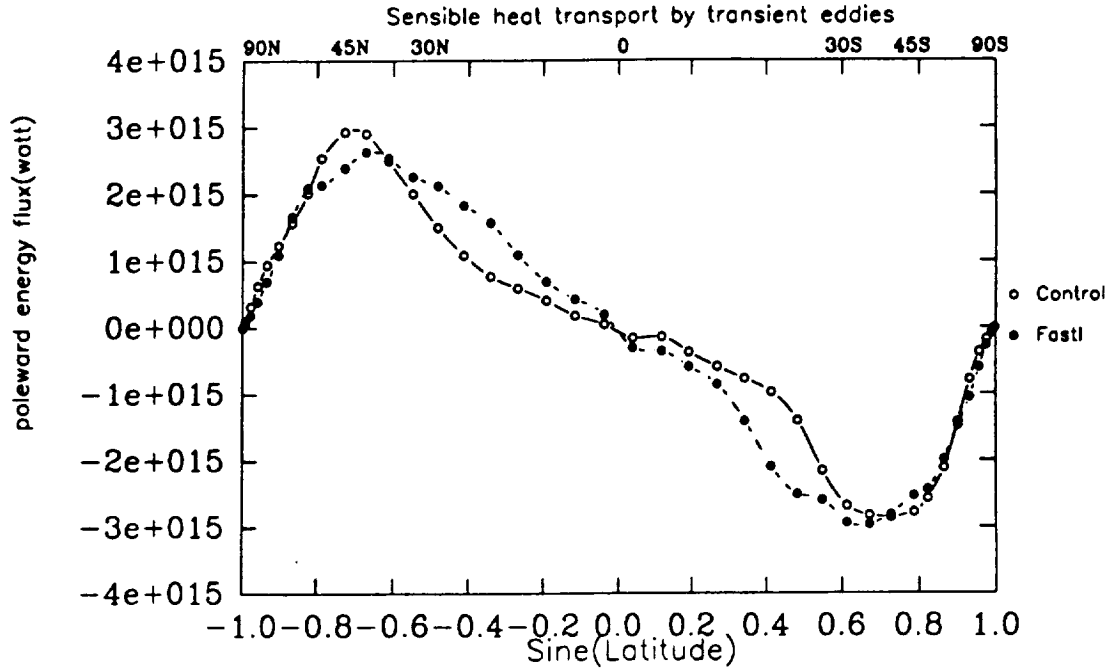
of the jet from observations and the control simulation. The maximum corresponds to those transient eddies associated with the jet. Therefore, when the jet is shifted equatorward with a faster rotation rate, the maximum heat transport also shifts equatorward. This allows for an increase in the low latitudes and a decrease in the middle latitudes of the upper troposphere. The latitudes poleward of the new maximum serve as a sink for the larger heat transport. This features occurs for all simulations with a faster rotation rate.

Heating in the upper tropospheric middle latitudes causes relative humidity and clouds to decrease, allowing more solar radiation to reach the ground. The larger solar radiation allows warmer surface temperatures, thereby reducing the impact of less efficient heat transport by transient eddies. Warmer surface temperatures in the middle latitudes are not shown in the other studies because no increases in the poleward eddy heat transport were noted. In addition, warming from cloud changes is not possible because of fixed zonal cloud fractions in the earlier GCM studies. While it is possible that higher resolution may show more similarities to the studies by Hunt and Williams, these results suggest that dynamics should not be consider alone.

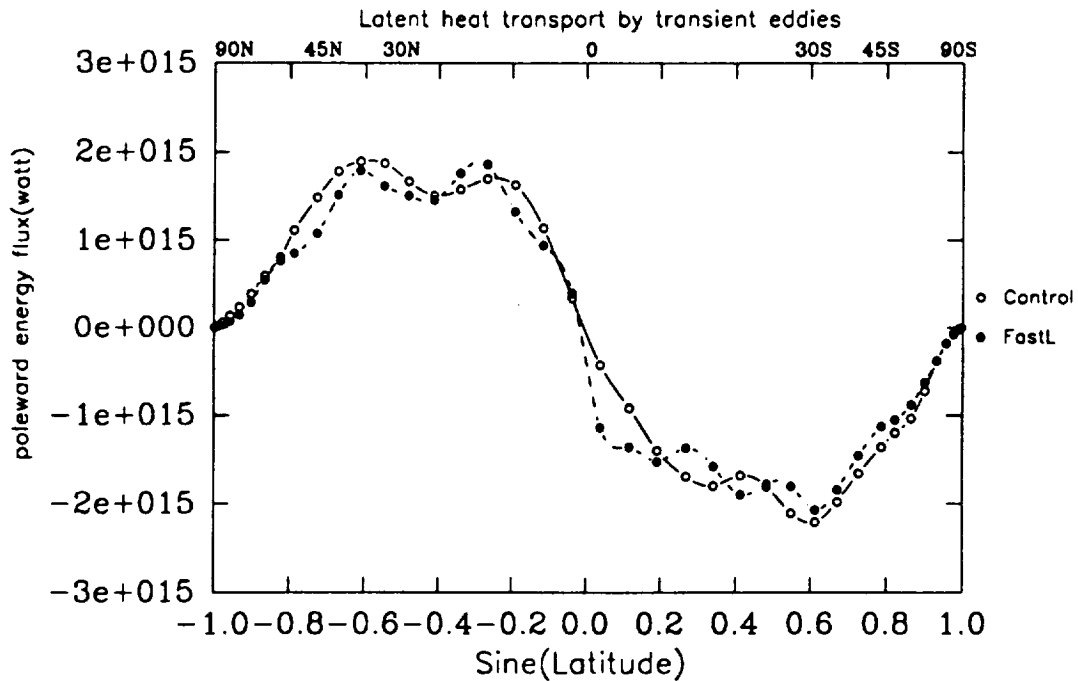
When a faster rotation rate is applied with a 10% reduction in the solar constant, significant warming occurs throughout the atmosphere (Figure 3.34). This unexpected warming is generated by larger poleward fluxes of latent heat transported by transient eddies (Figure 4.2). The decrease in clouds allows more solar radiation at the surface, which melts sea ice and allows for more atmospheric water vapor which is then transported by the transient eddies and mean motions. A slight decrease in sensible heat transported is noted in the midlatitudes.

4.2 Land Fraction

A global ocean is simulated under present-day solar luminosity in section 3.2 and

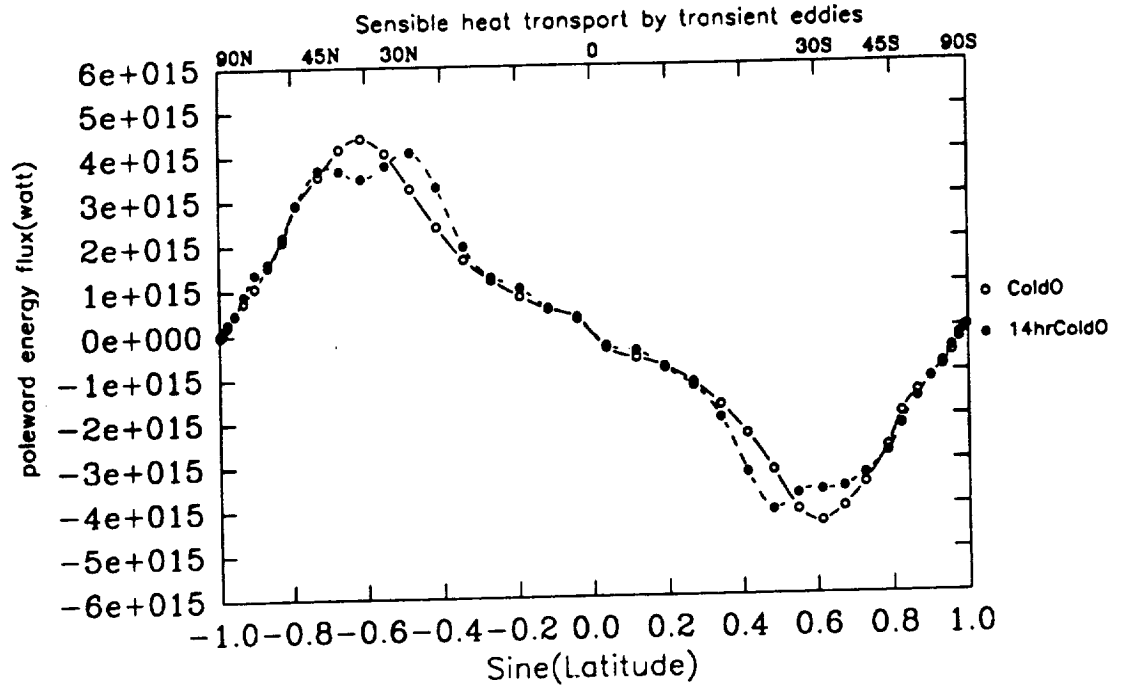


(a) Sensible heat. Units: Watts.

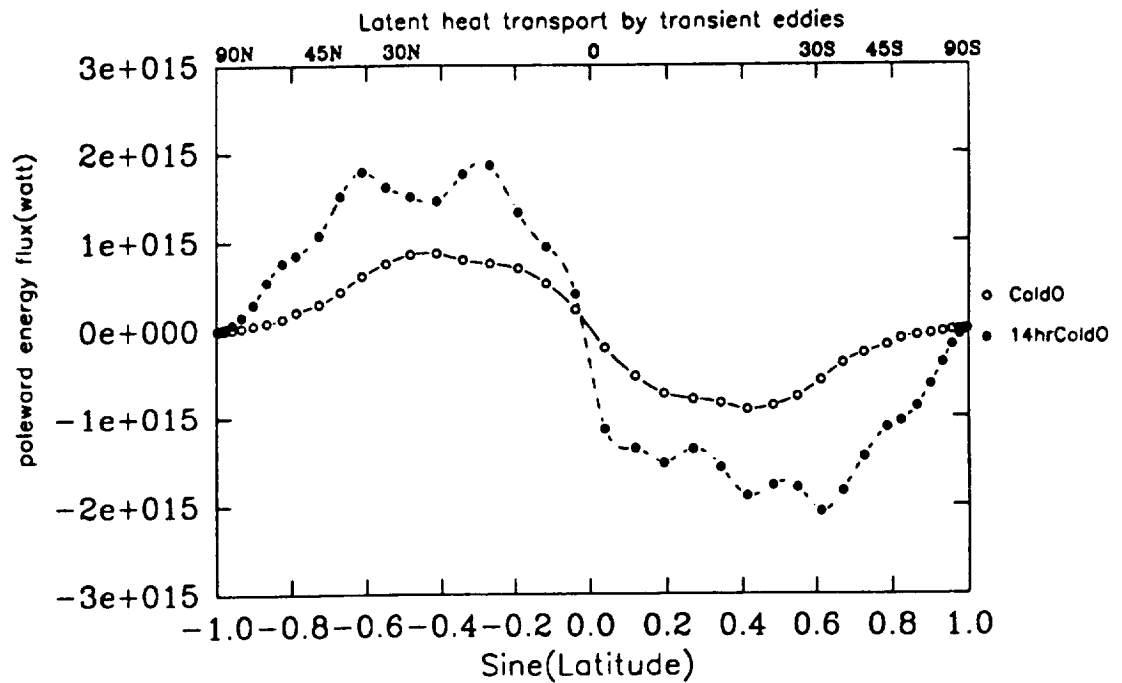


(b) Latent heat. Units: Watts.

Figure 4.1: Poleward flux of sensible and latent heat for FastL and the control. (a) sensible; (b) latent.



(a) Sensible heat. Units: Watts.



(b) Latent heat. Units: Watts.

Figure 4.2: Poleward flux of sensible and latent heat for 14hrColdO and ColdO. (a) sensible; (b) latent.

is compared to the present-day climate simulation. A summary of the results includes (1) warmer surface temperatures at all latitudes, (2) very small amounts of sea ice confined to the highest latitudes, (3) larger atmospheric water-vapor amounts, causing a large greenhouse effect in the troposphere, (4) higher precipitation, evaporation, absorbed solar radiation, and outgoing longwave radiation; (5) a slightly stronger jet than the control, and (6) increased tropospheric temperatures.

The studies of Kuhn et al. (1989) with an EBM indicate that continents have only a small effect on climate. But their model does not include a hydrologic cycle nor are atmospheric dynamics taken into account. In contrast, the results of this study show that significant warming occurs at all latitudes, with the largest amounts in polar regions due to a lower surface albedo.

The hydrologic cycle associated with a global ocean appears more vigorous with higher precipitation, evaporation, and atmospheric watervapor. The larger water-vapor amounts are carried poleward by transient eddies in the form of latent heat enhancing warming in the middle and high latitudes (Figure 4.3). The larger water-vapor amounts act as a strong greenhouse gas with a 36 W m^{-2} increase in the downward longwave radiation at the surface compared to the control (Table 3.2). An interesting feature is the change in cloud distribution compared to the control, where an increase in polar and high altitude clouds is noted (Figure 3.25). This pattern is very similar to that of current GCM CO_2 simulations in which CO_2 is doubled (Washington and Meehl, 1983).

4.3 Solar Luminosity

In section 3.2, solar luminosity is reduced by 10% (ColdO) and zero land fraction is assumed in the simulation. The results for this simulation are (1) colder surface and atmospheric temperatures, (2) a large reduction in water vapor, evaporation and precipitation rates; (3) decreased absorbed solar radiation by the earth-atmosphere

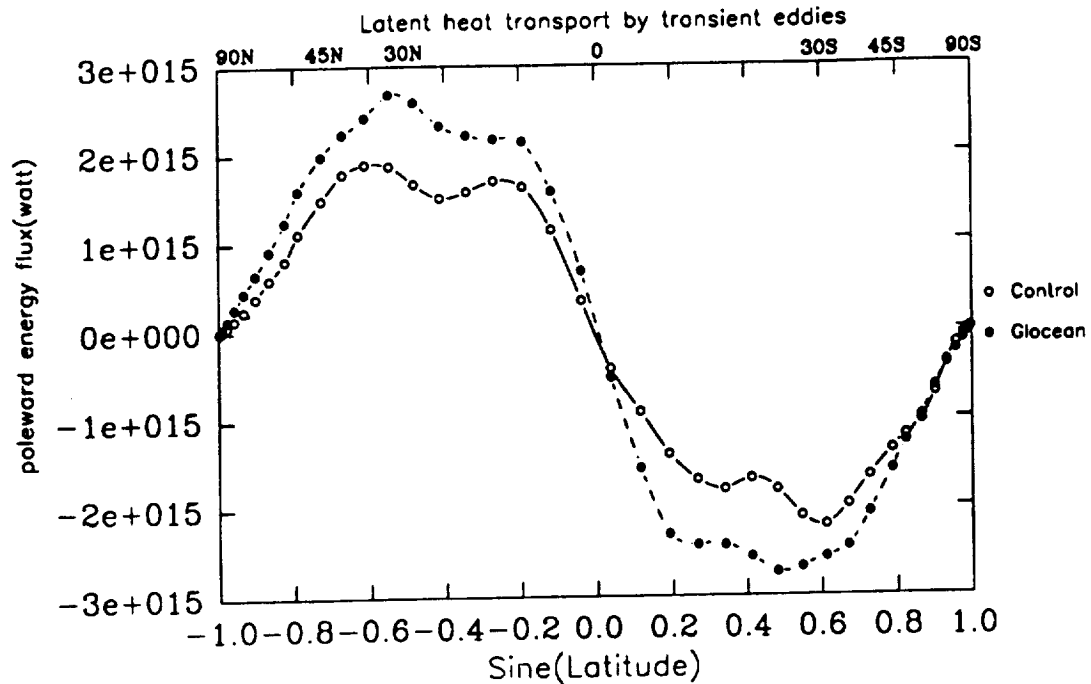


Figure 4.3: Poleward flux of latent heat. Units: Watts.

system and OLR, (4) decreased polar clouds and relative humidity, and (5) increased heat transport by transient eddies.

The earlier results of Sellers (1969) and Budkyo (1969) with EBM's suggest a frozen planet is possible with a few-percent decrease in the solar constant. Wetherald and Manabe (1975) conducted GCM experiments to examine the influence of solar-constant changes on climate. When the solar constant was reduced by 4%, they found a reduction in surface temperature, precipitation, evaporation, and poleward transport of moist static energy. The eddy kinetic energy and poleward transport of dry static energy increased with the lower solar constant. The solar constant had to be reduced by more than 4% to create an ice-cap instability that would lead to frozen-earth conditions.

The 10% reduction in the solar constant of section 3.2 does not produce a frozen earth, but it does allow sea ice in subtropical regions. Equatorial temperatures

are approximately 285 K (Figure 3.17), although the global mean temperatures are below the freezing point of sea ice (Table 3.2). The results in section 3.2 show many of the responses noted by Wetherald and Manabe (1975), namely, the reductions in precipitation, evaporation surface temperature, and decreases in poleward latent heat fluxes by transient eddies (Figure 4.4). The reduction in atmospheric moisture and the equatorward extent of sea ice limits latent heat transport by transient eddies. An increase in poleward sensible heat fluxes by transient eddies (Figure 4.5) and eddy kinetic energy (Figure 4.6) indicate greater baroclinicity near the sea-ice edge.

A decrease in polar clouds is noted with a lower solar constant because of smaller water-vapor amounts. Decreased water vapor causes lower relative humidity. Wetherald and Manabe used fixed clouds in their experiment and, therefore, no comparisons can be made. The cloud increases, caused by a slight shift in the Hadley cell occur at the poleward edge of the Hadley cell in the control. The colder atmosphere in the high latitudes allows more solar radiation to penetrate the atmosphere, thereby creating a negative feedback.

4.4 Carbon Dioxide

Two experiments are carried out with 4 and 8 times increases in the control CO_2 concentration (330 ppm). The solar constant is reduced by 10% in both experiments and zero land fraction is assumed. The experiments denoted 4ColdO and 8ColdO are compared to ColdO (section 3.2). The following results are noted: (1) an increase in surface and tropospheric temperature and a decrease in stratospheric temperatures, (2) an increase in water vapor, precipitation, and evaporation for 8ColdO; (3) an increase in global mean clouds and relative humidity, (4) an increase in the jet speed winds for both 8ColdO and 4ColdO, and (5) an increase in OLR, with a large increase in the global mean downward longwave radiation at the surface.

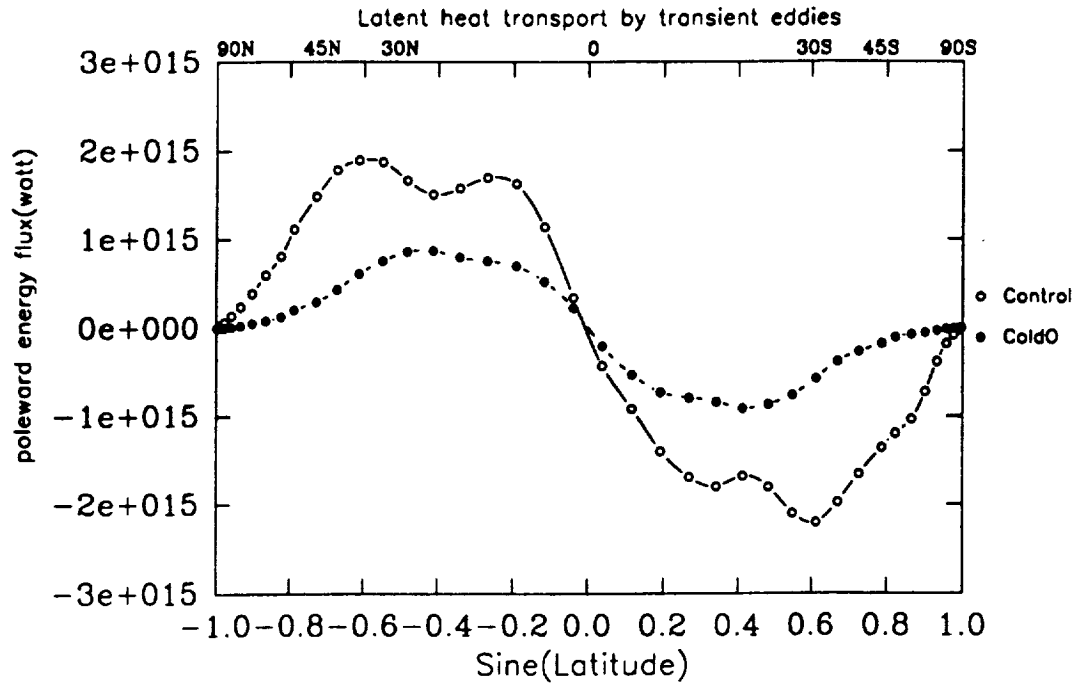


Figure 4.4: Poleward flux of latent heat. Units: Watts.

Tropospheric water vapor amounts rise with increasing CO_2 concentrations (Figure 3.43), allowing more absorption of longwave radiation and enhancing the tropospheric warming. The melting of sea ice makes available additional water vapor from the surface. The increased water vapor allows additional latent heat to be transported poleward by eddies (Figure 4.7). The increased water vapor and higher CO_2 concentrations bring about a strong greenhouse effect, with a large increase in downward longwave radiation at the surface (Table 3.3).

Because of the input of larger amounts of CO_2 into the atmosphere by anthropogenic sources, many studies of the effects of higher CO_2 concentrations have been undertaken to understand how climate is affected by this greenhouse gas (Schlesinger and Mitchell, 1987). The results of these studies show that when CO_2 concentrations are doubled, warmer tropospheric and cooler stratospheric temperatures evolve. Sea ice in high latitudes melt and add to the warming in high latitudes. High-altitude

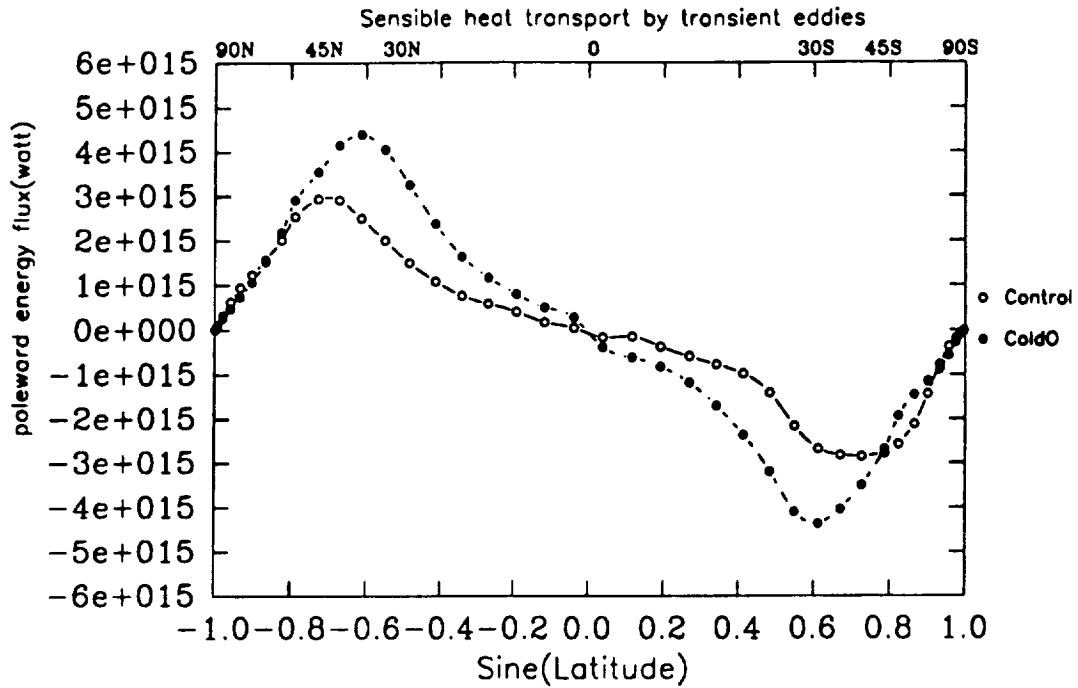


Figure 4.5: Poleward flux of sensible heat. Units: Watts.

and high-latitude clouds increase, with decreasing clouds in the middle and low latitudes below 300 mb. Similar occurrences are noted in the GCM simulations with higher CO_2 (section 3.3).

The results suggest that, if larger amounts of CO_2 are added under lower solar constant conditions, the melting of sea ice will add water vapor to the atmosphere and greater warming will occur.

4.5 Experiments with Combined Factors

Three experiments were carried out with 8 times CO_2 , zero land fraction, a rotation rate corresponding to a 14-hr day and 10, 15, and 20% decreases in the solar constant. The three experiments, denoted Ice1, Ice2, and Ice3, were compared to a global ocean experiment (Glocean) under present-day conditions (section 3.2). The following results were noted: (1) The global mean temperature decreased nonlinearly

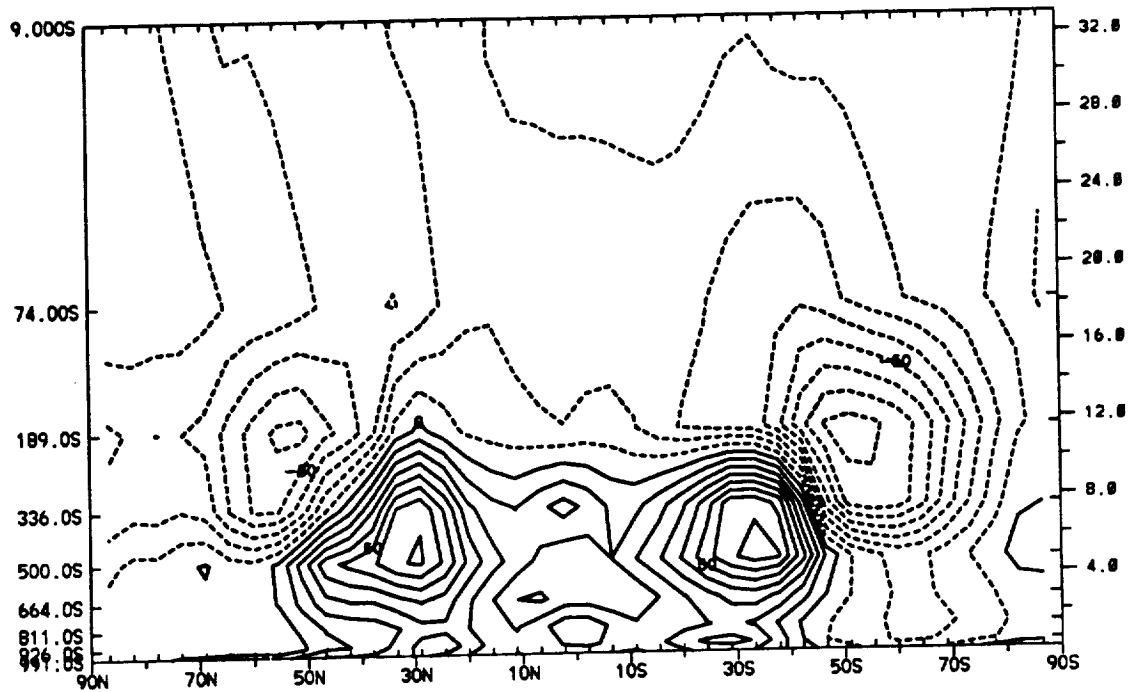


Figure 4.6: Difference in eddy kinetic energy. ColdO minus control.
Units: $\text{m}^{-2} \text{s}^{-2}$.

with decreasing solar constant. (2) A completely frozen surface did not occur for any of the cases considered. (3) Water vapor, evaporation, and precipitation decreased in all three cases in comparison to Glocean. (4) Clouds decreased in all three cases. (5) Absorbed solar radiation and OLR decreased. (6) An equatorial shift in the Hadley cell was noted in all three simulations. (7) There was a shift in spectral kinetic energy out to smaller wavelegnth.

The results of Kuhn et al. (1989) show that, even with the effects of land fraction and faster rotation rate (as a function of heat transport), very large amounts of CO_2 are needed to compensate for the lower solar constant. In contrast, the results of this study show that, although large amounts of CO_2 (at least 8 times the present) are needed to compensate for the lower solar constant, clouds and water vapor act as negative feedbacks and, therefore, high concentrations of CO_2 are not needed.

Water-vapor amounts are much smaller with lower solar constants and, therefore,

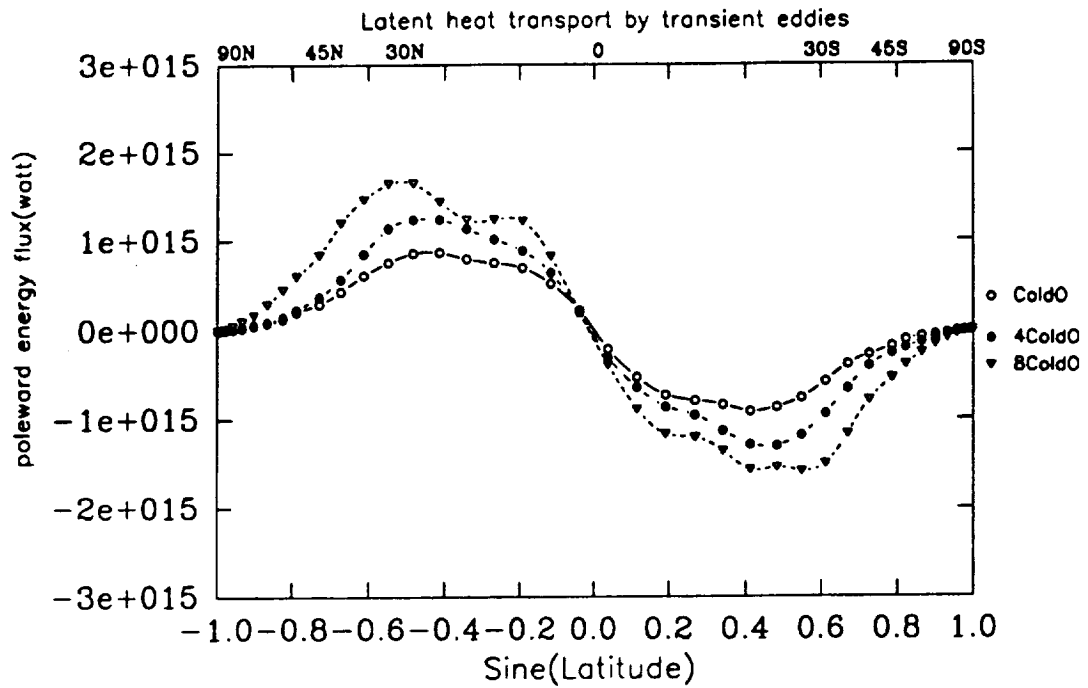


Figure 4.7: Poleward flux of latent heat. Units: Watts.

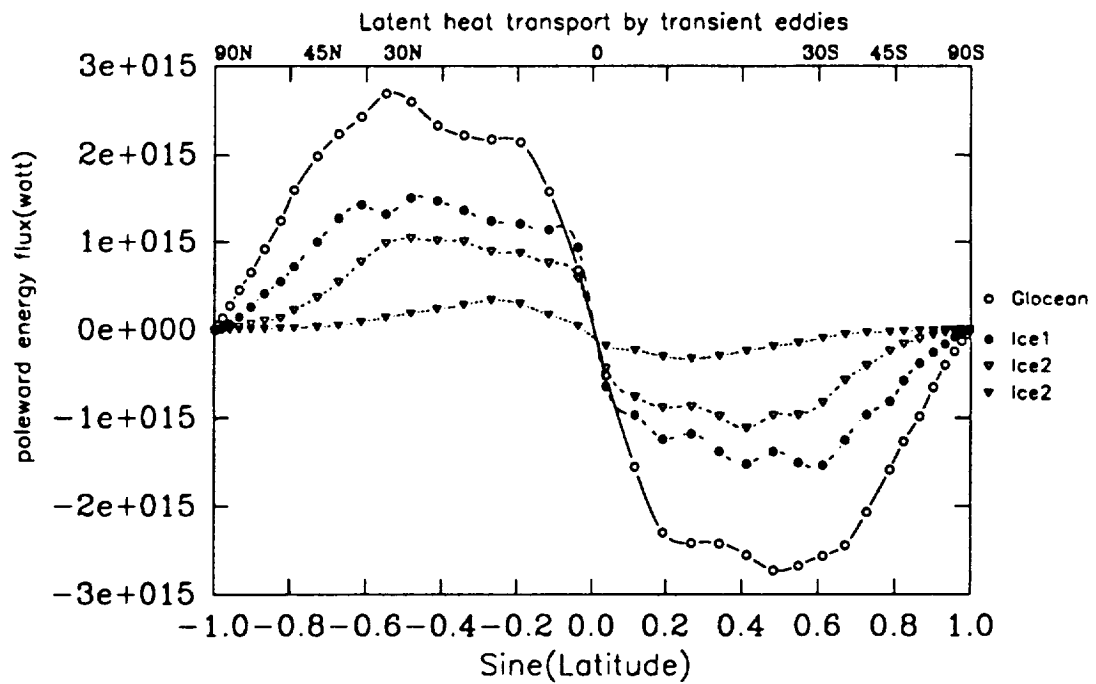


Figure 4.8: Poleward flux of latent heat. Units: Watts.

relative humidity and cloud fractions are reduced. The model results indicate that the vapor pressure—not the saturation vapor pressure is controlling factor—in determining relative humidity amounts. The lower solar constant acts as a negative feedback by reducing cloud fractions and allowing more solar radiation at the surface. If clouds were fixed, less solar radiation would reach the surface and sea ice would migrate to the equator with a solar constant of less than 20%. The smaller water-vapor amounts are reflected in the amount of latent heat transported poleward by transient eddies (Figure 4.8).

The faster rotation rate and higher CO₂ concentrations increase the surface temperature under the lower solar constant conditions. Decreases clouds from faster rotation allows more solar radiation at the surface, while increased CO₂ concentrations allows greater amounts of downward longwave radiation at the surface.

The implications of the results for the early Archean are (1) that smaller amounts of CO₂ concentrations are needed to keep sea ice from migrating to the equator, and (2) that clouds and water vapor have strong negative feedback properties with a lower solar constant, (3) dynamical changes cause clouds to decrease which allows more absorbed solar radiation at the surface.

CHAPTER V

CONCLUSIONS AND RECOMMENDATIONS

5.1 Conclusion

This study has evolved around the “Faint-Young Sun Paradox.” Results from earlier studies with simpler climate models suggest that the early earth had very large concentrations of CO_2 . These large concentrations counterbalanced the lower solar luminosity and kept the planet above freezing. The amount of CO_2 to keep the global mean surface temperatures above freezing has a lower limit of at least 25 times (Kiehl & Dickinson, 1987) the present concentrations. Previous studies used relatively simple models, such as energy balance and radiative-convective models.

In this study, the NCAR CCM is used with a swamp surface to investigate the roles of rotation rate, land fraction, higher CO_2 concentrations, and lower solar luminosity. The major conclusions of this study are as follows:

- A faster rotation rate, zero land fraction, and higher CO_2 concentrations increase the global and zonal mean surface temperatures. Reducing the solar constant lowers the global mean temperature.
- With a faster rotation rate, the total cloud fraction is reduced by roughly 20%. Both nonconvective and convective clouds decrease and are a result of

lower relative humidities. The smaller sized-eddies implicitly have smaller cloud fractions associated with them.

- A faster rotation rate causes the Hadley cell and jet to be shifted equatorward by approximately 10° , its intensity is reduced by one-half and the mean annual jet is reduced by approximately 10 m s^{-1} . Heat transport by transient eddies associated with the jets shifting equatorward causes relative humidity and clouds to decrease.
- Zero land fraction under present-day solar luminosity shows a global mean surface temperature increase of 4 K. Temperature increases are noted throughout the troposphere and parts of the stratosphere. Only small quantities of sea ice are noted.
- A decrease of 10% in the solar constant does not cause an ice-covered planet, but sea ice does migrate to near 30° of latitude. The global mean temperature is below freezing (264 K), but equatorial temperatures are near 285 K. Much colder polar regions diminished water-vapor quantities and reduce in relative humidity and, hence, clouds. Precipitation and surface evaporation rates have large declines.
- Larger CO_2 concentrations are added for a solar constant reduced by 10%. The results indicate that the global mean surface is increased by 5 K and 12 K for 4 and 8 times the present CO_2 concentration. Sea ice forms some $5\text{--}15^\circ$ poleward of its original position without elevated CO_2 concentrations. Tropospheric temperatures increase while stratospheric temperatures decrease. An increase in water vapor, precipitation, and evaporation occurs when CO_2 is added. Relative humidity and clouds increase for larger CO_2 concentrations. A large increase in downward longwave radiation causes surface temperatures

to increase. An increase in OLR is noted because of the warmer surface temperatures.

- The factor of 8 times the present CO₂ concentration, a rotation rate corresponding to a 14-hr earth day, zero land fraction, and a 10, 15, and 20% decrease in the solar constant are assumed in the final three simulations. Surface temperature decrease for all three experiments in comparison to a zero land fraction experiment with present-day solar constant. Temperatures decrease throughout much of the troposphere and stratosphere.
- A significant decrease in water vapor, precipitation, and evaporation takes place. OLR, downward longwave radiation, and absorbed solar radiation also decrease. The cloud field in each experiment decreases by roughly 20%. A significant reduction in relative humidity is also noted.
- An equatorial displacement in the Hadley cell is noted in all three experiments. Both the Hadley and Ferrel cells have been reduced in intensity. The mean annual jet has also been shifted equatorward. The maximum wind speeds with the jets are smaller in value. When a 20% decrease in the solar constant is assumed, three mean annual jets evolve—one centered over the equator and the others near 25°N and 25°S. These jets are lower in the atmosphere, and reflect the sinking of the polar tropopause to near .500s.
- Finally, a shift in the spectral kinetic energy out to longer wavenumbers is noted in all three experiments.

5.2 Recommendations

The use of the GCM to study climatic conditions of the Archean has revealed

many feedbacks that are necessary in order to properly examine the "Faint-Young Sun paradox." Considerable research must follow. These are recommendations:

- The significant changes of clouds to due rotation rate change warrant further research. Different cloud schemes and higher resolution may offer some insight into the changes in cloud reduction. The spectral kinetic energy diagrams also indicate that a peak occurs near the models truncation point. Higher resolution will resolve this problem. To understand more clearly summer and wintertime changes, the rotation rate should altered under wintertime solar conditions and, if possible, the entire annual cycle.
- A mixed-layer model should be incorporated into future studies. A swamp ocean does not allow heat storage, which may be significant, and the swamp ocean causes too much sea ice which is regulated by temperature alone. A mixed layer model will allow use of a thermodynamic sea ice model to give a better representation of sea ice. Because of its storage properties, a mixed-layer model will likely show larger temperature increases for higher CO₂ concentrations.
- Higher CO₂ concentrations should be included in the model. The results indicate that 8 times the present CO₂ concentration avoids an ice-albedo catastrophe. The work of Kiehl and Dickinson (1987) indicates that the 9.3 and 10.4 μm CO₂ absorption bands may be important for higher CO₂ concentrations.
- Ozone should eventually be taken from the model atmosphere in order to get the most accurate account of climatic conditions for the early earth. Kiehl and Boville (1988) have simulated the climate without ozone. However, if the other climatic factors, such as larger CO₂ concentrations, a faster rotation rate, and lower solar luminosity are assumed, model results would change significantly under zero ozone conditions.

BIBLIOGRAPHY

- [Washington and Parkinson, 1986] Washington, W. M., and Parkinson, C. L. An Introduction to Three-Dimensional Climate Modeling. University Science Books, Mill Valley, Calif. and Oxford University Press, N.Y., 422pp.
- [Washington and VerPlank, 1986] Washington, W. M., and VerPlank, L. J., A description of coupled general circulation models of the atmosphere and oceans used for CO₂ studies. NCAR Technical Note, Ncar/ TN-271+EDD, National Center for Atmospheric Research, Boulder, CO, 29pp., 1986.
- [Washington & Meehl, 1986] Washington, W. M. and Meehl, G. A. "General Circulation Model CO₂ Sensitivity Experiments: Snow-Sea Ice Albedo Parameterizations and Globally Averaged Surface Air Temperature." *Climatic Change* 8, 231-241, 1986
- [Wetherald and Manabe 1975] Wetherald R. T. and S. Manabe "The Effects of Changing the Solar Constant on the Climate of a General Circulation Model." *Journal of the Atmospheric Science* 32, 2044-2059, 1975.
- [Williams, 1988] Gareth P. Williams "The Dynamical Range of Global Circulations-I." *Climate Dynamics* 2: 205-260, 1988.